INVESTIGATION OF ALTERNATIVE BIOMASS FUELS AND TURKISH LIGNITES AT HIGH HEATING RATE PYROLYSIS AND COMBUSTION CONDITIONS

A THESIS SUBMITTED TO
THE GRADUATE SCHOOL OF NATURAL AND APPLIED SCIENCES
OF
MIDDLE EAST TECHNICAL UNIVERSITY

BY

DUARTE MAGALHAES

IN PARTIAL FULFILLMENT OF THE REQUIREMENTS
FOR
THE DEGREE OF DOCTOR OF PHILOSOPHY
IN
MECHANICAL ENGINEERING

FEBRUARY 2021

Approval of the thesis:

INVESTIGATION OF ALTERNATIVE BIOMASS FUELS AND TURKISH LIGNITES AT HIGH HEATING RATE PYROLYSIS AND COMBUSTION CONDITIONS

submitted by **DUARTE MAGALHAES** in partial fulfillment of the requirements for the degree of **Doctor of Philosophy** i**n Mechanical Engineering, Middle East Technical University** by,

Prof. Dr. Halil Kalıpçılar
Dean, Graduate School of **Natural and Applied Sciences** _____

Prof. Dr. Sahir Arıkan
Head of the Department, **Mechanical Engineering** _____

Assist. Prof. Dr. Feyza Kazanç Özerinç
Supervisor, **Mechanical Engineering, METU** _____

Prof. Dr. Ahmet Yozgatlıgil
Co-Supervisor, **Mechanical Engineering, METU** _____

Examining Committee Members:

Prof. Dr. Abdullah Ulaş
Mechanical Engineering, METU _____

Assist. Prof. Dr. Feyza Kazanç Özerinç
Supervisor, Mechanical Engineering, METU _____

Prof. Dr. Murat Köksal
Mechanical Engineering, Hacettepe University _____

Prof. Dr. Deniz Üner
Chemical Engineering, METU _____

Assist. Prof. Dr. Sıtkı Uslu
Mechanical Engineering, TOBB ETÜ _____

Date: 12.02.2021

I hereby declare that all information in this document has been obtained and presented in accordance with academic rules and ethical conduct. I also declare that, as required by these rules and conduct, I have fully cited and referenced all material and results that are not original to this work.

Name Last name : Duarte Magalhaes

Signature :

ABSTRACT

INVESTIGATION OF ALTERNATIVE BIOMASS FUELS AND TURKISH LIGNITES AT HIGH HEATING RATE PYROLYSIS AND COMBUSTION CONDITIONS

Magalhaes, Duarte
Doctor of Philosophy, Mechanical Engineering
Supervisor : Assist. Prof. Dr. Feyza Kazanç Özerinç
Co-Supervisor: Prof. Dr. Ahmet Yozgatlıgil

February 2021, 228 pages

The objective of this work was to investigate alternative Turkish fuels for their ignition, combustion, pyrolysis, and gasification behavior and to select alternative fuels for co-firing, co-pyrolysis, and co-gasification applications based on low and high heating rate experimental results. Agricultural biomass (olive residue, almond shell, and hazelnut shell) and Turkish lignites (Tunçbilek, and Soma) were chosen as the feedstocks. Several experimental rigs used such as thermogravimetric analyser; wire mesh reactor; drop tube furnace; and entrained flow reactor were used to fully characterise the fuels at different heating rates. The results showed that the ignition delay time of different feedstocks converged with increase in temperature and thus based on the ignition delay time biomass and lignites can be co-fired provided that in a similar particle size. Single particle observation during high heating rate combustion showed that torrefied biomass and Tunçbilek lignite had comparable burnout times, whereas extensive fragmentation of Soma lignite resulted in short burnout times. High heating rate combustion observations were found useful as coal classification tool. The pretreatment of biomass and co-firing allowed significant reduction of PM2.5. Results from fast pyrolysis of lignocellulosic

biomass showed that laboratory fractionated biomass provided high purity components and better predictions of the char yields as compared to commercial samples. The fast pyrolysis stage did not have a significant effect on the char co-gasification kinetics.

Keywords: alternative biomass; Turkish lignite; combustion; pyrolysis; high heating rate

ÖZ

ALTERNATİF BİYOKÜTLE VE TÜRK LİNYİTLERİNİN YÜKSEK ISITMA HIZLARINDA PİROLİZ VE YANMASININ İNCELENMESİ

Magalhaes, Duarte
Doktora, Makina Mühendisliği
Tez Yöneticisi: Dr. Öğr. Üyesi Feyza Kazanç Özerinç
Ortak Tez Yöneticisi: Prof. Dr. Ahmet Yozgatlıgil

Şubat 2021, 228 sayfa

Bu çalışmanın amacı, Türkiye'deki alternatif yakıtların tutuşma, yanma, piroliz ve gazlaştırma davranışlarını araştırmak, düşük ve yüksek ısıtma hızlı deneysel sonuçlara dayalı olarak birlikte yanma, piroliz ve gazlaştırma uygulamaları için alternatif yakıtların seçilmesidir. Tarımsal biyokütle (zeytin atığı, badem kabuğu ve fındık kabuğu) ve Türkiye linyitleri (Tunçbilek ve Soma) yakıt olarak seçilmiştir. Yakıtları farklı ısıtma oranlarında tam olarak karakterize etmek için termogravimetrik analizör, tel örgü reaktör, düşey borulu fırın ve sürüklenmiş akış reaktörü gibi çeşitli deneysel donanımlar kullanıldı. Sonuçlar, farklı yakıtların tutuşma gecikme süresinin artan sıcaklık altında birleştiğini ve dolayısıyla ateşleme gecikme süresine dayalı olarak biyokütle ve linyitlerin, benzer bir parçacık boyutunda olması koşuluyla, birlikte yakılabileceğini gösterdi. Yüksek ısıtma hızındaki yanma sırasında tek parçacık gözlemi, torifiye edilmiş biyokütle ve Tunçbilek linyitinin benzer yanma sürelerine sahip olduğunu, Soma linyitinin yoğun parçalanmasının ise kısa yanma sürelerine neden olduğunu göstermiştir. Kömür sınıflandırması için yüksek ısıtma hızında yapılan yanma gözlemleri yararlı bulunmuştur. Biyokütlenin ön ısıl işleme tabi tutulması ve birlikte yanma, PM2.5'te

önemli bir düşüşe imkan sağladı. Linyoselülozik biyokütlenin hızlı pirolizinden elde edilen sonuçlar, laboratuvarda parçalanmış biyokütlenin yüksek saflıkta bileşenler ve ticari numunelere kıyasla çar verimlerinin tahminlerini daha iyi sağladığını göstermiştir. Hızlı piroliz aşaması, çar birlikte gazlaştırma kinetiği üzerinde önemli bir etkiye sahip olmamıştır.

Anahtar Kelimeler: alternatif biyokütle; Türk linyiti; yanma; piroliz; yüksek ısıtma hızı

To Marta

ACKNOWLEDGMENTS

First and foremost I want to thank my advisor Asst. Prof. Dr. Feyza Kazanç for her support and friendly advice throughout my PhD. Her trust gave me the liberty and confidence to grow as a researcher. My co-advisor Prof. Dr. Ahmet Yozgatlıgil always supported and encouraged me with kind words and I am also grateful to him.

I would like to acknowledge the financial support from Tübitak (The Scientific and Technological Research Council of Turkey) through grants 3501 (no. 214M332) and 1001 (no. 218M473). Partial financial support was also given by the Royal Society Advanced through Newton Fellowship, Ref. No: NA140020 (UK). The support of Middle East Technical University – Scientific Research Projects (METU-BAP) through grants GAP-302-2018-2743 and TEZ-D-302-2021-10750 is also acknowledged.

During my PhD I had the opportunity to collaborate with a number of people from whom I learned a lot. I would like to name Prof. Mário Costa and Dr. Miriam Rabaçal from Instituto Superior Técnico, Dr. Juan Riaza and Prof. Hannah Chalmers from the University of Edinburgh, Dr. Aidin Panahi and Prof. Yiannis Levendis from Northeastern University, and Prof. Leonidas Matsakas from Lulea University. A special thanks to Dr. Anna Trubetskaya from the University of Limerick for all the collaborative studies we had and have together and for being a mentor to me during the last stages of my PhD.

At Middle East Technical University I would like to thank Prof. Altan Kayran for granting access to the Composite Material Characterisation Laboratory, Center for Wind and Energy Research, and allowing my studies to proceed much faster. I would like to thank my colleagues Dr. Evan Fair Johnson and Dr. Sina Shafee for their friendship and for sharing the ups and downs of a PhD life at METU. I also would also like to thank all the MSc students that crossed my path during this time, particularly Kaan Gürel, Şener Akın, Burak Özer, and Alican Akgül.

Last but not least, I thank my parents and my sister for their emotional support and understanding during this long journey away from home, and for their confidence in me. A final special thanks goes to Mahsa for her constant and unconditional support, love, and encouragement during good and bad days.

TABLE OF CONTENTS

APPENDICES

LIST OF TABLES

TABLES

LIST OF FIGURES

FIGURES

CHAPTER 1

INTRODUCTION

1.1 Motivation

Coal demand at a global level rose 1% in 2017 and represented 38% of the total electricity generation in the world [1]. In Turkey a similar trend was observed and coal accounted for 33% of the electricity generation in 2017 [2]. In the same period, indigenous lignites accounted for the largest share of electricity generation from coal, at 80%, while imported bituminous coal accounted for 19% [3]. In Turkey, the large reserves of indigenous lignites (estimated at 15.6 billion tonnes), allied with an effort to decrease the energy dependence on imported fossil fuels, have generated incentives to increase the total installed capacity of lignite power plants by up to three fold by 2023 [3]. However, the burning of lignite coals presents several issues, such as the emission of pollutants (NO_x, SO_x, and particulate matter) as well as the emission of CO_2 greenhouse gas [4–8].

Co-firing coal with biomass can provide a transition route to cleaner and sustainable energy with relatively minor modifications on existing power plants [9–11]. Consequently, for countries to meet their emissions allowance and renewable energy obligations, the operation of the conventional thermal power stations that remain on the grid will need to change [12]. This will create a challenge for thermal power plants to increase the use of biomass co-firing with fossil fuels, or build new units dedicated to neat biomass firing.

The European Commission has established the Renewable Energy Directive that sets a binding target of 32 % of renewables by 2030, as well as targets for a climate-neutral economy by 2050 [13]. In this landscape, carbon-neutral biomass is of crucial importance, since coal-fired power plants can be retrofitted, and new biomass-fired

plants can be commissioned. Moreover, biomass utilisation must be sustainable itself, and the minimisation of forest-intensive biomass and usage of biomass wastes is pressing. In this scope, agricultural residues are key to ensure a reduction in CO_2 emissions and prevent deforestation. Biomass energy production in Turkey using agricultural residues is expected to grow from 2.8 Mtoe in 2016 to 4.9 Mtoe by 2030, whereas the production of biomass from forest residues is expected to decrease from 4.8 Mtoe to 3.3 Mtoe [14]. However, agricultural biomass and lignite coals are very distinct fuels, and to properly burn them in the same boiler comprehensive knowledge of their flame characteristics, burnout times, particle temperatures, and combustion kinetics is required to ensure sufficient particle residence time in the boiler and allow for a stable flame and for sufficient energy output [15–17].

1.2 Objectives

The objective of the work presented herein is the characterisation of agricultural biomass and Turkish lignites for their ignition, combustion, pyrolysis, and gasification behaviours utilising a wide array of techniques with the aim of selecting alternative fuels for a smooth transition from pulverised coal power plants to co-firing, and, ultimately, biomass fired plants. Specifically, fuels will be analysed using different experimental rigs that allow their (co)-pyrolysis and/or (co)-combustion to be investigated in conditions that partially emulate those typically found in large scale pulverised combustion applications.

CHAPTER 2

LITERATURE REVIEW

In this Chapter a brief review of the literature is presented. In section 2.1 some of the physical and chemical properties of biomass and coal are given. The review then focuses on aspects relevant to the ignition (2.2), combustion (2.3), pyrolysis (2.4), and gasification (2.5) of biomass and coal fuels.

2.1 Biomass and coal properties

Biomass and coal present distinct properties. Biomass is composed of three main components: cellulose, hemicellulose, and lignin. Lignin closely resembles the structure of coal because of its aromatic compounds. Both cellulose and hemicellulose are polysaccharides. Cellulose is a linear polysaccharide and is therefore the largest single component that exists in biomass [18]. Hemicellulose is a polysaccharide composed of several monomers, and for that reason less stable than cellulose. Moreover, these three components can be distinguished by their degree of polymerization, which in ascendant order is: hemicellulose; cellulose; and lignin. Depending on its origin, there are numerous types of biomass, such as wood and woody, herbaceous and agricultural, animal biomass, and contaminated biomass [19]. More information on biomass properties can be found elsewhere [19–21].

Coal is originated from the compression at high pressures and temperatures of dead vegetation. Because of this fact, its properties are highly dependent on the geographical region and on the aging time. The most remarkable consequence is that with longer compression the carbon content increases. Accordingly, coal can be classified from younger to older as: lignite, sub-bituminous, bituminous, and anthracite [22].

Both biomass and coal are typically characterised by ultimate and proximate analyses. Ultimate analysis gives the content of carbon, hydrogen, nitrogen, oxygen, and sulphur elements and is a fast and convenient technique to categorise and compare fuels, using, for instance, the Van Krevelen diagram. In this diagram, the H/C and O/C molar ratios are plotted to categorize/compare coal and biomass fuels. Proximate analysis provides information on the moisture, volatile matter, fixed carbon, and ash content of the fuels.

In spite of their differences, there are pre-processing techniques that enable biomass properties to become coal-like. One of such techniques is torrefaction, which consists of heating raw biomass at 200-300 ºC under inert atmosphere. This process eliminates moisture and reduces the content of light hydrocarbons, with subsequent increase in calorific value, shelf-life, and grindability of the resultant biomass [23–25].

2.2 Ignition

In order to ensure a safe handling of solid fuels, the self-ignition propensity during processing, transportation, storage and conveying needs to be well understood. Flame stability during (co-)firing of coal and/or biomass is an issue to be taken into account when designing a new boiler or retrofitting existing ones and is largely dependent on the particle ignition behaviour. The fuel type and composition, and the surrounding oxidizing atmosphere temperature and composition are some of the parameters that strongly affect the ignition of solid fuels at both low and high heating rates.

2.2.1 Ignition at low heating rates

Thermogravimetric analyser (TGA) and TGA-DSC (differential scanning calorimetry) are commonly used to investigate the ignition at low heating rates,

whether it is the characteristic ignition temperature(s) [26–35], or the self-ignition risk of solid fuels [36–39].

A number of studies have focused on the influence of the fuel type [26,27,30,32–35], heating rate (5-40 K/min) [26,27] and atmosphere composition (air, O_2/N_2 and O_2/CO_2) [29,31,35] on the characteristic ignition temperatures. Both TGA and TGA-DSC experiments indicate that the ignition temperature of biomass fuels is typically lower than that of lignite fuels regardless of the biomass or lignite type. The ignition temperature of biomass fuels fall in a range between 470 - 540 K and that of lignite fuels in a range between 550 - 630 K [26–30,37,38,40,41].

Self-ignition risk assessment of biomass and lignite fuels is vital for their transportation and storage. More recently, a number of authors have assessed the self-ignition risk under low heating rates using TGA [36,38,39,42]. Since a comprehensive parameter to evaluate the ignition susceptibility of biomass and coal fuels is often needed, Querol Aragón et al. [43] established a TGA based self-ignition risk plot based on the TG characteristic temperature in combustion with pure oxygen and on the activation energy from conventional air combustion, which enables an easy classification of biomass and coal in terms of self-ignition. According with this criterion, biomass fuels and high volatile coals have a high to very high propensity of self-ignition, whereas low volatile coals present a medium- to low-risk of self-ignition [36,38,39,42].

The TGA-DSC technique was also used to determine the ignition mode of solid fuels by Chen et al. [41], who examined the effect of the coal rank on the ignition mode. According with Chen et al. [41], ignition can take place in three distinct modes: *homogeneous* when only gas-phase reactions occur between the volatiles and oxygen; *heterogeneous* for the case of solid-gas-phase reactions between char and oxygen; or *hetero-homogeneous* if both gas-phase and solid-gas-phase reactions are present at the moment of ignition.

2.2.2 Ignition at high heating rates

Technological advances have enabled high-speed cinematography to become reliable, accurate, and affordable, thus enabling the visualisation of ignition events that typically take place within milliseconds. Entrained flow reactor (EFR) and drop tube furnace (DTF) are typically focused for the analysis of the ignition mode and ignition delay time of single fuel particles [44–49] or dispersed particle jets [50–53]. A number of recent studies have addressed the effect of parameters such as the fuel type [45,46,48], particle size [46] and atmosphere temperature and composition [44–48] on the ignition delay time and ignition mode.

In most high heating rate studies, the ignition mode is defined with respect to the type of reaction occurring: homogeneous (gas-gas reaction), heterogeneous (gas-solid reaction), or mixed (both types of reactions), in line with low heating rate ignition. However, unless the diagnostics technique allows identifying tracers of homogeneous and heterogeneous reactions, it is not possible to distinguish between reaction modes (homo- or heterogeneous) close to the surface. More recently, Simões et al. [46], who captured the total light emitted by single particles, use the definition of gas-phase and surface ignition. As discussed by Howard and Essenhigh [54,55], the volatiles flame (homogeneous reaction) can lift from the particle or can "attach" to its surface.

The definition of ignition onset has been an ambiguous subject and depends largely on the type of diagnostics method used. A number of authors have applied high-speed imaging techniques to capture either chemiluminescence emission of diluted particle streams [50,52] or visible light signal of single particle ignition [44–46,48,49], and determine the ignition delay time and ignition mode. As a result, it is possible to find in the literature various definitions for the ignition mode and various ignition onset criteria, which are basically setup dependent. For instance, when the total emitted light was captured, the ignition criterion was either based on visual observation [45,48] or based on a given percentage of the maximum intensity

collected from each event [46,51]. This value is setup dependent and it is adjusted to provide the best results for all conditions studied.

The ignition mode of different rank coals was reviewed by Khatami and Levendis [56]. Anthracite and semi anthracite undergo homogeneous ignition, bituminous coals undergo homogeneous ignition, and lignite samples experience hetero-homogeneous ignition. As for biomass, Riaza et al. [48]reported homogeneous ignition for several residues, namely pine sawdust, torrefied pine sawdust, sugarcane bagasse and olive residues. Simões et al. [46] reported gas-phase ignition for pine bark, kiwi branches, vine branches and sycamore branches, and surface ignition for wheat straw particles.

Khatami et al. [57] use three-color pyrometry to measure the ignition delay time of various rank coals and define the ignition onset as the point of maximum particle temperature gradient (max. dT_p/dt). The authors observe that high rank coals tend to present the longest ignition delay times (~30 ms), followed by lignite (~15 ms), bituminous coal (~10 ms), and lastly by sugarcane bagasse (1-2 ms). In addition, Simões et al. [46] showed that different biomass fuels (wheat straw and pine bark), with the same particle size, present similar ignition delay times for the same test condition (15-20 ms under an atmosphere temperature of 1500 K, and 7-10 ms under 1800 K). The authors also report ignition delay times for 80-90 µm biomass particles (15-20 ms) lower than those for 224-250 µm biomass particles (20-30 ms). The oxygen concentration in the surrounding mixture also influences the ignition delay time due to changes in the reactivity of the mixture. Previous studies on coal ignition, namely by Molina and Shaddix [49,52] and by Khatami et al. [58], showed that the increase in the oxygen mole fraction from 20% to 80% led to lower ignition delay times under oxy-fuel conditions, whereas under O_2/N_2 mixtures the ignition times were not significantly affected. Furthermore, Simões et al. [46] observed that variations in the oxygen concentration from 3.5% to 7.6% resulted in a slight decrease of the ignition delay times of biomass fuels.

2.3 Combustion

The combustion of solid fuels can be divided into four main stages: drying (release of fuel moisture at ~100 ºC); devolatilization (conversion and release of volatile compounds); volatile combustion (oxidation of aforementioned volatile compounds), and char combustion (heterogeneous oxidation of the carbon). These stages are exemplified in Figure 2.1.

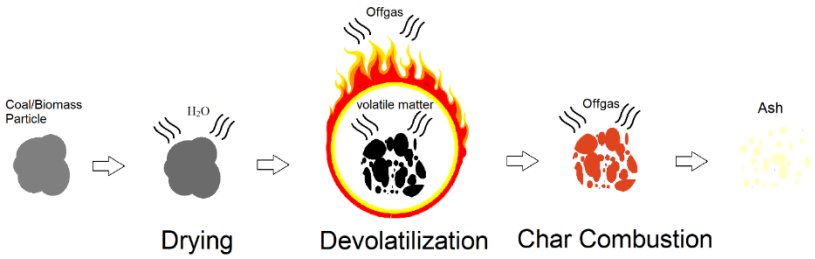

Figure 2.1. Main stages of the combustion of a coal or biomass particle [59].

It should also be mentioned that the combustion of solid fuels can be categorised in three different regimes, depending mostly on the temperature (see Figure 2.2). As described in Figure 2.2, at low temperatures the oxygen diffusion rate is very high, and the chemical reaction rate controls the process; at high temperatures the chemical reaction rate is high, and the oxygen diffusion controls the process. At intermediate temperatures, both chemical reaction and oxygen diffusion play an important role. The transition temperature from Regime I to Regime III is ~400 ºC for biomass fuels and ~450 ºC for lignite coal. These temperatures are obtained based on the calculation of the ratio of the carbon burnout rate over the mass transfer rate.

The combustion of solid fuels encompasses a multitude of research fields that include, but are not limited to, combustion behaviour; combustion kinetics; pollutant formation; particulate matter formation; and ash deposition. Furthermore, the aforementioned studies can be targeted for coals, biomass, or mixtures of the two.

Herein, emphasis will be given to previous studies on combustion behaviour (section 2.3.1), combustion kinetics (section 2.3.2), and particulate matter formation (section 2.3.3).

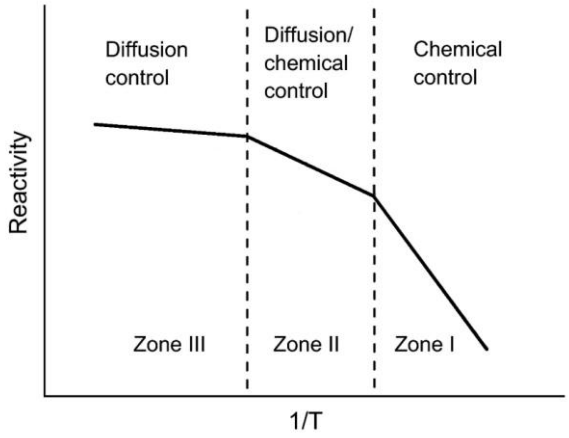

Figure 2.2. Rate-controlling regimes for solid fuel combustion [60].

2.3.1 Combustion behaviour

The combustion behaviour can be assessed using different types of experimental setups. Low heating rate combustion has been investigated using thermogravimetric analyser (TGA), whereas for high heating rate pulverized combustion researchers rely on equipment such as drop tube furnace (DTF) or entrained flow reactor (EFR). Low heating rate TGA studies give emphasis to the determination of the combustion behaviour and characteristic temperatures, as well as combustion kinetics (section 2.3.2).

The characteristic temperatures that describe the combustion process – decomposition temperature, ignition temperature, peak(s) temperature(s), and burnout temperature, can be determined from thermogravimetric-derivative thermogravimetric (TG-DTG) data. Since the heating rate is kept low, these temperatures are in fact minimum temperatures, meaning that, if exposed to higher

heating rates, a fuel can display significantly different combustion temperatures. The ignition of biomass typically occurs in the interval 200-250 ºC [32,40], regardless of the biomass type, whereas lignites tend to ignite at temperatures within 200-300 ºC, depending on the volatile matter content [33,34,40,61,62]. After ignition, the majority of low rank coals and biomass undergo devolatilization and volatile combustion during the first weight loss stage (200-400 ºC), followed by char combustion above 500 ºC [26,31,63]. For some low rank coals, however, combustion takes place in one single stage [26,62,64]. Biomass fuels generally experience burnout (i.e. the point at which all the fuel is oxidized and only the inorganic residue remains) at temperatures ranging from 500 to 600 ºC [31,32], and less frequently up to 800 ºC [26]. The burnout temperatures of lignite coals burning in air are typically in the order of 500-600 ºC [40,61,65,66], but can also reach 750 ºC [67].

In what concerns high heating rate combustion, in order to reduce the complexity of the process and obtain detailed data on combustion characteristics, studies use either diluted jets [68–73] or single particles [48,74–78]. These studies, albeit differing from large scale combustion systems, enable researchers to perform parametric analyses and provide important data for the validation of numerical models. As stated by Rabaçal et al. [79] in a recent review on the pulverised combustion of non-woody biomass residues, the main research groups currently working on single particle combustion opt to use non-intrusive techniques (e.g. high-speed cinematography, pyrometry, etc.), coupled to either drop tube furnaces [47,48,85,86,57,74,75,80–84] or entrained flow reactors [46,50,51,87–91], to (partially) emulate the conditions found in industrial furnaces. Recent studies have focused on fuel properties (e.g. coal rank [74], biomass type and origin [46,48,88–91], and inorganic content [89,92,93]), and on pre-treatment methods, such as torrefaction [75,82,83]. These parameters largely influence the combustion process; therefore their careful investigation is warranted. Levendis et al. [74] reported an overview on the coal rank dependency of the combustion characteristics and concluded that anthracite burned heterogeneously, bituminous coals burned in a dual-mode (homogeneous combustion of volatile matter in envelope flames, followed by heterogeneous char

oxidation), and lignites burned mostly hetero-homogeneously (simultaneous combustion) as a result of extensive fragmentation. Various biomass fuels such as sugarcane bagasse, pine sawdust, olive residue, and beech wood undergo dual-mode combustion [48,75,82,94], despite their considerable physical and chemical disparities. Nonetheless, biomass type and origin may affect important combustion parameters such as the flame and char temperatures, and the flame and char burnout times.

2.3.2 Combustion kinetics

Due to the complexity of combustion, devolatilization and volatile combustion, and char oxidation, are modelled separately. Devolatilization models can be of two types: semi-empirical (Arrhenius equation based), or predictive (phenomenological network) models that include detailed chemistry such as the coal percolation devolatilization (CPD) [95], or Bio-PoliMi [96] model, whereas Arrhenius models requires experimental combustion data, network models require a detailed chemical characterisation of the raw fuels.

For char oxidation, intrinsic kinetic models, based on the active site theory, have received major contribution from Langmuir-Hinshelwood [97]. In what respects predictive models, the combustion burnout kinetics (CPK) [98] is considered to be among the most inclusive. Moreover, less complex semi-empirical models have been developed [99,100], as described in the following paragraph.

In this review special emphasis will be given to the Arrhenius equation-based models since these models have been employed in the present work. Solid fuel Arrhenius type combustion kinetic modelling comprises two modelling approaches: model-free or model-fitting. Model free methods can be preferable to avoid modelling of complex reaction mechanisms. Since the chemical kinetic parameters are determined without using any specific model, the eventual errors which may arise from the selection of the reaction model are suppressed. Within the model-free methods, the

isoconversional methods such as the Kissinger-Akahira-Sunose (KAS) [101–103], the Flynn-Wall-Ozawa (FWO) [101,102,104], or the Friedman method [102,104,105] are largely applied to determine the activation energy as a function of the conversion. In model-fitting, different models are fit to the experimental data and the model which gives the best statistical fit is selected to evaluate the kinetic parameters [63]. Examples of model-fitting methods are the ones developed by Coats and Redfern [99], Freeman and Carroll [100], and Duvvuri et al. [106]. Model-fitting methods are usually easy to apply and enable a better insight into the reaction mechanisms responsible for each stage of combustion. The nucleation models [101,107]; reaction order and geometrical contraction models [63,101,107]; and diffusion models [63,107] are the most commonly applied.

2.3.3 Particulate matter formation

Particulate matter (PM) emission has contributed to an estimated 3.2 million premature deaths as a consequence of cardiovascular diseases and lung cancer [108]. For this reason, there is a renewed concern with the minimization of particulate matter. Research is needed to understand the formation mechanisms for the correct design of designing equipment suitable to capture submicrometer and supermicrometer PM.

The main PM formation mechanisms during coal combustion are related to the mineral content (included and/or excluded) [109], and to the fragmentation of char/ash particles at high temperatures [110]. The formation mechanisms of PM from biomass combustion are typically two: (i) the transformation of inorganic elements such as Ca, Si, Mg that do not volatilize and originate coarse particles (> 1 μm) oftentimes through fragmentation, and (ii) the vaporization of K, Na, and Cl into inorganic vapours (e.g. KOH, HCl, KCl, NaCl) and formation of fine particles (< 1 μm) following gas-gas reactions (nucleation-coagulation) and/or gas-solid reactions (heterogeneous condensation) [111].

Recent studies have analysed the PM emissions from coal under distinct combustion conditions. Factors such as fuel type [112–114], temperature [69,115,116], residence time [68,117], and atmosphere [114,118–120] have been observed to actively affect the PM formation from coal combustion. For biomass, fewer studies have been conducted [121–124], and further input is still needed in what concerns the formation mechanisms of PM, as well as on the influence of factors such as the biomass type, particle size, torrefaction, and interactions between biomass and coal during co-combustion.

Biomass combustion typically generates higher levels of submicrometer PM due to the presence of elements such as K, Na, and Cl that undergo vaporization and subsequent homogeneous nucleation [125–128]. The thermal pre-treatment of biomass such as torrefaction has an effect on PM formation. Shao et al. [125] observe that torrefaction of corn stalk resulted in 25-68 % higher PM values as compared to the raw feedstock and attribute it mainly to the increase in PM0.1-1 due to the presence of K_2SO_4 and decrease in Cl and S following torrefaction. Oppositely, Han et al. [121] conclude that the torrefaction of rice husk results in lower levels of PM1 due to enhanced transformation of vaporized K into coarse particles. In a recent study, Wang et al. [129] analyse the influence of torrefaction, slow pyrolysis, and hydrothermal carbonisation of straw and relate the yields of PM0.3 with the presence of Cl in the pre-treated biomass.

Co-firing is an attractive option to reduce the submicrometer PM from 100 % biomass firing. The interaction between aluminosilicates in coal and alkali elements in biomass is beneficial for the reduction of submicrometer PM and formation of coarser particles (typical of pulverised coal combustion) which can therefore be trapped by existing electrostatic precipitators. However, the biomass-coal ratios during co-firing strongly affect the occurrence of interactions, and the feedstock also plays an important role. For instance, a reduction of submicrometer PM is observed for blends of 50 % oat hulls with coal whereas no interaction is observed for 3.8 % wood chips-coal blends [130]; blends of rice husk-lignite coal (30-70 %) generate less PM1 as compared to the predicted value [121]; in the co-combustion of wheat

straw-bituminous coal with the increasing coal ratio from 0 to 50 % the PM1 yield is reduced below the predicted value [131]; and during co-combustion of cedar chip with bituminous coal interactions are only observed for ratios of cedar chip greater than 10 % with a shift of PM1 into coarser particles [132]. It is therefore clear that the influence of (i) the feedstock, (ii) the thermal pre-treatment of biomass, and (iii) the ratio of biomass-coal during co-combustion must be evaluated simultaneously to provide further understanding of the formation mechanisms of PM and thence minimise associated emissions.

2.4 Pyrolysis

Under heating and prior to ignition, coal and biomass fuels undergo thermal decomposition with the subsequent release of light gas species and tar, and formation of solid char. This process, when in the absence of oxygen, is termed pyrolysis. Pyrolysis encompasses the following primary mechanisms [133]: char formation; depolymerization; and fragmentation. Secondary reactions such as cracking and/or recombination [133] can also take place. These result in the formation of lighter volatile species, and, if taking place within the char matrix, secondary char.

Pyrolysis can take place under different heating rates and residence times. Accordingly, it is classified as: slow pyrolysis (heating rate < 1 ºC/s and residence times lasting hours to days), fast pyrolysis (heating rates > 10-200 ºC/s and residence times 0.5-10 s), and flash pyrolysis (heating rates 10^3 - 10^4 ºC/s and residence times < 0.5 s). Due to the relevance for solid fuel combustion and gasification applications, fast pyrolysis is reviewed in detail in the present work.

2.4.1 Fast pyrolysis of biomass and coal

The heating rate during pyrolysis has an influence on the yield, structure, morphology, and surface area of the formed chars. Even though a strong influence of the heating rate change (range of 1 to 10 ºC/s) on the pyrolysis behaviour has been

observed using thermogravimetric analysers (TGA) [105,134,135], recent studies using wire mesh reactors [136–142] have permitted to achieve higher rates (~10^3 ºC/s) and investigate the so called fast pyrolysis. Moreover, due to the close contact between wire mesh and sample, and low amount of the latter, the heating rate to the particle is expected to be similar to that of the wire mesh itself. is Recent studies have comprehensively reviewed the effect of operating parameters on the pyrolysis of biomass [133,143].

Morphology and structural changes [139,141,142,144–148] using Scanning Electron Microscopy (SEM), and surface area through Brunauer–Emmitt–Teller (BET) analysis are typically investigated [138,142,148–155] when characterising fast pyrolysis chars. During pyrolysis of either coal or biomass, an unstable intermediate phase – metaplast is formed [95], which determines the subsequent softening of the char particle. At low heating rates, cross-linking typically occurs before bridge-breaking, which reduces the plasticization of the char [139]. However, at high heating rates, the plasticization is enhanced as bridge-breaking takes place before cross-linking [139], which leads to higher fluidity, extensive melting, and swelling of the char. Trubetskaya et al. [139] and Panahi et al. [80] observed that biomass chars obtained at high heating rates underwent strong deformation along with the formation of macro-pores and substantial melting. Similarly, Le Manquais et al. [142] observed the extensive swelling associated with the plasticization of the coal chars produced from high heating rate pyrolysis.

The chemical kinetics of the heterogeneous reactions of the char and the associated reactivity depend on the number and accessibility of carbon-active sites, diffusion rates of the reactants [97], and the surface area of the char particles. Past studies measured BET surface areas of coals spanning 25 – 200 m^2 g^{-1} [134,135,142,148,156,157] at high temperatures (800-1300 ºC). Similarly, in previous fast pyrolysis studies conducted at a temperature range of 950-1250 ^{0}C, it was found that most biomass chars exhibited high surface areas (95 – 275 m^2 g^{-1}) [138,142,149,153,154]. Only a small number of chars displayed low surface areas (0.7 – 6 m^2 g^{-1}) [142,151,152]. Trubetskaya et al. [138] studied the temperature effect

on BET surface area with two biomass chars and observed that the increase of the pyrolysis temperature from 1250 to 1500 ºC resulted in 40% and 15% decrease in the surface area of rice husk chars, and wheat straw chars, respectively.

Another important parameter for the characterization the char is the volatile (gas-phase) yield during pyrolysis. The volatile yield depends on operating parameters such as temperature, heating rate, and residence time [139,142,143,152,158]. Le Manquais et al. [142] have observed 10% increase in the volatile yield of a bituminous coal with an increase in the heating rate from 2.5 ºC s^{-1} to 30 ºC s^{-1} at a final temperature of 1100 ºC. Similarly, Trubetskaya et al. [139] reported that increasing heating rate from 10 ºC s^{-1} to 600 ºC s^{-1} increased the volatile yield by ~30%, and there was no significant further increase in the yields for higher heating rates. Moreover, Trubetskaya et al. [139,144] observed that at a fixed heating rate of 1000 ºC s^{-1}, an increase of the temperature from 600 ºC to 1000 ºC increased the volatile yield up to ~30% for the high alkali (wheat and alfalfa straws) and high silica (rice husk) samples. The yields remained unchanged at higher temperatures.

The heating rate during pyrolysis has an influence on the reactivity of the resulting char [140,142]. Thermogravimetric analysis (TGA) has been extensively used to assess the reactivity, burnout [138,140–142,146,147,152], and the kinetic behaviour [138,141,142,145,146] of chars produced at high heating rate conditions. Several studies have observed a relation between higher char reactivity and shorter burnout times of both coal and biomass fuel chars from fast pyrolysis [92,140,142,145,148,159]. Nevertheless, the studies on biomass and coal char blends obtained at high heating rates is still scarce. In these studies, the presence of alkali metals resulted in increased reactivities and shorter burnout times of high temperature and high heating rate char blends from biomass and coal [92,141,148,160,161]. The catalytic effect of alkali metals on heterogeneous reactions is explained through: (i) the migration of oxidative intermediate compounds formed at catalytic sites towards carbon active sites, and/or (ii) the chemisorption/desorption at carbon-alkali metals bonds [97]. On the other hand, low amounts of alkali and alkali earth metals from the biomass can be sequestered by

coal minerals such as Si and Al, resulting in a decrease of the reactivity of the blend [162,163]. Specifically, Ellis et al. [163] conducted slow co-pyrolysis and concluded that catalytically active calcium from biomass interacted with aluminosilicates from coal and formed inert compounds that decreased the reactivity of the co-pyrolyzed char samples.

The apparent kinetic parameters of biomass and coal char oxidation have been analysed using isothermal techniques [140–142]. Le Manquais et al. [142] reported that an increase in the heating rate during pyrolysis resulted in higher rate constants for bituminous coal. Blending biomass and coal influenced the kinetic rate constants. Specifically, Farrow et al. [152] reported an increase in the rate constants up to 25% in biomass (pinewood and sawdust) and coal (South African bituminous) char blends with an increase in biomass fraction. In parallel, Le Manquais et al. [140] observed that the use of additives (e.g. calcium and sodium nitrates) increased the rate constants of a South African bituminous coal char sample up to three times, as compared to the coal char with no catalyst.

2.4.2 Fast pyrolysis of laboratory-fractionated biomass

The mechanisms and pathways occurring during pyrolysis of biomass have also been reviewed recently [133,164], with special emphasis given to the conversion and interaction of individual components (cellulose, hemicellulose, and lignin). As pointed out by Shen et al. [164], attention ought to be given to both sample preparation and interaction assessment in quantitative terms. The interaction between lignocellulosic biomass components has been investigated by Yu et al. [18] for a variety of biomass (oak, spruce, and pine), under both slow and fast pyrolysis conditions at temperatures below 600 ºC. The authors observe interactions between cellulose and the other two components, but not between xylan and lignin, therefore stating that the yields of the original biomass could not be predicted from the individual components. Similarly, Couhert et al. [165] measure the gas yields from the flash pyrolysis of lignocellulosic biomass (beechwood, a mix of spruce and fir,

rice husk, grass, and wood bark) and compare these yields with those from commercially available components (cellulose, xylan, and lignin), but they do not identify an additivity law that allows prediction of the yields during high-temperature pyrolysis and gasification. Previous studies [166,167] also show that the lignocellulosic compositional differences affect both the soot yield and oxidation reactivity and that the modelling accuracy can be improved by the consideration of the effects of primary and secondary reactions, as well as explicit mass and heat transfer during pyrolysis at temperatures above 800 ºC. The results presented above highlight that the interaction of all lignocellulosic compounds during high-temperature pyrolysis is important for the prediction of yields and composition. Other studies [168–170] have also reported clear non-additive behaviour during pyrolysis of individual components. There are, however, some studies that claim that no interaction between components takes place for their specific fuels and pyrolysis conditions [171–173].

In addition, chemical pretreatment and fractionation method of feedstocks have a significant effect on the composition of lignocellulosic compounds and their further decomposition during pyrolysis and gasification [174]. Due to the difficulty in extracting the components of lignocellulosic biomass, most studies use commercially available cellulose, hemicellulose, and lignin, to investigate the interactions between components during pyrolysis (e.g. [175–177]). However, a few studies use laboratory-extracted hemicelluloses [168,176]. Matsakas et al. [178,179] developed a hybrid fractionation method that combines organosolv and steam explosion pretreatment and allows retrieval of all three components from the wood and herbaceous biomass. Organosolv pretreatment is known as an effective method to fractionate biomass into cellulose, hemicellulose and lignin streams by using aqueous-organic solvent mixtures, with high solvent concentration (30–70%) at temperatures of 100–220ºC, with or without the addition of catalysts [180,181]. One of the main benefits of organosolv pretreatment is the isolation of high-quality lignin and cellulose fractions [182,183]. Other two advantages of the organosolv process are related to the relatively easy recovery and re-use of the commonly used organic

solvents (such as ethanol or acetone) and improved mass transfer and dissolution of lignin in the presence of an organic solvent [184,185]. Previous research showed that organosolv pulps have bleachability and viscosity retention which are comparable to those of cellulose soda and kraft pulps [186]. The valorisation and CO_2 reactivity of organosolv fractionated lignins have been shown strongly affected by the type of feedstock and operating conditions of organosolv fractionation [187]. The literature is scarce on the yields and composition of products from pyrolysis of organosolv fractionated lignocellulosic compounds.

2.5 Gasification

The co-gasification of the lignite and biomass mixture also shows the potential to provide sustainable and environmentally friendly energy, as well as the safe and effective use of disparate fuel types such as lignite coal and biomass [188]. Gasification of lignite coal, biomass, or co-gasification are suitable solutions to allow the combined usage of alternative biofuels (e.g. agricultural biomass), and to reduce the dependency of the transportation sector on fossil fuels through the production of second-generation biofuels. There have been few studies on co-gasification of coal with biomass (wood, straw) in entrained flow gasifiers [189,190], which focused on the gas products and soot formation, on the importance of the pyrolysis stage, and on the occurrence of synergies. However, the co-gasification behaviour is highly fuel-dependent and in this scope, research is needed to evaluate the effect of fuel properties and operational parameters on the co-gasification.

The parameters that influence the char gasification kinetics, the syngas composition, and the occurrence of synergies during gasification, are reported as fuel type, fuel/air ratio, heating rate, temperature, pressure, gasifying agent composition, blending ratios during co-gasification, and pre-treatment (biological, chemical and physical) of fuels [148,191,200,192–199].

The kinetic parameters of biomass and coal char gasification are determined using isothermal [196,201–205] and non-isothermal [105,135,201,206–209] techniques. Different factors influence the reaction rate at different conversion levels: the chemical structure and porosity have a stronger influence at the early stages of conversion whereas at higher conversions with the collapsing of pores and decrease in accessibility to active sites the catalytic activity of the inorganics in the ash plays a more active role [210]. The gasification kinetics of rice husk under isothermal conditions are studied by Alvarez et al. [210] and different kinetic models are fitted (namely, 1^{st} order, n^{th} order, random pore model, and modified random pore model), with the random pore model (RPM) providing the best fit. Recently, Wei et al. [211] study the non-isothermal co-gasification of 30 % rice straw hydrochar and 70 % coal blends and observe an equally good fit for both volumetric model (VM) and shrinking core model (SCM), the former a first order reaction model and the latter a phase boundary control reaction model. Several recent studies [105,135,201,206], analyze the gasification of high ash coals and oftentimes produce char in thermogravimetric analyzer (TGA) at heating rates in the order of 100-1000 ºC min^{-1} followed by non-isothermal gasification and determination of kinetic parameters. The authors in the mentioned studies [105,135,201,206] focus on the influence of parameters such as different heating rates during pyrolysis, CO_2 concentration and/or steam as gasifying agent, and heating rate and temperature during gasification, and use several kinetic models such as the volumetric model (VM), the grain model (GM), and the RPM.

Pyrolysis is the first step in gasification and thus plays an important role on the reactivity of the chars and subsequent gasification behavior [133,189,209,212]. Studies on the influence of fast pyrolysis on the solid product (char) focus on the evolution of the yields and on the change in physical and chemical characteristics of the chars with the experimental conditions such as temperature and heating rate, and the organic/inorganic matter of the char [144,154,156,158,213,214]. For instance, the effect of the pressure and heating rate on the structure of char from pine during pyrolysis in three different reactors (drop tube furnace, wire mesh reactor, and

tubular reactor) is investigated by Cetin et al. [153] and it is observed that the high heating rates result in significant bridge-breaking before cross-linking reactions and melting of chars, formation of large cavities. Moreover, chars from wood and straw biomass obtained from fast pyrolysis in a drop tube furnace are investigated by Trubetskaya et al. [144] who observe melting and development of macropores in the chars at all temperatures, and that the catalytic effect of K and Ca results in stronger cross-linking of herbaceous chars.

In entrained flow gasifiers the high heating rates and the presence of gasification agents during devolatilization and gas-phase reactions affect the heterogeneous reactions of the char and thus its reactivity [215]. To faithfully represent the conditions in entrained flow gasifiers, few studies in the literature determine the gasification kinetics of *in-situ* chars in entrained flow reactors or drop tube furnaces [215–217]. Other studies choose to generate *ex-situ* chars in fast pyrolysis conditions but in the absence of gasification agents to decouple the two stages (char generation and char gasification) and be able to examine the physicochemical properties of the chars and conduct detailed kinetic studies in TGA [210,218,219]. Specifically, Alvarez et al. [210] observe that the gasification reactivity of rice husk char from fast pyrolysis is dictated by the catalytic effect of the ash and the pore development, in line with Li et al. [207] who correlate the decrease in reactivity with the increase of the uniformity of the char structure for several biochars (corncob, palm shell, and soybean straw). Wang et al. [219] study the gasification of spruce and spruce residue chars produced from drop tube furnace (DTF) and observe a significant increase in gasification reactivity as compared to chars produced from TGA.

Whilst the co-gasification of biomass and coal appears advantageous, only recently the understanding of synergies and/or inhibiting effects during co-gasification has been the focus of researchers. Blended chars have higher reactivity compared to the coal char [189,196,220–222], and this is attributed to the catalytic effect of alkali and alkali earth metals (AAEM) in biomass that have an effect on the gasification reactivity of coal char [211,220,221]. Wei et al. [196] study the co-gasification reactivity of rice straw and bituminous coal blended chars prepared at 800 °C using

a fixed bed reactor and co-gasified in TGA and observe that the gasification reactivity increases with the rice straw proportion in the blend. Zou et al. [223] conduct isothermal co-gasification of food waste and coal chars pyrolysed at 800 °C for 30 min and observe that lettuce and fish waste chars catalyze the coal char gasification due to the migration of K and Ca to the surface of the coal char, whereas the gasification reactivity of rice straw-coal char blend is lower than that of the coal char. Zhang et al. [197] conduct combined non-isothermal co-pyrolysis and isothermal co-gasification of four biomass feedstocks and three coals using TGA and observe that the transfer of K in soybean stalk and orange peel chars has a catalytic activity on the co-gasification, whereas the Si content in peanut shell char eliminates the catalytic activity of K. In the same line, Dupont et al. [204] study the steam gasification of a wide variety of biomass feedstocks (wood, short rotation coppice, and agricultural biomass) pyrolysed at low heating rate, and define a ratio K / (Si + P) to predict the overall gasification behavior.

In general, the gasification reactivity increases with the increase in temperature since high temperatures enhance the reaction between SiO_2, Al_2O_3 and active Ca with formation of calcium aluminosilicates and hence minimize the deactivation of K [196,224,225]. Moreover, high temperatures during pyrolysis and/or gasification allow for the vaporization of alkali and alkali earth metals and formation of alkali silicates [226–228] that results in the loss of catalytic activity of the blended char [199,227,228]. However, to the best knowledge of the authors, only few studies in the literature [189,229] have focused on the influence of the pyrolysis at high temperatures and high heating rates (i.e. fast pyrolysis) on the char co-gasification behavior. Kajitani et al. [189] investigate the co-gasification reactivity of two bituminous coals, cedar bark, and their mixtures, pyrolysed at 1400 °C in DTF, and co-gasified in TGA at 850 °C and 950 °C. The authors observe that biomass-coal char blends have slightly higher reactivity as compared with the predicted reactivity due to K transfer from biomass to coal char. Recently, Guo et al. [229] produce fast pyrolysis chars of bituminous coal and its liquefaction residue using a high-frequency furnace (heating rate ~10^3 ºC s^{-1}) and investigate the co-gasification

reactivity under TGA. It is observed that the reactivity increases with the increase of gasification temperature, and that the reactivity of the blended chars is higher than that of the coal char. Therefore, the occurrence of synergies during co-gasification between 800-1000 ºC (at which the catalytic activity of alkali and alkali earth metals (AAEM) is observable) [189,228,230] of biomass and coal chars obtained from fast pyrolysis have been rarely reported and should further be investigated.

CHAPTER 3

MATERIALS AND METHODS

In this Chapter, the feedstocks studied, and reactors used are described. The experimental and numerical methodologies are presented in detail. The characterisation techniques are briefly exposed, and the uncertainty analysis is given.

3.1 Fuels

3.1.1 Fuel selection

Three biomass types and two lignite coals were selected for this study. All feedstocks are important endogenous resources of Turkey: olive residue (OR), almond shell (AS), hazelnut shell (HS), Tunçbilek lignite (TL), and Soma lignite (SL). Olive residue, an agricultural waste from olive/olive oil production, was supplied by the company Forazeytin. This company processes olives from the Havran, Balıkesir region, and delivered the olive residue ground to below 5 mm diameter and pre-dried to less than 10 wt.% moisture. Almond shell is an agricultural waste of almond production. In Turkey, Bademder is a cooperative that supports almond producers from the region of Gülnar, Mersin. This cooperative delivered the almond shell as chunks without any treatment. Similarly, hazelnut shell was obtained from the Levant region in Turkey, with no pre-treatment. The lignite fuels were supplied by the Turkish Coal Enterprises (TKI) from the mining regions of Tunçbilek – Tavşanlı, Kütahya, and Soma – Manisa. The annual tonnages of Tunçbilek and Soma lignite are 7 and 10.5 Mt, respectively [231]. Both lignite coals were washed by the supplier (TKI) to remove most of excluded mineral matter. This washing process was performed by a float and sink test, which is common practice when handling high-

ash coals, including Turkish lignites [3]. Photographs of each fuel samples (as received) are shown in Figure 3.1.

Whilst the aforementioned Turkish fuels were analysed in all four chapters of this thesis, other secondary fuels were also utilised. Specifically, olive stones from Spain along with its fractionated components (cellulose, hemicellulose, and lignin), and commercially available components. These fuels were exclusively used in a detailed study on the fast pyrolysis behaviour and are described in further detail in Chapter 6.

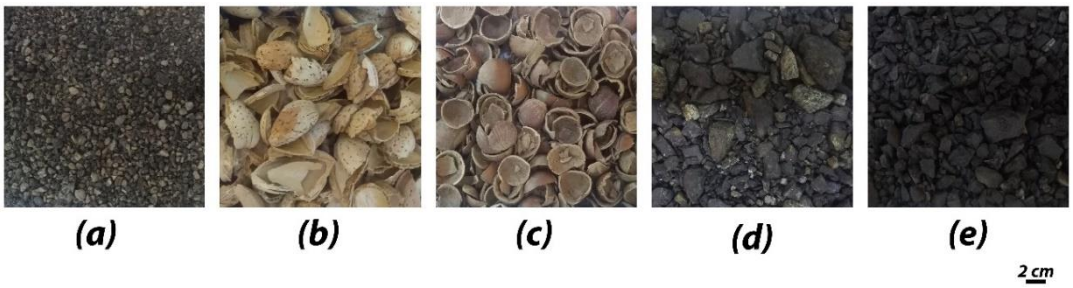

Figure 3.1. Photographs of various fuel samples of this study as received. (a) Olive Residue, (b) Almond Shell, (c) Hazelnut Shell, (d) Tunçbilek lignite, (e) Soma lignite. A size bar is included at the bottom right of this figure.

3.1.2 Fuel preparation

Both biomass and coal fuels were pre-processed in three main steps: drying, grinding, and sieving, all of which were conducted in the Department of Mining Engineering of Middle East Technical University. Fuels were firstly dried in bulk in an oven set to 105 ºC for a duration of ca. 24 h. Following drying, all samples were first ground to particle sizes lower than 1 mm using a roll crusher, and ground further using a ring mill to obtain finer particles. The fuels were sieved to obtain the desired particle size cuts using a Retsch sieve shaker and following the ASTM D4749 standard. According to the standard procedure, the mass of all sieves is measured at each interval and the samples are collectd when no mass variations below a specified

tolerance are observed. to Different size cuts were defined and obtained depending on the equipment in which these fuels would be used and on the specific objective of the study. Nonetheless, it can be stated that lignite coals were sieved to size ranges of 80-90 µm or 106-125 µm for usage in TGA, EFR, and DTF, and a larger size range of 212-250 µm was chosen for WMR studies. The former particle size (ca. 100 µm) is at the upper end of the typical coal particle size burned in practical pulverized coal applications. Larger particle sizes were chosen for WMR studies due to technical constraints. The biomass fuels were generally sieved to 106-125 µm for TGA and ~200-300 µm for WMR, EFR, and DTF. Moreover, the biomass particle size range was chosen to have relevance to large scale coal-biomass co-firing applications, according to the recommendations of Panahi et al. [82] and Livingston et al. [232]. The biomass fuels were used in either raw, torrefied, or pyrolysed state.

Torrefaction was conducted in a tubular oven at a plateau temperature of 275 ºC during 30 min under 100 % N_2 flow of 10 slpm, after which fuels were ground and sieved to the same size range as the raw biomass, in line with recent research [80].

Pyrolysis was conducted at low heating rate (~10 ºC/min) in a tubular oven at a plateau temperature of 500 ºC during 30 min under 100 % N_2 flow of 10 slpm.

The particle size cuts of the Turkish fuels used in each equipment are stated in Table 3.1.

Table 3.1 Particle size cuts (µm) chosen as a function of the equipment (TGA – thermogravimetric analyser; WMR – wire mesh reactor; DTF – drop tube furnace; EFR – entrained flow reactor).

Equipment	OR	AS	HS	TL	SL
TGA	106-125	106-125	106-125	106-125	106-125
WMR	212-250	212-250	-	-	212-250
DTF	212-300	212-300	212-300	106-125	106-125
EFR	80-90; 224-250	80-90; 224-250	-	80-90	80-90

3.1.3 Fuel characterisation

The results of proximate analysis, ultimate analysis, ash analysis, and the computed low heating values of the fuels, are presented in Tables 3.2 and 3.3. It should be noted that OR, TL, and SL, each were used from two different batches, and since the chemical characterisation differed for each batch it is given in Tables 3.2 and 3.3. The remaining fuels (AS and HS) were used from a single batch.

Table 3.2 Elemental analysis and energy content of OR, TL, and SL from 1st batch.

Parameter	OR	TL	SL
Proximate analysis (wt.%, dry basis)			
Volatile matter	78.7	35.6	38.7
Fixed Carbon[a]	19.0	46.9	32.0
Ash	2.3	17.5	29.3
Ultimate analysis (wt.%, dry ash free)			
C	48.3	57.3	45.3
H	6.2	5.3	3.1
N	0.7	2.1	0.6
S	0.1	1.3	1.3
O[a]	44.7	34.0	49.7
Ash analysis (wt.%, dry basis)			
SiO_2	16.6	52.7	18.7
Al_2O_3	5.2	22.3	12.8
Fe_2O_3	3.2	15.2	5.2
CaO	26.8	1.5	52.1
SO_3	1.5	0.1	7.2
MgO	6.0	2.2	1.3
P_2O_5	14.3	0.5	0.4
K_2O	18.1	2.7	0.4
Na_2O	7.8	0.2	0.2
Cl	-	-	0.5
Other oxides	0.5	2.6	1.2
Low Heating value (MJ/kg)	18.6	24.1	13.4

[a] by difference

Table 3.3 Elemental analysis and energy content of the fuels (OR, TL, and SL correspond to the 2nd batch).

Parameter	OR	OR-T	AS	AS-T	HS	HS-T	TL	SL
Proximate analysis (wt.% as received)								
Moisture	5.9	0.0	8.5	1.0	5.5	0.6	2.81	17.7
Volatiles	71.9	67.2	73.0	68.0	75.1	72.0	31.1	32.2
Fixed carbon[a]	17.4	28.7	17.6	26.1	18.5	26.4	52.1	37.0
Ash	4.8	4.1	0.9	4.9	0.9	1.0	14.0	13.0
Ultimate analysis (wt.% dry basis)								
C	46.6	56.6	45.4	56.5	47.9	56.5	61.8	61.2
H	6.40	5.84	6.34	6.00	6.32	5.70	5.60	4.66
N	0.58	0.32	0.36	0.19	0.35	0.31	2.65	1.15
S	-	-	-	-	-	-	1.45	1.30
O[a]	46.4	37.3	47.9	37.3	45.4	37.5	28.5	31.7
Inorganic species (wt.% dry basis)								
Si	4.60	0.92	0.36	0.91	1.48	1.28	33.3	31.6
Al	1.76	0.33	0.09	0.44	0.37	0.40	12.9	17.6
Fe	7.95	8.54	1.41	-	7.78	-	22.3	16.2
Ca	26.4	21.7	52.1	39.0	39.5	53.9	1.91	12.7
Mg	1.23	0.25	0.13	0.87	0.31	-	1.73	0.72
Na	-	-	-	-	-	-	-	0.46
K	48.6	48.7	41.2	51.2	25.7	31.4	3.16	3.83
P	1.98	3.08	2.02	0.46	5.22	5.37	0.12	0.25
Ti	-	-	-	-	-	-	2.87	1.98
Cl	4.46	2.16	0.34	0.21	-	-	-	0.06
S	2.37	-	0.46	-	2.09	1.50	19.1	14.1
High heating value ($MJ\ kg^{-1}$, dry basis)[b]	18.6	22.8	18	22.8	19.1	22.6	27.8	25.4

[a] by difference. [b] values obtained according to [233] and [234] for biomass and coal, respectively.

The proximate analysis was obtained using a thermogravimetric analyser, following the procedure described by Mayoral et al. [235]. The Ultimate analysis was undertaken according to the standard D5373-16, and the ash compositions were obtained with an X-Ray Fluorescence analyser, according to standard TS EN 15309. The low and high heating values of the biomass and coal samples were computed

according to the correlations presented by Friedl et al. [233] and Majumder et al. [234], respectively for biomass and coal.

The original coal and biomass fuels were also analysed for their particle shape and morphology using Scanning Electron Microscopy (SEM). Images of particles from coal and biomass fuels can be seen in Figures 3.2 and 3.3 for the size range and batches used in the Ignition (Chapter 4) and Combustion (Chapter 5) studies.

As depicted in Figure 3.3, all raw biomass particles displayed quasi-spheroidal shapes (low aspect ratios), and their torrefaction resulted in an increase in visible macro porosity of some particles, particularly almond shell (Figure 3.3d), although it was not extensive for any of the fuels. Both lignites were also quasi-spheroidal in shape with rounded edges. Aspect ratios (AR) of the raw and torrefied biomass particles and the two lignite coals were obtained by observation of SEM images of at least 20 particles per each sample; results are presented in Figure 3.4. Aspect ratios were calculated from the ratio of the major and minor axes, with the major axis defined as the diameter of the largest circle that enveloped the particle, and the minor axis as the diameter of the largest circle that can be inscribed in the particle. The AR of biomass is mostly dependent on its origin and size cut. The calculated aspect ratios were found to be in two distinct categories, i.e., biomass (both raw and torrefied) and lignite coal. Aspect ratios of biomass particles spanned the range of 1.4 – 1.8. These values were below those reported in the literature for a variety of many other biomass fuels [46,80,82] in the same size range; however, they were in line with those of pine bark [46], torrefied rice husk and torrefied corn-based DDGS [82], as well as torrefied forest residues [236] reported in the literature. Moreover, torrefaction had no obvious effect on the aspect ratio of these particular agricultural biomass types (see Figures 3.3 and 3.4), in contrast to other herbaceous and woody biomass types [82]. Aspect ratios of the lignite coal particles were 1.0 and 1.2 for TL and SL, respectively.

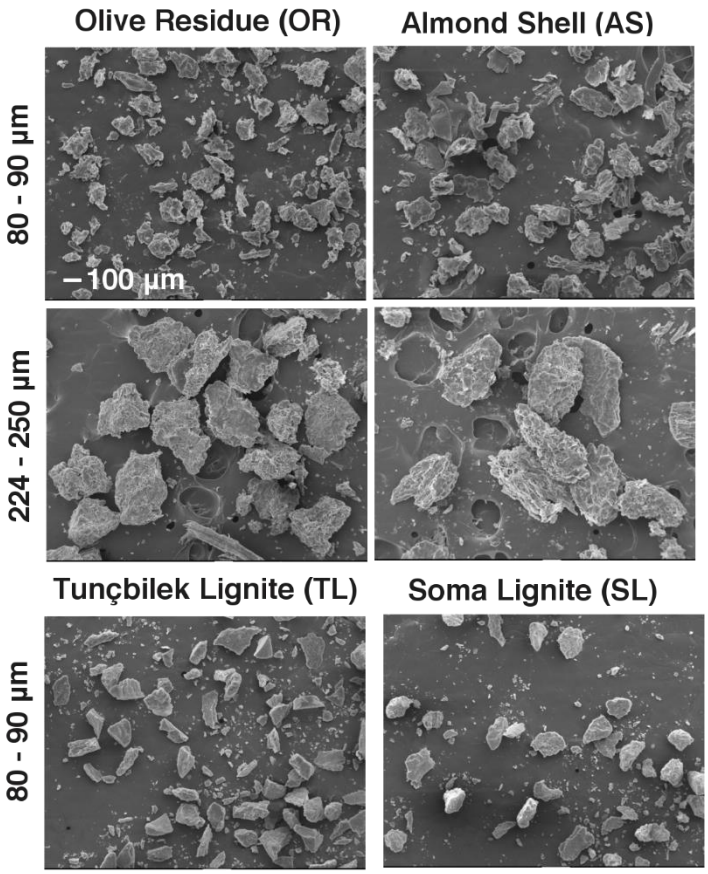

Figure 3.2. Scanning Electron Microscopy images for all fuels used in the ignition study (subsection 4.1). The scale bar represented applies to all images.

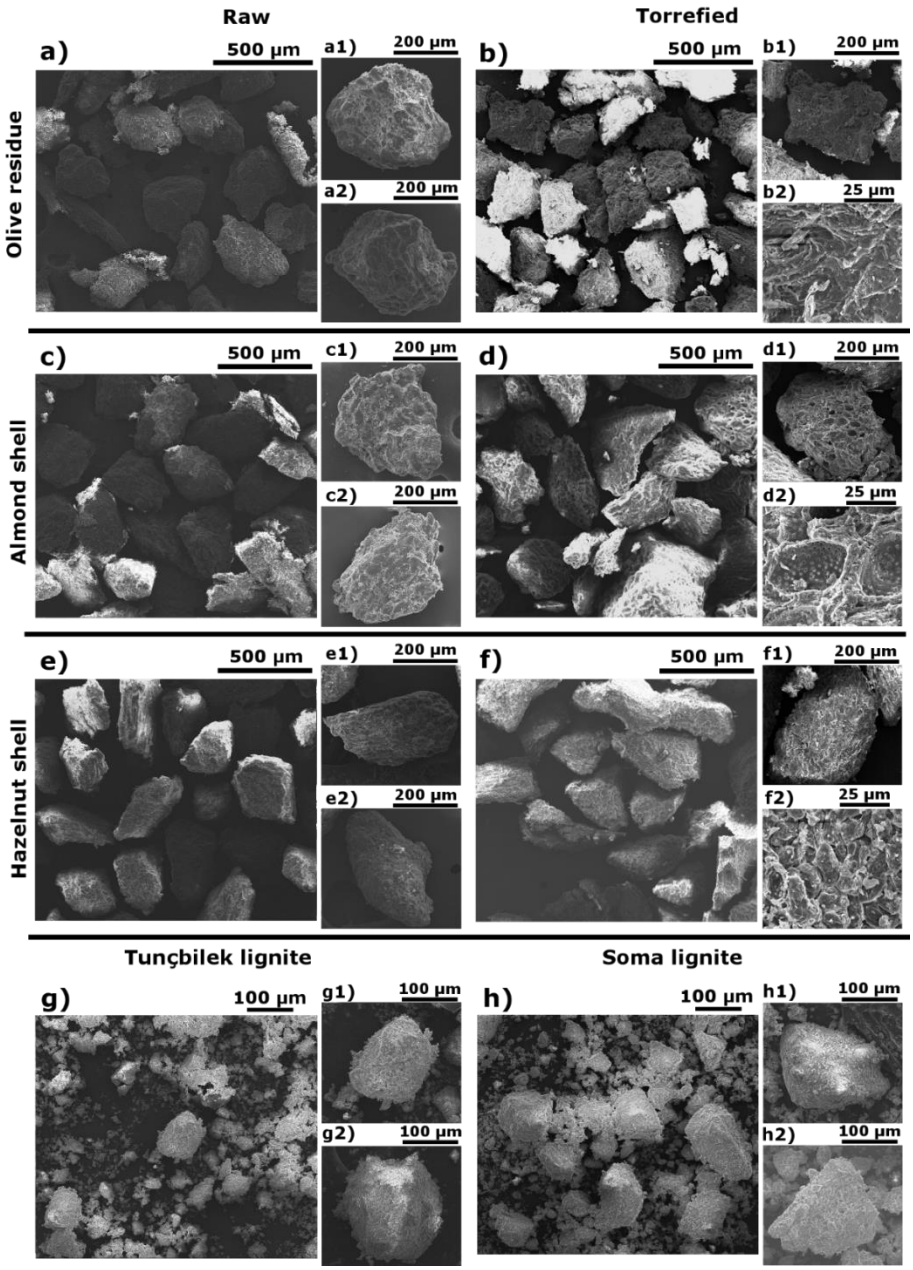

Figure 3.3. Scanning Electron Microscopy images for all fuels used in the combustion study (subsection 4.2). Biomass fuels (raw and torrefied) are in the size range of 212-300 µm, lignites are in the size range of 106-125 µm.

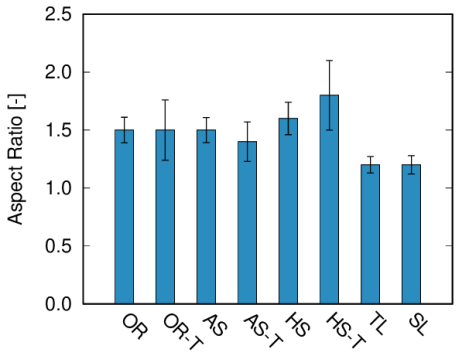

	OR	OR-T	AS	AS-T	HS	HS-T	TL	SL
mean particle length (μm)	334	310	385	400	380	422	91	93
mean particle diameter (μm)	277	260	326	348	312	336	84	84

Figure 3.4. Aspect ratios (top) of biomass and coal particles obtained from Scanning Electron Microscopy results of Figure 3.3, mean particle length and mean particle diameter (bottom). Vertical bars represent 98% confidence statistical errors.

3.2 Reactors

In this thesis, several laboratory scale reactors were used for the ignition, combustion, pyrolysis, and gasification studies. The main reactor used for the ignition studies was an entrained flow reactor (EFR) at the University of Lisbon. For the combustion studies, the drop tube furnaces at Middle East Technical University and at Northeastern University were used. Wire mesh reactors (WMR) at the University of Edinburgh and at Middle East Technical University were used for the pyrolysis studies. In all studies, thermogravimetric analysers (TGA) were used as supplementary reactors.

3.2.1 Thermogravimetric analyser (TGA)

TGA is widely used to study the thermal behaviour of materials. A TGA is mainly composed of a furnace in which the sample is placed, a thermocouple to monitor the temperature, a microscale to monitor the weight, mass flow controllers and valves to control the gas inlet, and a PC. Herein, two TGA were used: a Setaram Setsys 1750 (Central Laboratory of Middle East Technical University) and a PerkinElmer STA 4000 (Composite Material Characterisation Laboratory, Center for Wind and Energy Research, Middle East Technical University). For both, weight loss profiles as a function of time and/or temperature were obtained. The former (Setaram) also allowed to obtain the heat flow along time/temperature which was required in the ignition studies. The PerkinElmer STA 4000 was coupled with a Fourier-transform infrared (FTIR) spectrometer to obtain online gas composition as represented in Figure 3.5.

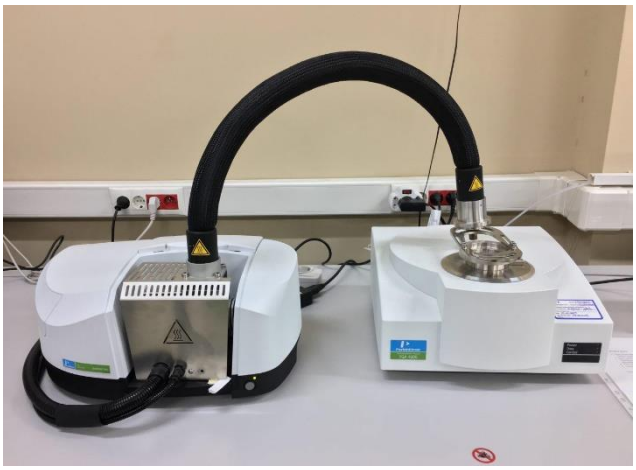

Figure 3.5. Thermogravimetric analyser coupled with a Fourier-transform infrared spectrometer present at the Composite Material Characterisation Laboratory, Center for Wind and Energy Research, Middle East Technical University.

3.2.2 Wire mesh reactors (WMR)

Two wire mesh reactors (WMR) were used: one in the Clean Combustion Technologies Laboratory at Middle East Technical University (WMR-METU) and the other University of Edinburgh (WMR-UoE), see Figures 3.6 and 3.7, respectively. Both reactors comprised a wire mesh, conductive electrodes, a welding machine as power source, a thermocouple, a glass chamber, and a pressure gauge. The setup was based on the design by Jon Gibbins and Kandiyoti [237]. In the WMR-METU, two stainless steel (SS316) wire meshes with a width of 40 mm, an aperture of 40 µm, and a wire diameter of 25 µm were used, whereas in the WMR-UoE the molybdenum mesh had an aperture of 60 µm and a wire diameter of 35 µm. The volume of the chamber of the reactor was ~0.04 L. Samples were heated by conductive and radiative heat from both the bottom and top meshes. The operating conditions of the wire mesh reactor were defined prior to the pyrolysis experiments using an R-type thermocouple welded to the bottom mesh. The thermocouples used in the WMR-METU had a wire diameter of 125 µm, whereas in the WMR-UoE the wire diameter was 50 µm. Schematic representations of both WMR can be found in Figures 3.6 and 3.7. Further details of the WMR-METU can found in [238], and of the WMR-UoE in [239].

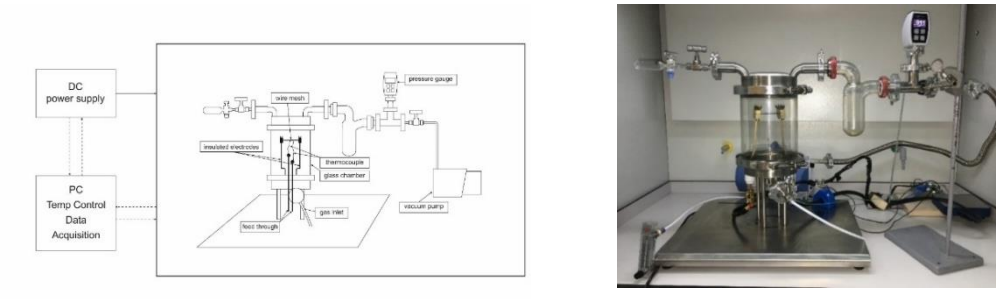

Figure 3.6. Wire mesh reactor at the Clean Combustion Technologies Laboratory of the Middle East Technical University, Turkey. Left-hand side: Schematic representation; right-hand side: Photograph [238].

Figure 3.7. Wire mesh reactor at the University of Edinburgh, U.K. Left-hand side: Schematic representation and sample photographs of the bottom mesh, (a) illustration of parent fuel, OR, before pyrolysis, b) illustration of char produced from OR after pyrolysis; right-hand side: Photograph.

3.2.3 Entrained flow reactor (EFR)

An entrained flow reactor (EFR) was used at the University of Lisbon. The EFR is schematically shown in Figure 3.8 and it is described in greater detail elsewhere [240,241]. It consisted of a solid fuel feeding unit, a McKenna flat flame burner, a gas feeding system and an image acquisition system. The fuel-feeding unit consisted of a rotameter, a 10 ml syringe and a vibrating motor. The solid particles stored in the syringe were fed (by gravitational force) into the stream of transport air and injected upward through the central hole of the burner (I.D. 1.55 mm) into the ignition zone. A vibrating motor avoided the clogging of particles in the syringe hole and ensured a low feeding rate. The Mckenna flat flame burner comprised a stainless-steel cylinder enveloping a water-cooled bronze porous sintered matrix of 60-mm diameter. Two mass flowmeters allowed the control of the methane and primary airflow rates to the burner. In addition, cooling water was fed to the burner through copper tubes. Above the burner, a high-grade fused quartz of I.D. 70-mm, height of 500-mm and thickness of 2-mm confined the flow and avoided the entrainment of ambient air, while providing optical access.

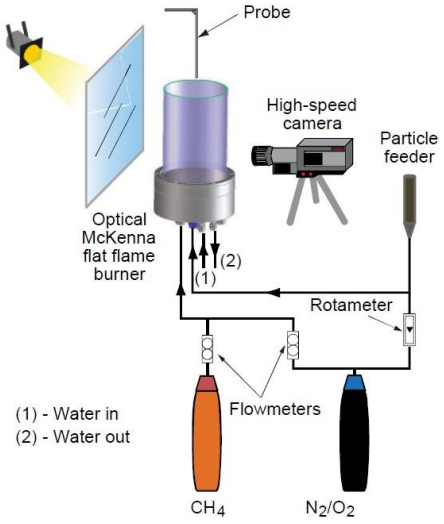

Figure 3.8. Schematic of the entrained flow reactor at IST, University of Lisbon, Portugal.

3.2.4 Drop tube furnaces (DTF)

Two drop tube furnaces (DTF) were used, one in the Clean Combustion Technologies Laboratory of the Middle East Technical University (DTF-METU) and the other at Northeastern University (DTF-NU), as seen in Figures 3.9 and 3.10, respectively.

The DTF-METU is an electrically heated furnace with silicon carbide and molybdensilicate thermal elements that supply a maximum power of 7.5 kW and reach temperatures of 1500 ºC. The DTF-METU, Protherm model PTF15.75.1000, was produced by AlserTeknik. For the experiments conducted in this study, the DTF was fitted with an alumina (60% Al_2O_3) reactor with a maximum operating temperature of 1100 °C in the hot zone. The vertical reactor has a length of 1500 mm, useful hot zone with length 1000 mm, and an inner diameter of 75 mm. The temperature is controlled with an S-type thermocouple to ensure a constant temperature throughout the useful hot zone. The injection of the gaseous mixture (primary+secondary) and particles is done via a water-cooled injector fitted to the reactor with a flange for sealing and alignment. The primary and secondary mixtures were dry air fed from industrial air cylinders, at flow rates of 4 and 16 slpm,

respectively. The DTF is fitted with a particle feeding unit and with a particle collection unit. Particles were down fed using a syringe pump to which a glass vial filled with particles was fitted to. The primary gas was injected into the vial, and the mixture primary gas+particles left the vial through a 2 mm capillary tube. A 12 V vibrating motor aided feeding and prevented the particles to sediment in the vial. The collection was accomplished either at the bottom outlet of the DTF (total collection) or at discrete levels in the furnace using a water-cooled particle collections probe. For both configurations, a single-stage or 3-stage particle impactor (Tecora MSSI) was used as detailedly described in the methodology section. The DTF-METU is represented schematically in Figure 3.9.

The optically accessible drop tube furnace at Northeastern University (DTF-NU) can be seen in Figure 3.10. The radiation cavity of the DTF is 25 cm long and is heated by six hanging molybdenum disilicide elements. The DTF was fitted with a 7 cm i.d. transparent quartz tube. The gas temperature profile, as measured along the centreline of the quartz tube with suction thermometry, was fairly constant throughout the length of the radiation zone at ~50-70 K below the wall temperature under quiescent gas flow conditions [81]. Heating rates of the falling particles in the DTF were calculated to be as high as 10^5 K/s. Fuel particles were introduced through a port at the top of the injector by first placing them on the tip of a bevelled needle syringe. Tapping of the needle induced the fall of the particles into the injector and, thereafter, into the furnace.

Pyrometric observations of single particles were conducted from the top of the furnace injector, as shown in Figure 3.10, viewing downwards along the central axis of the furnace, which aligned with the path of a falling particle. Therefore, the entire luminous burnout histories of single particles – from ignition to extinction – were monitored. A fused silica optical fibre transmitted light from the furnace to the pyrometer assembly. The pyrometer used two dichroic edge filters as spectrum splitters to direct the light to the three interference filters, with wavelengths centred at 640, 810 and 998 nm with bandwidths (FWHM) of 70 nm. In conjunction with these interference filters, silicon diode detectors were selected to maximize the signal

sensitivity. Details of the pyrometer optics, electronics, calibration and performance are given by Levendis et al. [242]. The voltage signals generated by the three detectors were amplified and then processed by a microcomputer using the *LabView* software. Cinematographic observations were conducted from the side of the furnace through a transparent quartz window, as shown in Figure 3.10. Images were recorded by an Edgertronic camera viewing through a long-range Infinity K-2 lens.

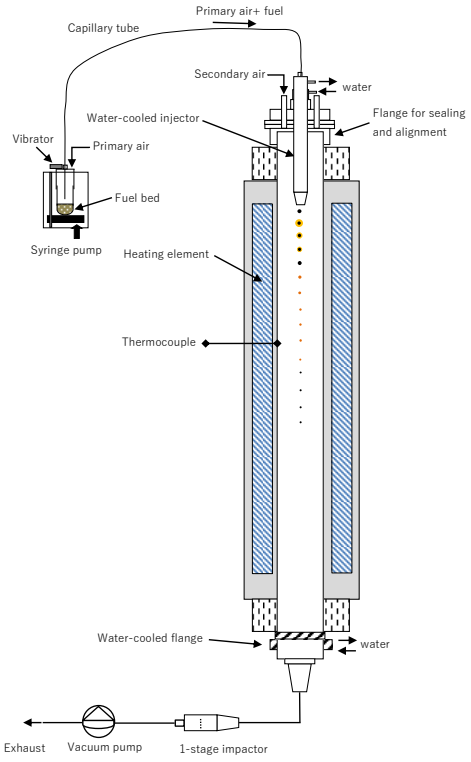

Figure 3.9. Schematic representation of the drop tube furnace at the Clean Combustion Technologies Laboratory of the Middle East Technical University, Turkey, fitted with feeding and collection for total collection. The illustration of a single particle combustion event is not to scale.

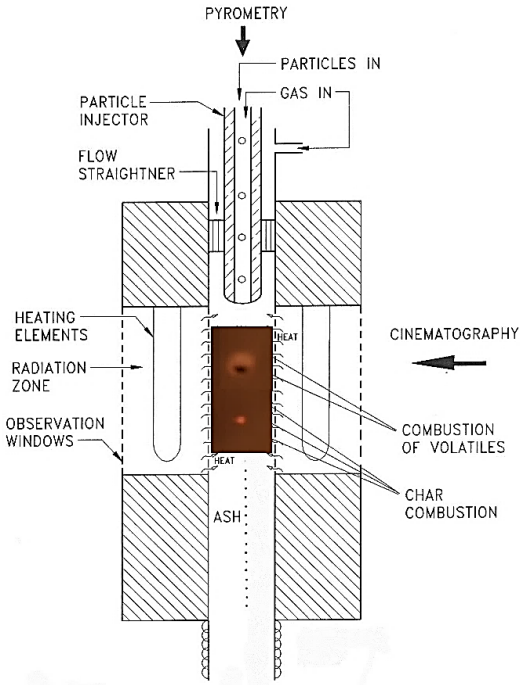

Figure 3.10. Schematic illustration of the drop tube furnace at Northeastern University, U.S., with particle introduction, location of the pyrometric and cinematographic observations, and illustration of a single particle combustion event (not to scale).

3.3 Experimental and numerical methodologies

3.3.1 Ignition characteristics using TGA

The experiments at low heating rates were performed in a TGA-DSC. Combustion experiments were performed in a dry air atmosphere. Pyrolysis experiments were also carried out in a nitrogen atmosphere, as a complement to the combustion experiments for the determination of the ignition mode and particle ignition temperature. For all experiments, the gas flow rate was set to 120 mL/min. The samples were heated from room temperature to 1200 K at a heating rate of 20 K/min. The initial amount of the sample was ~10 mg for both type of experiments.

Ignition mode

The ignition mode during low heating rate experiments was determined from the TGA-DSC data using the procedure described by Chen el al. [243]. Accordingly, ignition is defined in three distinct modes: (i) homogeneous, i.e. gas-phase, when two exothermic peaks are observed before and after the separation point between the combustion and the pyrolysis TG curves, with the first peak corresponding to the volatiles combustion and the second to the char combustion; (ii) heterogeneous, when only one strong (exothermic) peak is observed and the separation between the combustion and the pyrolysis TG curves occurs before a substantial amount of release of volatiles, indicating burning of the whole particle; or (iii) hetero-homogeneous, when both volatiles and char ignite simultaneously, with a strong exothermic peak occurring after partial release of volatiles.

Characteristic temperatures

In this work, the characteristic ignition temperatures of each solid fuel were determined from both the TGA and TGA-DSC methods. Ignition temperatures were determined for either volatiles ignition or particle ignition, in line with the ignition mode definition employed herein for the TGA-DSC [243]. Volatiles ignition occurs when the volatiles/air mixture surpasses the lower flammability limit, and was determined from the DSC profiles as the temperature at the onset of a rapid exothermic reaction ($T_{vol.}$). Particle ignition corresponded to the occurrence of heterogeneous reactions (solid-gas-phase) and took place at the temperature that the pyrolysis/combustion TG profiles separated ($T_{part.}$). The exothermic peak temperatures (T_{DSC1} and T_{DSC2}) were also determined by simply using the DSC profiles for each fuel.

Self-ignition risk

The self-ignition risk was evaluated in accordance with the ignition risk plot first proposed by Querol Aragón et al. [42]. According with this method, the self-ignition risk was quantified through four regions (very-high-risk; high-risk; medium-risk; and low-risk), outlined by both characteristic TG-O_2 temperature (major weight loss temperature in TG graph obtained from combustion of fuels in a pure O_2 atmosphere) and apparent activation energy. A linear correlation between the TG-O_2 characteristic temperature and the first DTG peak temperature was observed by Torrent et al. [37] (Figure 6, therein), and this correlation was taken into account in the present study in order to define the limits of the risk regions. As a result, the first DTG peak temperature during conventional air combustion was used here instead of the TG-O_2 characteristic temperature. The apparent activation energy was determined following the Cummings method [42], and plotted against the DTG peak temperature for each fuel. The Cummings method is based on the weight loss during air combustion as a function of the temperature, and follows an Arrhenius type equation given by Eq. (3.1),

$$\ln\left(-\frac{1}{w}\frac{dw}{dt}\right) = \ln A - \frac{E_a R}{T} \tag{3.1}$$

where w is the weight of the unburned sample; $\frac{dw}{dt}$ is the instantaneous rate of weight loss; A is the Arrhenius pre-exponential factor; E_a is the apparent activation energy; R is the universal gas constant; and T is the absolute temperature. From this method, a straight line was fitted to the experimental data in the plot $\ln\left(-\frac{1}{w}\frac{dw}{dt}\right)$ versus $\frac{1}{T}$ in the first region of weight loss after ignition, and the apparent activation energy was calculated from the slope of the line.

3.3.2 Ignition mode and ignition delay time using EFR

The ignition behaviour at high heating rates was characterised using an entrained flow reactor (EFR) coupled with a high-speed imaging apparatus. The EFR is described in section 3.2.3 of this thesis. The image acquisition system consisted of a CMOS high-speed camera Optronis CamRecord CR600x2 and a diffuse led backlight. The camera was equipped with two lenses, a 2x tele-converter and a Nikkor 60 mm f/2.8D. The camera settings used were a constant exposure time of 1/15000 s along with frame rates between 2000 and 3500 frames per second, which yielded resolutions between 250×452 and 250×600. The camera was positioned with its optical axis perpendicular to the axis of the burner and calibrated using a millimeter marked target. With this image acquisition setup, the visible light intensity was captured. Although this signal includes soot and char emission, it is a simple approach that has been shown to be a more suitable method to properly observe the ignition of single particles [46,49] in comparison with CH* emission based methods [244].

The different temperature conditions (T1, T2 and T3) were established by increasing the burner thermal input, while maintaining the excess air coefficient constant, and thereby a constant oxygen concentration was achieved (approximately equal to that of condition O3). To establish the different oxygen concentration conditions (O1, O2, and O3), both the thermal input and the excess air coefficient were varied to yield the same temperature (approximately equal to that of condition T3). The oxygen range concentration was selected to represent the typical conditions that are experience by particles when injected in the product recirculation zone of swirl burners. The particle transport airflow rate was kept equal to 140 mL/min for all tests.

The ignition zone located above the flat flame was characterized in terms of mean gas temperature and oxygen concentration. Mean temperature was measured using 76 µm diameter fine wire platinum/platinum: 13% rhodium (type-R) thermocouples, and the “true” gas temperature was estimated following the method proposed by

Shaddix [245]. Mean O_2 dry volume concentrations were measured with the aid of a water-cooled stainless-steel probe and a paramagnetic analyser. Figure 3.11 shows both the mean gas temperature and the oxygen concentration profiles.

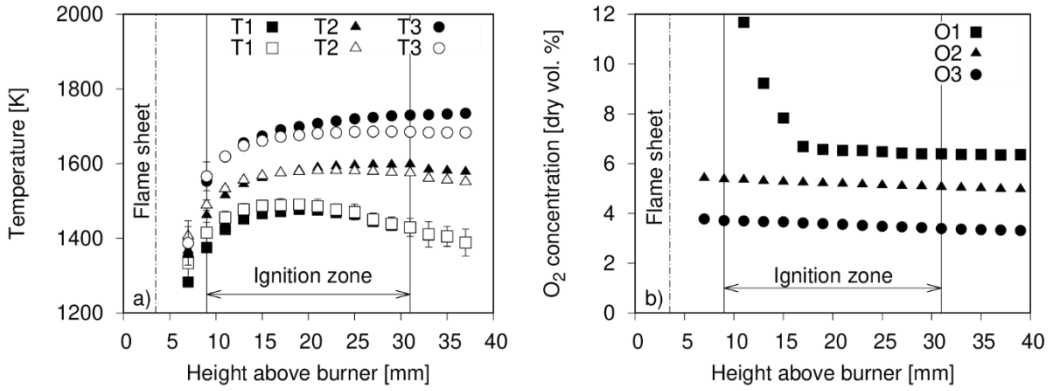

Figure 3.11. a) Measured (open symbols) and corrected gas temperatures (solid symbols) for conditions T1-T3. Vertical bars represent 98% confidence statistical errors. b) Measured oxygen concentrations for conditions O1-O3.

Ignition mode

The ignition mode was determined by direct visual observation of the recorded images and defined as gas-phase ignition or surface ignition. Gas-phase ignition corresponded to the occurrence of homogeneous reactions detached from the particle surface. Conversely, surface ignition corresponded to the existence of homogeneous reaction with a flame attached to the particle surface, heterogeneous reaction, or a combination of the two. The diagnostics technique employed in this work did not allow identifying tracers of homogeneous and heterogeneous reactions, and therefore it was not possible to distinguish between reaction modes (homo- or heterogeneous) close to the particle surface.

Ignition delay time

Ignition delay time was measured by image post-processing. Single particles were traced from the instant they entered the reactor until ignition onset. The method developed in a previous work [46] was improved to yield more precise values of the ignition delay times. The particles were identified in each frame with the Canny method and the edge function of Matlab. For each particle, a set of frames was collected and the signal corresponding to the maximum luminosity of each frame was normalized by the maximum luminosity found in that specific set of frames. Subsequently, a filtering procedure was applied to the signal as follows:

$$\mathrm{Signal}^1(\mathrm{j}) = \omega * \mathrm{Signal}(\mathrm{j}) + (1-\omega) * \mathrm{Signal}^1(\mathrm{j}-1) \tag{3.2}$$

$$\mathrm{Signal}^2(\mathrm{j}) = \mathrm{Signal}(\mathrm{j}) - \min(\mathrm{Signal}^1) \tag{3.3}$$

$$\mathrm{Signal}^3(\mathrm{j}) = \mathrm{Signal}^2(\mathrm{j})/\max(\mathrm{Signal}^2) \tag{3.4}$$

$$\mathrm{Signal}^4(\mathrm{j}) = \omega * \mathrm{Signal}^3(\mathrm{j}) + (1-\omega) * \mathrm{Signal}^4(\mathrm{j}-1) \tag{3.5}$$

$$\mathrm{Signal}^5(\mathrm{j}) = \mathrm{Signal}^4(\mathrm{j})/\max\,(\mathrm{Signal}^4) \tag{3.6}$$

The filter weight ω was kept the same for all particles. Several values have been tested and 0.4 produced the most suitable results. Eq. (3.2) leads to a noise reduction that allows to identify the medium background noise defined as $\min(\mathrm{Signal}^1)$. Eq. (3.3) corresponds to a translation that eliminated the background light of the original signal, followed by a normalization of Signal^2 in Eq. (3.4). Eq. (3.5) smooths the noise, and Eq. (3.6) normalises again to re-establish the scale between 0 and 1. The improved algorithm, that resulted in a higher signal to noise ratio than in previous work [46], allowed to reduce the ignition criterion from 15% to 5% of the maximum luminosity without false ignition detections. The same criterion for ignition onset was applied regardless of the ignition mode (gas phase or surface ignition). For each test condition and solid fuel, an average of 45 individual particles was visualized to calculate the averaged ignition delay times and associated standard deviations.

3.3.3 Combustion behaviour and kinetics using TGA

Combustion behaviour

Thermogravimetric experiments were carried out under a dry air atmosphere. A thermogravimetric analyzer (TGA) from Setaram, model Setsys 1750, was used to perform the TG-DTG experiments. The atmosphere inside the furnace consisted of dry air fed from a gas cylinder and was regulated by a flow meter to 120 mL/min for all trials. Samples were heated from ambient temperature to 1000 ºC under three different heating rates, 15, 20, and 40 ºC/min. In order to further analyze the thermal behavior of Soma lignite during combustion, the heat flow profile and the absorbance infrared spectra were obtained by using a TGA-DSC, along with a FTIR spectrometer under dry air background gas at a heating rate of 20 ºC/min. A different TGA was used since the Setaram instrument was not able to be coupled with DSC or FTIR. The TG-DTG curves for both instruments showed a very good agreement, and this validated the results. The TGA and FTIR instruments were connected by a heated line at 270 ºC in order to avoid condensation of the flue gases. The spectra were collected with a resolution of 4 cm^{-1}, and ranging from 700-4000 cm^{-1}. The characteristic wavelengths of each gas absorbance were plotted as a function of temperature. The strongest infrared absorbance wavelengths of CO_2, CO, SO_2, and COS were observed to be 2392 cm^{-1}, 2182 cm^{-1}, 1342 cm^{-1}, and 2042 cm^{-1}, respectively [34,246,247].

The initial amount of sample was about 10 mg for all experiments. A small amount of sample and slow heating rates was used to avoid heat transfer limitations and to minimize mass transfer effects. Furthermore, the Biot number was calculated to evaluate the importance of the temperature gradients within the particle using the expression Bi = hd/2k, where h is the convective heat transfer coefficient of air (W/m^2K), d is the diameter of the particle (m), and k is the thermal conductivity of the particle (W/mK). The convective heat transfer coefficient was assumed equal to 8.4 W/m^2K [248]. The thermal conductivities of the biomass and coal particles were taken from the works of Di Blasi [249] and Maloney et al. [250], respectively. The

Biot number for every sample was always << 1, which enabled the assumption of uniform temperature distribution inside the particles.

Using the TG/DTG curves, the major characteristic temperatures were calculated. The decomposition temperature was defined when a rate of weight loss equal to 1%/min was reached after moisture release stage [66]. The ignition temperature was calculated according to the TG-DTG tangent method [40]. For each major stage of weight loss, the peak temperature was observed when the maximum weight loss rate was reached. The burnout temperature was defined when the rate of weight loss became lower than 1 %/min after all stages of combustion [33].

In addition to the characteristic temperatures, the combustibility index - S was calculated for all samples and heating rates. According to Zou et al. [78], the combustibility index was defined as follows:

$$S = \frac{|dW/dt|_{max.}|dW/dt|_{mean}}{T_{ig}^2 T_B} \tag{3.7}$$

Where $|dW/dt|_{max.}$ and $|dW/dt|_{mean}$ represent the absolute maximum and mean rate of weight loss (wt.% min^{-1}). T_{ig} and T_B represent the ignition and burnout temperatures (^oC), respectively. The calculation of the combustibility index enabled a more rigorous measure of the reactivity of each fuel since this index is sensitive, not only to the maximum rate of weight loss, but also to the ignition and burnout temperatures.

Combustion kinetics using TGA

The solid-state decomposition and combustion of coal and biomass fuels is typically modelled based on the apparent rate equation given by Eq. (3.8):

$$\frac{dx}{dt} = kf(x) \tag{3.8}$$

Where dx/dt is the conversion rate, k is the reaction rate, and f(x) represents the reaction mechanism. The conversion ratio x is computed using the TG data, and by application of the following expression:

$$x = \frac{w_0 - w_t}{w_0 - w_\infty} \tag{3.9}$$

Where w_0, w_t, and w_∞ are the initial weight of the sample, the weight of the sample at the examined time t, and the final weight of the sample at the end of the process, respectively. The Arrhenius expression is commonly used to express the reaction rate as a function of temperature:

$$k = Ae^{-E_a/RT} \tag{3.10}$$

Where A is the pre-exponential factor (min^{-1}), E_a is the apparent activation energy (kJ/mol), and T is the temperature (K). The conversion rate is obtained as a function of time, whereas the reaction rate is a function of temperature. Since the heating rate β is constant, it can be expressed by $\beta = dT/dt$. Therefore, the Eq. (3.11) can be written as follows:

$$\frac{dx}{f(x)} = (k/\beta)dT \tag{3.11}$$

In Eq. (3.11) above, the left-hand side is a function of the conversion ratio (x), and the right-hand side is a function of the temperature (T). By integration of both sides of equation (3.11), the following expression is obtained:

$$g(x) = \int_0^x dx/f(x) = A/\beta \int_{T_0}^{T} \exp\left(-\frac{E_a}{RT}\right) dT \tag{3.12}$$

g(x) is solely a function of the conversion ratio x, and illustrates the mechanism of reaction, see Table 3.4. The Coats-Redfern method [99] was chosen herein to integrate both sides of Eq. (3.13), giving:

$$\ln\left(\frac{g(x)}{T^2}\right) = \ln\left(\frac{AR}{\beta E_a}\left(1 - \frac{2RT}{E_a}\right)\right) - \frac{E_a}{RT} \tag{3.13}$$

The Coats-Redfern method has been extensively applied to model the kinetics of coal and biomass combustion [63,65,101,102,105,251]. The model-fitting approach employed in the present work enabled the fitting of different mechanisms, represented by a mathematical function g(x). In this work, three main mechanisms were evaluated: reaction order controlled, phase boundary reaction controlled, and diffusion controlled, as represented in Table 3.4. The plots of $\ln\left(\frac{g(x)}{T^2}\right)$ vs $1/T$ were drawn for each mechanism (i.e. g(x) function), and the apparent activation energy E_a was determined after selection of the model with the best fitting. Herein, the fitting was evaluated by determination of the coefficient of determination R^2, which indicated the proportion of the variance in the dependent variable that can be predicted from the independent variable.

The models termed as reaction order (O1-O3) state that the chemical reaction is controlled by chemical kinetics, and models O1, O2, and O3 correspond to first, second, and third order, respectively [63]. In the phase boundary-controlled models (R2 and R3), the reaction is controlled by the movement of an interface at constant velocity with the reaction occurring almost instantaneously, resulting that the surface of each particle is covered with a layer of the product. Within the phase boundary controlled models, the contracting cylinder model (R2) emulates a reaction zone consisting of a circular disc reacting from the edge inward, whereas the contracting sphere model (R3) emulates a sphere which reacts from the surface inwards [252]. Models termed as D1-D4 correspond to diffusion-controlled mechanisms, meaning the reaction is controlled by diffusion of the oxidizer into the reacting particle. 1-D diffusion represents a uni-dimensional diffusion in which the reaction rate is solely a function of the thickness of the diffusion barrier [253]; 2-D diffusion represents a two-dimensional diffusion process into a cylinder with the reaction rate as a function of the radius; and both D3 and D4 represent diffusion models that have into account all three directions, and consider the particle as a sphere [252].

Since the diffusion-controlled models only have into account diffusion effects, the values of the calculated activation energies should be assumed as apparent values.

For this reason, the activation energies obtained from these models should not be directly compared with those obtained from the remaining solid-state reaction models.

Table 3.4 Reaction models and correspondent f(x) and g(x) functions applied in this work, according to previous works by Gil et al. [63], and Phadnis & Deshpande [252].

Model	**f(x)**	**g(x)**
Reaction order controlled [63]		
O1 – first order	$(1-x)$	$-\ln(1-x)$
O2 – second order	$(1-x)^2$	$(1-x)^{-1}$
O3 – third order	$(1/2)(1-x)^3$	$(1-x)^{-2}$
Phase boundary controlled [252]		
R2 – contracting cylinder	$2(1-x)^{1/2}$	$1-(1-x)^{1/2}$
R3 – contracting sphere	$3(1-x)^{2/3}$	$1-(1-x)^{1/3}$
Diffusion controlled [252]		
D1 – 1-D diffusion controlled	$(1/2)(x)^{-1}$	x^2
D2 – Valensi, 2-D	$(-\ln(1-x)^{-1}$	$(1-x)\ln(1-x)+x$
D3 – Jander, 3-D	$2(1-x)^{2/3}\left(1-(1-x)^{1/3}\right)-1$	$(1-(1-x)^{1/3})^2$
D4 –Ginstling-Brounshtein, 3-D	$(3/2)\left((1-x)^{-1/3}-1\right)$	$1-2x/3-(1-x)^{2/3}$

Char combustion kinetics using TGA

Firstly, the temperatures for oxidation of biochars and lignite chars using TGA were chosen to ensure that the combustion would take place in a kinetically controlled regime. The influence of temperature on the biochar burnout behaviour was evaluated herein for three distinct temperatures (400, 450, and 525 ºC), and the results are presented in Figs. 3.12 and 3.13. The results showed that the carbon burnout and carbon burnout rate were clearly affected by the oxidation temperature for temperatures equal to or above 450 ºC. The chosen temperatures for char oxidation are in line with recent studies conducted for biomass [152,254,255], coal

[142,152], and biomass-coal chars [152]. Specifically, Morin et al. [255] examined the influence of temperature on the oxidation of biomass chars and concluded that temperature should not go above 400 ºC to maintain a kinetically controlled reaction.

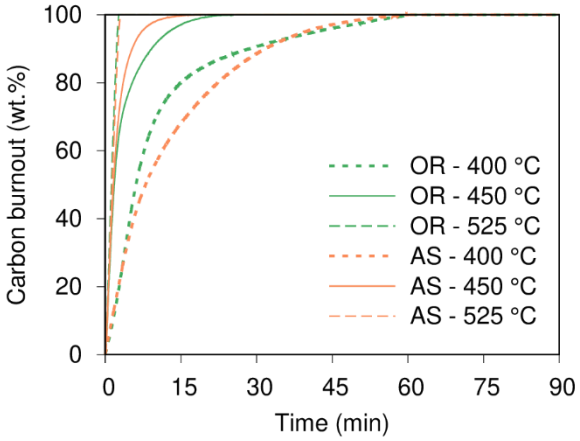

Figure 3.12. Carbon burnout vs time for both biomass fuels (OR – olive residue, and AS – almond shell) for three temperatures (400, 450, and 525 ºC).

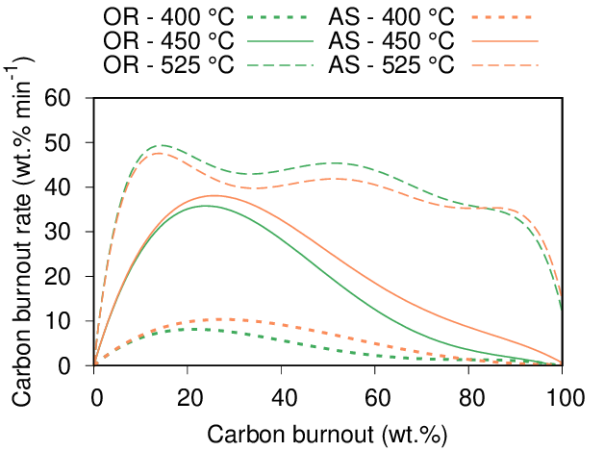

Figure 3.13. Carbon burnout rate vs burnout for both biomass fuels (OR – olive residue, and AS – almond shell) for the three isothermal preliminary trials at 400, 450, and 525 ºC. Curves represent 4th order polynomials fitted to the experimental data.

Furthermore, mass diffusion rates were determined, and the ratio of carbon burnout rate over mass diffusion rate was calculated. The method presented herein is largely based on the work by Trubetskaya et al. [167]. Mass transfer effects due to convection were neglected and only molecular diffusion was considered. Moreover, the char sample in the crucible was assumed homogeneous and non-porous. The mass transfer rate of O_2 in N_2 to the surface of the char sample (r_{diff}) was calculated from Eq. (3.14),

$$r_{diff} = \frac{A_c}{h_c} \frac{M_c C_b D_{AB}}{m_{char}} \times 60 \times 100 \quad (3.14)$$

In Eq. (3.14), A_c and h_c are the area and height of the crucible, respectively, M_c is the molecular weight of carbon, m_{char} is the initial mass of char in the crucible, D_{AB} is the binary diffusion coefficient based on Chapman Enskog [256], and C_b is the bulk concentration of O_2 in the inlet dry air, and given by Eq. (3.15),

$$C_b = \frac{P x_{O2}}{R T} \quad (3.15)$$

In Eq. (3.15), P is the total pressure, x_{O2} is the molar fraction of O_2 in the inlet dry air, R is the universal gas constant, and T is the temperature.

The mass transfer rates, carbon burnout rates, and respective ratios are presented in Table 3.5 below.

Table 3.5 Mass transfer rates and carbon burnout rates for the individual chars

	OR	AS	SL
Temperature, T (ºC)	400	400	450
Mass transfer rate, r_{diff} (wt.% min^{-1})	44.1	44.1	41.1
Carbon burnout rate, r_{carbon} (wt.% min^{-1})	8.26	10.4	3.09
Ratio r_{carbon} / r_{diff}	0.187	0.236	0.075

Following the initial assessment of the combustion regime, Thermogravimetric experiments were carried out to obtain the burnout profiles of all chars obtained from fast pyrolysis. A Perkin Elmer STA 4000 thermogravimetric analyzer (TGA) was used to perform the TG-DTG experiments. Following the preliminary trials to ascertain the temperature for conducting the isothermal oxidation of the chars, 400 ºC for the biochars (OR and AS), and 450 ºC for all remaining samples (SL and blends), were chosen.

The samples were initially heated from ambient temperature to the plateau temperature under 20 mL min^{-1} nitrogen flow at a heating rate of 30 ºC min^{-1}, to ensure the removal of any trapped moisture and/or volatiles. Upon reaching the plateau temperature, and after a holding time of 3 min to stabilize the system, the atmosphere inside the furnace was switched to air at 100 mL min^{-1}, and the chars were kept at this temperature for 3 h. The amount of sample was kept low, at 2 mg. Experiments for each char sample were conducted at least twice.

From the TG curves, the burnout extent was calculated as follows:

$$\text{burnout} = \frac{w_0 - w_t}{w_0 - w_f} \tag{3.16}$$

where, w_0, w_t, and w_f are the initial weight, the weight at time t, and the final weight after isothermal oxidation, respectively.

The reaction rate constants for each char sample were obtained using the TGA burnout profiles of the chars. A global one-step reaction model was used for isothermal char oxidation [257], as defined in Eq. (3.17):

$$\frac{\partial \alpha}{\partial t} = k(1 - \alpha) \tag{3.17}$$

where, k is the reaction rate constant, t is time, and α is the fractional weight conversion given by:

$$\alpha = 1 - C/C_0 \tag{3.18}$$

where, C is the remaining char weight, and C_0 is the original char weight. Integration of the above equation and using the initial condition $\alpha = 0$ at t = 0 gives:

$$-\ln(1-\alpha) = kt \quad (3.19)$$

The first order rate constants in this study were obtained by linear fitting to the experimental data of $-\ln(1-\alpha)$ vs t.

3.3.4 Combustion behaviour using DTF

Combustion behaviour

An optically accessible DTF was used at the Northeastern University to study the combustion behaviour of single particles of biomass and coal. Fuel particles were introduced through a port at the top of the injector by first placing them on the tip of a bevelled needle syringe. Tapping of the needle induced the fall of the particles into the injector and, thereafter, into the furnace, while a gas flow of 1 slpm into the furnace forced the particles downwards. A high-speed camera positioned on the side of the DTF allowed for optical access. In line with the ignition study using EFR, the ignition mode was defined as gas-phase or surface ignition. The combustion mode was defined as one-stage or two-stage. In one-stage combustion, volatiles and char burn simultaneously and a clear volatile flame detached from the char surface cannot be observed (this is obviously setup-dependent as higher camera resolutions may enable this distinction). In two-stage combustion, the combustion of the volatiles takes place on the vicinity of a not-ignited char particle (black in appearance) and is followed by char combustion. Fragmentation was also observed and analysed. The occurrence of fragmentation was classified as pre/post ignition, and the number of fragments originated from the main particle were quantified.

Combustion times and temperatures

An optically accessible DTF was used at the Northeastern University to study the combustion times of single particles of biomass and coal. The combustion behaviour of the fuels was further analysed from application of pyrometry techniques to obtain temperature-time profiles of single particles of each fuel throughout their combustion histories. Details of the technique and calibration of the apparatus have been provided by Bejarano and Levendis [258]. The signal from the pyrometer was processed using a Matlab code based on Wien approximation. Average burnout times and temperatures for volatile matter and char combustion of ca. 20 detected particles were calculated.

It should be remarked that the measurement of the volatile and char combustion times and temperatures was not concurrent with the observation of the combustion mode using high-speed camera since these two setups were not synchronised.

Particulate matter sampling

The DTF at Middle East Technical University was used for particulate matter collection. The combustion of the particles in the drop tube furnace took place at a constant wall temperature of 1000 ºC or 1200 ºC, and the heating rate was estimated to be on the order of 10^4 ºC/s. The total flow of dry air used, i.e. primary air + secondary air, was 20 L/min, which resulted in a residence time of ~3 s in the isothermal reaction zone. The mass flow of particles was kept low at 10±1 g/h to maintain lean combustion conditions.

Particles were collected at the outlet of the drop tube furnace using a collection system that consisted of a 3-stage stack impactor (Tecora MSSI PM10-2.5 Multistage Stack Impactor) fitted with 47 mm quartz microfiber filters and a vacuum pump (Tecora Bravo Plus). Quartz filters were heat treated before sampling, according to the ASTM standard for coal ashing (D3174-12) to remove impurities and moisture.

The drop tube furnace particulate matter experiments were carried out by the following steps: (1) empty filters were placed in the impactor which was coupled to the bottom of the DTF and vacuum pump; (2) the loaded vial was placed in the feeding unit; (3) the air inlet flows were set and the vacuum pump switched on and allowed 5 min to stabilise the system; (4) the vibration motor and syringe pump were activated and the timer started.

Sampling was performed for a duration of 10 min, and the experiments demonstrated a good repeatability as seen from the 98% confidence interval error bars represented in the plotted results. Collected particles were categorised in the sizes PM>10, PM10, PM2.5-10, and PM2.5.

After each experiment, selected filters were ashed in a muffle furnace in compliance with the ASTM standard D3174-12 [259] for coal and ASTM E1755-01 [260] for biomass, to determine the ash weight fraction. Subsequently, the particle burnout, ψ, was calculated in accordance with the procedure in the standard CEN/TS 14775 as follows.

$$\psi = \frac{1 - \frac{\omega_f}{\omega_x}}{1 - \omega_f} \tag{3.20}$$

In this equation, ω_f represents the ash weight fraction in the input fuel, and ω_x is the ash weight fraction in the collected sample. During PM collection, selected samples were ashed and the burnout was calculated always above 95 %.

3.3.5 Pyrolysis and char yield calculation using WMR

In this thesis, two WMR were used, at the Middle East Technical University and at the University of Edinburgh. Since these reactors are identical the procedure described below applies to the experiments conducted in both WMR.

Char yield calculation

The experimental char yield, Y_{exp}, which includes moisture and inorganic content in both initial and char samples, was calculated using Eq. (3.21),

$$\mathrm{Y_{exp}\ (wt.\%)} = \frac{\mathrm{m_{f\ (mesh+char)}} - \mathrm{m_{f\ (mesh)}}}{\mathrm{m_{i\ (mesh+sample)}} - \mathrm{m_{i\ (mesh)}}} \times 100 \tag{3.21}$$

where $\mathrm{m_{f\ mesh+char}}$ is the final mass of the mesh and char, $\mathrm{m_{f\ mesh}}$ is the final mass of the mesh after removal of the char, $\mathrm{m_{i\ mesh+sample}}$ is the initial mass of the mesh and the raw sample, and $\mathrm{m_{i\ mesh}}$ is the initial mass of the mesh.

Initially, the required holding time to ensure complete pyrolysis of the samples was determined. The importance of the holding time in high heating rate pyrolysis and the relation between holding time and volatile yield was first observed by Gibbins and Kandiyoti [237]. Accordingly, in the present study preliminary tests were conducted for different biomass and coals that are out of the scope of this paper, and it was observed that the volatile yield increased as expected until reaching a plateau at 4 s. Moreover, a series of experiments were conducted for almond shell due to its high volatile content, the results of which coincided with the results of the preliminary tests (see Figure 3.14). Therefore, the trials were set to 4 s: the first second for the transient heating up period and approximately 3 s for the exposure of the samples to the constant temperature of 1600 ºC. This value is in the same order as the residence times in the radiative zone of pulverized fuel boilers [261] and resembles the holding time chosen by the previous researchers who conducted fast pyrolysis of a wide range of coals [262,263] and biomass fuels [139] using wire mesh reactors.

The experimental procedure was as follows: (1) the sample was weighed and gently spread on the bottom mesh; (2) the glass chamber was placed onto the reactor, and the control volume vacuumed to a pressure of 5 mbar; (3) nitrogen (or helium) was introduced into the control volume until atmospheric pressure was reached; (4) the heating rate and temperature conditions were selected based on prior knowledge of the voltage and current of the welding machine; (5) the reaction was triggered using

a LabVIEW interface, and the heat source was kept on, and the mesh was heated to the specified plateau temperature and for the specified holding time; (6) upon completion of the experiment the mesh was allowed to cool down under inert atmosphere until reaching room temperature; (7) upon reaching room temperature, the glass chamber was removed, the mesh and sample weighed to obtain the values of the char yields, and the char was collected for further analysis.

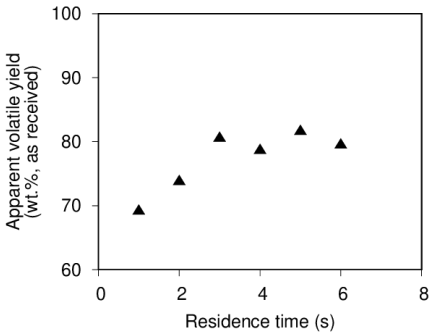

Figure 3.14. Volatile yield as a function of the wire-mesh reactor pyrolysis residence time for almond shell.

3.3.6 Pyrolysis of biomass and coal using DTF

The DTF at Middle East Technical University was used for char production. The configuration of the DTF and experimental procedure is identical to the one described above for *Particulate matter sampling.* For char production, however, a flow of 100% N_2 was fed into the DTF, and the char was collected only from the first stage (PM>10) of the 3-stage impactor.

3.3.7 Gasification kinetics using TGA

The chars produced from fast pyrolysis in the DTF were gasified and co-gasified in a TGA. Three distinct char blends of OR and SL were mechanically prepared co-gasification trials in TGA: 50 wt.% OR – 50 wt.% SL, 25 wt.% OR – 75 wt.% SL,

and 10 wt.% OR – 90 wt.% SL. A TGA was used to obtain the TG-DTG curves. The isothermal runs were done at 800, 900, and 1000 ºC. Initially, the sample was heated under 100 mL/min of 100 vol.% N_2; upon reaching the gasification temperature, the system was stabilized for 5 min; 100 mL/min of 100 vol.% CO_2 was introduced into the furnace, and the temperature was held for 60 min. For all runs, the initial sample weight was kept low at 5 (±0.5) mg to ensure uniform temperature distribution within the sample bed. From the TG curves, the conversion was calculated as,

$$\text{conversion (wt.\% daf)} = (w_0 - w_t)/(w_0 - w_f) \tag{3.22}$$

where, $w_0, w_t,$ and w_f are the initial weight, the weight at time t, and the final weight after gasification, respectively.

Each kinetic model was applied for conversion levels within 5 - 95 % and provided a different expression for the function f(α). Regardless of the model fitted, the change in conversion α as a function of time is given by Eq. (3.23),

$$\partial\alpha/\partial t = k(T)f(\alpha) \tag{3.23}$$

where k is the reaction rate constant, t is time, and α is the fractional weight conversion given by Eq. (3.24),

$$\alpha = 1 - C/C_0, \tag{3.24}$$

where C is the remaining char weight, and C_0 is the original char weight.

Three different models widely applied in the literature [194,201,205,264,265] to study the gasification kinetics of coal and biomass chars are chosen herein: the volumetric model (VM), the grain model (GM), and the random pore model (RPM). The VM assumes that the reaction of char-CO_2 is homogeneous with uniform diffusion of CO_2 outside and inside the particle. The GM defines the particle as a porous network of spherical grains on which the reaction occurs [266]. The RPM considers the overlapping of pores and subsequent reduction of accessible active sites with the evolution in conversion. This model is more realistic since it considers the competing effects of pore growth for low conversions and the overlapping and

coalescence of pores for higher conversions. Apart from the conversion level α, the RPM requires an additional parameter Ψ as input. This parameter is related with the pore structure of the unreacted char and an approximated value given by Eq. (3.25) is used herein following the work of Fermoso et al. [267].

$$\Psi = 2/(2\ln(1-\alpha_{max})+1) \tag{3.25}$$

The differential and integral forms for each model are given in Table 3.6. The rate constants (k_{VM}, k_{GM}, k_{RPM}) were obtained by linear fitting of the experimental data to the integrated equations. The initial condition for integration was $\alpha = 0$ at t = 0.

Table 3.6 Differential and integral forms of Eq. (3.23) for each model. VM – volumetric model; GM – grain model; RPM – random pore model.

	Differential form	Integral form
VM	$\frac{\partial\alpha}{\partial t} = k_{VM}(1-\alpha)$	$-\ln(1-\alpha) = k_{VM}t$
GM	$\frac{\partial\alpha}{\partial t} = k_{GM}(1-\alpha)^{2/3}$	$3(1-(1-\alpha)^{1/3}) = k_{GM}t$
RPM	$\frac{\partial\alpha}{\partial t} = k_{RPM}(1-\alpha)\sqrt{1-\psi\ln(1-\alpha)}$	$\frac{2}{\psi}\left(\sqrt{1-\psi\ln(1-\alpha)}-1\right) = k_{RPM}t$

3.4 Uncertainty analysis

In all reactors, the first step – sample preparation – is critical and a frequent source for error. For this reason, the samples used in all reactors were ground and sieved following specified standards. Moreover, samples were sieved down to narrow size cuts to minimise size heterogeneities.

3.4.1 Thermogravimetric analyser

During analysis in TGA uncertainties arise mostly from weight and temperature measurements. The proper calibration of the instrument is paramount for the minimisation of errors associated with the measurement, and the TGA 4000 used herein was calibrated following balance, furnace, and temperature calibration as specified by the manufacturer. The TGA 4000 has a balance accuracy of ± 0.02 % and precision of ± 0.01 %, and temperature accuracy of ± 1 ºC and precision of ± 0.8 ºC.

3.4.2 Wire mesh reactor

In the WMR the experimental uncertainties arise mostly from non-uniform temperature distribution on the wire mesh, and sample collection. Herein, the temperature measurement was done using an R-type thermocouple with wire diameter 125 µm and with ± 0.1 % error limit. As concluded by Uluca [268], the combustion in a WMR results in the formation of an ash residue that affects temperature uniformity in the wire mesh, and the re-use of a wire mesh must be done with caution. To minimise this effect, the amount of sample was kept low at 10 mg in the WMR at the Middle East Technical University and 100 mg in the WMR at the University of Edinburgh, and the same wire mesh was re-used at most three times. Sample collection for further analysis and measurement of char yields is critical during WMR analysis. Accordingly, the char yield measurements were performed at least in triplicate and the results presented are the result of the arithmetic mean of all measured yields. The error bars which represent the 98% confidence interval limits are represented in the plotted results, and the error was calculated to be within ± 4 wt.% for all samples and conditions. The inaccuracy during measurement of char yields was mainly due to weighing errors.

3.4.3 Entrained flow reactor

During experiments in the EFR experimental uncertainties arise from temperature measurement, gas composition measurement, and particle observation. The mean temperature in the ignition zone was measured with a 76 µm diameter R-type unsheated thermocouple, and the values were corrected for radiation loss following the method proposed by Shaddix [245] to obtain the "true" mean gas temperatures. The gas composition was measured with a calibrated paramagnetic analyser. As aforementioned, single particles were observed using a high-speed camera system. For each test condition and solid fuel, an average of 45 single particles was collected to calculate the averaged ignition delay times and associated standard deviations. The confidence intervals for each data set were calculated and are presented alongside with the averaged ignition delay times as error bars. The number of samples was high enough to guarantee statistical significance, which was confirmed by the convergence of the standard deviation with the increase of the samples.

3.4.4 Drop tube furnace

During analysis using DTF errors arise from particle feeding and collection. The feeding was accomplished using a syringe pump feeder which was calibrated ahead of the experimental trials for each fuel and size cut. For all trials, the feeding rate was measured and always within 10 (±1) g/h. During particle collection uncertainties arise from the fact that the whole of the char/ash sample cannot be collected and the mass balances closed. The main reason is the fact that char/ash particles often stick to surfaces of the reactor and/or impactor. The collection efficiency during measurement was measured and always above 70 %.

3.5 Supplementary characterisation techniques

The original samples and chars were characterised using a large array of experimental techniques. Elemental analysis (ultimate and proximate) was performed for all original samples and was the primary chemical characterisation technique used. Scanning electron microscopy (SEM) was extensively used in this thesis to characterise the morphology of the original and char samples. Particle size distribution (PSD) was for the original samples and chars. N_2 adsorption analysis was used to characterise the surface area of the chars. The ash composition was typically determined using X-ray fluorescence (XRF).

Elemental analysis

The proximate analysis of the biomass and coals was obtained using a thermogravimetric analyser (TGA) and following the procedure described by Mayoral et al. [235]. Through this analysis, the contents of moisture, volatile matter, and ash were determined, and the fixed carbon content was obtained by difference. The ultimate analysis was undertaken according to the standard D5373-16 to obtain the contents of carbon, hydrogen, nitrogen, and sulphur, with oxygen content obtained by difference.

Scanning Electron Microscopy

Scanning Electron Microscopy (SEM) was used to observe the particle shape and morphology of the original coal and biomass fuels and also of the chars. Samples were placed on a carbon tape and coated with Au/Pd before analysis to prevent charging. Imaging was performed using a FEI Quanta 400F instrument under high vacuum, a voltage of 20 kV, and magnifications ranging 100-25000×. Energy-dispersive X-ray spectroscopy (EDS) was also applied to infer the chemical composition of characteristic structures of the original fuels and chars.

Particle Size Distribution

Particle size distribution (PSD) was used when needed as a confirmation tool after sieving of original samples and after collection of chars. The analysis was conducted in a Mastersizer instrument under wet conditions.

N_2 adsorption analysis

The surface area of the chars and parent fuels were obtained using nitrogen adsorption. Samples were initially flushed with nitrogen at 350 ºC for 3 hours to ensure the removal of any remaining volatiles. The surface area was calculated using a multi-point adsorption based on Brunauer–Emmitt–Teller (BET) theory and using nitrogen isotherms at its boiling point (77 K).

Ash compositional analysis

The composition of the ash was obtained with an X-Ray fluorescence analyser, according to standard TS EN 15309. Through this analysis the main inorganic species were identified and quantified. The scanning was done for species ranging Fluor to Uranium.

TGA-FTIR

The gas composition was determined using a FTIR spectrometer coupled to a thermogravimetric analyser (TGA, model Perkin Elmer STA 4000). The amount of initial sample was kept at 10 (±1) mg, and the gas flow into the TGA furnace was set to 100 mL/min to ensure sufficient concentration of gases for proper FTIR detection. The gases were flushed through a heated line to the FTIR spectrometer gas cell. The heated line was set to 270 ºC to prevent condensation and secondary reactions. A pump was used at a flow rate of 85 mL/min downstream of the gas cell of the FTIR to ensure removal of the off-gas. The scan rate of the FTIR was 0.2 cm/s, the resolution 4.0 cm^{-1}, and the wavenumber range 4000 - 450 cm^{-1}. The gases under analysis (with indication of the specific wavenumber) were H_2O (1374 cm^{-1}), CH_4 (3000 cm^{-1}), CO_2 (2360 or 2392 cm^{-1}), CO (2182 cm^{-1}), COS (2042 cm^{-1}), and SO_2 (1342 cm^{-1}) [269].

CHAPTER 4

RESULTS AND DISCUSSION

In this chapter, the results are presented and discussed. The chapter is subdivided into four subchapters focusing on Ignition, Combustion, Pyrolysis, and Gasification. The Ignition and Combustion subchapters focus on the comparison of the ignition and combustion behaviour at low and high heating rates with final recommendations for co-firing applications to ensure both combustion efficiency and emissions minimisation. The Pyrolysis subchapter gives special emphasis to the fast pyrolysis of biomass and coal under conditions relevant to pulverized applications, and to the fast pyrolysis of biomass fractions whose results have importance for entrained flow gasification and biorefinery applications. In the last subchapter, Gasification, a study is presented on the effect of the fast pyrolysis step on the char properties and kinetics during co-gasification of biomass and coal, and the results are useful for entrained flow gasification applications.

4.1 Ignition

There is still a gap in the literature on what concerns the ignition behavior of Turkish biomass and lignite fuels. TGA and EFR are complimentary techniques that allow studying ignition at distinct heating rates, but have been seldom used in combination, as in the present study. The low heating rate ignition data, obtained from TGA, is relevant to ensure the safe handling of solid fuels during its processing, storage, and transportation. In addition, the EFR allows attaining heating rates that are very close to those encountered in industrial equipment (e.g. pulverised coal and biomass combustors) and thus allow studying ignition under realistic conditions. Hence, the main objective of the study presented in this chapter is to use both techniques to study comprehensively the ignition behaviours of Turkish biomass and lignite fuels.

To this end, the solid fuels were firstly tested using a low heating rate of 20 K/min and a dry air atmosphere in a TGA-DSC. The ignition mode, characteristic ignition temperatures and self-ignition risk of the fuel samples were determined by analysis of the TG, DTG and DSC profiles. Subsequently, the ignition mode and ignition delay time of the same solid fuels were evaluated under high heating rates (~10^5 K/s) using an EFR. Here, six different operating conditions were used, with independent variation of the temperature and oxygen concentration of the atmosphere (see Table 4.1 below). The fuels under study were olive residue from 1st batch (termed OR throughout this section), almond shell (AS), Tunçbilek lignite from 1st batch (termed TL throughout this section), and Soma lignite from 1st batch (termed SL throughout this section). The chemical characterisation of these samples is given in Tables 3.2 and 3.3. The results presented in this Chapter are reprinted with permission from Magalhães D, Kazanç F, Ferreira A, Rabaçal M, Costa M. Ignition behavior of Turkish biomass and lignite fuels at low and high heating rates. Fuel 2017;207:154–64. Copyright (2017) Elsevier.

Table 4.1 Summary of the operating conditions used in the EFR experiments.

Parameter	T1	T2	T3	O1	O2	O3
Thermal input, kW	0.7	1	2.2	1.1	1.2	2.2
Excess air coefficient λ, dimensionless		1.44		1.18	1.29	1.40
Mean O_2 concentration, dry vol. %		6.88		3.52	5.16	6.49
Mean gas temperature, K	1460	1560	1660		1680	

4.1.1 Characteristic temperatures and self-ignition risk

Table 4.2 presents the characteristic ignition temperatures during TGA experiments for all studied fuels. The volatiles ignition temperature, determined as the temperature at the onset of a rapid exothermic reaction, was similar for all solid fuels studied herein with a value of ~500 K. The type of biomass has a low influence on

the ignition temperature, with different biomass fuels presenting ignition temperatures between 470 K and 540 K [26,27,29,32,37,38,40]. Even though the origin of the biomass fuels is distinct, they are all characterized by a high volatile matter content (60-80 wt.% dry basis), which appeared to be a more critical factor for the onset of ignition than the type of biomass. In what concerns the present lignite coals, the volatiles ignition temperature values (500 K) are within the range obtained by Ramírez et al. [38] for different rank coals (490-540 K). However, most authors do not distinguish between volatiles and particle ignition temperatures, and since the ignition mode of lignite fuels depends on several factors, the present results cannot be directly compared to those found in the literature.

The particle ignition temperature, which was defined herein as the temperature at the pyrolysis/combustion TG profiles separation, was approximately 660 K for all fuels. The result for the Tunçbilek lignite is in line with the results reported by Chen et al. [243] for the particle ignition temperature of a Chinese bituminous coal with a similar fixed carbon and volatile matter content.

The temperatures of maximum heat release were different for the biomass and lignite fuels, which reflected the different ignition behavior of these two types of fuels. For almond shell and olive residue, the first heat release peak occurred at a temperature (T_{DSC1}) lower than the particle ignition temperature (600 K *versus* 660 K), stating that the maximum heat release is reached during volatiles combustion. The Tunçbilek and Soma lignite coals presented a heat release peak temperature (T_{DSC1}) higher than the particle ignition temperature (~820 K *versus* ~660 K).

In practical terms the results indicate that the temperature of either biomass residue or lignite coal should not go over 500 K, for instance during pre-heating, in order to prevent volatiles ignition. This can have more severe consequences for the case of the biomass residues since the maximum heat release is reached at only 600 K, and at this temperature ~50 wt.% of both biomass fuels would have been consumed.

Table 4.2 Characteristic ignition temperatures during TGA experiments for all studied fuels.

Fuel	Characteristic temperatures, K			
	$T_{vol.}$	$T_{part.}$	T_{DSC1}	T_{DSC2}
AS	510	660	596	745
OR	516	670	614	778
TL	508	656	810	-
SL	500	655	833	-

The characteristic ignition temperatures obtained in TGA experiments are typically lower than those obtained in EFR experiments. Khatami and Levendis [44] studied the single particle ignition of sugar cane bagasse and two lignite coals in a drop tube furnace at a heating rate of ~10^4 K/s and reported ignition temperatures of ~700 K for the biomass and ~1050 K for the lignite coals. These values were approximately 200-300 K higher than those obtained in this work at low heating rates. The ignition criterion used for the TGA experiments and the drop tube furnace experiments is not the same so deviations are to be expected. It is important to note that in the case of the TGA experiments, the reported temperature does not correspond to the sample temperature, whereas in the study of Khatami and Levendis [74] the reported temperature corresponds to the particle surface. Both homogenous reaction in the vicinity of the sample and heterogeneous reactions in the sample can increase the fuel temperature at the onset of ignition. These results appeared to indicate that the ignition temperature obtained by TGA could not be directly compared with the ignition temperature at high heating rates. In any case, the minimum ignition temperature (i.e. from TGA) determined in the present work can be of interest in terms of safety of storage and delivery of the studied solid fuels.

The self-ignition risk was assessed for all solid fuels using the low heating rate results from TGA. The self-ignition risk plot, Figure 4.1 was obtained by plotting the first DTG peak temperature as a function of the activation energy based on the approach of Querol and Aragón [42]. Figure 4.1 reveals that the investigated fuels formed two groups: biomass fuels (high ignition risk), and lignite fuels (low ignition risk). In the

case of the present study, if only the activation energies were evaluated as a measure of the ignition risk, all fuel samples would be attributed a very-high propensity for spontaneous combustion, similarly to the reported by Torrent et al. [36] for the fuels studied therein. As a consequence, the additional parameter DTG peak temperature was used along with activation energy to classify the ignition risk propensity of fuels. Likewise, Jones et al. [39] outlined the self-ignition risk map for various coal and biomass fuels based on DTG peak temperature and activation energy. The activation energies of the majority of fuels therein were lower than 79 kJ/mol which would indicate a very high risk of self-ignition if the DTG peak temperature was not considered as supplementary self-ignition criterion. It is thus clear that the use of two criteria enabled a more complete and detailed separation of the ignition risk per fuel.

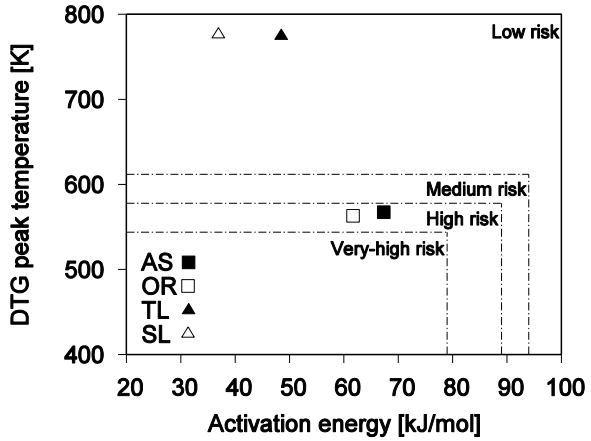

Figure 4.1. Risk of self-ignition map.

Other parameters such as the H/C and O/C ratios may also be important to classify biomass residues in terms of self-ignition tendency. As observed by Torrent et al. [36], who studied the ignition of ten different biomass fuels, lower characteristic TG-O_2 temperatures, i.e. lower oxidation temperatures in pure oxygen atmospheres, were related with higher H/C and lower O/C ratios. In addition, Torrent et al. [37] observed a correlation between the oxidation temperature in pure oxygen combustion and the

DTG peak temperature in air conventional combustion. In this work, both biomass residues presented similar H/C and O/C ratios: ~1.6 and ~0.7, respectively, as well as similar DTG peak temperatures: ~565 K, which is in line with the findings of Torrent et al. [36]. Therefore, the H/C and O/C ratios can also be used as an initial assessment of the low temperature ignition risk of the almond shell and olive residue.

4.1.2 Ignition mode

Figure 4.2 shows the TG and DSC profiles obtained in this work for all solid fuels in a dry air atmosphere and heating rate of 20 K/min. These profiles were used to determine the ignition mode following the procedure used by Chen et al. [243]. Both biomass residues presented two exothermic peaks, the first one before and the second one after the divergence point of the TG curves (cf. Figures 4.2 a-b). Therefore, according with Chen et al. [243], both biomass residues ignited homogeneously, with the volatiles ignition taking place at the first heat release peak and the devolatilized particle ignition at the second heat release peak.

Lignite fuels presented one exothermic peak after the divergence point of the TG curves. Analysis of the heat flow profiles for these fuels revealed that the exothermic reaction started to take place before the separation point of the pyrolysis/combustion TG profiles (cf. Figures 4.2 c and d). The increase of the rate of heat release before separation of the TG curves was an indicator of volatiles ignition. Since only one exothermic peak was observed, the ignition of the solid particles was assumed to take place while volatiles were still burning, and the hetero-homogeneous mode of ignition was attributed to both lignite coals.

In brief, under low heating rate combustion, lignite coals had a tendency to ignite in a hetero-homogeneous mode, and the biomass residues in a homogeneous mode. The ratio of volatile matter/fixed carbon may be an indicator to predict ignition mode at low heating rates. The biomass residues present a volatile matter/fixed carbon ratio of ~ 4.1, whereas the lignite coals present values of 0.76 and 1.2, respectively. This

suggests that fuels with higher volatile matter/fixed carbon ratios tend to ignite homogeneously. However, the study of a larger number of fuels would be necessary to enable a solid correlation between the volatile matter/fixed carbon ratio and the ignition mode.

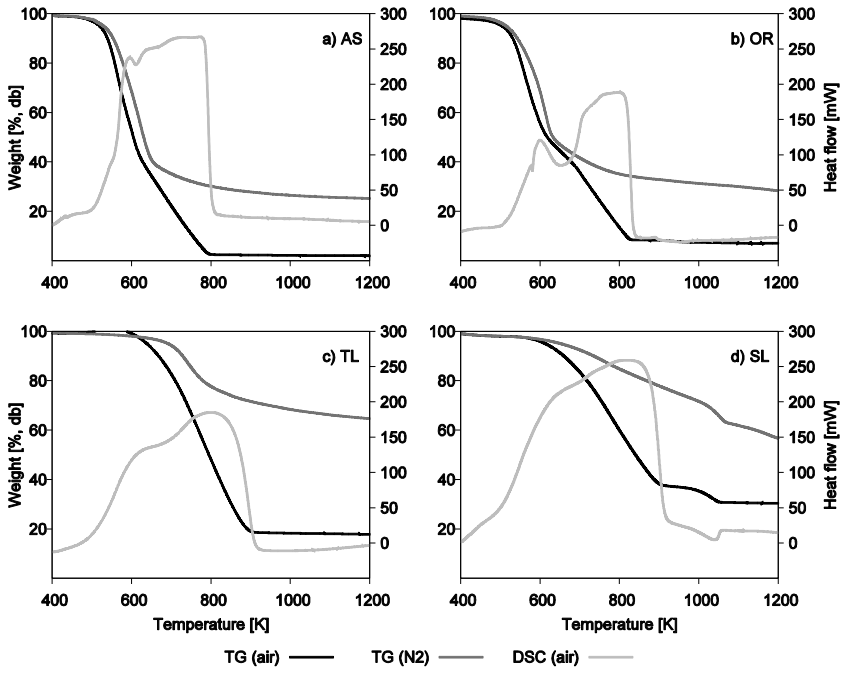

Figure 4.2. TG – combustion (black lines); TG – pyrolysis (dark grey lines); and DSC – air (light grey lines) profiles for all studied fuels under 20 K/min. a) AS; b) OR; c) TL; d) SL.

In the case of the EFR experiments, the ignition mode was evaluated by direct visual observation of the recorded images and classified as gas-phase ignition mode or surface ignition mode. Figure 4.3 shows typical ignition events for a number of individual particles during the EFR experiments. The filtered light intensity signal is depicted for five distinct ignition events of TL, AS, and OR in Figure 16a, along with the correspondent recorded frames in Figure 4.3b. Event a) shows the gas-phase

ignition of the studied Tunçbilek lignite, events b) and d) show the surface ignition of small size almond shell and olive residue particles, respectively. Similarly, events c) and e) present the gas-phase ignition of large size almond shell and olive residue particles, respectively. For events a) and e), it is possible to clearly distinguish the two stages of combustion as follows: frame 1 corresponds to the heat-up phase; frame 2 reveals the onset of ignition; frame 3 presents the maximum visible light during the volatiles combustion; frame 4 shows the last stage of the volatiles combustion and the beginning of the char oxidation; and frame 5 corresponds to the maximum visible light during the char oxidation. As for events b) and d), it is not possible to distinguish clearly between the different stages of combustion and, since char oxidation produces very intense luminosity that may hinder the luminosity generated by the volatiles flame, it is not possible to identify if this is a heterogeneous ignition or a hetero-homogeneous ignition. The volatile clouds originated from the combustion of TL (cf. Figure 4.3, event a) are much brighter than those originated from the biomass volatiles burning, as depicted in Figure 16b, events c) and e). Similar observations for coal were reported by Khatami and Levendis [56] and Molina and Shaddix [244], who attributed them to the formation of soot during the devolatilization of the individual coal particles.

The percentage of gas-phase ignition occurrence for each solid fuel is shown in Figure 4.4a and b for conditions T1-T3 and O1-O3, respectively. The TL fuel and the largest particles of AS and OR undergo gas-phase ignition, regardless of both temperature and oxygen concentration in the ignition zone, as corroborated by the high percentage of gas-phase ignitions (>74%). The high percentage (~100%) of gas-phase ignition for the OR particles in the size range 224-250 μm, regardless of the test condition, was consistent with the work of Simões et al. [270]. In the case of the smallest particles of biomass, a decrease of the percentage of the gas-phase ignition was observed as the mean gas temperature increased. The smaller size biomass particles under condition T1 showed a significant amount of surface ignitions (60-73%), in contrast with the larger size biomass particles for the same conditions (<20%). The transition in the ignition mode was documented by Howard and

Essenhigh [54]. These authors defined a critical particle diameter such that, for particles below the critical diameter, the ensuing volatiles flame does not lift from the particle, and volatiles and char burned simultaneously on the particle surface. It appears that for the present biomass residues the critical diameter was located between 80-90 μm and 224-250 μm.

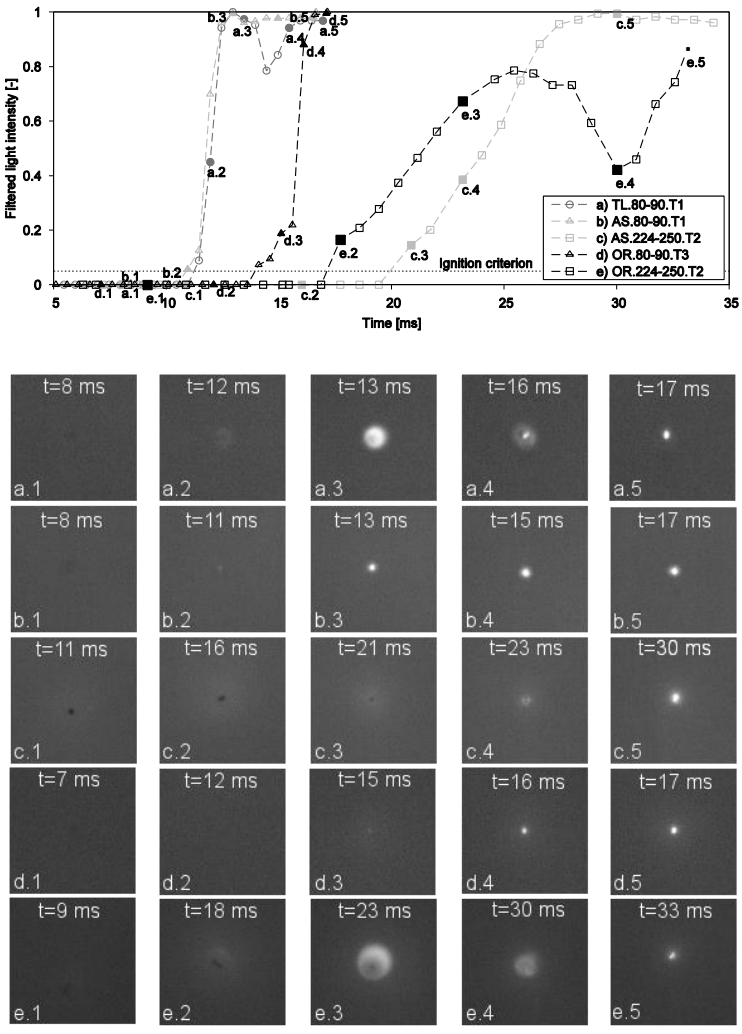

Figure 4.3. Typical ignition events of individual particles during the EFR experiments: (top) filtered and normalized light intensity and the ignition criterion; (bottom) recorded frames for selected events.

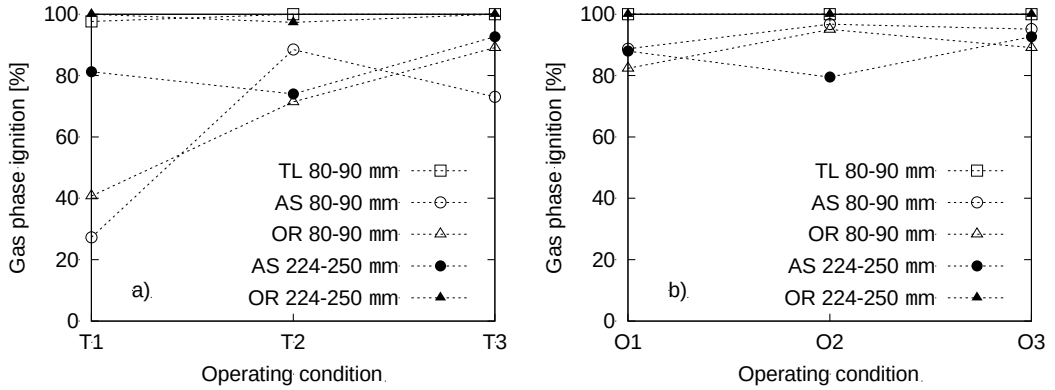

Figure 4.4. Percentage of gas-phase ignition for all solid fuels, except Soma lignite, during the EFR experiments. a) Conditions T1-T3; b) conditions O1-O3.

Under either low or high heating rates, almond shell and olive residue generally ignited in the gas-phase (i.e. homogeneous ignition). This is likely a consequence of the high amount of volatiles present in the biomass residues, particularly the low-density volatiles that prompt the gas-phase ignition, regardless of the heating rate. In addition, the Tunçbilek lignite presented a distinct ignition behavior under different heating rates. Hetero-homogeneous ignition was observed at low heating rates, whereas at high heating rates the ignition was homogeneous. A major difference between the TGA and the EFR is the reaction controlling mechanism: in the TGA the reaction is controlled by intrinsic kinetics, whereas in the EFR the reaction is likely to take place in the diffusion controlled regime. At low heating rates there is sufficient oxygen diffusion to oxidize both the volatiles released and the particle surface, which allows for the hetero-homogeneous ignition of the Tunçbilek lignite to occur. In contrast, in the EFR experiments the chemistry is rapid enough, and the oxygen diffusion is controlling the reaction of the volatiles-oxidizer mixture. In addition, the volatiles may act as oxygen barrier and further prevent the oxygen from reaching the particle surface.

4.1.3 Ignition delay time

Ignition delay times were determined under high heating rates from the EFR experiments. Figures 4.5 and 4.6 show the ignition delay times for all solid fuels, under operating conditions T1 to T3, and O1 to O3, respectively. Ignition delay times systematically decreased as the temperature increased. It was observed that with the increase in the gas temperature, ignition delay times for all solid fuels within the same size range converged to the same value, as seen in Figure 4.5. This suggested that as the particle heating rate increases, the differences in composition became less important, as also observed by Simões et al. [46].

Figure 4.5 shows that the ignition delay times do not change significantly for any of the oxygen concentrations within the range tested. It has been reported a tendency for ignition delay times to decrease with the increase in the O_2 concentration due to the increase in the reactivity of the fuel-oxidizer mixture[45,74,271], but this was not observed here presumably because the range of oxygen concentration studied was too narrow. Note that the oxygen range was kept narrow, i.e. low oxygen concentrations, in an attempt to replicate the conditions found in conventional coal-firing burners.

The solid fuels studied have very distinct compositions and this is reflected in the different ignition delay times, even for the same test conditions. The TL presented the lowest ignition delay times with 10 (+/-0.7) ms. The SL presented ignition delay times close to those of the biomass residues, varying from 15.5 (+/-0.8) ms for condition T1, to ~10 (+/-0.5) ms for condition T3. The ignition delay time for the SL at 1460 K (condition T1) resembled the 15 (+/-5) ms determined by Khatami and Levendis [74] for a North American lignite at 1350 K, whereas the ignition time for the TL was lower in approximately 5 ms. In fact, the ignition times of the TL resembled those of the North American bituminous coal [74]. Interestingly, the moisture content of both lignites studied here was similar to that of the lignite and bituminous coals studied by the mentioned authors. The results suggested that the moisture content has a more preponderant impact on the ignition of coal particles

exposed to high heating rates than the rank of coal. In what concerns the size influence, for condition T1, the larger biomass particles showed a higher ignition delay time than the smaller particles: 28 (+/-2.5) ms and 16 (+/-1.1) ms, respectively, due to the higher thermal-inertia of the larger particles.

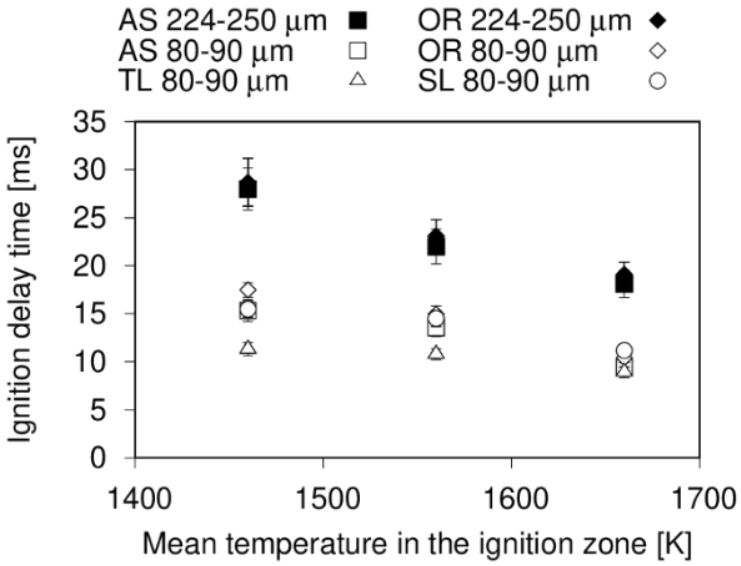

Figure 4.5. Ignition delay times for all solid fuels and operating conditions T1 to T3. Vertical bars represent 98% confidence statistical errors.

In general, the ignition delay times of the lignite coals appear to be longer than those encountered in large-scale pulverized boilers. This fact can be a consequence of a multitude of factors such as: (i) slightly higher particle size range (106-125 µm) in comparison with the size cuts used in industry, which can be as low as 50 µm, and subsequent magnification of the ignition delay in up to threefold [53]; (ii) the turbulent effects that enhance convection/diffusion in a large-scale boiler and that are not reflected in the EFR; (iii) radiative heat transfer observed in industrial boilers but not in the EFR; or (iv) high moisture content of the lignite coals, which were

simply air-dried prior to the EFR tests, contrasting with the practice in industrial coal firing.

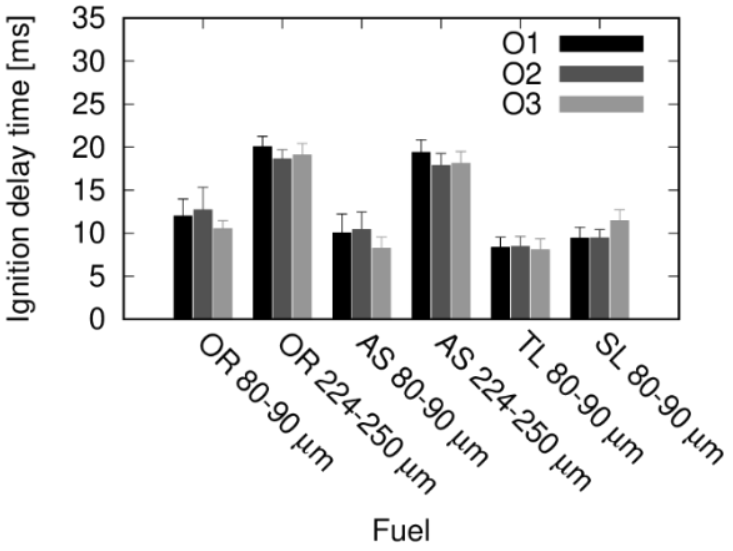

Figure 4.6. Ignition delay times for all solid fuels and operating conditions O1 to O3. Vertical bars represent 98% confidence statistical error.

Riaza et al. [271] and Khatami and Levendis [74] reported shorter ignition delay times for biomass fuels in comparison with lignite and coal fuels. The most obvious difference between the biomass residues studied in this work and those investigated by the aforementioned authors is the moisture content. These authors dried the fuels beforehand, whereas the fuels analyzed in this study were used as received. Figure 4.7 shows the ignition delay time of all studied solid fuels as a function of their moisture content for operating conditions T1-T3. The observed trend is an increase of the ignition delay time as the moisture content increases up to 10%. Beyond that the ignition delay time stabilizes. The apparent decrease of the point corresponding to T1 above 10% of moisture content is within the repeatability of the results. For high moisture content in the fuel (> 10 wt.%) two reactions play an important role

on the ignition. On the one hand, the steam shift reaction ($CO + H_2O \leftrightarrow CO_2 + H_2$) is faster at the high temperatures (1200-1400 ºC) that the particles are exposed to and the exothermic nature of the reaction combined with the production of H_2 (that increases reactivity) facilitate ignition. On the other hand, the steam gasification reaction ($C + H_2O \rightarrow CO + H_2$) that also occurs at high temperatures also produces H_2 but is endothermic.

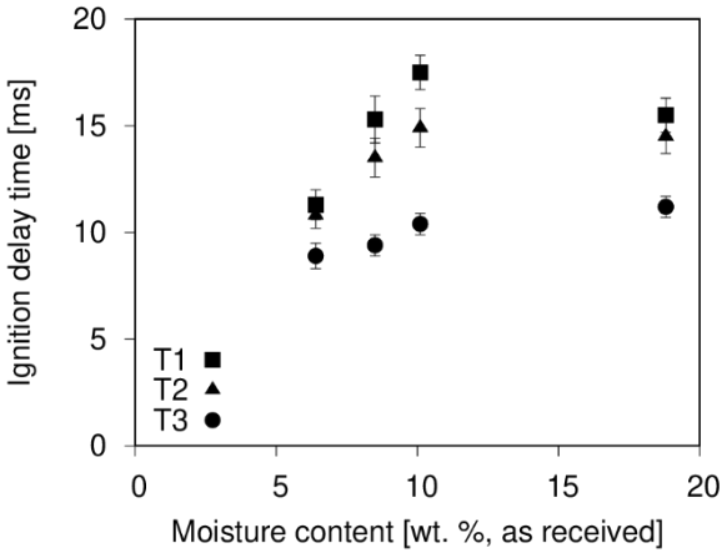

Figure 4.7. Ignition delay time for all solid fuels as a function of moisture content for operating conditions T1-T3. Vertical bars represent 98% confidence statistical error.

4.2 Combustion

In this section, the combustion behaviour of all fuels is investigated and discussed. In subsection 4.2.1 the combustion behaviour and kinetic parameters obtained at low heating rates are investigated. The results presented are reprinted with permission from Magalhães D, Kazanç F, Riaza J, Erensoy S, Kabaklı Ö, Chalmers H.

Combustion of Turkish lignites and olive residue: Experiments and kinetic modelling. Fuel 2017;203. Copyright (2017) Elsevier.

In subsection 4.2.2 the single particle high heating rate combustion behaviour, analysed using high-speed cinematography and three-colour pyrometry, is presented. This includes aspects such as the combustion mode, the volatile and char burning times and temperatures, and, based on the former two, the co-firing potential of different fuels and fuel mixtures. The results presented are reprinted with permission from Magalhães D, Panahi A, Kazanç F, Levendis YA. Comparison of single particle combustion behaviours of raw and torrefied biomass with Turkish lignites. Fuel 2019;241:1085–94. Copyright (2019) Elsevier.

In subsection 4.2.3 the investigation on particulate matter formation during co-combustion of biomass-coal blends is given. These fuels and blends are selected based on the combustion kinetics and high heating rate combustion behaviour from subsections 4.2.1 and 4.2.2, respectively.

4.2.1 Low heating rate combustion behaviour and kinetics

In this subsection, combustion kinetics modelling results are presented and discussed for low heating rates. The low heating rate kinetics are obtained from TGA experiments.

4.2.1.1 Combustion mode

Combustion experiments of all fuels in this study, were performed under three heating rates, namely 15, 20, and 40 ºC/min, using a thermogravimetric analyzer. The thermogravimetric (TG) and derivative thermogravimetric (DTG) curves from the combustion experiments were obtained as a function of the sample temperature. Based on the TG and DTG curves, the characteristic temperatures were determined for each fuel under all heating rates. TG/DTG profiles along with the characteristic

temperatures identified three different conversion stages where moisture release stage was not considered.

The first stage (stage A) is related to the decomposition of the fuels before ignition, and took place between decomposition temperature (T_d) and ignition temperature (T_{ig}). During this stage, the bonds between the aromatic clusters of coal were cleaved [272], and the hemicellulose in biomass was decomposed [273]. The second stage (stage B) is the major stage of combustion, which started with the ignition of fuels at T_{ig}. Stage B is represented by the first peak after moisture release in DTG curves depicted in Figure 4.8.

Third stage (stage C) is characterized by the second peak release in DTG curves and was only observed for olive residue and Soma lignite. Stage C is the second stage of combustion for olive residue as typically volatiles and char burn separately during biomass combustion [147,274]. A less pronounced peak at stage C for Soma lignite took place at higher temperatures around 800 ^{0}C which is attributed to phase transitions and cracking of the mineral matter such as calcium carbonate [275].

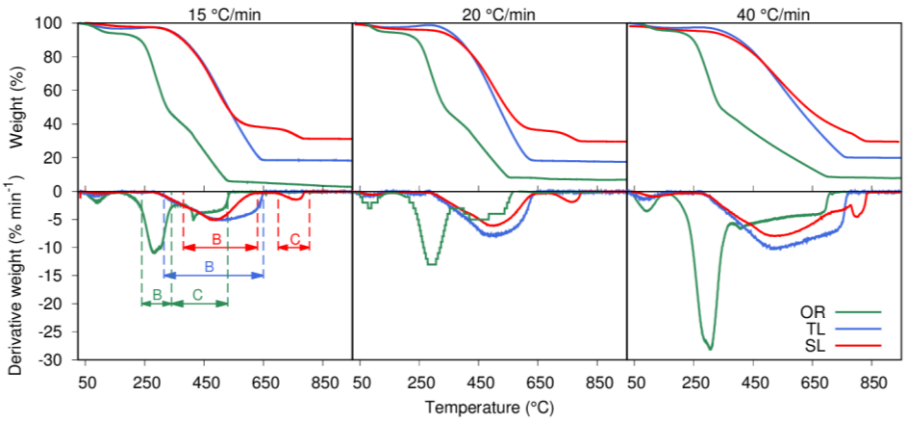

Figure 4.8. TG (top row) and DTG (bottom row) profiles for the studied fuels under: 15 ºC/min (left-hand side column); 20 ºC/min (center column); and 40 ºC/min (right-hand side column), with indication of the weight loss stages for all fuels (excluding moisture release and decomposition) in the 15 ºC/min DTG graph.

The weight loss during each conversion stage (A, B, and C) was determined from TG data and is outlined in Table 4.3 along with respective ash content following ASTM ashing standards for coal and biomass, obtained from Table 3.2. Thermal behavior and combustion characteristics of the fuels at all heating rates used in this study will be further outlined and discussed in the following subsections based on the effects of fuel type and heating rate.

Table 4.3 Weight loss per stage of conversion, total weight loss, ash content, and unaccounted weight for all the fuels studied in this work at the intermediate heating rate (20 ºC/min).

Fuel	Loss (wt.%, db)				Ash content[a] (wt.%, db)	Unaccounted (wt.%, db)
	Stage A	Stage B	Stage C	Total		
OR	4.4	42.8	42.6	89.9	5.3	4.8
TL	7.1	74.2	-	81.2	17.5	1.2
SL	6.7	50.6	6.2	63.5	33.3	3.2

[a] values according to the ASTM standards for determination of ash content of coal and biomass (see Table 3.2).

4.2.1.2 Characteristic combustion temperatures and combustibility

Effect of the fuel type on the combustion characteristics

The onset of thermal decomposition of the fuels was highly dependent on the rank of the fuel. The decomposition of Tunçbilek lignite occurred at a temperature close to that of Soma lignite (~300 ºC) whereas olive residue presented fairly low decomposition temperature (~200 ºC) at all heating rates, see Table 4.4. The weight loss during decomposition, stage A, was typically low for all fuels, approximately 7 wt.% for both lignites, and 4.4 wt.% for olive residue.

Table 4.4 Characteristic temperatures (T_d – decomposition temperature; T_{ig} – ignition temperature; $T_{p,B}$ – stage B peak temperature; $T_{p,C}$ – stage C peak temperature; T_B – burnout temperature), for all fuels under 15, 20, and 40 ºC/min.

Fuel	Heating rate (ºC/min)	T_d	T_{ig}	$T_{p,B}$	$T_{p,C}$	T_B
OR	15	208	240	286	414	531
	20	201	245	290	423	551
	40	185	242	316	410	703
TL	15	318	380	505	-	646
	20	310	380	502	-	630
	40	305	382	516	-	767
SL	15	325	380	490	775	590
	20	321	382	500	770	620
	40	309	405	535	800	830

Thermal decomposition was followed by combustion during which each fuel presented a distinct behavior. According to Figure 4.8, olive residue presented two stages of weight loss, stage B and stage C, during combustion. Stage B for this fuel occurred between 240 – 340 ºC with a distinctive peak at 290 ºC, and for stage C the temperature range was 340 – 530 ºC, with a less pronounced peak at 420 ºC. As indicated in Table 4.3, olive residue experienced a weight loss of approximately 43 wt.% during each stage (B and C). This may be attributed to partial volatile combustion during stage B and remaining volatile combustion along with char combustion during stage C which is in line with the findings of Yuzbasi and Selçuk [31] who also observed two distinct stages of combustion for olive residue. On the other hand, both lignites showed a single stage of weight loss (stage B) during combustion, see Figure 4.8, suggesting that volatiles and char burned simultaneously. Similarly, one major weight loss during combustion was also observed in the literature for Turkish lignite coals from Tunçbilek, Seyitömer, and Orhaneli [26], and a lignite coal from Thailand [62], all with similar volatile matter content to the lignites studied herein (~40 wt.%). This combustion stage started at approximately 380 ºC (T_{ig}), registered a peak temperature of 490 ºC, and extended until 600 ºC for both lignites. The total weight loss during the combustion stage for

Tunçbilek lignite was 74.2 wt.%, whereas for Soma lignite the value was 50.6 wt.% (Table 4.3). These values are lower than the sum of volatile matter and fixed carbon content obtained from Table 3.2 which indicated the volatile release started taking place during decomposition, stage A, for both lignites.

The burnout of the fuel samples was highly dependent on the fuel type. Under the same heating rate (20 ºC/min), lignite coals showed the highest burnout temperatures (~630 ºC) followed by olive residue (~550 ºC). The lowest burnout temperature of olive residue may have been the consequence of several factors such as the higher volatile matter / fixed carbon ratio, or the higher porosity and aspect ratio of biomass [273].

The reactivity of each fuel was assessed through calculation of the combustibility index during the major stage of combustion (stage B), presented in Figure 4.9.

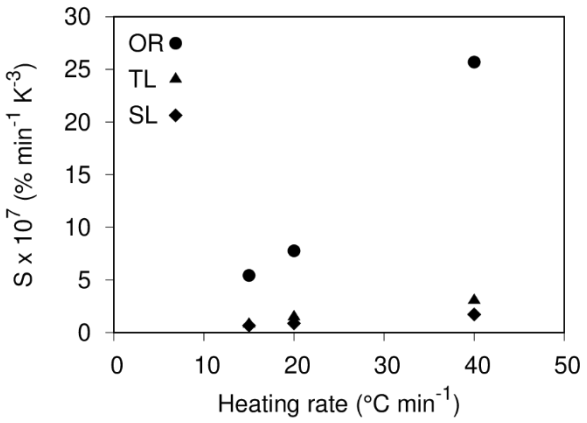

Figure 4.9. Combustibility index – S as a function of the heating rate for all three fuels (OR, TL, and SL) during the major stage of combustion (stage B).

It was observed that the combustibility index of olive residue was always at least five times higher than those of the lignites, specifically 7.8 x 10^7 % min^{-1} K^{-3} at 20 ºC/min, as expected due to the higher reactivity of biomass compared to the lignites [31].

Among lignites, Tunçbilek presented the highest combustibility values, which were approximately twice of those of Soma lignite, at the intermediate heating rate (20 ºC/min). Specifically, Tunçbilek presented a combustibility of 1.5 x 10^7 % min^{-1} K^{-3}, whereas Soma presented 0.9 x 10^7 % min^{-1} K^{-3}. The higher combustibility of Tunçbilek in comparison with Soma was a consequence of the slightest higher rate of weight loss during stage B. Furthermore, the combustibility index for both lignites is in line with the results of C. Zou et al. [78] who studied the combustion of two coals with similar ash content to those studied herein.

Effect of the heating rate on the combustion characteristics

The heating rate affected the combustion of both lignites and olive residue. The decomposition and ignition temperatures appeared to be generally independent of the heating rate. Similarly, the temperature at which the maximum derivative weight loss was observed (i.e. peak temperature) did not alter significantly with the change of the heating rate. On the other hand, the reactivity of all fuels, represented by the maximum derivative weight loss during combustion stage(s), increased with the increase of heating rate, particularly when shifting from 20 to 40 ºC/min, as visible in Figure 4.9, in line with previous results by Idris et al. [34]. Following the same trend, the combustibility index, another indicator of the reactivity that includes the effects of the ignition and burnout temperatures, was influenced by an increase on the heating rate [78]. For instance, the combustibility index values of both lignites increased in approximately two-fold when moving from 20 to 40 ºC/min, but were constant for either 15 or 20 ºC/min. Following a similar trend, the combustibility of olive residue underwent a drastic increase of three-fold when shifting from 20 to 40 ºC/min.

The burnout of the samples showed a distinct tendency to move to higher temperatures with the increase in the heating rate. When moving from 20 to 40 ºC/min, the burnout point of all fuels shifted ~150 ºC to higher temperatures. Under the two lower heating rates Tunçbilek lignite experienced burnout at ~640 ºC,

contrasting with the ~770 ºC at the highest heating rate [78]. The burnout of Soma lignite followed a similar trend and shifted from 590 to 830 ºC with the increase in the heating rate. Likewise, olive residue underwent burnout at 530 ºC at 15 ºC/min, and 700 ºC at 40 ºC/min [40,276,277]. This increase in the burnout temperature was due to the fact that under higher heating rates the reaction time was shortened, and the combustion process was inevitably moved to higher temperatures.

It should be remarked that in the case of Soma lignite at 40 ºC/min, the end of stage B (combustion stage) was overlapped with the initial part of stage C (demineralization stage), suggesting that this heating rate may not be suitable to distinguish individual mechanisms which were discernible at lower heating rates.

4.2.1.3 Kinetic behaviour

The combustion kinetic behaviour was characterized by determination of the ruling mechanisms and apparent activation energies for each combustion stage of each fuel under all heating rates. The temperature interval of each combustion stage, the fitted mechanism, the R^2 values, and the apparent activation energies for each heating rate and fuel are presented in Tables 4.5-4.7. In addition, Figure 4.10 presents the apparent activation energies as a function of the heating rate for all fuels, under both combustion stages (B and C).

Effect of the fuel type

The fuel type presented a major influence on the apparent activation energy during combustion. The combustion of Tunçbilek lignite, which occurred in one single stage B was best characterized by a diffusion-controlled mechanism. This suggested that the diffusion of oxygen to the char particle and of volatiles from the particle controlled the combustion process from ignition until burnout. Tunçbilek had apparent activation energy of ~100 kJ/mol for stage B at 20 ºC/min heating rate. Stage B of Soma lignite, however, was controlled by reaction kinetics, particularly a

first order mechanism. The stage B of Soma conversion presented apparent activation energies of ~40 kJ/mol at 20 ºC/min heating rate, as observed by Ozbas et al. [275] who presented activation energies of the same lignite at the same heating rate. It should be noted that the fitted mechanisms for stage B of both Tunçbilek and Soma lignite describe both volatile and char burning. Since it is not possible to ascertain if either volatile and/or char combustion are the controlling step mechanism, the obtained activation energies should be interpreted as apparent values [278], and in this study the apparent activation energy values were merely used for comparison purposes. Similarly, Gil et al. [63,278] and Inmas et al. [279] reported activation energy values for the combustion stages where simultaneous combustion of volatiles and char took place. The higher apparent activation energies of Tunçbilek in comparison with Soma lignite can be a consequence of (i) the higher carbon content of Tunçbilek lignite at the expense of oxygen resulting in a lower reactivity; (ii) the higher content of alkaline earth metals (specifically calcium) in Soma lignite which is known to show catalytic effects during thermal processes [62], as opposed to Tunçbilek lignite which presents mainly acidic mineral constituents (silica and aluminium oxides); or even due to a combination of these two factors.

Stage B of olive residue was controlled by reaction kinetics, particularly a first order mechanism. The apparent activation energy values of olive residue (~45 kJ/mol) were in line with those obtained by Álvarez et al. [101] who studied the kinetic behaviour of various biomass fuels, including olive stone and olive tree pruning, using the Coats-Redfern method. Gil et al. [63] studied pine, a typical woody biomass, and reported higher activation energy values (see Table 5 therein) compared to those of the olive residue in this study at the same conditions (see Table 4.7 herein). The low values of activation energy of olive residue may be a consequence of the relatively high content of lignin. In fact, it has been shown that the activation energy required for lignin to start decomposing may be similar or even lower than that of hemicellulose or cellulose [280,281]. This can be related to the fact that the decomposition of lignin starts at low temperatures, although it spans over a broad temperature interval because the tightly bound fibres are not

immediately cleaved [282], enabling the formation of char which is only oxidized at higher temperatures. The lower apparent activation energies of olive residue in comparison with Tunçbilek lignite can be attributed to the higher volatile matter / fixed carbon ratio (~4 for the olive and ~0.8 for Tunçbilek). Similar activation energies of olive residue and Soma lignite may be the consequence of two competing factors; i) higher volatile matter / fixed carbon ratio of the olive residue (~4) compared to Soma (~1.2) ii) lower alkaline content (CaO, MgO, K_2O, and Na_2O) of the olive residue (~3) compared to Soma (~18).

Stage C, i.e. the last stage of combustion, was only observed for olive residue. In this stage, at 15 and 20 ºC/min the uni-dimensional diffusion-controlled mechanism (D1) presented the best fit, whereas at 40 ºC/min the bi-dimensional diffusion controlled mechanism (D2) was chosen. Stage C of olive residue was likely due to partial volatile burning together with decomposition and char burning, as discussed previously. Apparent activation energies were approximately constant with the heating rate, with values of 13 kJ/mol and 9 kJ/mol, under 15 and 40 ºC/min, respectively.

According to the observations, when moving to higher temperatures the diffusion became the controlling mechanism for olive residue, as previously observed by Gil et al. [63] who studied the combustion of pine under similar heating rates. This was most likely due to the fact that at such temperatures (350-500 ºC) the chemical reaction clearly took place in a lower time scale as compared to the oxygen diffusion.

Table 4.5 Temperature intervals and correspondent model and apparent activation energy for each stage of combustion of Tunçbilek lignite.

Heating rate (ºC/min)	Stage B			
	T (ºC)	Model	E_a (kJ/mol)	R^2
15	380-650	D3	94.1	0.999
20	380-630	D3	103.1	0.999
40	380-770	D3	74.3	0.997

Table 4.6 Temperature intervals and correspondent model and apparent activation energy for each stage of combustion of Soma lignite.

Heating rate (ºC/min)	Stage B			
	T (ºC)	Model	E_a (kJ/mol)	R^2
15	390-600	O1	45.9	0.992
20	390-600	O1	43.3	0.999
40	400-800	O1	28.0	0.997

Table 4.7 Temperature intervals and correspondent model and apparent activation energy for each stage of combustion of olive residue.

Heating rate (ºC/min)	Stage B				Stage C			
	T (ºC)	Model	E_a (kJ/mol)	R^2	T (ºC)	Model	E_a (kJ/mol)	R^2
15	240-340	O1	44.2	0.978	340-530	D1	13.4	0.988
20	245-340	O1	46.5	0.980	340-550	D1	12.1	0.991
40	240-350	O1	47.7	0.985	350-700	D2	9.1	0.997

Effect of the heating rate on the kinetic behavior

The dependence of the apparent activation energies with the heating rate was minor and is illustrated in Figure 4.10 for all fuels. Typically, moving from 15 to 20 ºC/min

showed no influence in the apparent activation energies, whereas further increase in the heating rate to 40 ºC/min translated in a visible decrease, especially for the lignites. The influence of the heating rate on the apparent activation energies during stage C was marginal. Apparent activation energies were similar under all three heating rates for olive residue, with values of ~10 kJ/mol.

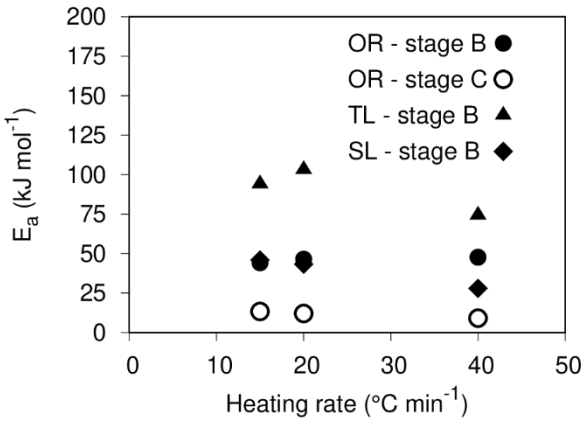

Figure 4.10. Apparent activation energy as a function of the heating rate for all fuels.

4.2.2 Single particle combustion behaviour at high heating rates

In this subsection, the combustion behaviour of all fuels is investigated using a DTF coupled with a high-speed camera and a three-colour pyrometer. Fuels under analysis are olive residue (OR), torrefied olive residue (OR-T), almond shell (AS), torrefied almond shell (AS-T), hazelnut shell (HS), torrefied hazelnut shell (HS-T), Tunçbilek lignite (TL), and Soma lignite (SL). The chemical characterisation is given in Table 3.3. The conditions achieved in the DTF are wall temperature of 1400 K, heating rates in the order of 10^5 K/s, and non-quiescent flow of 1 slpm air at atmospheric pressure.

Representative high-speed back-lit cinematography stills of all studied fuels are presented in Figure 4.11. Each column of this figure illustrates the combustion sequence of a representative single particle of each fuel. It should be noted that the first frame does not correspond to the time at which the particle enters the hot zone of the DTF, instead it corresponds to the time at which the particle becomes visible in the observation window and is recorded by camera. Likewise, the last frame in each sequence does not represent the point of char burnout, instead it represents the last event observed before the particle moved away from the observation window. The time specified in each frame denotes the cumulative time, in milliseconds, from the first to the last observation of the particle. Following initial remarks by Howard and Essenhigh [283], recently confirmed by Khatami et al. [81] and Simões et al. [46], the ignition of all fuels herein was classified as homogeneous (gas-phase), since the evolving volatile matter appeared to ignite first, while the devolatilizing particle still remained dark at the centre of an envelope flame. Thereafter, regardless of pre-treatment, all biomass fuels displayed two clearly distinguishable combustion phases: volatile matter combustion followed by char combustion, with no observable overlapping of these two stages. The non-overlapping of the volatile and char combustion stages was likely a consequence of the low aspect ratio of these particles as also observed by Riaza et al. [48] and Magalhães et al. [91]. Simões et al. [46] reported that the particles of pine bark, kiwi branches, vine branches and sycamore branches of similar sizes to this work also ignited homogeneously, however some highly irregular particles of wheat straw (with high aspect ratios) ignited heterogeneously at hot-spot sites. Herein, upon ignition of the evolving volatile matter, the ensuing envelope flames of raw and torrefied biomass fuels exhibited different shapes and brightness levels. Volatile envelope flames of torrefied AS and HS were typically more spherical and brighter, as compared to the particles of their raw biomass precursors. For raw OR, 60% of the observed particles displayed flames comparable in brightness and shape to those of torrefied OR. Moreover, torrefied biomass from OR, AS, and HS presented similar volatile flame brightness and shape.

The char combustion phase was similar for all biomass fuels, as discussed in the following subsections.

The two lignite coals presented major differences in their ignition and combustion behaviours. Tunçbilek lignite (TL) particles ignited homogeneously and their volatile matter flames were sooty and bright, with formation of elongated envelope flames with soot trails observed for 85 % of these particles, whereas the remaining particles displayed rather circular envelope flames. TL particles underwent some limited fragmentation (fragments ≤5) before ignition of ~40 % of the observed particles, followed by subsequent surface ignition of the fragments. Limited fragmentation was also observed by Rabaçal et al. [90] for two types of sub-bituminous coals (Brazilian and Colombian origin), of a similar size range (125-150 μm), burning under conditions similar to those of the present study. The results collected therein can also be used to shed light on the ranking of Turkish lignite coals burned herein. Overall, the combustion behaviours of most TL particles resembled those of typical bituminous coals, which ignite homogeneously and burn in two sequential phases, first of bright and sooty volatile flames forming contrails [74] and then of distinctly separate char combustion. While it is true that TL exhibited some fragmentation (~40 % of the particles), which is characteristic of lignite combustion [74], its most prevalent burning characteristics may classify it as a bituminous coal. The combustion behaviour of Soma lignite (SL) was highly dependent on the fragmentation behaviour of this fuel. The vast majority of SL particles (93 %) experienced extensive fragmentation before ignition, and from these, 60 % also underwent fragmentation during the volatile matter combustion of the main particle. The small fragments always underwent simultaneous volatile and char combustion on their surfaces. This is an agreement with findings of Levendis et al. [44] and Riaza et al. [57] for other lignites.

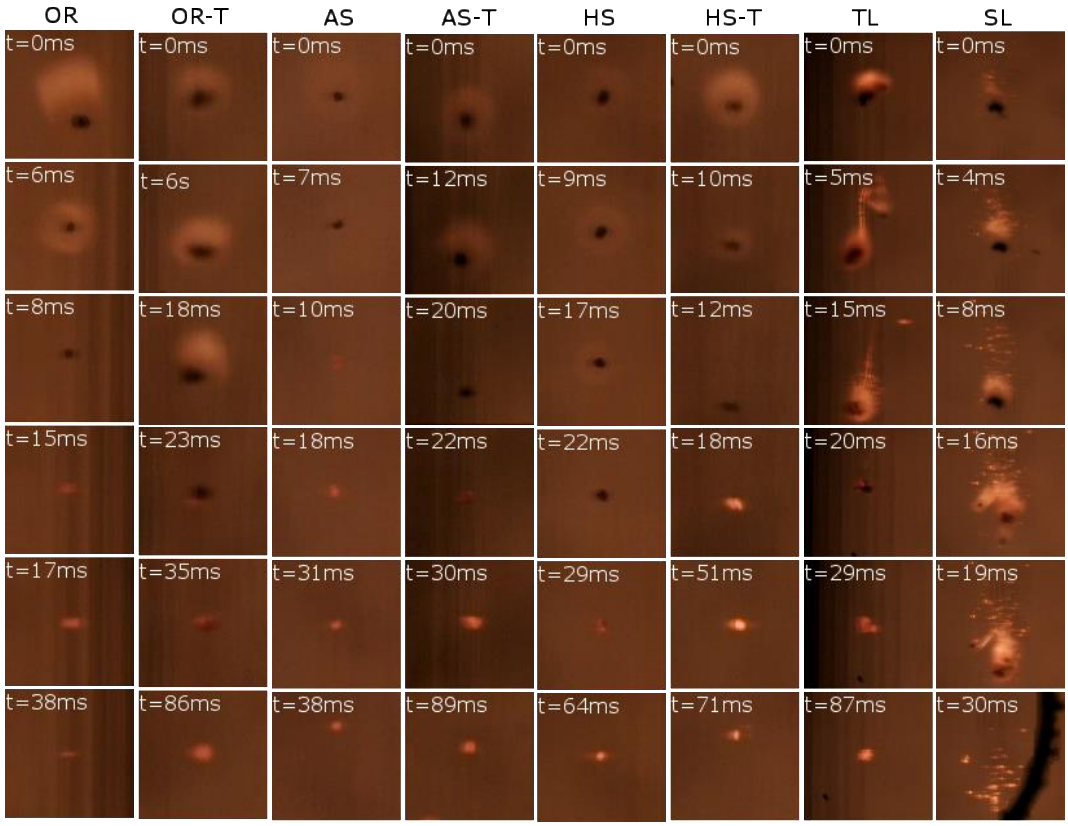

Figure 4.11. High-speed cinematography stills of typical combustion events of single particles of all studied fuels. For sizing purposes the diameter of the wire shown in the last frame of the SL sequence is 240 µm.

4.2.2.1 Volatile and char burning times of biomass and lignite particles

The combustion behaviour of the fuels was further analysed from application of pyrometry techniques, as described in [44,258], to obtain temperature-time profiles of single particles of each fuel throughout their combustion histories. Average burnout times for volatile matter and char combustion of 20 detected particles are displayed in Figure 4.12. The displayed numbers in each frame denote milliseconds, where zero does not mark the beginning of combustion, it merely represents the beginning of each depicted sequence. The time in the last frame of each sequence does not correspond to the char burnout time but rather to the last observed moment of the char combustion.

The volatile matter burning times of the raw biomass fuels were overall comparable to those of the torrefied biomass fuels, all in the range of 35-50 ms, with the latter being typically longer by several milliseconds, as shown in Figure 4.12. Panahi et al. [82] reported similar volatile burning times for other types of torrefied biomass fuels of similar particle size. This was expected since the volatile contents of raw and torrefied fuels were analogous (see Table 3.3). However, this appears to be inconsistent with the slightly lower volatile matter content of the torrefied fuels. Most likely, such difference may be attributed to the presence of different hydrocarbon molecules in the pyrolyzates of the raw and torrefied biomass fuels. The latter contain hydrocarbons generated by dehydration, dihydroxylation, and decarboxylation reactions [284] that burned longer. The volatile burning times of the Tunçbilek lignite (TL) coal were in the neighbourhood of 44 (+/-10) ms and are comparable to those of the biomass fuels, even though the volatile matter content of TL was 40% lower than those of the biomass fuels. This fact illustrates that the volatiles from TL were composed of heavier hydrocarbons, with lower diffusivity in air, which decreased their rates of devolatilization and/or combustion. Khatami and Levendis [33] reported volatile matter burnout times of other bituminous and sub-bituminous coals to be somewhat briefer at 10-20 ms.

The char burning times presented more salient variations between raw and torrefied biomass. On the one hand, the raw biomass chars of OR were burnt in 66 ms, whereas the raw chars of HS and AS were burnt in 45 ms. On the other hand, the torrefied chars of OR were burnt in 110-130 (+/- 30) ms, the torrefied chars of AS were burnt in similar times to OR, whereas the torrefied chars of HS were burnt in 81 (+/- 16) ms. Such discrepancies in the burning times of the different types of biomass chars (OR, AS, HS) may be caused by dissimilarities in their physical structures (densities, porosities, shapes) and in their chemical compositions. The differences in burning times of raw and torrefied chars of all biomass types was attributed to the much higher fixed carbon content of the latter (see Table 3.3). The aforesaid burning times are in line with burn-out times measured by Panahi et al. [35] for torrefied biomass chars (70-100 ms).

Tunçbilek lignite char burnout time was the longest of all fuels, at 131 (+/- 32) ms. However, a fraction of the TL particles (~30%) were consumed in 30-50 ms as a consequence of pre-ignition fragmentation; those particles were not taken into account in Figure 4.12. As mentioned previously, cinematography showed that limited fragmentation occurred in the cases of 37 % of the observed TL particles, which is in line with the frequency of the aforesaid short char burning times (30-50 ms) measured from pyrometry (in the cases of 30 % of the particles). The observed burnout times of Soma lignite (SL) fragment clouds were 34 (+/- 6) ms. The char burnout times of the two Turkish lignite coals are, as expected, a little longer than those reported earlier [44] for US lignite coals of smaller particle size.

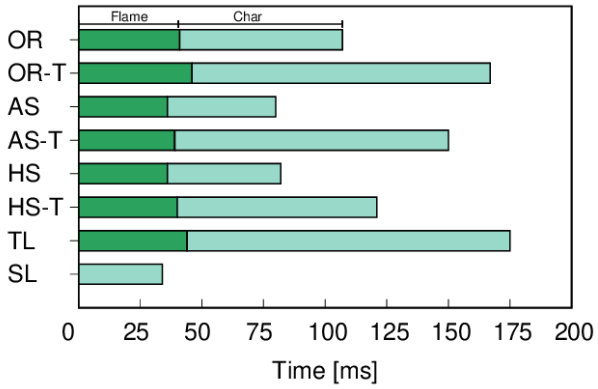

Figure 4.12. Flame (dark green bars) and char (light green bars) burnout times for all studied fuels, as measured by pyrometry.

4.2.2.2 Volatile and char temperatures of biomass and lignite coal particles

The pyrometrically-measured temperatures of the volatile flames and char particle surfaces are presented in Figure 4.13 for all fuels. These temperatures correspond to average peak values in the temperature-time profiles of 20 particles, two of which are exemplified in Figure 4.14; details on derivation of such profiles are given in Refs. [58, 59]. In the profiles of Figure 4.14 the TL coal has two separate peaks, the

first corresponds to the volatile flame combustion and the second to the char combustion. The SL coal has one peak, corresponding to simultaneous combustion of volatiles and char fragments. There is some uncertainty in the volatile matter flame temperatures of the biomass particles shown in Figure 4.13, particularly those of raw biomass which form dim flames, because of their low soot content [48]. Such low-luminosity flames generate low-intensity pyrometric signals, which impair the temperature calculation. That was not the case for the coal particles.

The average peak volatile temperatures of torrefied biomass were in the range of 2250-2340 K, whereas those of raw biomass were in the range of 2100-2300 K. Volatile flame temperatures of Tunçbilek were in the neighbourhood of 2000 K, below those of the biomass fuels, possibly due to the different composition of the pyrolyzates and the radiative heat losses from these highly-sooting flames.

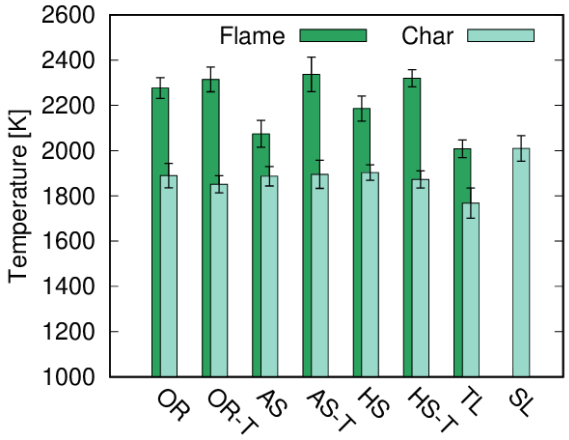

Figure 4.13. Flame (dark green bars) and char (light green bars) temperatures from pyrometry measurements for all studied fuels. Vertical bars represent 98% confidence statistical errors.

All biomass chars (both raw and torrefied) burned at ~1900 (+/- 40) K, in accordance with previous work by Riaza et al. [48] and Panahi et al. [35] . Chars of Tunçbilek

lignite burned with lower char temperatures (1768 (+/-) 67) K, likely because of the different their physical structure and chemical composition. Particularly the catalytic effects of Ca [285] and K, which exist in much higher concentrations in biomass, see Table 3.3, are likely to have increased the heat generation rates in biomass chars, which resulted in higher temperatures. In the case of Soma lignite, its extensive fragmentation produced small particles which can support simultaneous combustion of chars and volatiles on their surfaces [58,283]. Therefore the recorded temperatures for these coal particles, 2010 (+/- 57) K, were higher than those of the Tunçbilek lignite. In fact, they were very close to the temperatures of similarly fragmenting lignite coals reported by Levendis et al. [61].

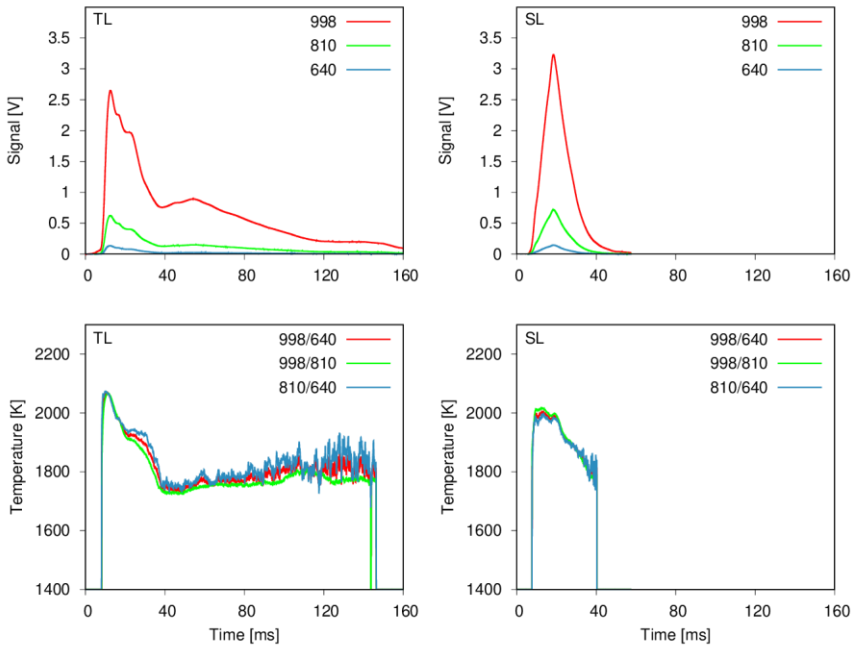

Figure 4.14. Three-color pyrometric intensity signals at wavelengths of 998, 810, 640 nm and derived temperature profiles of Tunçbilek lignite (TL) and Soma lignite (SL), based on the wavelength ratios of 998/640, 998/810 and 810/640.

4.2.2.3 On the co-firing potential of these biomass and lignite coals

The potential of the studied fuels for co-firing with coal is discussed herein. Firstly, the cumulative burnout times of all studied fuels are presented in Figure 4.15. Secondly, possible catalytic synergisms of certain inorganic elements in biomass and coal are considered to provide guidance on suitable biomass-coal ratios for co-firing and results are presented in Figures 4.16 and 4.17.

Burnout times of biomass and lignite particles

For the pulverized biomass to be co-fired in TL-burning furnaces, the cumulative burnout times of their particles (volatile matter + char) should be comparable. This seems to be the case, based on the results presented in Figure 4.15 for all three biomass fuels examined herein, whether raw or torrefied. For instance, it can be observed from Figure 4.12, that whereas raw and torrefied OR exhibited similar volatile burnout times, their char burnout times were significantly different. This resulted in cumulative burnout times ~50 % longer for the torrefied biomass. These longer burnout times of torrefied OR approximately matched those of TL; particularly torrefied OR (OR-T) was burnt in 167 ms, which is close to the 175 ms of TL. The cases of the other two torrefied biomass types (AS and HS) were also in line, i.e., they burned in cumulative times equal or less to those of TL. Moreover, all raw biomass types burned in cumulative times significantly lower than those of TL. To the contrary, the SL lignite exhibited much shorter burnout times, in fact shorter than TL by a factor of 5, and also much shorter than any of the biomass types. Hence, it would not be appropriate to co-fire biomass in furnaces designed for SL fuel. Instead, it is recommended to co-fire the biomass fuels in furnaces designed for TL combustion. With the same argument, the fast-burning SL coal can also be co-fired in TL boilers. Currently, electricity generation from TL and SL accounts for 0.38 % and 1.26 %, respectively, of the total installed capacity for electricity generation in Turkey [286].

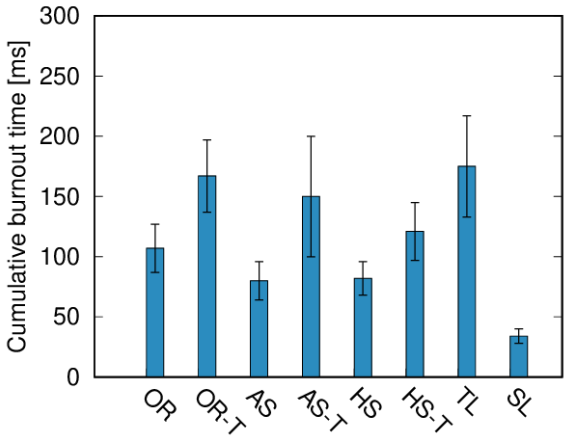

Figure 4.15. Cumulative burnout times from pyrometry measurements for all studied fuels. Vertical bars represent 98% confidence statistical errors.

K/Al ratios for biomass-coal blends

When biomass and coal are co-fired, some of the alkali and alkali earth metals released from biomass can be sequestered by coal minerals such as Si and Al, resulting in a decrease of the reactivity of the generated chars [163]. Nonetheless, it is also known that the alkali and alkali earth metals from biomass can synergistically interact with Al or Si from coal and catalyse both carbon oxidation and gasification reactions. In a recent work, Masnadi et al. [162] concluded that ratios of K/Al > 1 resulted in synergistic effects during co-firing. Accordingly, the K/Al ratios for different mixtures of the two coals with the three biomass fuels (both raw and torrefied) were calculated and are shown in Figures 4.16 and 4.17. Results for SL-biomass blends of various proportions are shown in Figure 4.16, whereas those for analogous TL-biomass blends are shown in Figure 4.17. In these figures, the horizontal line K/Al = 1 delimits the threshold above which synergistic effects are expected to occur. For blends of biomass with Soma lignite (SL), ratios above 50 % of biomass balanced with coal may produce synergistic effects for OR (raw or torrefied) and torrefied AS. For all remaining biomass fuels, ratios of 50-50 % or more are required, and such ratios are not practical in large-scale applications. Blends of Tunçbilek lignite (TL) with biomass are likely to present synergistic effects so

long as the content of OR-R, OR-T, or AS-T biomass is above 30 %. It is thus concluded that HS is the least viable fuel to promote synergies with coal ash elements. In summary, ratios of biomass above 50 % and 40 % in SL and TL, respectively, may enhance the reactivity of the blend through catalytic effects, however such ratios may not always be desirable in practical applications, due to the higher alkali contents of biomass and its lower heating values. Moreover, propensity of slagging and/or fouling due to the presence of K needs to be considered during selection of appropriate biomass-coal co-firing ratios.

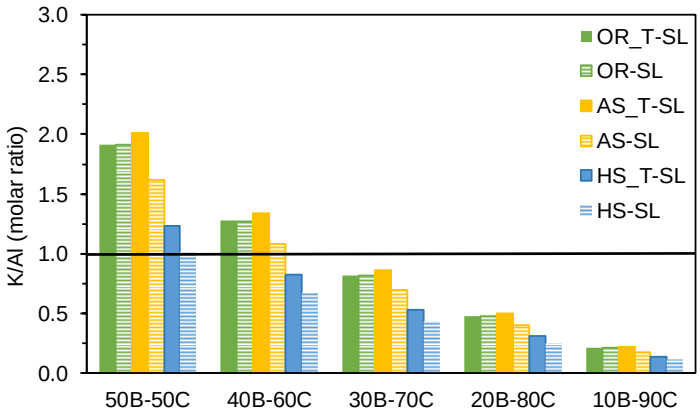

Figure 4.16. K/Al molar ratios for each blend of biomass (B) and Soma lignite (C). The horizontal line demarks the threshold above which synergistic effects may be observed for biomass-coal mixtures.

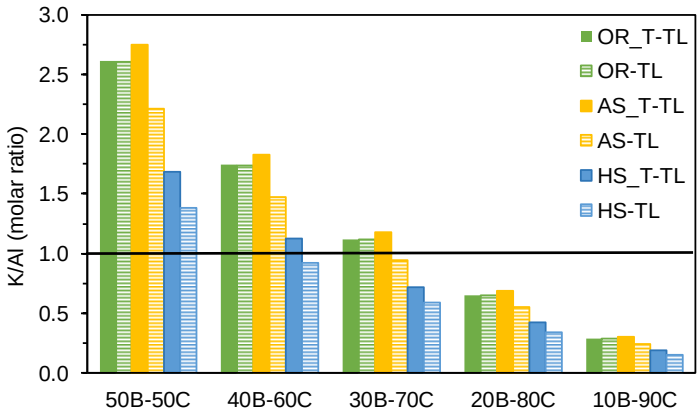

Figure 4.17. K/Al molar ratios for each blend of biomass (B) and Tunçbilek lignite (C). The horizontal line demarks the threshold above which synergistic effects may be observed for biomass-coal mixtures.

4.2.3 Particulate matter formation during co-combustion

The PM formation during pulverised co-combustion of biomass and coal was investigated with special focus on the influence of the biomass thermal pre-treatment and biomass-lignite co-firing. To this effect OR was selected as biomass feedstock in a particle size of 212-300 µm, and TL was chosen as the coal in 106-125 µm. The biomass was thermally pre-treated via torrefaction (at 275 ºC) and slow pyrolysis (at 500 ºC) using a tubular oven. The chemical composition and heating values of the fuels are given in Table 4.8.

In the previous subsection, it was concluded that biomass torrefaction had a considerable impact on the combustion behaviour. Specifically, torrefaction led to an increase of the burnout times of olive residue (OR) and almond shell (AS) to values similar to those of Tunçbilek lignite (TL). Moreover, torrefaction increased the heating value of biomass by ~20 % to values close to the typical heating values of lignite coal. These two observations strongly suggested that torrefied OR could be completely co-fired in existing lignite fired furnaces with no detriment for combustion efficiency or heat output. Nevertheless, biomass typically generates high

levels of PM2.5 and PM10 which constitute a human-health hazard and whose minimisation is pressing.

Table 4.8 Elemental analysis and energy content of the fuels.

Parameter	Olive residue			Tunçbilek lignite (TL)
	Raw (OR)	Torrefied (OR-T)	Char (OR-C)	
Proximate analysis (wt.%, as received)				
Moisture	5.9	0	0	2.81
Volatiles	71.9	67.2	28.5	31.1
Fixed carbon	19.3	29.6	59.7	52.1
Ash	2.9	3.2	11.8	14.0
Ultimate analysis (wt.% daf)				
C	46.6	56.6	74.6	61.8
H	6.40	5.84	2.74	5.60
N	0.58	0.32	0	2.65
S	-	-	1.87	1.45
O	46.4	37.3	20.8	28.5
Inorganic species (wt.% db)				
Si	4.60	1.07	2.35	33.3
Al	1.76	0.385	0.762	12.9
Fe	7.95	9.97	8.39	22.3
Ca	26.4	25.3	27.5	1.91
Mg	1.23	0.29	0.612	1.73
Na	-	-	-	-
K	48.6	56.8	57.1	3.16
P	1.98	3.59	1.58	0.12
Ti	-	-	0.446	2.87
Cl	4.46	2.52	0.90	-
S	2.37	-	0.41	19.1
Heating values (MJ kg^{-1})				
Low heating value (LHV)	16	21.5	26.8	25.7
High heating value (HHV)	18.6	22.8	27.4	27.8

The three biomass fuels (raw, torrefied, and biochar) were co-fired with Tunçbilek lignite in a ratio of 50:50 wt.% in the drop tube furnace at the Clean Combustion Technologies Laboratory of the Middle East Technical University. The combustion of the particles in the DTF took place at a constant wall temperature of 1000 ºC or

1200 ºC, the heating rate was estimated to be on the order of 10^4 ºC/s, and the residence time ~3 s in the isothermal reaction zone. The mass flow of particles was kept low at 10±1 g/h to maintain lean combustion conditions. The PM was collected and quantified using a 3-stage stack impactor and categorised as PM2.5, PM2.5-10, and PM10 based on the aerodynamic diameters.

4.2.3.1 Effect of the biomass particle size

Two distinct size ranges (106-125 and 212-300 µm) of the biomass feedstock (OR) were chosen to assess the influence of the particle size on PM formation at 1000 ºC. The PM results from combustion of small and large size OR are represented in Figure 4.18. Both PM2.5 and PM10 were similar for both size ranges, specifically 370-385 and 450-470 mg/g ash input, respectively.

These results are of significance for grinding purposes. As reported in the literature [287], the grinding energy to grind biomass to diameters between 250 and 500 µm varies from 120 kWh/t for aspen wood to 50 kWh/t for straw. By comparison typical coal grinding energy ranges from 7 kWh/t to 36 kWh/t. Moreover, according to the work of Svoboda et al. [288], the power consumption for grinding biomass to a particle size below 200 µm using a vibration mill is 0.03 kW_e/KW_{th}, whereas a particle size below 35 µm requires twice as much power. The current results showed that OR can be used in 212-300 µm without an increase in PM emissions, and thus allowing considerable savings in grinding costs. Accordingly, the largest OR was used in the subsequent investigations.

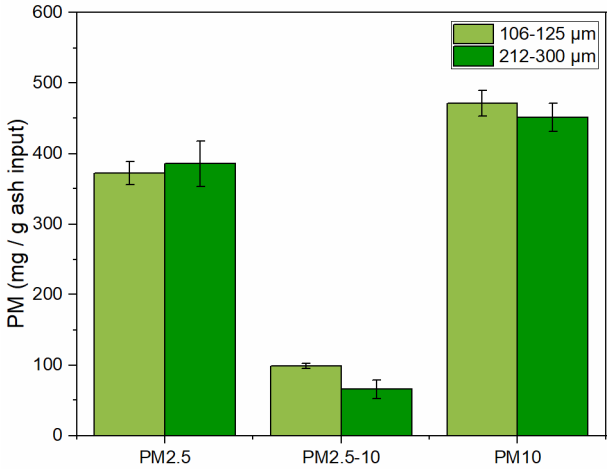

Figure 4.18. PM concentration (mg / g ash input) from the combustion of 106-125 and 212-300 µm size olive residue at 1000 ºC in the drop tube furnace. Vertical bars represent 98 % confidence statistical error.

4.2.3.2 Effect of the temperature

The effect of the DTF wall temperature (1000 vs 1200 ºC) was evaluated for OR in the size range of 212-300 µm. According to CFD results conducted in Clean Combustion Technologies Laboratory [59], the gas temperature in the useful heated zone was approximately equal to the furnace wall temperature and the temperatures presented herein were taken as the gas temperatures. The PM results from combustion at 1000 and 1200 ºC are represented in Figure 4.19. The PM2.5 values were slightly lower for 1200 ºC as compared with 1000 ºC, 325 vs 350 mg/g ash input, respectively. In line with the PM2.5, the PM2.5-10 values at 1200 ºC were also below those from combustion at 1000 ºC. As observed by Yang et al. [289], an increase in temperature from 1000 to 1200 ºC resulted in an increase of ultrafine PM0.1, but an overall decrease of PM1 emission during combustion of cotton stalk.

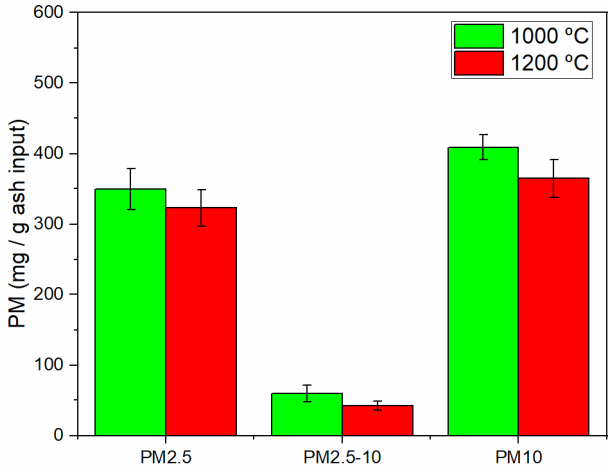

Figure 4.19. PM concentration (mg / g ash input) from combustion of 212-300 µm size olive residue at two distinct temperatures (1000 and 1200 ºC) in the drop tube furnace. Vertical bars represent 98 % confidence statistical error.

4.2.3.3 Effect of the biomass thermal pre-treatment

The thermal pre-treatment of biomass is promising since it largely improves the carbon content, calorific value, shelf-life, and grindability of the biomass. The PM results after combustion of raw OR, torrefied OR, and OR char, are presented in Figure 4.20 in different bases. The results per ash input allow to eliminate differences in the ash content of each feedstock and analyse the interactions between inorganic elements during devolatilization and combustion; the results per fuel input allow direct comparisons of different feedstocks; and the results per useful energy (i.e. lower heating value) input are of practical importance.

Due to the increasing ash yield with the pre-treatment temperature, the PM2.5 values per fuel input increased with torrefaction by 13 %, and further with pyrolysis by 31 %, in line with the increase in ash yield (see Table 4.8 and Figure 4.20a). Ruscio et al. [290], utilized olive residue under conditions similar to the ones employed herein and measured PM2.5 at ~26 mg / g fuel input, above the values measured herein (9.4 mg / g fuel input) due to the higher ash yield (7.6 wt. % vs 2.9 wt.% herein).

Upon normalization with respect to the useful energy input (see Table 4.8 for the lower heating values), the PM2.5 and PM10 for OR raw and char were similar at ~590 and ~670 mg / MJ input (see Figure 4.20b). The results showed that both raw olive residue and olive residue char can be used to provide the same useful energy output with no significant negative effect on PM2.5 emissions. Moreover, PM2.5 was lowest for torrefied OR as compared to either raw or char. Results in the literature on PM formation during biomass combustion at 1400 ºC in a drop tube furnace show that (i) the combustion of mallee leaf results in PM10 of ~100 mg / MJ input [127], whereas (ii) the combustion of straw results in higher PM10 levels of 911 mg / MJ input [111] which more closely resemble the results obtained herein for raw OR.

The PM results in an ash basis are presented in Figure 4.20c. The formation of PM2.5 from OR raw and torrefied was similar (323-338 mg / g ash input), whereas for OR char a considerable decrease was observed (133 mg / g ash input). On the other hand, PM2.5-10 increased slightly with torrefaction and then decreased with pyrolysis treatment. The causes for these variations were attributed to the change in inorganic species during torrefaction and slow pyrolysis and will be examined using SEM-EDS results.

As shown in Table 4.8, the heat treatment resulted in a decrease in both chlorine and sulphur which are known to form submicrometer PM (i.e. PM1) through vaporisation and nucleation-coagulation reactions [114]. Moreover, a decrease of silicon and aluminium was also observed. The SEM results are displayed in Figure 4.21 and the chemical composition from EDS analysis in Figure 4.22. The SEM results showed similar ash particles for all three biomass samples. For all samples, PM2.5 showed the presence of agglomerated particles. The PM2.5-10 particles were mainly composed of aluminosilicates cenospheres with size 2.5-5 μm.

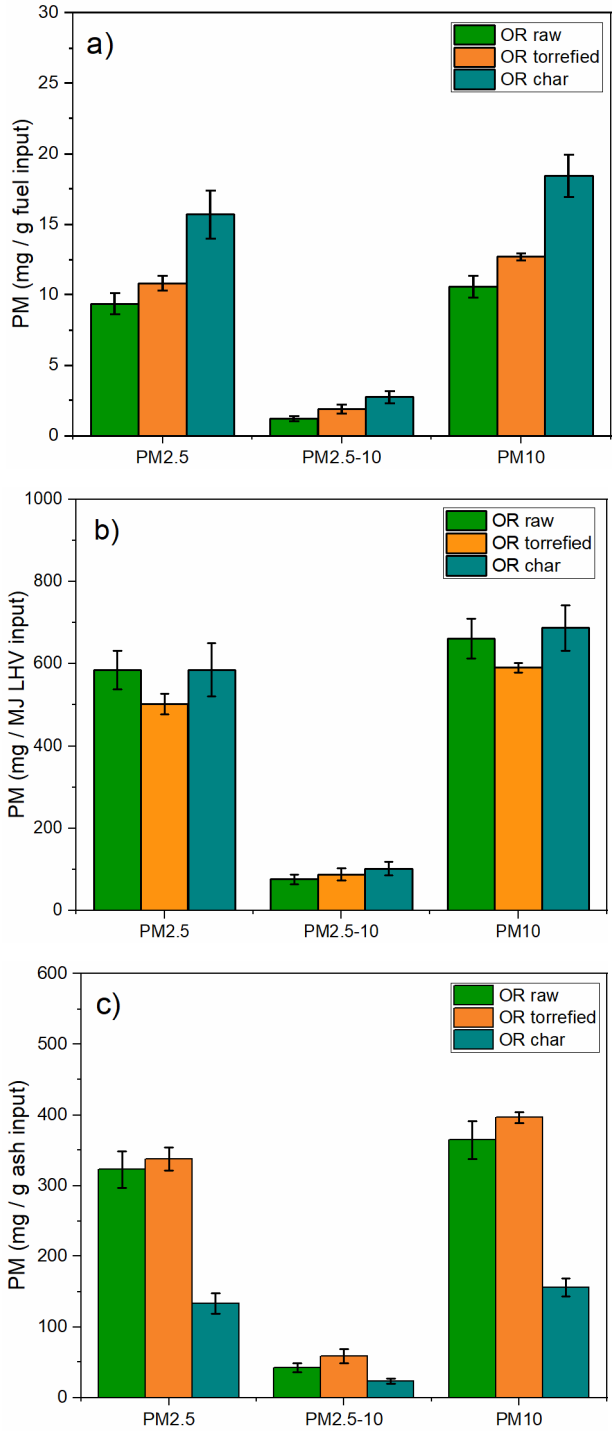

Figure 4.20. PM concentration from combustion of 212-300 µm size raw olive residue, torrefied olive residue, and olive residue char at 1200 ºC in the drop tube furnace. Vertical bars represent 98 % confidence statistical error. a) fuel input basis, b) useful energy (LHV) input basis, c) ash input basis.

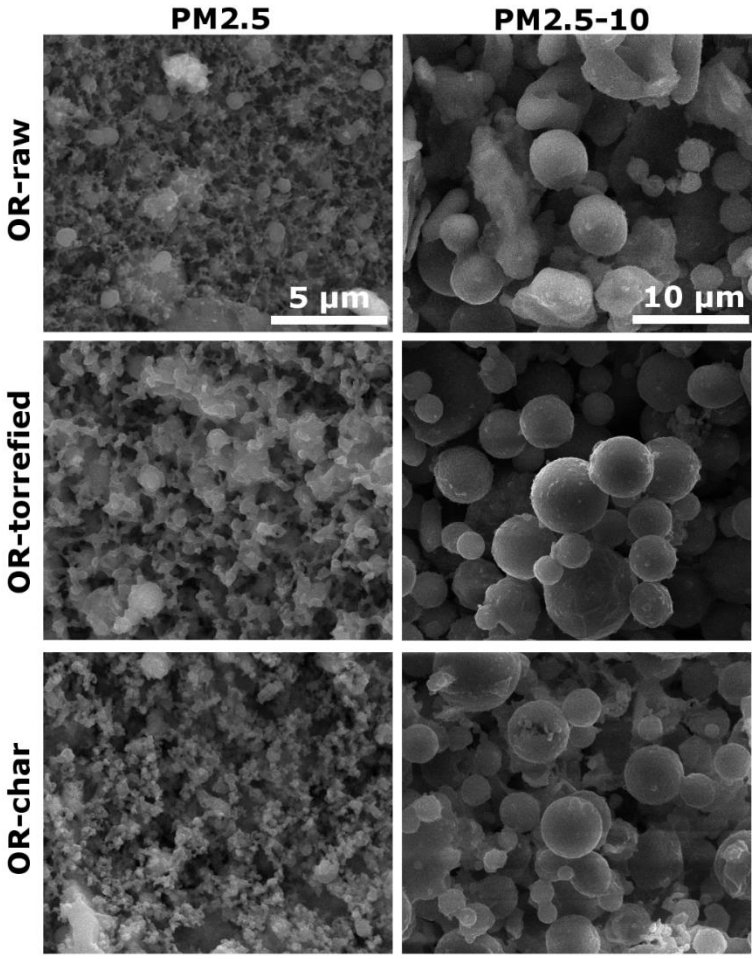

Figure 4.21. Scanning electron microscopy micrographs from PM2.5 and PM2.5-10 resulting from the combustion at 1200 ºC in the drop tube furnace of olive residue (raw, torrefied, and char).

The EDS results presented in Figure 4.22 show the content of major inorganic species in PM2.5 and PM2.5-10 from the combustion of raw, torrefied, and char from OR biomass. In general, PM2.5 was composed of K, Cl, S, and Si, whereas the species present in PM2.5-10 were Si, K, Al, Ca, and Fe. Moreover, the amount of K, Cl, and S were greater in PM2.5, and Si, Al, Ca, and Fe were dominant in PM2.5-10, in line with the literature [111,124,125,127,289].

The torrefied biomass contained less chlorine than the raw feedstock (see Table 4.8). This loss in Cl after torrefaction is highly advantageous since it allows for reduction in PM1 and PM2.5 levels. Herein, even though the Cl in the fuel reduced after torrefaction, the PM2.5 from combustion of raw and torrefied OR presented similar Cl content and as a consequence similar PM2.5 levels (in a basis of ash input). On the other hand, OR char presented PM2.5 emissions lower by three-fold as compared with either raw or torrefied OR, and this was in line with a decrease in Cl in both feedstock and PM2.5. The presence of Cl permitted the release of alkali and alkali earth metals (AAEM) to the gas phase by formation of alkali salts such as KCl, NaCl, KOH, and K_2SO_4. In the absence of Cl, these AAEM are known to be retained in the fuel as silicates and/or aluminosilicates and increase the levels of PM1-10 [111,289]. Moreover, a considerable presence of Si in PM2.5 from both raw and torrefied OR may be explained by the fragmentation of particles containing SiO_2 and/or silicates.

Analysis of the molar ratios (K+Na)/(Cl+2S) and (K+Na)/(Cl+2S+3P) provides valuable information on the compounds of the AAEM in PM2.5. Ratios close to unity would confirm that most K and Na are present in PM2.5 in the form of chlorides, sulphates, and phosphates, whilst ratios above unity show that AAEM are also present as silicates and aluminosilicates. The aforementioned molar ratios are presented in Table 4.9 for OR raw, torrefied, and char. As seen, the (K+Na)/(Cl+2S+3P) molar ratios for OR raw and torrefied were 0.99 and 1.18, and it can be concluded that K and Na are present only as chlorides, sulphates, and phosphates. For OR char, however, the molar ratios were greater than unity (2.00-4.41) which unequivocally proved that K and Na were also present in the form of silicates and aluminosilicates formed through coalescence and fragmentation. The results obtained showed that the mechanisms responsible for the formation of PM2.5 and PM2.5-10 in biomass feedstocks are also applicable for torrefied olive residue and biochar from olive residue.

Following heat treatment (torrefaction and slow pyrolysis), the Ca and Mg amounts in PM2.5-10 increased because the higher ash yields allowed for greater proximity among ash forming elements and the reactions between Ca/Mg and Si/Al containing

species were fostered. Concurrently, the amount of Si in PM2.5-10 diminished with increase of heat treatment temperature likely because of formation of PM>10 during combustion of OR torrefied and char. The typical cause for reduction of Si in PM2.5-10 is the fragmentation of SiO_2 during combustion, but since the amount of Si also decreased in PM2.5 such cause can be discarded.

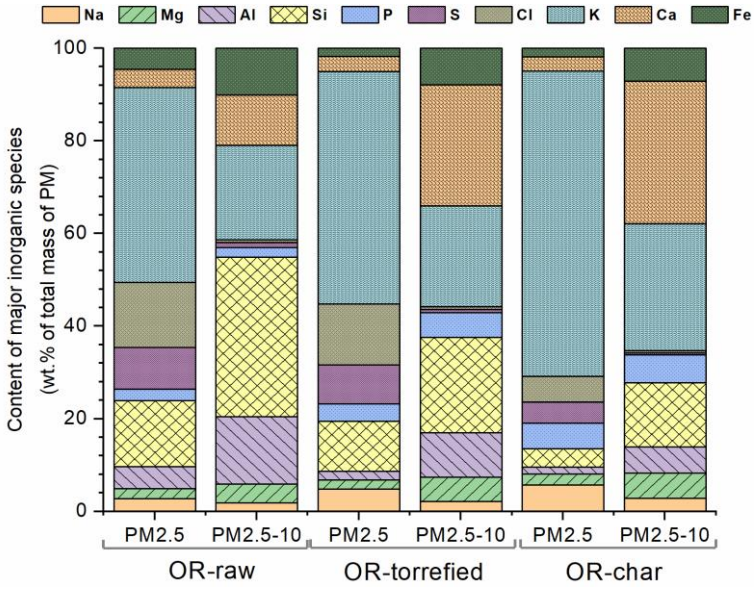

Figure 4.22. Energy dispersive spectroscopy results of concentration of major inorganic species present in PM2.5 and PM2.5-10 for raw olive residue, torrefied olive residue, and olive residue char.

Table 4.9 Molar ratios for PM2.5 from combustion of olive residue raw, torrefied, and char.

	K/(Cl+2S)	(K+Na)/(Cl+2S)	(K+Na)/(Cl+2S+3P)
OR raw	1.12	1.24	0.99
OR torrefied	1.44	1.67	1.18
OR char	3.84	4.41	2.00

4.2.3.4 Effect of co-firing

Biomass fuels (OR raw, OR torrefied, and OR char) were co-fired with Tunçbilek lignite (TL) to investigate synergies on PM formation during co-combustion. The PM2.5, PM2.5-10, and PM10 from co-firing trials are represented in Figure 4.23. As in the previous subsection (4.2.3.3), the results in this section are plotted per ash input, per fuel input, and per useful energy input into the furnace. The predicted values are also displayed to facilitate the identification of synergies between components. The PM2.5 and PM2.5-10 (in fuel input basis) from combustion of OR (raw, torrefied, and char) were always below those of TL. This was a consequence of the lower ash yields of OR raw and torrefied. For OR char and TL, which had similar ash yields (11.8 and 14 wt.%, respectively), the PM2.5 was lower for OR char (15.7 mg/g fuel input) as compared to TL (25.5 mg/g fuel input).

In a previous study, Kazanç and Levendis [291] reported the values of PM2.5 for a lignite coal at ~10 mg / g fuel input that is two-fold below the values measured in this work for TL (25.5 mg / g fuel input). Even though the lignite coal used by [291] had similar ash content (15.3 wt.%) to that of TL (14 wt.%), the inorganic composition was different and likely affected the PM2.5 formation. Specifically, K was higher for TL (0.44 wt.% fuel basis) as compared with the lignite coal used by [291] (0.07 wt.% fuel basis), even though Si and Al percentages were similar for both coals.

The PM results in ash input basis are represented in Figure 4.23 (a, b, c). Co-firing of raw OR with TL showed lower PM2.5 as compared to that from TL combustion, whereas for ORT-TL and ORC-TL the PM2.5 was even below that of the biomass fractions. Moreover, the PM2.5 from co-combustion of the blends was always below that of the predicted blends, particularly for ORT-TL and ORC-TL. These interactions between inorganic elements will be discussed further by analysis of the chemical composition of the PM2.5. The PM2.5-10 emissions showed a reverse result with values slightly above the predicted ones, and in overall the PM10 values of experimental ORT-TL and ORC-TL were below those of the predicted blends.

The PM results in useful energy input basis are represented in Figure 4.23 (d, e, f)In existing lignite-fired power plants, the addition of biomass would reduce the useful energy input as a consequence of the lower heating value of biomass. Therefore, the analysis of PM emissions normalized to the useful energy input will result in higher PM emissions for biomass fuels (as compared to a fuel input basis). Herein, for the same energy input, the levels of PM2.5 from combustion of OR, ORT, and ORC (585, 503, and 586 mg / MJ input, respectively) were below those of TL (992 mg / MJ input). In a recent study, Yani et al. [127] also compared the PM2.5 emission (per equivalent energy input as in the present study) from raw biomass (straw) with a Victorian lignite coal and observed that the PM2.5 from combustion of straw was ~60 % of that from lignite. In our study, co-combustion resulted in clear reduction of PM2.5 emission to values close to those of the biomass fuel, and below the predicted values. Specifically, combustion of OR-TL, ORT-TL, and ORC-TL blends resulted in 646, ORT-TL in 408, and 559 mg / MJ input, respectively.

The PM results in ash input basis are represented in Figure 4.23 (g, h, i). This basis for the PM allows to infer interactions between the inorganics in biomass and coal that occurred during co-combustion. In particular, the comparison of the PM2.5 emission from experimental blends with the respective predicted values allows for a clear identification of synergies / deactivations during co-combustion. The PM2.5 emission from the co-combustion of biomass-coal blends was always below the respective predicted values for all blends. This result was in line with previous studies that investigated the co-combustion of rice husk (raw and torrefied) with lignite coal [127], and the co-combustion of straw with bituminous coal [111]. Moreover, the PM2.5-10 results of experimental and predicted blends were similar, and conservation of mass dictated that the interaction between biomass and coal inorganics resulted in an increase of PM>10. Importantly, it was observed that the PM2.5 emission from combustion of OR-TL was at levels similar to those of TL (146 and 164 mg / g ash input) and that for ORT-TL and ORC-TL blends the PM2.5 emission was below TL. As in the previous subsection (4.2.3.3), the causes for these

variations were attributed to interactions during co-firing and will be examined using the chemical composition of PM2.5 from SEM-EDS results.

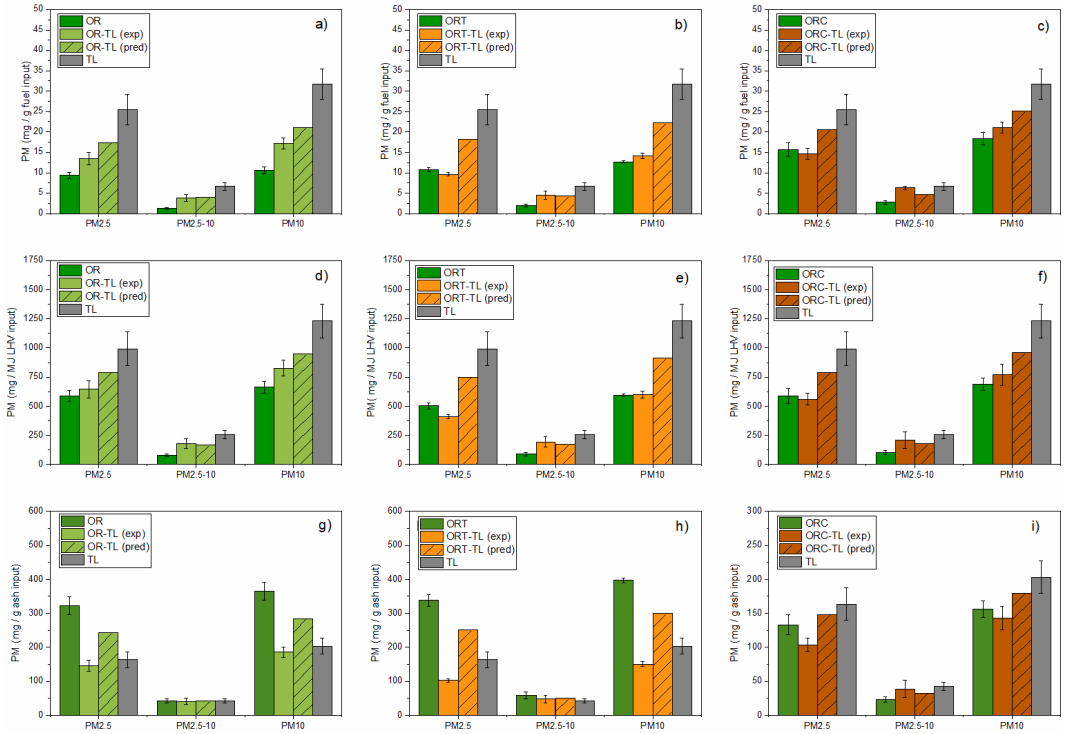

Figure 4.23. PM concentration from combustion of 50:50 blends of 212-300 µm size raw olive residue, torrefied olive residue, and olive residue char with 106-125 µm Tunçbilek lignite at 1200 ºC in the drop tube furnace. Vertical bars represent 98 % confidence statistical error. a-c) fuel input basis, d-f) useful energy input basis, g-i) ash input basis.

The SEM results of PM2.5 from co-firing trials are displayed in Figure 4.24. The SEM results showed similar ash particles for all three blends. TL showed a large presence of aluminosilicates in the form of cenospheres with diameter 0.5-2.5 µm. Similarly, all three blends showed the presence of both aluminosilicates cenospheres and agglomerated particles in all blends. The cenospheres varied slightly in average

diameter for each blend, specifically 1.5, 1.4, and 1.0 μm for OR-TL, ORT-TL, and ORC-TL, respectively.

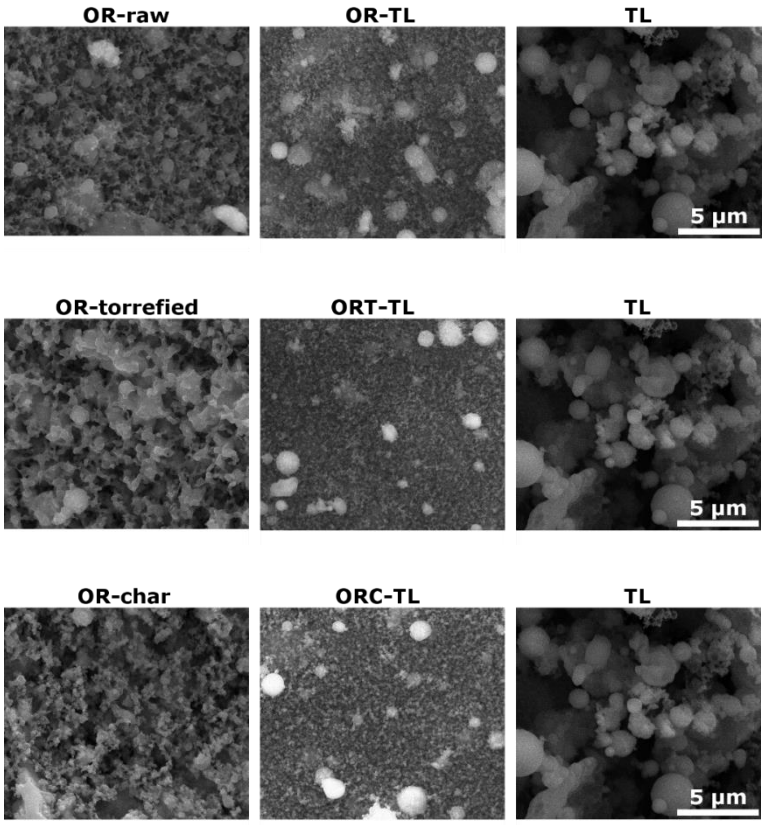

Figure 4.24. Scanning electron microscopy micrographs from PM2.5 resulting from the combustion at 1200 ºC in the drop tube furnace of olive residue (raw, torrefied, and char) and 50:50 blends with Tunçbilek lignite.

The EDS chemical composition for the major inorganic species in PM2.5 from co-firing of all three blends is given in Figure 4.25. In the figure, the chemical composition for the individual fuels is given for comparison purposes. TL showed high values of Si, Al, and Fe due to the presence of silicates and aluminosilicates. Accordingly, blending resulted in a decrease in Cl and K, and in an increase of Si, Al, Fe, and S, as compared to the values for the corresponding individual biomass

type. The two aforementioned factors contributed to the overall reduction of PM2.5 (in ash input basis) as stated before. Moreover, Figure 4.25 shows that the Si, Al, and Fe in PM2.5 after co-firing was below the additive values of Si, Al, and Fe for OR+TL, ORT+TL, and ORC+TL. This proved that silicates and aluminosilicates were mostly present in PM>2.5 rather than PM2.5. Nevertheless, these silicates/aluminosilicates were still present in sufficient amount to capture K and allowed for the reduction of PM2.5 as compared with the predicted blends (see Figure 4.23). The PM2.5 of the blends also showed low levels of Cl. As aforementioned, in the absence of Cl, the AAEM are known to be retained in the fuel as silicates and/or aluminosilicates. This provided another justification for the decrease in PM2.5 at the expense of increase in PM>2.5.

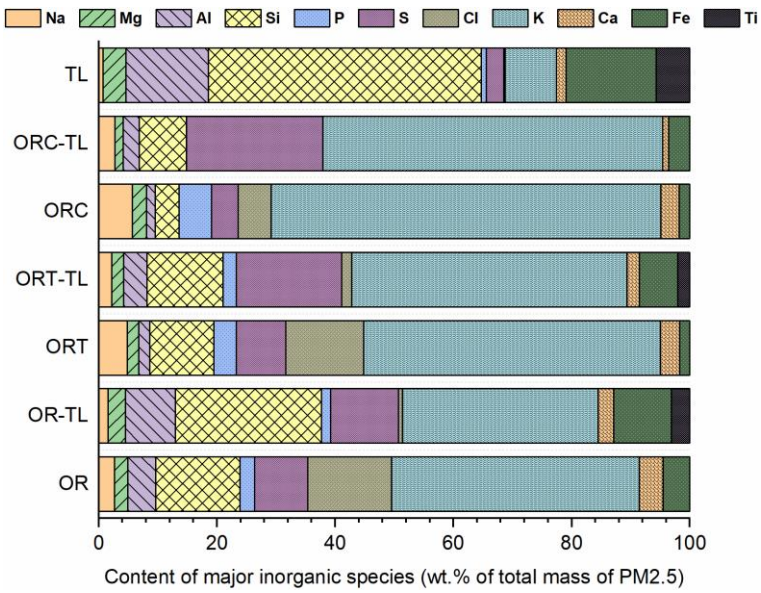

Figure 4.25. Energy dispersive spectroscopy results of concentration of major inorganic species present in PM2.5 for raw olive residue, torrefied olive residue, olive residue char, Tunçbilek lignite, and respective blends.

The results obtained showed that the mechanisms responsible for the formation of PM2.5 during biomass and coal combustion are also applicable to biomass-coal blends of raw, torrefied, and char biomass. Special attention must be given to the content of Si, Al, and Fe in the coal/lignite ash since these are known to capture alkali elements and reduce PM2.5 formation and increase PM2.5-10 and PM>10 [121,292]. Particularly, the heterogeneous condensation of KCl and KOH near Si and/or Al minerals must be considered as it shifts the PM formation from fine to coarse particles. This shift is likely to allow the capture of PM from biomass-coal co-firing by conventional coal-PM traps in existing coal power plants.

4.3 Pyrolysis

In this section, the results on pyrolysis and presented and discussed. Firstly, in subsection 4.3.1, the co-pyrolysis of biomass with coal is investigated. Based on the co-pyrolysis results of subsection 4.3.1, a detailed study on the pyrolysis of olive stones and lignocellulosic compounds from olive stones fractionation is introduced in subsection 4.3.2. Both studies are accomplished using identical wire mesh reactors operated under fast pyrolysis conditions.

4.3.1 Co-pyrolysis of biomass with coal

There is still a limited number of studies on the characteristics of chars produced at high heating rates, particularly on the reactivity and morphology of fast pyrolysis chars that are produced from the blends of agricultural biomass and low-grade coal. Therefore, the present work aims at characterising neat and blended chars from different fuels obtained from high temperature, high heating rate, and low residence time pyrolysis using a WMR. The produced chars are analysed for their morphology, combustion characteristics, and combustion kinetics. The fuels studied were olive residue (OR), almond shell (AS), and Soma lignite (SL). The chemical characterisation can be found in Table 3.2 for OR and SL, and Table 3.3 for AS.

Blends of Soma lignite-olive residue and Soma lignite-almond shell were prepared in proportions of 75:25 and 50:50 wt.%, respectively. A wire mesh reactor was used for the (co-)pyrolysis of the samples in a controlled inert atmosphere at a uniform temperature of 1600 ºC and at a heating rate of above 10^3 ºC s^{-1}. The results presented in herein are reprinted with permission from Magalhães D, Riaza J, Kazanç F. A study on the reactivity of various chars from Turkish fuels obtained at high heating rates. Fuel Processing Technology 2019;185:91–9. Copyright (2017) Elsevier.

4.3.1.1 Volatile yield

The volatile yields during pyrolysis were calculated for all individual char samples, and are presented in Figure 4.26. Obtained yields from the high heating rate WMR (1600 ºC) were compared with those from the low heating rate proximate analysis (PA) (900 ºC) in order to observe the difference between the standard analysis and the practical combustion conditions. Volatile yield of Soma lignite obtained from WMR tests (53 wt.%) was higher than that obtained from the proximate analysis (31 wt.%). Yields of both biomass fuels from WMR were always slightly above those from PA (76 vs. 71 wt.% for OR, and 82 vs. 73 wt.% for AS) within a 98% confidence interval. The main reason behind the higher yields during WMR trials for either coal or biomass was the enhanced devolatilization at high temperature and high heating rates as Trubetskaya et al. [139] and Man et al. [262] observed for a variety of biomass fuels and different rank coals, respectively. The ratio of the volatile yields of SL from WMR trials and PA was 1.7 in the present study. This is in line with the previous results obtained by Man et al. [262], who presented the same ratio as 1.6 for two low-rank South African coals with ash and volatile contents similar to Soma lignite obtained in a WMR under comparable conditions of heating rate and temperature (see Figure 1a, therein). Moreover, the BET surface area of SL following fast pyrolysis increased eight-fold when compared to biomasses showing similar values of BET surface areas for the parent fuels and chars (cf. Table 4.10). This was

an indicator of extensive devolatilization of SL, i.e. a high volatile yield, during fast pyrolysis in the WMR.

Another reason for the enhanced volatile yield may be the char-CO_2 gasification reactions during the WMR trials since the pyrolyzed gases (which include CO_2) were confined inside the reactor, and the temperature reached (1600 ºC) was above the minimum temperature of 800 ºC for char-CO_2 gasification [97]. Gil et al. [146,147] also concluded that char-CO_2 gasification enhanced the volatile yields of various coal and biomass chars.

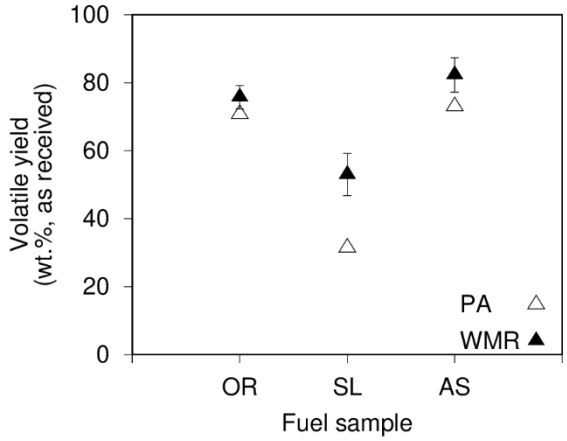

Figure 4.26. Volatile yield of individual fuel samples. PA – proximate analysis, WMR – wire mesh reactor. Vertical bars represent 98% confidence statistical error.

4.3.1.2 Char morphology and surface area

Char samples were examined morphologically using scanning electron microscopy (SEM) to gain insight into the morphological changes after fast pyrolysis. The SEM micrographs of OR, SL, and AS chars, and correspondent blends (50OR-50SL and 50AS-50SL) are depicted in Figure 4.27.

The Soma lignite (SL) char SEM micrographs are shown in Figure 4.27c. As seen, SL char particles exhibit relatively angular shapes with rounded edges when

compared to the parent fuel particles that were typically angular with sharp edges [91], which indicated a partial fluidization (cf. Figures 4.27c1 and 4.27c2). When exposed to high heating rates, lignite coals maintained their shape and did not experience extensive melting [293,294].

The particle size of SL did not change significantly during pyrolysis resulting in char particles with similar sizes (212-250 μm) (cf. Figure 4.27c). In the same way, Zeng et al. [293] and Fermoso et al. [294] did not observe any particle shrinkage for low-rank coal chars obtained at high temperature and high heating rate, since crosslinking in low-rank coals takes place before significant release of tar [295,296].

Both AS and OR chars kept their initial shape prior to pyrolysis (cf. Figure 1 of [91], and Figures 4.27a and 4.27e of this text). This was expected to occur for herbaceous/agricultural biomass fuels due to the high lignin content that usually enables stronger cross linking when compared to (e.g.) woody biomass. Similarly, both OR and AS chars appeared porous as seen in Figures 6.2a and 6.2e, respectively. AS chars were swollen and exhibited large macro-pores and cavities formed throughout their surface (cf. Figures 4.27e1 and 4.27e2), due to the high volatile release rate. As hypothesized by Trubetskaya et al. [139] and Dall'Ora et al. [297], potassium and calcium were responsible for enhancing the crosslinks of the biochar, which may have led to extensive cavity formation in AS char whilst maintaining the char structure. OR chars were less porous and displayed small degassing bubbles (cf. Figures 4.27a1 and 4.27a2), which can be a consequence of volatile release during the softening stage, as concluded by Zeng et al. [293]. These bubbles suggested that OR char had the highest level of softening, which prevented extensive formation of large cavities as those observed in AS chars.

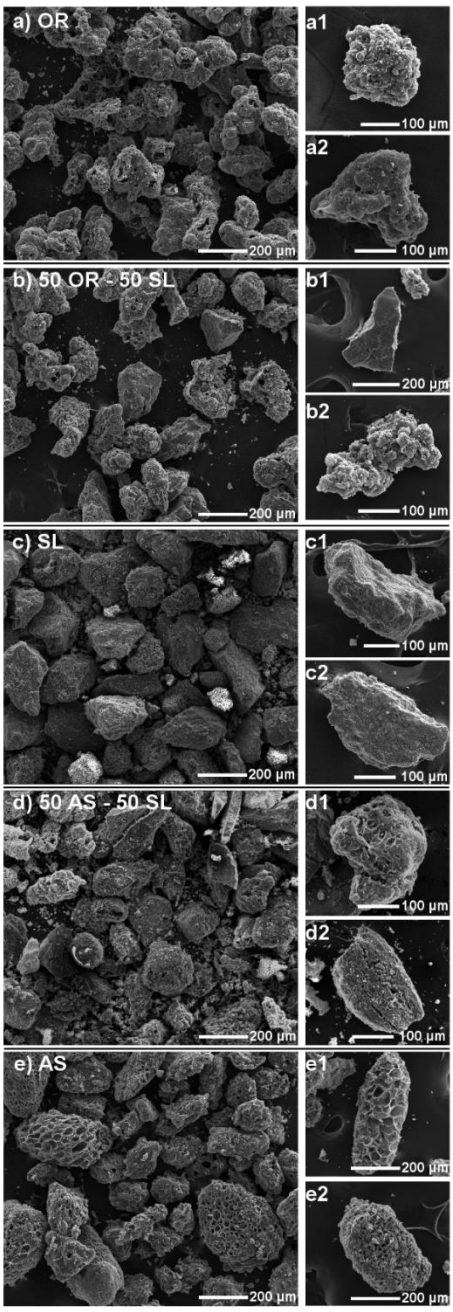

Figure 4.27. Scanning electron microscopy micrographs of char samples pyrolyzed in the wire mesh reactor. On left-hand side column, groups of particles; and on the right-hand side column, representative individual particles for the corresponding groups of particles were presented. a) olive residue; b) 50 wt.% olive residue – 50 wt.% Soma lignite blend; c) Soma lignite; d) 50 wt.% almond shell – 50 wt.% Soma lignite blend; e) almond shell.

Unlike the lignite char, both biomass chars displayed a high number of cavities and macro-pores; however, blending fuels affected the morphology of the individual chars depending on the biomass. While the 50OR-50SL blend is a simple addition of SL and OR char particles with no visible interaction (cf. Figures 4.27b and 4.27c), the 50AS-50SL blend showed clear signs of interaction between fuels during pyrolysis. The morphology of the 50AS-50SL blend (Figure 4.27d) indicates an interaction between AS and SL during pyrolysis, since highly porous and swollen AS particles were not visible in Figure 4.27e. This interaction was likely due to the presence of aluminosilicates from Soma lignite (4.5 wt.% of SiO_2 and 3.1 wt.% of Al_2O_3, fuel basis) and calcium from almond shell (6 wt.% of CaO in fuel) that formed inert gehlenite during co-pyrolysis and resulted in unaltered particle shape/morphology of both SL and AS particles.

OR chars from OR-SL blends were equally porous as those from the individual OR (cf. Figures 4.27a2 and 4.27b2, both representing OR chars). In these blends, some of the SL particles had a glassy surface (see Figure 4.27b1), which may have occurred due to the presence of potassium (from OR) bringing the SiO_2 fusion point to temperatures below 1700 ºC [139]. K and Ca are known as the catalyzers of char-bridge formation and repolymerization reactions [139]. However, in this study, high contents of K and Ca from the studied SL-OR blends did not have any visible effect on the morphology, which may be due to the presence of Si from both OR and SL.

Surface areas of the individual chars and parent fuels were determined using BET analysis and are presented in Table 4.10. BET surface area allows for detection of macro- ($d > 50$ nm) and mesopores ($2 < d < 50$ nm), but not micropores ($d < 2$ nm). Nevertheless, as stated by L. Burhenne et al. [157], micropores do not participate actively in char oxidation due to diffusion limitations. The surface areas of OR, AS, and SL chars were 14, 13, and 81 $m^2\ g^{-1}$, respectively. Under high heating rates, biomass chars were expected to become porous and present high surface areas (95 – 275 $m^2\ g^{-1}$) [138,142,149,153,154]. The low surface areas of the biochars were due to the rapid release of a large amount of gases resulting in large cavities that forced pores to shrink and restructure with subsequent reduction of the surface area, as

observed by Zhai et al. [155] for rice husk char pyrolyzed at temperatures above 1000 ºC. Conversely, SL chars presented high surface areas and exhibited a shape and morphology that resembled those of the parent fuel SL (see Figure 3.3), which allowed the pore structure of the char to remain unspoiled after WMR pyrolysis. The high surface area and the unchanged morphology of SL may be a consequence of the formation of schisms and canyons that typically prelude fragmentation, which is commonly observed for lignite coals [44].

Table 4.10 BET surface areas of the parent fuels and fast pyrolysis chars.

	BET surface area (m^2 g^{-1})	
	Parent fuel	WMR Char
OR	7.93	13.7
AS	7.64	12.6
SL	10.1	80.7

4.3.1.3 Char combustion behaviour

Reactivity and burnout of individual chars

The carbon burnout rate, carbon burnout, and burnout time of all individual chars were investigated by isothermal TGA tests at 400 ºC for olive residue (OR) and almond shell (AS) chars, and at 450 ºC for all remaining chars. The carbon burnout profiles of the individual chars (SL, OR and AS) are shown in Figure 4.28. The carbon burnout rate is plotted as a function of the carbon burnout in Figure 4.29, and the maximum burnout rates and burnout times are listed in Table 4.11. Note that burnout/carbon burnout and burnout rate/carbon burnout rate are used in this text interchangeably. The burnout rates of both biomass chars were similar (~8-10 wt.% min^{-1}), and that from Soma lignite was about three times lower (~3 wt.% min^{-1}). This may be due to the more stable aromatic C-C bonds in coal, in contrast to the weaker aliphatic bonds of biomass carbon [298]. Le Manquais et al. [142] also obtained similar maximum carbon burnout rates (~3.5 wt.% min^{-1}) for a bituminous coal char pyrolyzed in a drop tube furnace at 1300 ºC (see Figure 2, therein).

Both biomass chars had similar 90% and 100% burnout times of ~30 min due to their high reactivity. In contrast, the time to reach 90% burnout for the lignite was approximately 130 min, because of its lower burnout rate. For all the chars studied, higher maximum burnout rate was linked with shorter burnout times (see Figure 4.28 and Table 4.11) [92,140,142,145,148,159]. According to Figure 4.29, the maximum rate of burnout was reached at burnout levels of 20-30 wt.% for the biochars, and at 10 wt.% for SL char. The burnout rate was halved when burnout surpassed 30 wt.% for SL, 50 wt.% for OR, and 60 wt.% for AS.

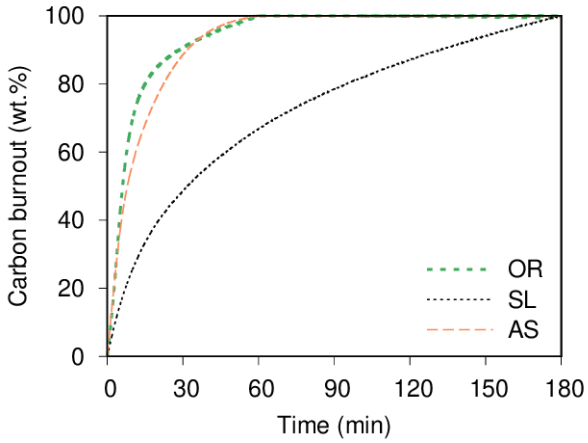

Figure 4.28. Carbon burnout as a function of time for the individual chars. Olive residue (OR) and almond shell (AS) chars were oxidized at 400 ºC and Soma lignite (SL) char was oxidized at 450 ºC.

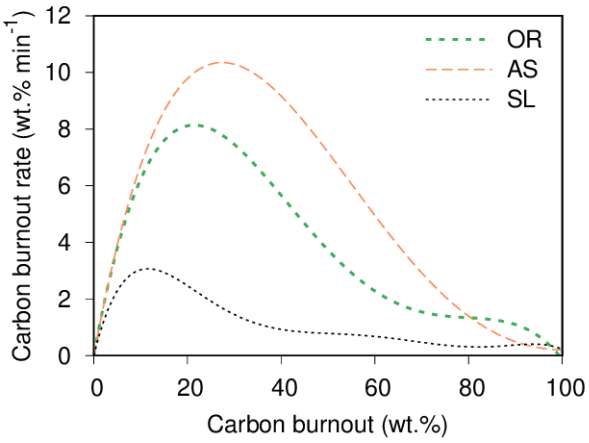

Figure 4.29. Carbon burnout rate as a function of burnout for the individual chars. Olive residue (OR) and almond shell (AS) chars were oxidized at 400 ºC and Soma lignite (SL) char was oxidized at 450 ºC.

Effect of blending ratio on char reactivity and burnout

The chars obtained from pyrolysis of blends were characterized using TGA and the burnout profiles are depicted in Figure 4.30. Subsequently, both experimental and predicted profiles were used to calculate the burnout rates, which are represented in Figure 4.31 as a function of the burnout. The predicted profiles in Figures 4.30 and 4.31 were calculated from the weighted sum of the char burnout profile of each individual fuel (all at 450 ºC).

According to Figure 4.30 and Table 4.11, the combustion behavior of both blends with 25 wt.% biomass – 75 wt.% coal matched that of the predicted blends, with similar maximum burnout rates and 90% burnout times. Moreover, the 25 wt.% biomass – 75 wt.% coal blends resembled the combustion behavior of the neat Soma lignite char. The reason for this behavior was the major contribution of SL char in the 25-75 blends which was 85 wt.% for OR blends and 88 wt.% for AS blends.

Oppositely, both OR and AS blends with 50 wt.% biomass presented distinct combustion characteristics depending on the biomass fuel. Experimental 90%

burnout times of OR blends (50OR-50SL) were 48 min, significantly lower than the predicted value of 94 min. Moreover, the experimental burnout rates were two times higher than the predicted ones. The observed differences between experimental and predicted profiles of 50OR-50SL blends were a clear result of the synergies between these two chars. These synergies had a particular effect on the maximum burnout rate as the values for the blend even surpassed that of OR char.

Table 4.11 Maximum reactivity and 90% burnout times of individual chars and blends (experimental and predicted values).

Sample		Maximum carbon burnout rate (wt.% min^{-1})	90 % burnout (min)
Individual	OR	8.26	29
	SL	3.09	132
	AS	10.4	32
Blends (experimental)	50 OR - 50 SL	11.6	48
	25 OR - 75 SL	4.24	108
	50 AS – 50 SL	1.27	151
	25 AS - 75 SL	3.49	120
Blends (predicted)	50 OR - 50 SL	4.79	94
	25 OR - 75 SL	3.86	118
	50 AS – 50 SL	4.89	99
	25 AS - 75 SL	3.87	120

For AS blends (50AS-50SL), the experimental 90% burnout times were increased by one-third as compared to the predicted values. Moreover, as shown in Figure 4.31, the increase in AS in these blends from 25 to 50 wt.% decreased the maximum carbon burnout rate to values below those of SL char. The comparison of the maximum rate of carbon burnout values showed that the experimental values were ~ 1.3 wt.% min^{-1}, whereas the predicted profiles gave a maximum of ~5 wt.% min^{-1}. The longer burnout time and lower maximum burnout rate were a clear indication of a deactivation effect between AS and SL. A loss of reactivity in coal-biomass blends was also observed by Ellis et al. [163], who claimed that non-crystalline phases from

biomass such as calcium carbonate, and aluminosilicates from coal interacted during co-pyrolysis to form catalytically inert gehlenite. Furthermore, the SL-AS char blends (Figure 4.27d) did not resemble the apparent texture of individual AS char particles (Figure 4.27e), and as observed by Fei et al. [299] for a blend of a high calcium lignite with a high swelling bituminous coal, organic volatile matter may have reacted with calcium and prevented extensive swelling of AS. The lack of porosity resulted in a loss of reactivity and longer burnout times [142], which may be a consequence of the reduced surface area of these blends (not determined in this study) that affected the number and accessibility of active carbon sites.

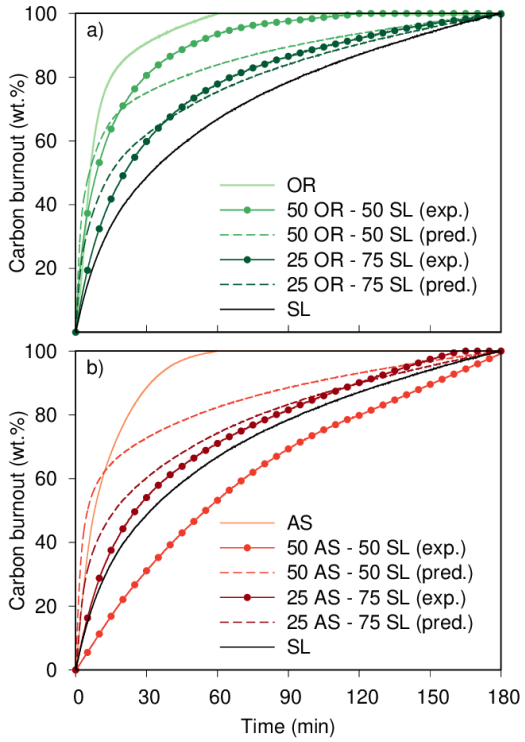

Figure 4.30. Carbon burnout profiles of the blended char samples (experimental and predicted values). a) OR – SL blends; b) AS – SL blends. Individual profiles of SL, OR, and AS are represented for comparison purposes. Olive residue (OR) and almond shell (AS) chars were oxidized at 400 ºC and all remaining chars were oxidized at 450 ºC.

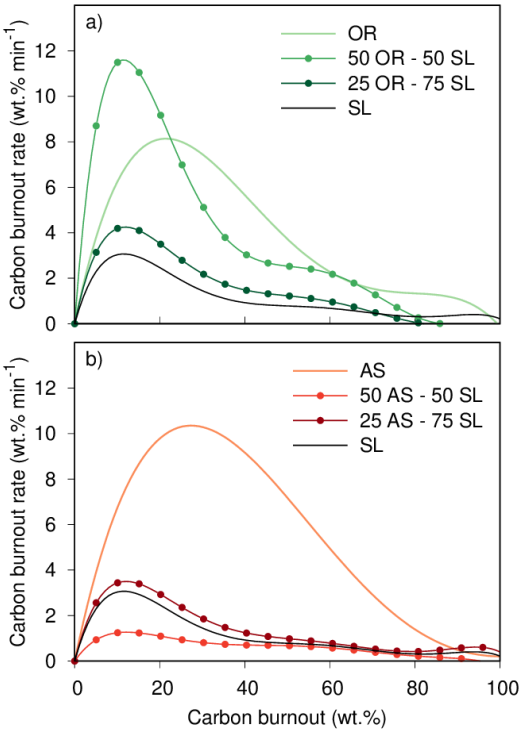

Figure 4.31. Carbon burnout rate vs. burnout for all fuels and respective blends (experimental values). Olive residue (OR) and almond shell (AS) chars were oxidized at 400 ºC and all remaining chars were oxidized at 450 ºC.

Char combustion first order kinetics

The apparent first-order rate constants were determined for both experimental and predicted profiles for all fuels and blends, and are presented in Figure 4.32. The experimental rate constants were obtained by linear fitting of the data. The predicted rate constants were obtained by the weighted-averages of the individual rate constants. The isothermal temperature of 400 ºC for biochars and 450 ºC for SL char and blends were chosen to ensure that the char oxidation takes place in regime I – kinetically controlled regime, so that the mass transfer limitation is minimized [142]. This approach follows recommendations given in a recent work by Morin et al. [255], and is in accordance with several other recent studies [142,152,254,255]. Moreover, combustion regime in this work is also calculated based on previous work

by Trubetskaya et al. [167] and the calculation justified the kinetically controlled regime (see subsection 3.3.3). In Figure 4.32, the left-hand side and right-hand side extremes represent OR and AS, respectively, and the center point represents SL. Therefore, each of the two halves of the plot shows the influence of the OR and AS content on the biomass-coal char blends.

The reaction rate constants of OR and AS were similar (0.081 and 0.074 min^{-1}, respectively). In contrast, SL presented the lowest rate constant among the individual chars, with 0.018 min^{-1}. When compared to the biochars, the lower rate constant of SL char was likely due to the higher number of aromatic rings in coal char [298]. Moreover, the high alkali content of OR and AS, and subsequent catalytic effect on the char oxidation may also play a role [97,152]. In the same way, the 10% higher rate constant of OR chars compared to AS chars may be attributed to the higher content of K and Na of OR.

The left-hand side of Figure 4.32 indicated that the decrease in OR fraction in the blend resulted in lower rate constants and reached a minimum for SL. For 25OR-75SL blends, the predicted and experimental values were in line. On the other hand, the experimental rate constant for 50OR-50SL blends was ~20% higher when compared to the predicted value, displaying a synergistic effect in this blend. The early melting of K_2CO_3 at ~900 ºC allowed for an increase in the heat transfer rate that fosters $CaCO_3$ decomposition [161], and the presence of alkali carbonates can lower the decomposition temperature of $CaCO_3$ [160]. The decomposition of alkali and alkali earth metal carbonates is known to catalyze the oxidation of char through one of two theories [97], namely, geometric theory and electronic theory, and was the reason for the registered synergistic effects in the 50OR-50SL blends.

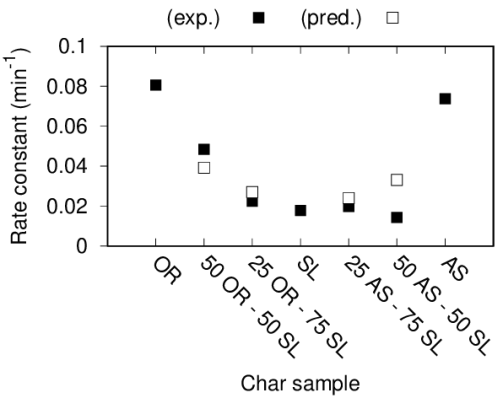

Figure 4.32. First order rate constants of individual chars and corresponding blends (experimental – filled symbols, and predicted – open symbols).

Similarly, the right-hand side of Figure 4.32 depicted the influence of the AS content. AS char had a higher reaction rate than SL; thus, an increase in AS content increased the overall reaction rate of the predicted blend. On the contrary, the experimental results in the right-hand side of Figure 4.32 showed a different trend; the increase in AS mass fraction in the blend resulted in lower reaction rate constants, which was a clear effect of deactivation on these blends. The low rate constants of SL-AS blends were in agreement with the loss of reactivity for these blends and were probably a consequence of the presence of aluminosilicates in lignite coal and calcium oxide in almond shell. The presence of aluminosilicates from Soma lignite (4.5 wt.% of SiO_2 and 3.1 wt.% of Al_2O_3, fuel basis) and calcium from almond shell (6 wt.% of CaO in fuel) was likely to form inert gehlenite during co-pyrolysis and resulted in a deactivation effect for the 50AS-50SL blend. This is in line with the observations of Ellis et al. [163], according to which the formation of gehlenite took place during co-pyrolysis of a bituminous coal (6.7 wt.% of SiO_2 and 3.7 wt.% of Al_2O_3, fuel basis) with pine sawdust (0.8 wt.% of CaO, fuel basis). Moreover, Chen et al. [300] concluded that alkali / alkali earth-rich particles can coalesce with kaolin and form large ash particles which could further reduce the reactivity of the char.

4.3.2 Fast pyrolysis of laboratory-fractionated biomass

In this subsection the fast pyrolysis behaviour of olive stones (raw and torrefied) and fractionated olive stones (i.e. cellulose, hemicellulose, and lignin) is investigated in detail. Different commercial lignocellulosic compounds are used for comparison purposes. Olive stones are torrefied in a continuous industrial torrefaction unit. The raw olive stones are fractionated into their main components in an organosolv reactor at temperatures from 170 to 190°C in the presence or absence of an acidic catalyst. The detailed characterisation of the feedstocks and experimental techniques including organosolv fractionation are given in the Appendix B.

Given the complexity and diversity of the chemical composition of biomass, the aim of the present study was for the first time to compare the char yields and composition from commercial and fractionated lignocellulosic compounds from olive stones in high-temperature pyrolysis. The specific objectives were to: (1) use an organosolv process to fractionate olive stones into cellulose, hemicellulose and lignin, and (2) measure the char yield, and gas composition of commercial and fractionated lignocellulosic compounds and (3) develop an empirical model to relate the char and gas yields to the decomposition of raw and torrefied olive stones during high-temperature pyrolysis. Furthermore, the addition of an acid catalyst during fractionation is highlighted, and the effect on the yields and composition of the pyrolysis products is analysed. Pyrolysis performance is highly dependent on reactor conditions. Thus, experiments were performed in a well-characterised wire mesh reactor system to permit model validation. The conditions applied in the wire mesh reactor were: T1 (800 ºC, 400 ºC/s); T2 (1000 ºC, 800 ºC/s); and T3 (1150 ºC, 1150 ºC/s). The results presented herein are reprinted with permission from Magalhães D, Gurel K, Matsakas L, Christakopoulos P, Pisano I, Leahy JJ, et al. Prediction of yields and composition of char from fast pyrolysis of commercial lignocellulosic materials, organosolv fractionated and torrefied olive stones. Fuel 2021;289:119862. Copyright (2021) Elsevier.

4.3.2.1 Characterisation of fractionated lignocellulosic compounds

Table 4.12 shows the results of chemical composition of fractionated cellulose and hemicellulose. Fractionation of olive stones at 180 ºC with and without an acid catalyst gave significantly higher cellulose content in the pre-treated solids compared to that from fractionations at 170 or 190 ºC. Low amounts of residual hemicellulose and acid soluble lignin were detected in the fractionated cellulose at 180 ºC treatment, with lignin contents of 14.3 and 15.7 wt. %, demonstrating that treatment at 180 ºC was the optimal to deliver pre-treated solids with high cellulose content and low hemicellulose and lignin contents. Introduction of the acid catalyst at 170 and 180 ºC resulted in lower hemicellulose content, as is expected due to the acidic conditions that promote hemicellulose solubilisation. Further increase of the organosolv treatment temperature to 190 ºC, resulted in severe treatment conditions that promoted degradation of cellulose.

The hemicellulose fraction overall contained a low concentration of glucose (< 2.6 wt. %), and the major component was hemicellulosic sugars. Lignin was present mainly as acid soluble lignin, and the total lignin (both acid soluble and acid insoluble) was less than 9.9 wt. % for all samples except 170 ºC without acid. The hemicellulose from extraction at 180 ºC yielded the highest content in hemicellulosic sugars which was 50.6 or 45.9 wt. % of xylose and mannose with the small portion of lignin varying between 6.5 and 8.9 wt.% and traces of glucose which were below 2.6 wt. %. The incorporation of acid at 170 ºC produced a hemicellulose fraction (48.1 wt. %) which was similar to those obtained by the fractionation without catalyst at 180 ºC. At 190 ºC, the mass balances could not be closed for hemicellulose likely because at higher temperatures a higher dissolution of feedstock into the liquid phase could occur, together with decomposition of the dissolved compounds to degradation products such as furfural, HMF and other light organics could evaporate during fractionation. In addition, the results from fractionation at 170 ºC using an acid catalyst and at 190 ºC without using an acid catalyst showed reasonable yields of mannose, xylose, arabinose, rhamnose and galactose above 38.8 wt. % in total

indicating a significant influence of both pretreatment temperature and catalyst addition on the chemical composition of fraction. In general, the results of analysis showed that the mass balances could be accurately closed for the fractionated cellulose with greater than 85 wt. % db.

The fractionated lignin presented a high degree of purity with at most 4 wt.% of hemicellulose present and no cellulose detected. The lignin fractionated at 180 ºC without acid showed the highest purity with only 0.9 wt.% of hemicellulose.

Table 4.12 Chemical content of cellulose, hemicellulose, lignin acid-soluble and lignin acid-insoluble in fractionated cellulose and hemicellulose.

	Cellulose	Hemicellulose	Lignin acid-soluble	Lignin acid-insoluble
Fractionated cellulose, wt. % db				
170ºC, no acid	35.1	14.0	35.5	0.0
170ºC, acid	45.4	6.8	35.0	0.6
180ºC, no acid	80.4	7.3	14.3	0.3
180°C, acid	75.3	6.7	15.7	0.4
190°C, no acid	59.2	16.4	18.5	0.3
Fractionated hemicellulose, wt. %, db				
170ºC, no acid	0.5	31.0	31.2	3.7
170ºC, acid	1.3	53.2	5.9	0.8
180ºC, no acid	2.6	55.5	8.9	1.0
180°C, acid	0.6	51.0	6.5	0.4
190°C, no acid	0.6	41.0	6.1	1.3

The molecular weight of olive stones lignin is represented in Table 4.13. The size exclusion analysis showed a broad variation of the lignin molecular weight from 3670 to 7200 Da. In general, the molecular weight of the fractionated lignin samples with and without acid treatment was greater than that of the organosolv, Soda, Alcell, and Kraft lignins that varied from 726 to 4660 Da [301]. This highlighted the milder reaction conditions of the steam organosolv treatment in the present study. Overall, lower molecular weight fractions showed lower polydispersity, corresponding to

previous results [302,303]. Additionally, the polydispersity index of lignin in the present study varied from 4.1 to 7.1 and thus, was greater than that of lignin samples reported in the literature (organosolv wheat: 2.0, organosolv poplar: 2.1, organosolv spruce: 2.2, Soda P1000: 3.5, Alcell: 3.3, and Indulin Kraft: 4.1) [301]. The greater polydispersity index suggests a broader molecular weight distribution and less uniformity of the polymer mixture [301]. The molecular weight and polydispersity index of non-treated and acid-treated lignin isolated at 180°C were similar to the values of lignin from Lignoboost process [304].

Table 4.13 Molecular weight as a function of the pretreatment temperature and addition of acid.

Lignin	Weight average, M_w (Da)	Polydispersity index
170ºC, no acid	6640	6.7
170ºC, acid	5570	5.7
180ºC, no acid	4630	4.4
180°C, acid	3670	4.1
190°C, no acid	7200	7.1

4.3.2.2 Char yield

The char yields of all commercial samples are represented in Figure 4.33. The yields of torrefied olive stones were slightly above those of the raw olive stones. Torrefaction led to a decrease in cellulose and hemicellulose contents while the lignin content appeared unaffected. Thus, the greater char yield from pyrolysis of torrefied olive stones was likely related to secondary char formation due to decomposition of cellulose, and hemicellulose.

The yields from the commercial hemicelluloses (with the exception of xylan), under condition T1, were within 5.7 – 6.6 wt.% (Figure 4.33). However, during condition T2 two groups were identified: xyloglucan and galactomannan with 7.1 and 8.1 wt.%, respectively, and arabinoxylan and arabinogalactan, both with yields of ~12

wt.%. Compared to the other hemicelluloses, xylan had a lower degradation temperature, an overall exothermal behaviour, and higher char formation [174], with yields of 19.8 and 17.2 wt.% for conditions T1 and T2, respectively. Xylan showed the highest ash content (3.7 wt.%) among the hemicelluloses. Since alkali metals are known to favour char formation, it is likely that the observed differences in higher char yield formation during xylan pyrolysis were related to the catalytic effect of alkali metals, confirming previous results [305,306].

The char yields of olive stones fractionated compounds obtained from condition T1 are presented in Figure 4.34. For the components extracted without acid treatment, the cellulose and hemicellulose fractions from 170 and 180 ºC had similar yields, but the char yield of lignin was greatly affected by the pre-treatment temperature (14.8 wt.% for 170 ºC and 29 wt.% for 180 ºC). Moreover, the char yields from pyrolysis of cellulose and hemicellulose using 180 ºC non-acid and acid treatment were similar. However, the lignin char yield was greater from non-acid treatment at 180 ºC than from the acid fractionation. The char yields of each of the three components fractionated at 170 and 180 ºC in the presence of an acid catalyst resembled each other, which showed the more important effect of the acid catalyst rather than the temperature during fractionation under these conditions. For the highest temperature, 190 ºC, and the absence of acid catalyst resulted in cellulose with lower char yield and hemicellulose and lignin with similar yields.

It should also be noted that the char yields of the hemicelluloses were always above those of the celluloses. Particularly for the case of treatment at 190 ºC without acid, the yield of hemicellulose was three-fold that of cellulose, likely due to the different thermal stability of monomers of these polysaccharides. The lower char yield observed during pyrolysis of cellulose than hemicellulose decomposition was also due to the differences in crystallinity. The amorphous phase in hemicellulose underwent further rearrangement reactions which promoted higher char yields than during the pyrolysis of cellulose that mostly contains a crystalline structure, confirming previous results of Alen et al. [307]. Moreover, catalytic effects during

char formation [185] may have also resulted in higher char yields for the hemicelluloses as it presented higher ash content as compared with the celluloses.

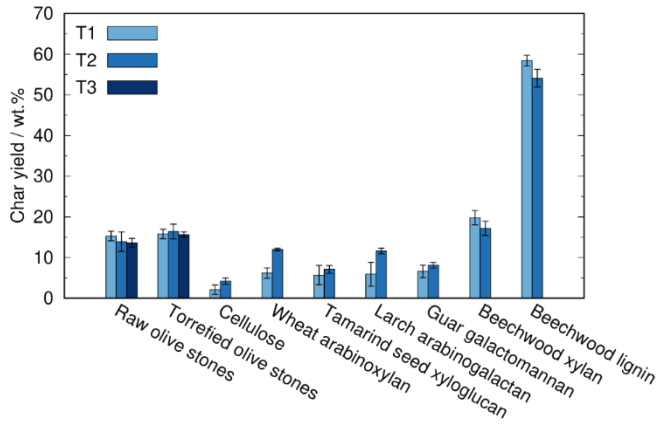

Figure 4.33. Char yields of all commercial samples (T1 and T2), and raw and torrefied olive stones (T1, T2, and T3). Conditions: T1 - 800 ºC, 400 ºC/s; T2 - 1000 ºC, 800 ºC/s; and T3 - 1150 ºC, 1150 ºC/s.

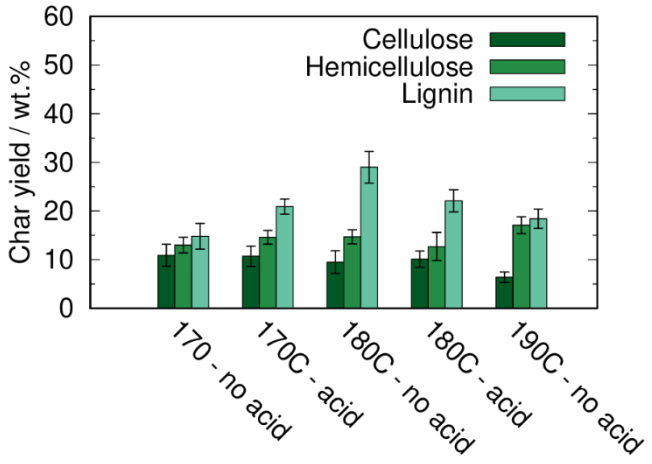

Figure 4.34. Char yields of all fractionated compounds obtained at condition T1 (800 ºC, 400 ºC/s).

The highest char yield was observed during lignin pyrolysis. The high content of benzene rings led to strong depolymerization and cross-linking of lignin compounds during pyrolysis. In addition, the high alkali metal content in lignin could lead to the greater char yield, as it was previously suggested [305,308].

The char yields of raw and torrefied olive and fractionated compounds (180 ºC acid and no acid) are represented in Figure 4.35 for the three applied temperatures (800, 1000, and 1150 ºC). In general, the char yield decreased slightly with an increase in temperature and heating rate. However, no significant effect attributable to either temperature (800-1150 ºC) or heating rate (400-1150 ºC/s) was observed. The effect of temperature and heating rate during fast pyrolysis in a wire mesh reactor was investigated by Trubetskaya et al. [139] for softwood, hardwood, straws, and rice husk. In line with the results obtained herein, the authors concluded that temperatures over 800 ºC and heating rates above 600 ºC/s had a negligible effect on the char yields. On the other hand, the char yields of crystalline cellulose, wheat arabinoxylan and larch arabinogalactan increased with the rise in temperature (800 to 1000 ºC) and heating rate (400 to 800 ºC/s), as seen in Figure 4.35.

The increase in char yield during pyrolysis of cellulose, arabinoxylan and larch arabinogalactan was attributed to secondary char formation from the interaction between pyrolysis vapours and primary char. Formation of the main degradation compounds from arabinose, xylose, mannose and arabinitol during pyrolysis is known to give similar products [309]. However, pyrolysis of arabinoxylan, glucomannan and arabinogalactan is known to yield a greater amount of propanal-2-one and glycolaldehyde compared to xylan pyrolysis [175]. Thus, the increased polymerization and cross-linking of propanal-2-one and glycolaldehyde could lead to greater char yields with the increased heat treatment temperatures.

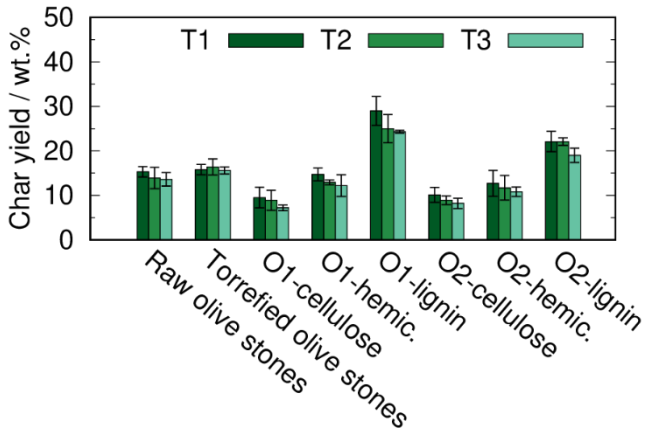

Figure 4.35. Char yields of raw and torrefied olive stones and compounds (O1: 180ºC, no acid; O2: 180ºC, acid) obtained for the three conditions (T1, T2, and T3) in the wire mesh reactor.

4.3.2.3 Char morphology and structural transformation

The morphology of selected chars obtained at 1000ºC was investigated using SEM-EDS. Selected images of chars are presented in Figure 4.36 for raw and torrefied olive stones, and commercial hemicelluloses and lignin. Chars from both raw and torrefied olive stones displayed particles of similar size and morphology to the original fuel. The chars from torrefied olive stones appeared to be more porous than the chars from raw olive stones (see Figures 4.36a and 4.36b). The chars from commercial hemicelluloses presented significant differences with respect to morphology and particle size. Arabinoxylan chars were long, fibrous and mostly non-porous, with the formation of scale-like particles which indicated partial fluidisation, and EDS indicated the presence of Mg. Xyloglucan chars showed large cavities and micropores, and the presence of large flat structures indicated fluidization followed by repolymerisation and cross-linking. Galactomannan displayed large structures with micron-sized vesicles and micropores (see Figure 4.36e2), and few of the particles underwent fragmentation into fibre-like ~100 µm

length particles. EDS analysis revealed that the inorganic elements on the surface of the galactomannan char were mainly Na, Ca, and Si. Arabinogalactan chars were of two distinct sizes, likely due to fragmentation during pyrolysis. Regardless of the particle size, the surface of all chars was covered by calcium-rich ordinated structures ~10 μm in length (see Figure 4.36f2). Xylan from beechwood presented some porous particles and needle-like structures rich in Na and Ca on the outer surface of the chars (see Figure 4.36g2). Chars of beechwood lignin were nonporous, the surface of which displayed micron-sized vesicles of 5-10 μm (see Figure 4.36h2). The inorganic elements in these chars were mainly Na and S, likely due to the presence of Na_2SO_4 (melting point 884 ºC).

The chars from the lignocellulosic compounds from 180 ºC no acid (O1) and 180 ºC acid (O2) fractionation are represented in Figure 4.37. These chars showed significantly different morphologies. In the case of the fractionated cellulose, the fibres lost their integrity through the thermal degradation process with a much broader fibre dimension. The structure of the fractionated cellulose looked similar to that of an amorphous cellulose [169,310] that went through the formation of a liquid intermediate with bubbles formed from liquid boiling during pyrolysis [310–312]. Acid treatment resulted in chars which were more fluidised than non-acid treated chars, as a result of a more extensive melting during char formation. It is known that during fast pyrolysis, cellulose has a tendency to form a depolymerised liquid intermediate, and this greatly influences the morphology of the cellulose char. Micropores were observed for O1 cellulose, but not for O2 cellulose as a consequence of the extensive melting of the latter char which caused collapsing of micropores. Ca and S were detected on the surface of O2 cellulose chars (see Figure 4.37b2), which could have been from Ca in olive and traces of S from the acid catalyst. Chars from hemicellulose with and without acid treatment displayed clear differences. Char from O1 hemicellulose presented large flat structures with a high degree of melting and formation of micropores and vesicles. As mentioned by Yu et al. [18], these vesicles are formed from the release of volatiles when the surface of the char is significantly melted, allowing bubbles to form and oftentimes burst into

spherical micropores. O2 hemicellulose chars did not undergo extensive melting, and therefore cross-linking reactions were allowed to take place and resulted in fibrous non-coalesced particles with a few micropores on their surface.

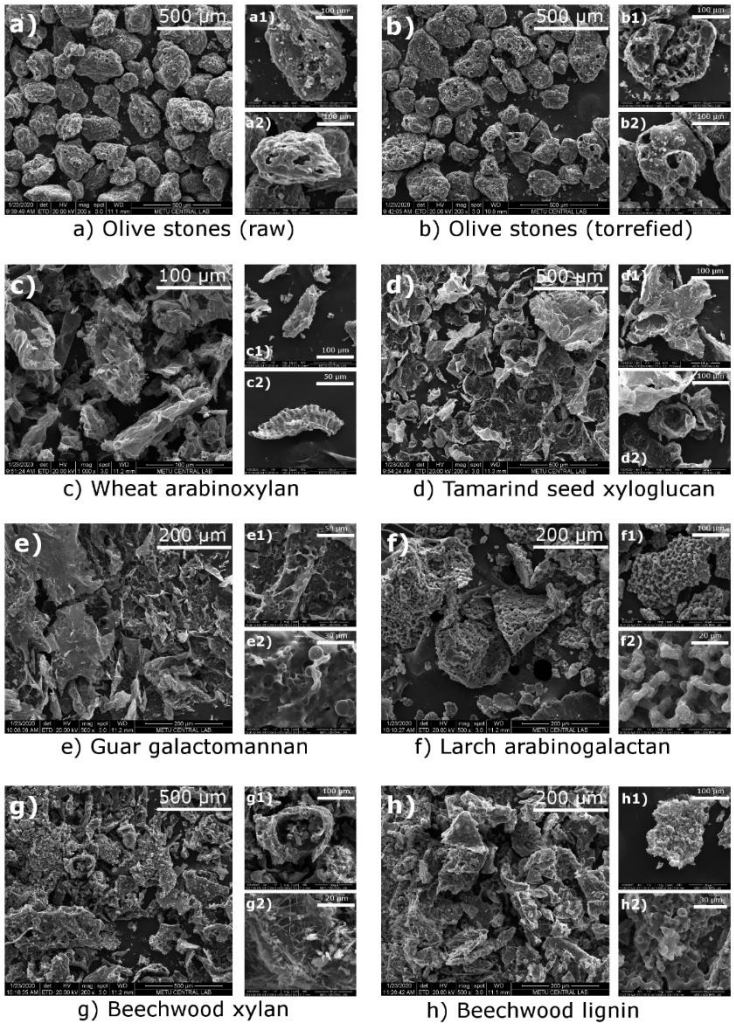

Figure 4.36. Scanning Electron Microscopy images of chars from raw and torrefied olive stones, wheat arabinoxylan, tamarind seed xyloglucan, guar galactomannan, larch arabinogalactan, beechwood xylan, and beechwood lignin.

Both lignin chars (with and without acid treatment) showed smooth surfaces (Figure 4.37e1 and 4.37f1), which was a consequence of the formation of a liquid intermediate. Particularly acid-treated lignin (O2) displayed more coalesced and melted structures and a higher number of micropores and vesicles formed, as a clear consequence of the acid treatment that increased fluidisation of lignin during pyrolysis and subsequent ejection behaviour [311]. Non-acid treated lignin showed fewer micropores and vesicles, and resembled the results reported by T.J. Hilbers et al. [169] for organosolv lignin (see Figure 2 therein).

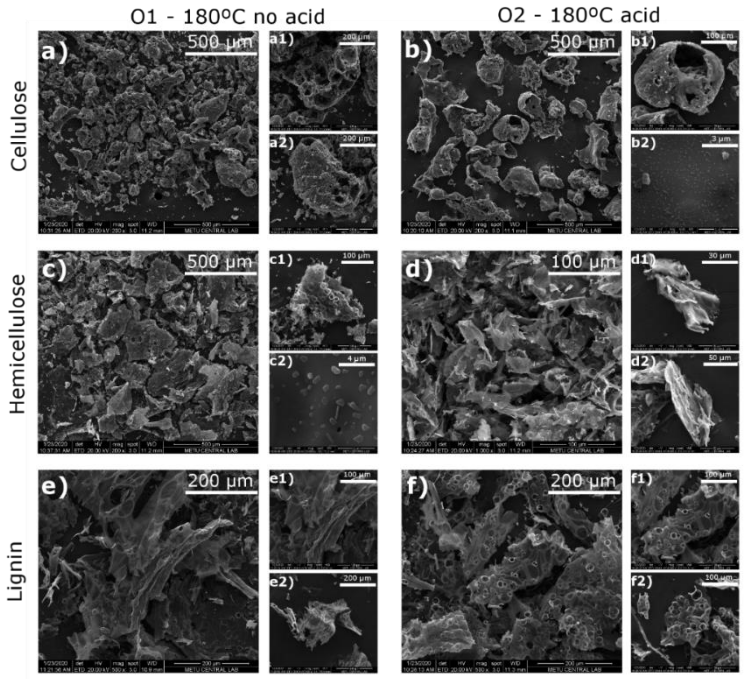

Figure 4.37. Scanning Electron Microscopy (SEM) images of cellulose, hemicellulose, and lignin chars from olive stones fractionated at 180 ºC (LHS column: O1, without acid treatment, RHS column: O2, with acid treatment).

4.3.2.4 Gas composition using TGA-FTIR

Since the WMR did not enable online gas collection, the pyrolysis gas composition was determined through pyrolysis of the raw samples in a TGA coupled FTIR

spectrometer. The raw lignocellulosic compounds obtained at 180ºC without acid treatment (O1) and with acid treatment (O2) were also analysed using TGA-FTIR and the profiles are represented in Figure 4.38.

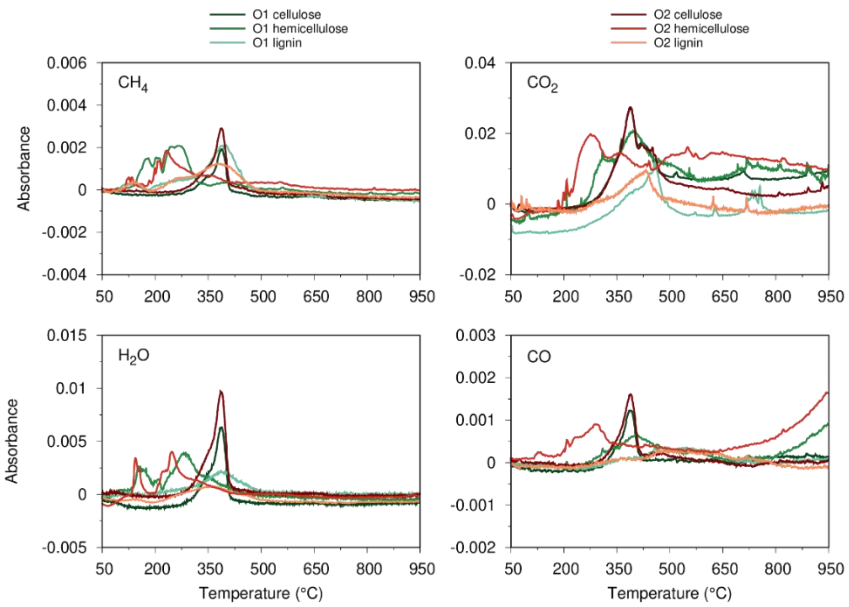

Figure 4.38. Infrared absorption profiles of CH_4, CO_2, CO, and H_2O from TGA-FTIR for the pyrolysis of olive stones fractionated compounds.

Spectra were identical for both O1 and O2 cellulose with the main peak observed from 300 to 400 ºC due to depolymerisation and, to a lower extent, fragmentation. The onset of fractionated cellulose was 25-50 ºC lower than that of the commercial cellulose. This indicated that the commercial cellulose had a more crystalline structure than the fractionated cellulose from olive stones. The pyrolysis spectra of CH_4 and H_2O for the O1 and O2 hemicellulose were similar. The absorption of H_2O due to dehydration (200-300 ºC) was more notable for the hemicelluloses than for either cellulose or lignin due to the high moisture content (7-11 wt.%). The CO spectrum of acid-treated hemicellulose (O2) showed that the main decomposition stage initiated at a lower temperature (200 ºC) than that of O1 hemicellulose (275 ºC). Both lignins, with and without acid treatment, displayed an initial peak around

150 ºC in the CH_4 spectrum, followed by a broad stage from 200-500 ºC detected for all species except CO. In addition, a broad stage was observed from 425-650 ºC in the CO spectrum of both lignins due to the conversion of oxygenated groups such as ether and hydroxyl.

4.3.2.5 Char elemental composition

The elemental composition of all chars obtained under condition T2 (1000 ºC, 800 ºC/s) is represented in Figure 4.39 in the form of a Van Krevelen diagram. Chars from raw and torrefied olive stones showed similar elemental composition. The elemental analysis of commercial hemicelluloses showed variations in H/C and O/C composition. The H/C ratios of galactomannan and arabinoxylan were similar (ca. 0.25). The H/C of arabinogalactan was 0.31, and the O/C was lowest among the hemicelluloses (0.07) while the H/C of xyloglucan was the highest (0.37) among the hemicelluloses. Galactomannan (62 % mannose) showed a greater O/C ratio (0.18) compared to arabinogalactan (85 % galactose). This was due to the higher yields of 5-hydroxymethylfurfural and water from pyrolysis of d-mannose than from pyrolysis of d-galactose [313]. The elemental O/C ratios of arabinoxylan (50% xylose), xyloglucan (36% xylose) and beechwood xylan were similar due to the presence of xylose units in all three samples. Lignin from beechwood showed the highest H/C and O/C among all chars, due to its low carbon content of 27 wt.%. This result, which differed significantly from the carbon content of lignin chars from softwood (79.6 wt.%) and wheat straw (73.6 wt.%) obtained by Trubetskaya et al. [166] under similar pyrolysis conditions, showed the strong effect of the lignin species on the composition and yield of the char.

The addition of an acid catalyst at 170 and 180 ºC decreased cellulose O/C and H/C ratios by 60-80 % and 20-40 %, respectively, as compared to the fractionation without acid catalyst. The ability of cellulose to interact with the acid catalyst depends on the ratio of amorphous and crystalline regions in the polymer [314]. However, the present results indicate that the extensive dehydration reactions during

acid pretreatment were mostly affected by the treatment temperature greater than 160 ºC and could, therefore, accelerate the penetration of acid into both crystalline and amorphous regions [315]. Small concentrations of acid (< 1%) are known to be sufficient to interact with cellulose chains located at the surface of crystallites and lead to the formation of new hydrogen bonds [316,317]. When the pyrolysis temperature increases, the depolymerization of the dehydrated cellulose occurs, i.e. the splitting of the glycoside bonds produces the volatile products.

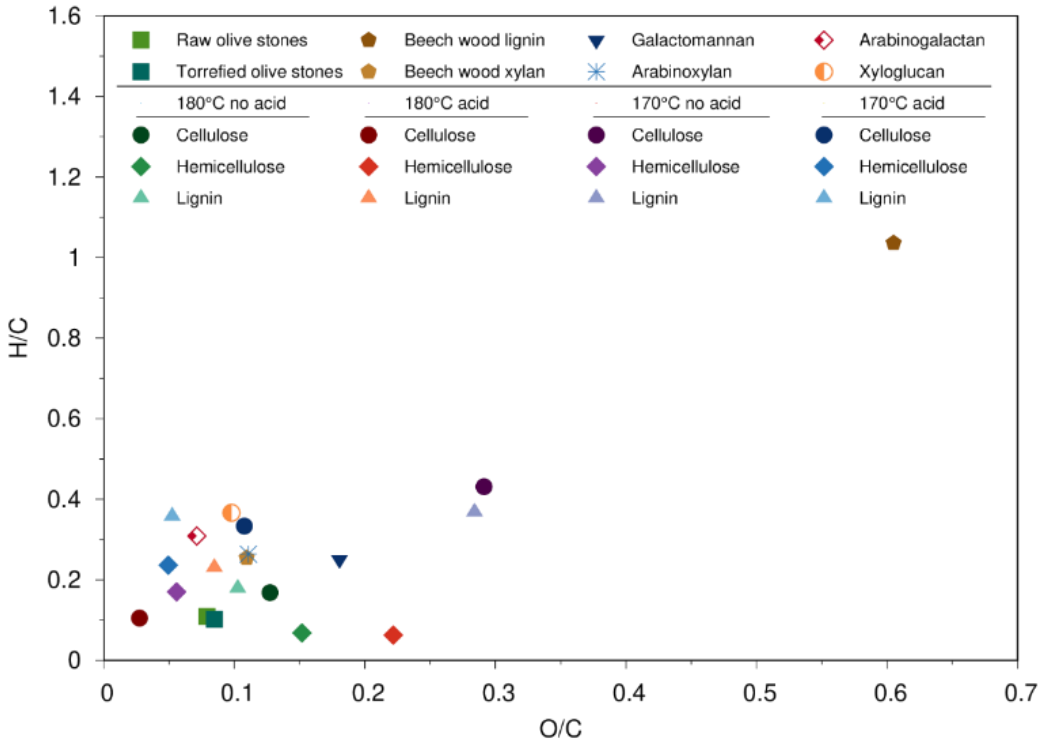

Figure 4.39. Van Krevelen diagram of all studied WMR chars obtained at condition T2 (1000 ºC, 800 ºC/s).

On the other hand, the addition of an acid catalyst during pretreatment at 170 and 180 ºC led to an increase of 30% of H/C and O/C ratios in pyrolysis of hemicellulose. This was due to the catalytic influence of acids that can inhibit the formation of

furfural during pyrolysis [318,319]. The fast hydrolysis of hemicellulose at temperatures > 130 ºC and retention times below 10 min could accelerate the conversion of cellulose to glucose and thus, decrease the formation of furfural [320].

The acid pretreatment showed a greater influence on the composition of lignin fractionated at the lowest temperature (170 ºC) with the O/C ratio decreasing by 80%, whereas lignin fractionated at 180 ºC showed a smaller change (~20%). This was related to the increased solubilization of lignin during pretreatment in the temperature range 170-180 ºC leading to an increase in carbon content and decrease in oxygen content of lignin char [321]. The present results suggest that the lignin yield increased at 170 ºC and decreased at higher temperatures during fractionation, whereas an opposite trend was observed for hemicelluloses leading to an increase in yields with greater temperatures. Moreover, these results were in line with the carbon content of raw lignin (44 and 64 wt.%, respectively for 170 ºC and 180 ºC, both no acid), which showed that the acid pretreatment had a clear effect on the elemental composition of the char. The present results clearly indicated that an increase in the pretreatment temperature from 170 to 180 ºC influenced the composition of cellulose and hemicellulose, particularly, whereas lignin was less affected.

4.3.2.6 Modelling

Based on the experimental results, a model was developed to estimate the char yields from pyrolysis of biomass at conditions relevant to entrained-flow gasification. Previously, Couhert et al. [165] and Yu et al. [322] attempted to model pyrolysis gas yields based on the weight fraction additivity law using the yields obtained from isolated cellulose, xylan, and lignin feeds to predict the yields observed for pyrolysis of biomass sample of known composition. However, the model predictions deviated significantly from the experimental, suggesting that more sophisticated models may be required to capture the observed trends. The present model is based on the additivity law, whereas the measured char yield from pyrolysis of olive stones was compared with the predicted char yield using fractions from commercial or

fractionated lignocellulosic compounds. In Eq. (4.1), Y_i is the product yield obtained from pyrolysis of the isolated lignocellulosic compound and α, β and γ are the mass fractions of lignocellulosic compounds in the untreated olive stones and torrefied olive stones (see Appendix B).

$$Y_{pred.}\,(wt.\%) = \left(\alpha \,.\, Y_{cellulose} + \beta \,.\, Y_{hemicellulose} + \gamma \,.\, Y_{lignin}\right) \times 100 \qquad (4.1)$$

The predicted char yields calculated using the fractionated compounds from 170, 180, and 190ºC and the results are compared with the measured char yield of olive stones and torrefied olive stones, as shown in Figures 4.40 and 4.41.

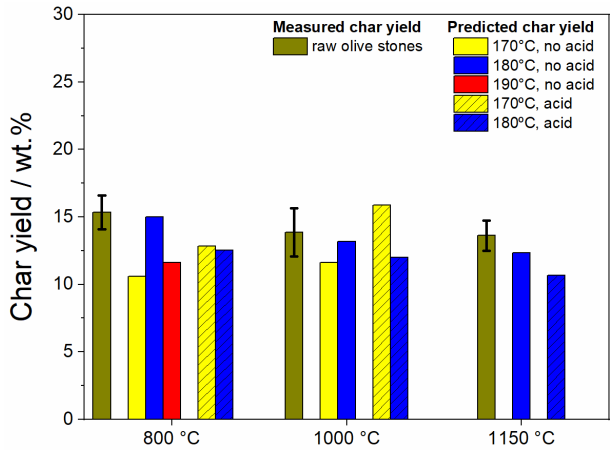

Figure 4.40. Predicted and measured char yields from raw olive stone pyrolysis at 800, 1000, and 1150 ºC in the wire mesh reactor based on the additivity law using fractionations of cellulose, hemicellulose, and lignin obtained from organosolv pretreatment.

Only the chars obtained from fractionation at 180 ºC (with acid or no acid) showed a relatively small difference to the measured char yield of olive stones for pyrolysis under conditions T1 and T2 (800 and 1000 ºC). For condition T3 (1150 ºC), however, 180 ºC no acid samples presented a better fit as compared to the acid treated samples. Similar to raw olive stones pyrolysis, an accurate prediction of char yield from

pyrolysis of torrefied olive stones was achieved using the char yields of lignocellulosic compounds fractionated at 180 ºC without any catalyst for all three temperature conditions. Thus, the overall trends of the model predictions for both raw and torrefied olive stones are in general agreement with the experimental data.

Figure 4.42 shows the predicted char yields of olive stones using the char yields from commercial lignocellulosic compounds for pyrolysis at 800 and 1000 ºC. The cellulose used in the model was the crystalline cellulose from Sigma Aldrich used in this study. The hemicellulose char yield was varied using yields of xylan, arabinoxylan, xyloglucan, arabinogalactan, and galactomannan. The yields of lignin were also varied using the data for the lignin from beech wood, and softwood and wheat straw lignin from previous studies [166]. The results indicated that the char yield of lignin of beech wood overestimated the char yield of olive stones and torrefied olive stones. This was due to the greater concentration of alkali metals and sulphur in the lignin from beech wood than in the two other lignin samples (softwood and straw). Alkali metals are known to act catalytically in pyrolysis reactions enhancing the formation of solid char. Due to a similar ash content and composition of softwood and wheat straw lignin samples, the influence on the predicted char yield of olive stones was small.

The highest yield of olive stones was obtained from a prediction that used the measured char yield of xylan. The variation in other hemicelluloses had a less significant impact on the predicted char yield of olive stones for both pyrolysis operating conditions at 800 and 1000 ºC. Specifically for 800 ºC, mixtures with any hemicellulose (except xylan) and softwood or straw lignin gave acceptable predictions of the yields of raw and torrefied olive stones. For 1000 ºC, the same mixtures showed a good fit for raw olive stones, whereas for torrefied olive stones mixtures with xylan and softwood or straw lignin provided the most accurate predictions.

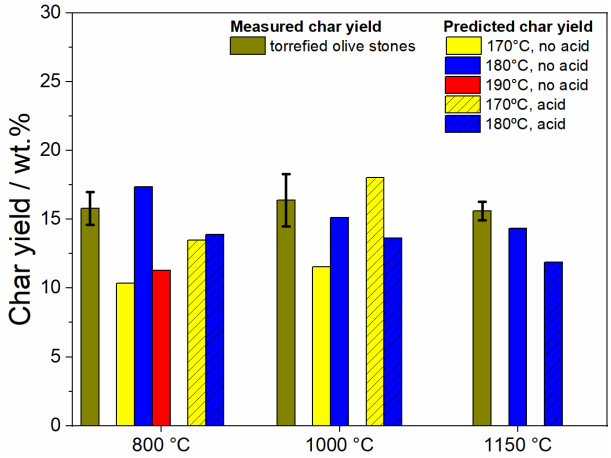

Figure 4.41. Predicted and measured char yields from torrefied olive stone pyrolysis at 800, 1000, and 1150 ºC in the wire mesh reactor based on the additivity law using fractionations of cellulose, hemicellulose, and lignin obtained from organosolv pretreatment.

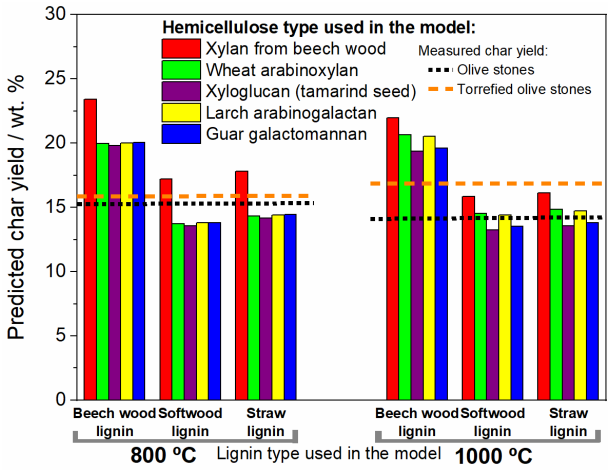

Figure 4.42. Predicted char yields from olive stones and torrefied olive stone pyrolysis at 800 and 1000 ºC in the wire mesh reactor based on commercial cellulose, hemicellulose, and lignin.

It was thus showed that the usage of commercial compounds for prediction of char yields may result in under or overpredictions. Compared to fractionated lignocellulosic compounds at 180 ºC without acid catalyst, the use of char yields from commercial lignocellulosic compounds gave in general a less accurate prediction of olive stone char yield.

4.3.2.7 Discussion

The results of the present study showed that the fractionation conditions, particularly the acid catalyst, had a great effect on the char characteristics. At 180 ºC, the acid catalyst addition resulted in lignin with more coalesced and melted structures, along with a decrease in the char yield. It can be concluded that the acid catalyst increased the fluidisation/melting of lignin during fast pyrolysis which subsequently decreased its char yield as compared to the case without acid catalyst.

The fractionated lignins were significantly different from the commercial beechwood lignin. The char yield of commercial beechwood lignin was high (54 wt.%) compared with chars from commercial lignins obtained under similar conditions, namely softwood (34 wt.%) and wheat straw (35 wt.%) [166]. Moreover, the char yield of commercial beechwood lignin was approximately twice that of the fractionated lignins (54 vs 22-25 wt.%), leading to the overprediction of the char yields (see Figure 4.42). Based on the comparison of the SEM images, the results showed that commercial beechwood lignin chars were highly cross-linked with only minor melting due to the high ash content (46 wt.%), whereas the 180 ºC fractionated lignin chars underwent clear fluidisation.

The fractionated celluloses displayed differences in morphology with acid treatment resulting in more fluidised chars (see Figure 4.37). However, these morphological differences had no effect on the char yields which were 8.9 wt.% for both acid treated and non-acid treated celluloses. For the 180ºC acid treated cellulose, an intermediate compound (metaplast) appeared to start to form, but complete fluidisation of the

particles was not achieved due the occurrence of competing cross-linking. This is in line with the mechanism proposed by Bradbury et al. [323] according to which, the pyrolysis of cellulose is defined by means of two competitive reactions (char and gases formation, and tar and gases formation). For the 180ºC acid treated cellulose, an intermediate compound was apparently not extensively formed, from the lack of fluidisation of the chars, which suggested that a single-step reaction, i.e. not considering intermediate dehydrocellulose, could be fitted.

The self-fractionated hemicelluloses had char yields similar to those of arabinogalactan and arabinoxylan. Even though these chars were morphologically different, they appeared to have similar degrees of cross-linking. Xylan was among the hemicelluloses with highest char yield (17-20 wt.%). This is explained from observation of the SEM pictures of xylan and galactomannan that showed a more extensive fluidisation of galactomannan chars as compared to xylan for which cross-linking took place before extensive fluidisation resulting in higher char yield.

The fractionation at 180 ºC without acid catalyst gave the cellulose and hemicellulose with highest degree of purity and resulted in the most accurate predictions of the experimental yields of raw and torrefied olive stones (see Figures 4.40 and 4.41). On the other hand, fractionation at 170 ºC and 190 ºC without acid resulted in the least pure cellulose and hemicellulose and subsequent underestimation of the char yields of raw and torrefied olive stones. The data strongly suggested that the additive behaviour of the samples was mostly related to the degree of purity of its cellulose and hemicellulose. Moreover, the results show that interactions between the components were not significant and that the char yields of olive stones could be predicted from the pyrolysis of its individual components.

4.4 Gasification

The determination of optimal ratios during co-gasification is crucial to enhance synergistic effects and/or minimize inhibitory effects. This is particularly relevant

during co-gasification of lignite coals with agricultural biomass since lignites contain a high content of inorganics (Si, Al, Fe) and agricultural biomass contains a relatively high content of alkali and alkali earth metals (K, Na, and Ca). Since the pyrolysis conditions strongly affect the morphology and inorganic composition of the chars, the objective of this study is to investigate the effect of high heating rate and high temperature pyrolysis on the char characteristics and subsequently the effect of the char characteristics on the co-gasification behavior. This study combines a drop tube furnace that allows to replicate the heating rates experienced by particles in entrained flow gasifiers, with a TGA to conduct a detailed characterization of the char co-gasification behavior of different biomass-coal blends. The novelty of this study is the investigation of the effect of the fast pyrolysis stage on the morphology and chemical composition of chars from low rank feedstocks rich in inorganics (lignite coal and agricultural biomass), and the correlation of the physicochemical properties of the chars with the subsequent co-gasification behavior and kinetics with focus on the selection of optimal blending ratios to ensure synergies. The results presented herein are reprinted with permission from "Magalhaes D, Akgul A, Kazanç F, Costa M, Interactions during CO2 co-gasification of biomass and coal chars obtained from fast pyrolysis in a drop tube furnace, Energy & Fuels 2021". Copyright (2021) American Chemical Society.

4.4.1 Co-gasification of biomass with coal

4.4.1.1 Elemental and mineral composition

The elemental composition (proximate and ultimate analysis) and ash compositional analysis of the chars is presented in Table 4.14. The H content in both chars decreased substantially as compared to the respective feedstocks as shown in Table 4.14. Oppositely, the C content increased for both OR and SL chars. The amount of volatiles in the chars of OR and SL (42.5 and 19.1 wt.%, respectively) showed that the pyrolysis was not complete. Similarly, Farrow et al. [324] observed the presence

of residual volatiles in sawdust chars devolatilized in DTF. The result herein was due to the short residence time (~3 s) in the DTF, which is similar to the case in entrained flow gasifiers. However, the residual volatiles did not influence the gasification behavior of the chars since a low heating rate (10 ºC min^{-1}) was chosen during heating of the chars in the TGA to enable release of residual volatiles before the gasification ensued. In line with the volatile matter, both OR and SL chars showed a relatively high content of H due to incomplete devolatilization. Importantly, the K content of the ash from OR char was unchanged after fast pyrolysis. Potassium is present in biomass in both organic and inorganic fractions. Whereas the potassium bound to organic structures (usually < 10 %) [325] is typically released at low temperatures (200-500 ºC), the inorganic potassium is retained in the char and released at temperatures above 600 ºC [325]. Herein, the similar potassium contents before and after pyrolysis showed that most inorganic potassium is still present in the OR char, due to the short residence times in the DTF that prevented its vaporization.

The XRD patterns of the chars are displayed in Figure 4.43, along with the patterns for both raw feedstocks for comparison purposes. As visible in Figure 4.43, quartz related peaks at 20.9 and 26.6 º were registered for both OR and SL chars and showed the highest intensity for SL.

SL chars in particular showed hematite (35 º) and mullite (35 and 50 º) peaks as a consequence of the presence of Fe and Al in the SL ash. Hematite and mullite peaks overlap and therefore a distinction between these two minerals cannot be done confidently. Moreover, kaolinite (19.7 º) was still present in the SL char despite the pyrolysis temperature (1000 ºC) that should be sufficient for complete kaolinite decomposition, as a consequence of the short residence time in the DTF.

It was challenging to unambiguously attribute the peaks to specific mineral phases of the OR char. Since K was the major element in OR ash, followed by Ca, the peaks at 29.1 and 30.6 º were likely due to $K_2Ca(CO_3)_2$. The presence of KCl (at 28 and 50 º) [326] and NaCl (at 27, 32, and 46 º) [327] was also identified. The peaks at 29.5 º

and 60º were assigned to calcite ($CaCO_3$), and those at 31, 33.5, and 41 º to arcanite (K_2SO_4), even though these latter peaks coincide with dolomite ($MgCa(CO_3)_2$) and cannot be clearly attributed to either mineral phase.

Table 4.14 Proximate, ultimate, and ash compositional analyses of the chars.

Parameter	Olive residue (OR)	Soma lignite (SL)
Proximate analysis, wt.% db		
Volatiles	42.5	19.1
Fixed carbon[a]	28.4	42.9
Ash	29.1	38
Ultimate analysis, wt.% daf		
C	56.6	64.9
H	1.41	1.74
N	1.98	1.59
S	0.210	0.666
O[a]	39.8	31.1
Ash compositional analysis, wt.% db		
Si	4.63	25.9
Al	1.64	15.3
Fe	7.98	20.8
Ca	27.3	18.7
Mg	1.62	0.754
Na	0.904	0.803
K	47.1	3.79
P	3.62	0.373
Ti	0.625	2.98
Cl	2.00	-
V	-	0.444
S	1.73	9.17
Other species	0.851	0.986

[a] by difference.

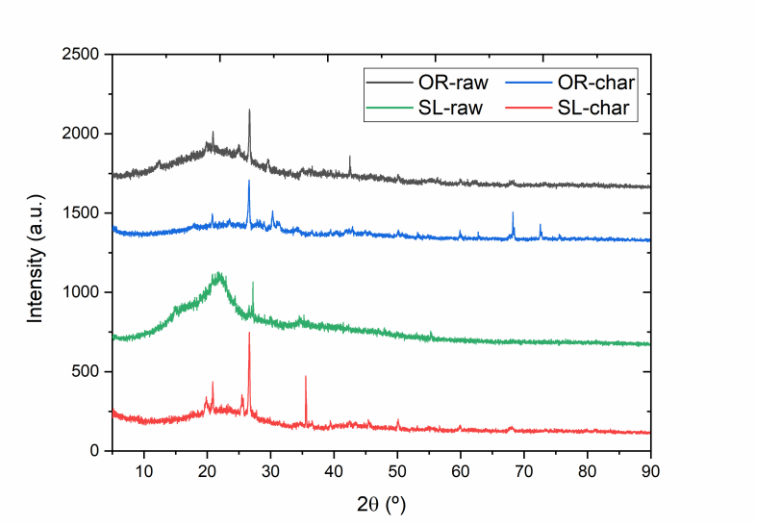

Figure 4.43. X-Ray Diffraction patterns of the chars. Patterns of the raw feedstocks are included for comparison purposes.

4.4.1.2 Particle size, morphology, and surface area

The particle size distributions of the raw feedstocks and chars are displayed in Figure 4.44, and the mean diameters in Table 4.15. The results showed unimodal distributions for all samples. Following pyrolysis in the DTF, the SL chars did not change in size significantly likely due to the high ash content which catalyzed cross-linking reactions and prevented extensive melting. The OR chars, on the other hand, underwent a diameter reduction from 88.1 to 81.7 μm (volume-weighted mean).

The SEM results are shown in Figure 4.45 for the DTF chars of OR and SL, and the SEM results of the raw OR and SL samples can be found elsewhere [91]. Firstly, it was observed that the SL char retained its initial shape, was angular, and did not shrink significantly (in line with the PSD results). However, the OR char became quasi-spherical, underwent extensive melting, size reduction, and formation of macropores due to sudden ejection of volatiles. This quasi-spherical morphology of OR chars was observed in the literature for several biochars (wheat straw, rice husk, pine wood, and mallee wood) with similar particle size, and pyrolyzed under similar conditions to those applied in this study [138,328]. The results shed evidence on the

importance of the formation of metaplast during pyrolysis and its effect on the subsequent char morphology and surface area. During pyrolysis of OR, an intermediate phase - metaplast was formed, which resulted in the softening of the particles and the overlapping of micro and mesopores for OR chars.

Comparison of the present results with those presented in subsection 4.3.1 in which OR and SL were pyrolyzed in a wire mesh reactor (WMR), with a heating rate of 1000 ºC s^{-1}, showed that the SL chars produced in DTF displayed similar morphology to both the WMR chars and the raw SL. For OR, however, the DTF chars showed more extensive melting and in general more disparate morphology as compared with either WMR chars or raw feedstock. It can thus be concluded that the heating rate during pyrolysis had a significant effect particularly on the morphology and surface area of the biomass char (OR).

Consistent with the SEM observations, the surface area of OR measured by BET analysis decreased from 7.9 for the raw fuel to ~3 m^2 g^{-1} following fast pyrolysis (see Table 4.15), due to melting and collapse of micro and mesopores. As stated previously [207], the presence of K_2O in large amount led to a low melting temperature of the ash. On the other hand, SL chars did not melt and retained the initial aspect ratio and morphology, even though the BET surface area increased three-fold from 10.1 to 31.3 m^2 g^{-1}. It should be noted, however, that even though the chars were flushed by nitrogen at 350 ºC prior to the surface area measurement, tars may block the pores during char cooling upon collection from the DTF. In the literature, even though most studies report biochars with high surface areas (~100-300 m^2/g) [138,142,149,153,154], some studies also report low surface areas (< 5 m^2/g) [142,151,152], and this disparity can indeed be related with the blockage of pores by tar during cooling of the chars.

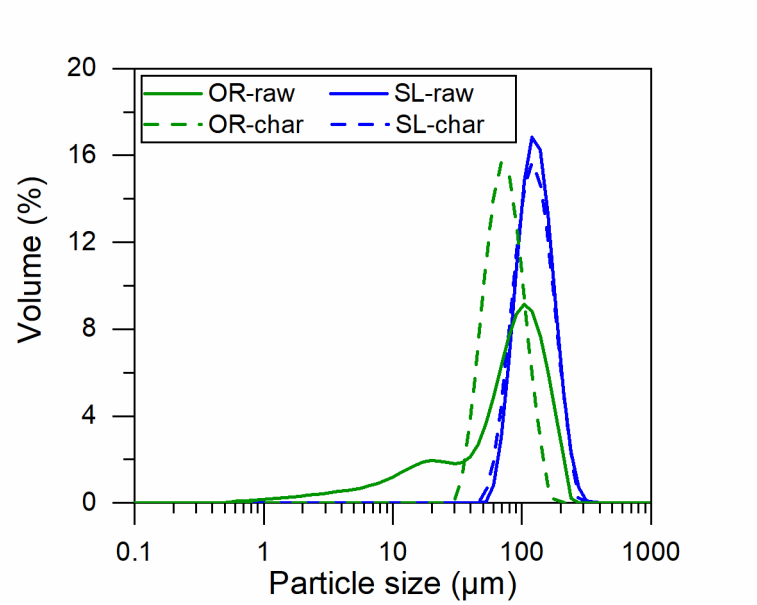

Figure 4.44. Particle size distribution of the raw feedstocks and chars of olive residue and Soma lignite.

Table 4.15 Mean diameters and BET surface areas of the raw feedstocks and chars

	Raw feedstock		Char	
	OR	SL	OR	SL
Surface weighted mean D [3,2], µm	86.5	129	77.3	123
Volume weighted mean D [4,3], µm	88.1	142	81.7	137
BET surface area, $m^2 g^{-1}$	7.93	10.1	2.99	31.3

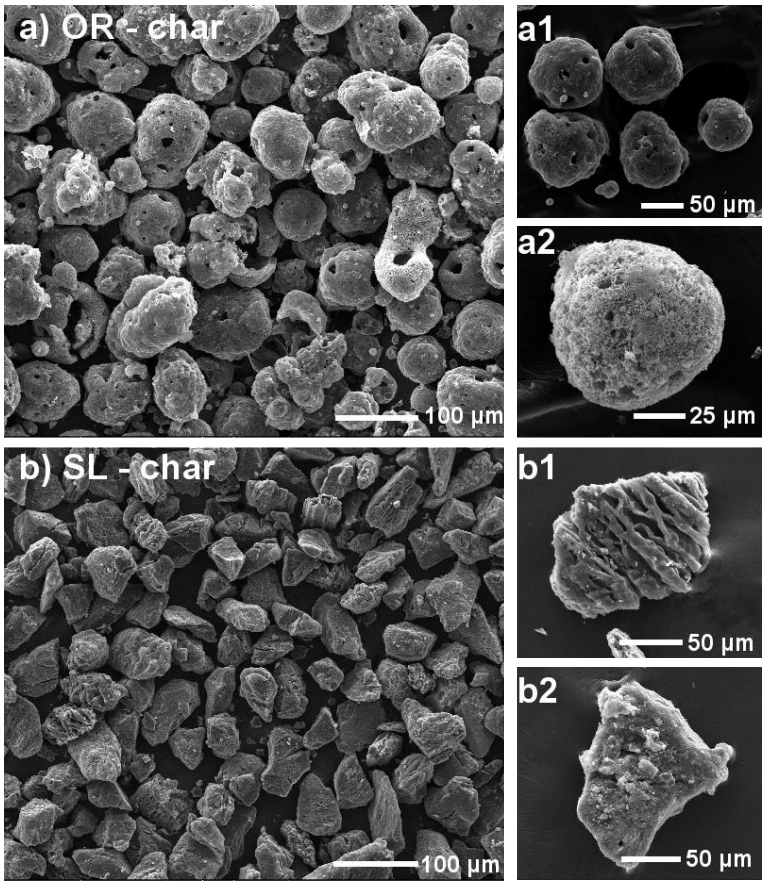

Figure 4.45. Scanning electron microscopy micrographs of chars from (a) olive residue and (b) Soma lignite obtained from fast pyrolysis in the drop tube furnace.

4.4.1.3 Gasification behaviour

The gasification behavior of the chars and blends was investigated through thermogravimetric isothermal tests. Four temperatures were chosen (800, 900, 950, and 1000 ºC) to assess the influence of the temperature on char gasification reactivity and kinetics. Moreover, the effect of the blending ratio was evaluated by three distinct blends of OR and SL chars: 50 wt.% OR – 50 wt.% SL, 25 wt.% OR – 75 wt.% SL, and 10 wt.% OR – 90 wt.% SL, hereinafter termed 50OR-50SL, 25OR-75SL and 10OR-90SL, at the intermediate temperature (900 ºC). The experimental gasification curves and parameters of the experimental blends were compared with

the predicted blends (calculated from the weighted sum of the individual conversion profiles) to infer synergies/inhibitions during gasification.

Gasification profiles of individual chars

The conversion curves of both OR and SL are presented in Figures 4.46 and 4.45. Regardless of the temperature, OR chars presented higher gasification rates and shorter 90% conversion times as compared to SL chars. Specifically at 900 ºC the gasification rates were 63.4 and 7.9 wt.% min^{-1} respectively for OR and SL. As a consequence of the higher reactivity, the 90% conversion times of OR were shorter (1.9 min) as compared with those of SL (38 min). Even though the OR char had lower surface area than the SL char, and typically the (high) gasification reactivity is correlated with the high surface area [329], the OR char herein had higher reactivity than the SL char. Therefore, the higher reactivity of OR compared to SL was attributed to the catalysis of inherent alkaline and alkaline-earth metal (AAEM) species, especially K and Ca [189,204], and to the lower inhibiting minerals such as Si, Al, and P [194,204]. The SL char contained high amount of Si and Al which, along with low amounts of K and Ca resulted in low reactivity due to the formation of potassium and calcium aluminosilicates and subsequent K-deactivation [203].

It was observed that both OR and SL chars presented maximum gasification rates at the initial times. Moreover, SL showed maximum gasification rates at low conversions (< 4 wt.%) whereas for OR, the reactivity increased with increasing conversion and reached a maximum at 14 wt.% (for 800 ºC) and ~36 wt.% (for 900 and 1000 ºC).

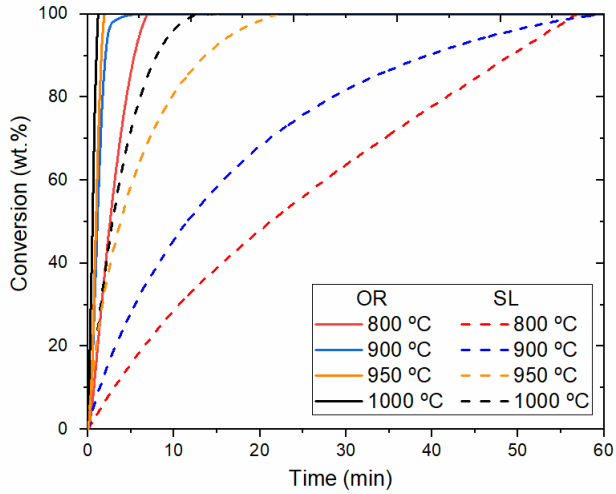

Figure 4.46. Conversion profiles of olive residue and Soma lignite chars during isothermal gasification in TGA at 800, 900, 950, and 1000 ºC.

Effect of the gasification temperature

The increase in temperature always resulted in the increase in gasification rate and decrease in 90% conversion time for both OR and SL chars. The gasification of OR at 800 ºC presented a maximum rate at ~14 wt.% conversion followed by a decrease in the gasification rate. The increase in temperature resulted in the maximum gasification rates to be reached in a shorter time. The variation of the gasification rate with the conversion degree showed a different trend. For SL the maximum rate was reached at conversion degrees below 5 wt.%, whereas for OR the gasification rate tended to increase with the increase in conversion, particularly at temperatures above 800 ºC, as observed previously in the literature [267,330]. In fact, Fermoso et al. [267] gasified two bituminous coals (low and high ash) and two types of biomass (chestnut residues and olive stones) prepared under fixed bed reactor with heating rate of 15 ºC min^{-1}. The authors observed maximum reactivities at 70-80 % conversion for olive stones, at 20-30 % conversion for high ash coal, and the two other samples (low ash coal and chestnut residues) showed a constant decrease in reactivity with increase in conversion. The results herein for OR and SL (maximum

reactivities at 40 % and 5 % conversion, respectively) were in line with the observed by Fermoso et al. [267] for biomass chars and low ash coal chars, respectively. Moreover, Liu et al. [265] observed that the maximum reaction rate was located at conversions of 20 % for chars prepared from two tri-high coals in a fixed bed reactor at 950 ºC.

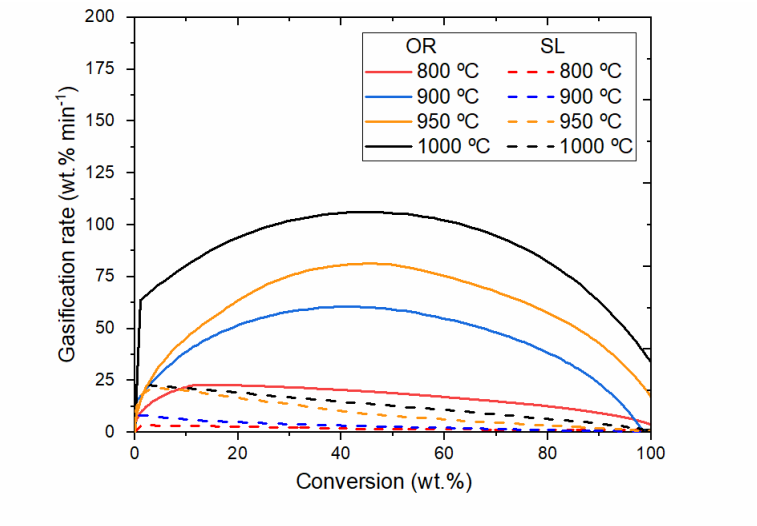

Figure 4.47. Gasification rate vs conversion profiles of olive residue and Soma lignite chars during isothermal gasification in TGA at 800, 900, 950, and 1000 ºC.

Effect of the blending ratio

Blends were mechanically prepared using the neat chars produced under fast pyrolysis. Three blends with distinct blending ratios were prepared to infer catalytic and/or deactivation effects during co-gasification at the intermediate temperature (900 ºC). Predicted blends were calculated by the weighted sum of the gasification conversion profiles of the neat chars. The conversion profiles of the experimental and predicted blends are presented in Figure 4.48, and the gasification rate vs conversion curves in Figure 4.49. In both figures, the OR and SL curves are included for comparison purposes. The experimental blends 50OR-50SL and 25OR-75SL

reached total conversions in a shorter time as compared with the predicted blends, as also observed by Kajitani et al. [189] for 30 % woody biomass - 70 % coal blends. Specifically, the experimental 90 % conversion times of the 50OR-50SL and 25OR-75SL blends (5.8 and 17.5 min, respectively) were shorter than those of the predicted blends (27 and 34 min, respectively). For the 10OR-90SL blend, however, the 90 % conversion times were similar for both the experimental and the predicted blend. This showed that synergies occurred between OR and SL for blends with OR content equal to or above 25 %, which resulted in shorter conversion times. The maximum rate of gasification, however, showed a different behavior for the experimental and predicted blends. The highest maximum gasification rates were achieved for the predicted blends as seen by the initial slopes of the curves in Figure 4.48 and the maxima in Figure 4.49. The gasification rates of the predicted blends (50OR-50SL and 25OR-75SL) reached their maxima at lower conversions as compared with the corresponding experimental rates which extended until 80-100 % conversions. These results can be explained by the dependency of the char reactivity on the morphology and on the inorganic composition [210]. At low conversions the porosity and accessibility of active sites mostly affect the reactivity of the char, and at higher conversions the catalytic activity of the ash plays a major role. The maximum gasification rates and 90 % conversion times reported herein showed that the morphology of the OR and SL chars did not affect the reactivity during co-gasification, whereas the catalytic activity of the inorganics was a significant factor for the increase in reactivity.

The experimental blend of 10OR-90SL closely resembled the behavior of the neat SL char due to an existing deactivation effect in this blend throughout the whole conversion. The ash content following gasification of the experimental blend (42 wt.%) was close to the one of the predicted blend (43.5 wt.%), which unequivocally indicated the presence of OR in the blend. Interestingly, the 25OR-75SL experimental blend and the 10OR-90SL predicted blend had the same reactivity (~13 wt.% min^{-1}) and overlapping rate vs conversion profiles until ca. 20 % conversion degree.

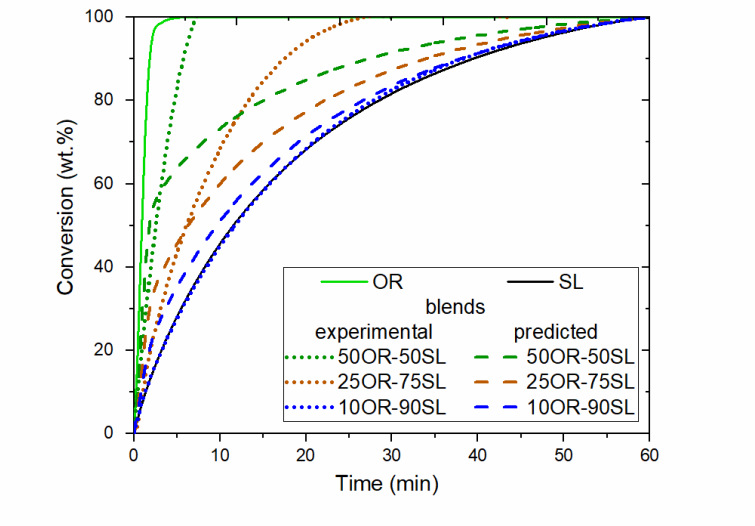

Figure 4.48. Conversion profiles of experimental and predicted (additive) blends during isothermal gasification in TGA at 900 ºC. Olive residue and Soma lignite curves are included for comparison purposes.

Both OR char and 50OR-50SL blend showed constant gasification rates until high conversions. As defined by Dupont et al. [204], the reaction rates of biomass samples with a ratio K / (Si+P) > 1 are mostly ruled by the catalysis of K and are expected to display such behavior. The results obtained herein showed that the influence of K in the gasification of OR and 50OR-50SL chars was still significant, as proved by the XRD results. Moreover, the XRF results show that the OR char ash had similar K content as the raw OR ash (47.1 vs 48.6 wt.%, respectively), proving that K did not vaporize extensively during fast pyrolysis in the DTF, likely due to the short particle residence time, and had a large influence on the gasification behavior.

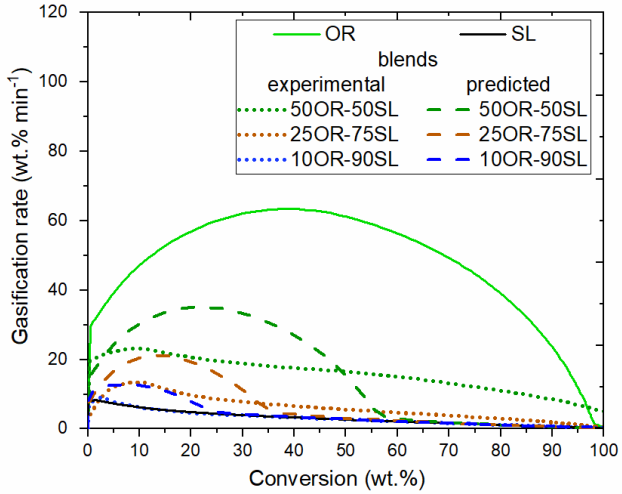

Figure 4.49. Gasification rate vs conversion for all experimental and predicted (additive) blends during isothermal gasification in TGA at 900 ºC. Olive residue and Soma lignite curves are included for comparison purposes.

4.4.1.4 Gasification kinetic parameters

Effect of the gasification temperature

The effect of the gasification temperature on the computed kinetic rates is shown in Figure 4.50 in the form of an Arrhenius plot. An increase of the rate constants with increasing temperature was observed in general for all chars and kinetic models (VM, GM, and RPM), as observed by other researchers [201,206]. The rate constants of SL chars increased more severely when moving from 900 to 950 ºC for all three models. For OR chars, on the one hand, a more monotonous increase was registered over the whole range (800-1000 ºC) for both VM and GM. On the other hand, for the RPM the rate constants at 800 and 900 ºC were similar (0.36×10^{-2} vs 0.47×10^{-2} s^{-1}, respectively), and a more notorious increase was registered for 1000 ºC (0.92×10^{-2} s^{-1}). This was due to the shift in gasification regime from chemically controlled to diffusion controlled, as represented by the change in slope of the Arrhenius fitted curves when moving from 900 to 950 ºC (Figure 4.50). This regime shift was best captured by the RPM for OR, and by both GM and RPM for SL.

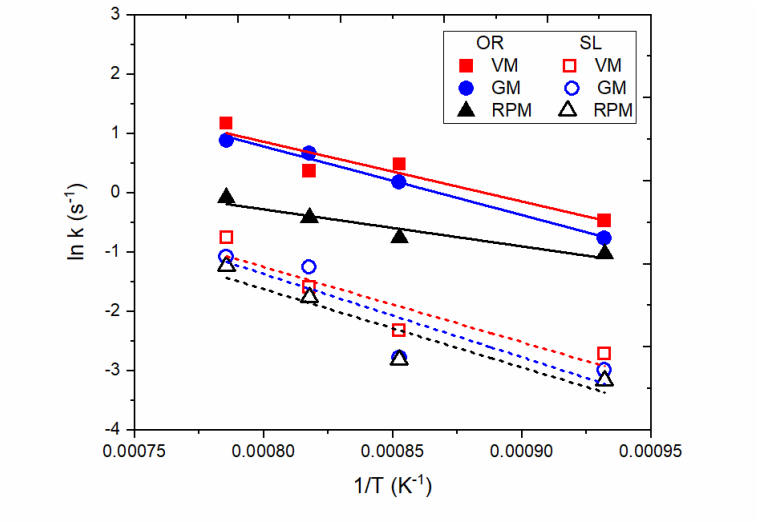

Figure 4.50. Arrhenius plot of the individual chars (from fitting of different kinetic models.

The rate constants from fitting of the RPM to SL char gasification (0.042 x 10^{-2} and 0.060 x 10^{-2} s^{-1} for 800 and 900 ºC) were below those by Ding et al. [194] who obtained 0.073 x 10^{-2} and 0.20 x 10^{-2} s^{-1} for gasification of a lignite coal char with similar size at 800 and 900 ºC, respectively. The SL char was produced herein in high temperature and high heating rate pyrolysis in the DTF (unlike the slow pyrolysis in the work of Ding et al. [194]) and thermal annealing is unlikely. However, during slow gasification in TGA, the SL chars might have been thermally annealed with more ordinated polyaromatic structures in the char, and consequent deactivation as observed previously [138,213,219].

As visible from the slopes of the fitted lines in Figure 4.50, the activation energies were similar for SL from all three models (~100 kJ mol^{-1}), slightly below the results obtained by Jayaraman et al. [201] for an Indian lignite char gasified under similar conditions and obtained from pyrolysis in TGA at 800 K min^{-1} (see Table 7 therein).

For OR, on the other hand, the activation energies were different for each model, namely 84, 96, and 52 kJ mol^{-1} for the VM, GM, and RPM, respectively.

Effect of the blending ratio

The effect of the blending ratio on the rate constants is shown in Figure 4.51 for all blends and kinetic models. Firstly, it must be pointed out that, for the same gasification temperature, the rate constants of the OR char were above those of the SL by one order of magnitude. This occurred regardless of the low surface area of OR char which was significantly below that of the SL char. Thus, the results show that the surface area and pore structure was not a predominant parameter to ensure high gasification reactivity of the char, as other researchers concluded [205,207]. The migration of active K during fast pyrolysis, and subsequent catalytic effect during gasification was likely the factor that enabled high gasification rate constants for the OR char.

Even though the maximum gasification rates for the 50OR-50SL and 25OR-75SL experimental blends were below those of the predicted ones, the gasification process extended to higher conversions (unlike the predicted blends, cf. Figure 4.49), and this had a clear effect on the kinetics since the kinetic models are fitted to the whole extent of the conversion (5-95 %) and better reflect the catalytic activity of the ash at high conversion values.

The kinetic modelling showed that synergies were only observed for blends with OR content equal or above 25 wt.%, and particularly for the 50OR-50SL blend. Recently, Wei et al. [331] analyzed the influence of the addition of rice straw ash (rich in K and Si) on the gasification behavior of anthracite (rich in Si and Al) and bituminous coal (rich in Si and Ca) chars. The authors [331] observed a strong correlation between the increase in active alkalis (i.e. alkalis in the form of inorganic salts or combined with oxygen containing groups) and the increase in reactivity of the coal-biomass ash blend. In the present study, the identification of active alkalis in the OR

char was performed using XRD, according to which KCl, NaCl, $K_2Ca(CO_3)_2$, and K_2SO_4 and/or $MgCa(CO_3)_2$ are present in OR ash. Since synergies are observed for the 25OR-75SL and 50OR-50SL blended chars, the results of the present study strongly suggest that the findings of Wei et al. [331] are also applicable to blends of low rank coal char (Soma lignite) with K-rich biochar from olive residue.

Since the XRD patterns of the chars displayed both K-related phases in OR and aluminosilicate phases in SL, which may combine during gasification and result in deactivation of the active K, further investigation was required. As stated in the literature [194,196,326,332], blends of biomass (rich in K) and coal (rich in Si and Al) may display synergies (due to migration of active K), and/or inhibitions due to formation of minerals such as $KAlSiO_4$, $KAlSi_3O_8$, or K_2CaSiO_4 [333]. Specifically, the threshold to the occurrence of synergies during co-gasification was defined by Masnadi et al. [334] as the molar ratios K/Al > 1 and K/Si > 1 (K from the biomass char and Al and Si from the coal char). Herein, the K/Al ratios of the 10OR-90SL, 25OR-75SL and 50OR-50SL char blends were 0.24, 0.71, and 2.13, respectively. Moreover, the K/Si ratios of the 10OR-90SL, 25OR-75SL and 50OR-50SL char blends were 0.15, 0.43, and 1.30, respectively. According to the results, synergies would only take place for the 50OR-50SL blend. However, synergies were also observed in the 25OR-75SL blend likely due to the presence of Ca, a known catalyzer that further prevented the deactivation of K [196,228], which was present in the OR char (27.3 wt.%) but not in the switchgrass biochar used by Masnadi et al. [334] The results strongly suggested that in the presence of Ca the threshold for K/Al and K/Si in the blend for which synergies can be observed, which coincided with the 25OR-75SL blend, was K/Al = 0.7 and K/Si = 0.4, rather than K/Al = 1 and K/Si = 1. The present results also showed that, in general, the K/Al and K/Si ratios defined previously for co-gasification of slow pyrolysis chars can also be applied to fast pyrolysis chars (provided that K vaporization during pyrolysis does not take place extensively as in this work).

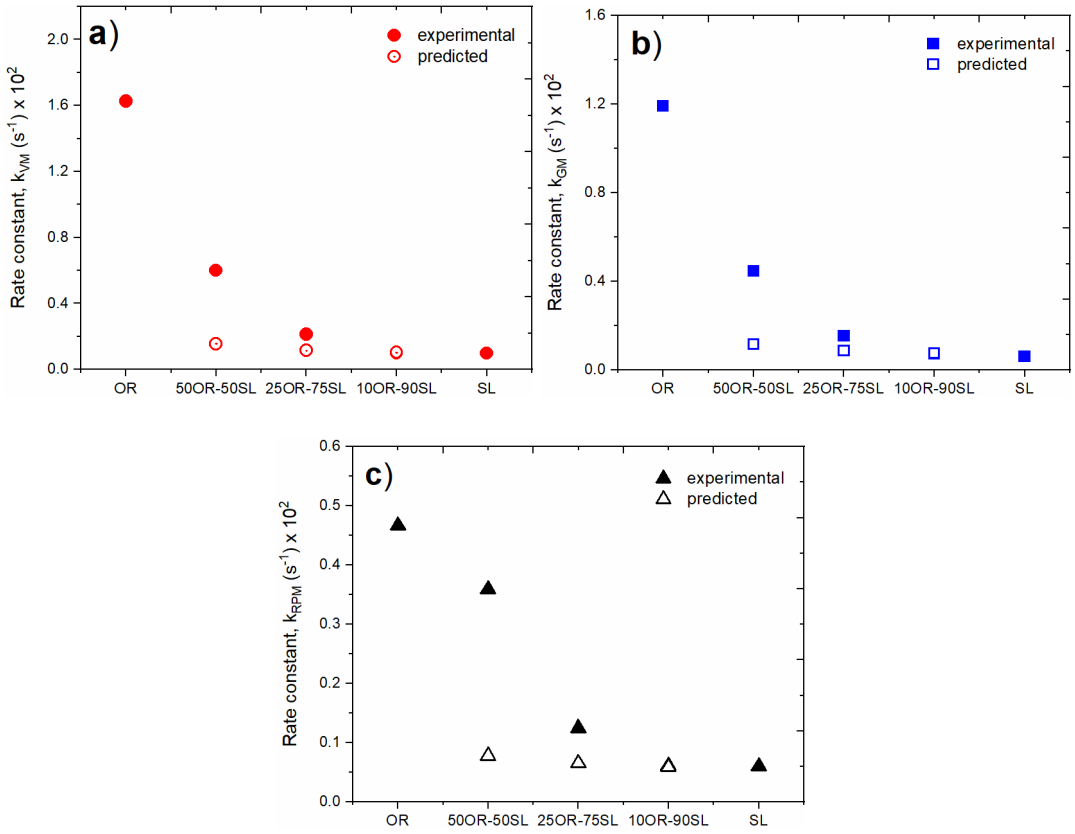

Figure 4.51. Rate constants of the blends from fitting of a) the volumetric model, b) the grain model, and c) the random pore model from isothermal gasification at 900 ^{o}C.

CHAPTER 5

CONCLUSIONS

5.1 Ignition

Ignition mode at low and high heating rates

Under low heating rates, both biomass residues ignited homogeneously, whereas the lignite coals underwent hetero-homogeneous ignition. Under high heating rates, all solid fuels showed a predominantly gas-phase ignition. Thus it was seen that the ignition mode of lignite coal was strongly dependent on the heating rate. For biomass, the dependence was seen with the particle size, and the smaller size biomass fuels exhibited an increasing tendency for surface ignition in comparison with the large diameter particles, particularly at lower temperatures.

Ignition delay time at high heating rates

Even though all fuels show similar characteristic ignition temperatures, both biomass residues and the Soma lignite presented higher ignition delay times than the Tunçbilek lignite. The relatively high moisture content of the biomass residues may have significant impact on the ignition delay time. The ignition delay times tend to converge with the increase of the atmosphere temperature, including those of the largest tested particles, indicating that the properties of the particles become less dominant as the temperature augments. For the oxygen concentration variation range studied, the ignition delay times were not affected.

5.2 Combustion

Kinetic modelling

The combustion behaviour was affected by both the fuel type and the applied heating rate. The studied biomass fuel presented lower decomposition, ignition, and burnout temperatures, along with higher combustibility, in comparison with both lignites. Increasing heating rate clearly increased the reactivity, combustibility, and burnout temperatures of all fuel samples.

The major stage of combustion was best fitted by diffusion-controlled mechanisms for Tunçbilek lignite, and by chemical reaction-controlled mechanisms for Soma lignite and olive residue. During the major stage of combustion, and at 20 ºC/min, Tunçbilek presented values of apparent activation energy of ~100 kJ/mol, and the remaining fuels presented apparent activation energies of approximately 40 kJ/mol. The last stage of combustion, observed only for olive residue, was best described by diffusion-controlled mechanisms, and apparent activation energies were in the order of 10 kJ/mol, regardless of the heating rate. Activation energies decreased with a shift in the heating rate from 20 to 40 ºC/min, whereas no change was observed between 15 and 20 ºC/min.

Observations on combustion behaviour at high heating rates

All biomass particles ignited homogeneously and burned forming large and circular envelope flames followed by a distinguishable char combustion stage. Torrefied biomass particles burned with brighter flames and longer char burnout times than those of raw biomass.

Tunçbilek lignite also burned with two distinguishable phases, initially displaying bright sooty flames, typically elongated and forming contrails, that resembled those observed during combustion of bituminous coals; some limited fragmentation was present.

Soma lignite exhibited extensive fragmentation which resulted in surface ignition of the fragments and gas-phase ignition of the remaining non-fragmented particle. The fragments appeared to exhibit simultaneous volatile and char combustion.

Overall burnout times of raw and torrefied biomass 212-300 μm particles were shorter or equal to those of Tunçbilek lignite 106-125 μm particles, suggesting that they might be completely burned in existing TL-fired furnaces.

Overall burnout times of raw and torrefied biomass 212-300 μm particles were much longer than those of Soma lignite 106-125 μm particles, suggesting that they may not be completely burned in existing SL-fired furnaces. A much finer biomass grind size may be required for those furnaces.

Particulate matter formation during co-combustion

Upon normalization with respect to the useful energy input the PM2.5 for OR raw and char were similar, and that of torrefied OR was reduced as compared to OR raw. Therefore, these biomass feedstocks can be used to provide the same useful energy output with no significant negative effect on PM2.5 emissions. The heat treatment resulted in a decrease in both chlorine and sulphur which are known to contribute to submicrometer PM. OR char presented PM2.5 emissions lower by three-fold as compared with either raw or torrefied OR, and this was in line with a decrease in Cl in both feedstock and PM2.5. The presence of Cl permitted the release of alkali and alkali earth metals to the gas phase by formation of alkali salts. The results obtained showed that the mechanisms responsible for the formation of PM2.5 and PM2.5-10 in raw biomass feedstocks are also applicable for torrefied olive residue and biochar from olive residue.

Co-combustion resulted in clear reduction of PM2.5 emission below the predicted values. The silicates/aluminosilicates present in PM2.5 from TL retained K and allowed for the reduction of PM2.5 as compared with the predicted blends.

The results obtained showed that the mechanisms responsible for the formation of PM2.5 during biomass and coal combustion are also applicable to biomass-coal blends. Special attention must be given to the content of Si, Al, and Fe in the coal/lignite ash since these are known to retain alkali elements and shift the PM formation from fine to coarse particles. This shift is likely to allow the capture of PM from biomass-coal co-firing by conventional coal-PM traps in existing coal power plants.

5.3 Pyrolysis

Co-pyrolysis of biomass with coal

High heating rate pyrolysis results indicated a higher volatile yield when compared to the slow pyrolysis for SL. On the other hand, the biomass yields from high heating rate pyrolysis were only slightly higher than those obtained from slow pyrolysis. Unlike the Soma lignite chars, the biomass chars, especially almond shell char, presented large cavities, although the surface areas of the biomass chars were low (~13 $m^2 g^{-1}$), when compared to Soma lignite (80 $m^2 g^{-1}$).

Biomass chars (OR and AS) presented lower burnout times, higher carbon burnout rates, and higher rate constants, when compared to lignite char. The 50OR-50SL blend displayed synergies that may justify its use, even though this blending ratio is not used in large scale co-firing applications. In spite of the high calorific content of OR, other aspects of biomass-coal burning such as pollutant emissions and ash deposition need to be investigated to ascertain the feasibility of this blend in large scale co-firing. On the other hand, blends with almond shell and Soma lignite were not found suitable for co-firing.

Fast pyrolysis of laboratory-fractionated biomass

The results showed that the acid treatment of biomass during fractionation had a strong effect on the char yield and composition during pyrolysis, whereas the organosolv process temperature was a less preponderant factor. Importantly, it has been shown for the first time that the fractionated lignocellulosic compounds at 180 ºC without an acid catalyst, provided the most accurate prediction of raw and torrefied olive stone char yields, as compared to the commercial lignocellulosic compounds. The results obtained provide relevant information to understand the effect of the fractionation conditions on the purity of organosolv lignocellulosic compounds, and on the product yields and properties of chars obtained from fast pyrolysis which is of great importance for kinetic modelling and biorefinery applications for which the knowledge of the char yield of each component (cellulose, hemicellulose, and lignin) is required.

5.4 Gasification

Co-gasification of biomass with coal

The high heating rates during the pyrolysis step strongly influenced the morphology and surface area of the chars. However, the morphological traits of the char following fast pyrolysis in the DTF were not decisive factors influencing the gasification behaviour. Moreover, according to XRF and XRD results, potassium did not vaporize during fast pyrolysis and was present in the biochar, particularly in active forms (e.g. $K_2Ca(CO_3)_2$ and KCl). Therefore, the presence of inorganics in the biomass char was the main contributor to the catalytic behavior during co-gasification.

The maximum gasification rates and 90 % conversion times reported herein for both 25-75 and 50-50 char blends showed that the morphology of the OR and SL chars did not affect the reactivity at low conversion levels during co-gasification, and that

the catalytic activity of the inorganics was a significant factor for the increase in reactivity at higher conversions.

Synergies only took place for blends with ratios of olive residue equal to or above 25%, and that ratios of 10% of olive residue result in deactivation and behavior similar to the Soma lignite char. The results strongly suggested the existence of a threshold for K/Al and K/Si in the char blend for which synergies can be observed, which coincided with the 25OR-75SL blend, specifically K/Al = 0.7 and K/Si = 0.4, and that the presence of Ca as a catalyst must be considered.

5.5 Concluding remarks on the applicability of the results

Even though the ignition mode of biomass was dependent on the particle size, the ignition mode did not have a visible influence on the ignition delay time. Therefore, the ignition delay times for biomass are still relevant for applications which employ similar conditions, even if in those applications the ignition mode shifts from gas-phase to surface ignition. Nevertheless, the results ought not to be blindly used for validation of results from large-scale furnaces since conditions such as turbulence and radiative heat transfer are not observed in the entrained flow reactor used here.

Since the experimental conditions and the procedure for calculation of the ignition delay time are well defined, the results in this work can be used to tune devolatilization/pyrolysis models. The results showed that the gas phase ignition was the defining step at high heating rates and special care must be given to the homogeneous reactions through the usage of detailed devolatilization/pyrolysis models that can adequately capture the rapid chemistry during the early stages of combustion.

As with the ignition delay times, the volatile and char burning times obtained from high heating rate combustion were obtained under well-defined conditions and can therefore be used to validate CFD models of coal or biomass combustion. Moreover,

the usage of the burnout times of single particles as indicative values for pilot scale applications is encouraged.

As observed herein, the combustion mode of the lignite coals was strongly dependent on the heating rate, and phenomena such as fragmentation that do not occur during low heating rate combustion, strongly affected the combustion kinetics and burnout times. Accordingly, the usage of combustion kinetic parameters from low heating rate combustion in the modelling of high heating rate processes is not advisable.

The combined use of the burnout times of single particles and the particulate formation from 100 % biomass firing and co-firing is recommended as a preliminary step to select feedstocks for large scale applications. However, the co-firing ratio strongly affects the particulate matter formation and special care must be given when investigating these same feedstocks in different ratios.

The co-gasification kinetic parameters presented in this study for high heating rate chars ought to be used with care when modelling entrained flow gasification processes and can particularly be used as a pre-selection tool for pilot scale entrained flow gasification. The significance of the results is twofold: firstly, if a blend did not show synergy or deactivation during TGA co-gasification where the contact between the particles is very intimate, then that blend will likely also not show any interactions during entrained flow gasification. Secondly, the blends that showed synergy or deactivation during TGA co-gasification can be used as indicative blends for pilot scale entrained flow gasification trials. During pilot scale trials, the occurrence of synergies will be confirmed by measurement of the syngas composition, and maximization of the syngas yield can be attained.

CHAPTER 6

RECOMMENDATIONS FOR FUTURE WORK

This work focused on the investigation of alternative biomass fuels towards co-firing, co-pyrolysis, and co-gasification applications under pulverized conditions. The following recommendations are given below as a continuation to the present work.

Recent efforts have been given to the fundamental study of the ignition of biomass fuels under high heating rates. Agricultural biomass is highly heterogeneous and the ignition data (i.e. ignition mode and ignition delay time) still lacks in the literature for a high number of feedstocks. Moreover, the study of 2nd and 3rd generation feedstocks, which present significantly different properties, has not yet received attention. Studies on ignition and combustion of streams of agricultural biomass and lignite and its effect on flame stability also lacks in the literature. Particularly with focus on the interaction between inorganics during the early stages of combustion.

The studies on the combustion and co-combustion of agricultural (non-woody) biomass with lignite coal under high heating rates are still scarce. The utilization of 2nd and 3rd generation feedstocks has seldom been achieved in pulverized combustion conditions. Lab-scale tests for various blending ratios of agricultural biomass-lignite coal are necessary to supply fundamental data useful as a guide for tests in large scale furnaces. Moreover, the detailed investigation of agricultural biomass firing at a large scale and in 100% biomass conditions with emphasis on the combustion efficiency and pollutant formation still lacks in the literature.

The co-pyrolysis of agricultural biomass (i.e. using various biomass feedstocks) appears attractive but few studies have focused on the optimization of the pyrolysis conditions that maximise char yields and/or gas yields through synergies between different feedstocks. The extension of the organosolv fractionation presented in this

work to be used for other feedstocks with different lignocellulosic and inorganic composition such as woody biomass is also recommended. The study of tailored applications for agricultural biochar obtained from fast pyrolysis conditions has not yet been attained in the literature.

The co-gasification study presented herein provides some headlines on the interactions between biomass and coal during gasificaiton. Nevertheless, studies are still needed on (i) co-pyrolysis of biomass and coal under conditions relevant to entrained flow gasification followed by co-gasification of the same chars in a lab-scale entrained flow reactor; (ii) the usage of various blending ratios in the former studies; and (iii) pilot scale tests based on the data of the former two points. For the aforementioned gasification and co-gasification studies, data on solid yields, gas yields and composition, and tar yields and composition still lacks in the literature. Moreover, the study of gasification of 2^{nd} and 3^{rd} generation feedstocks is recommended, with focus on the solid and gas yields, tar formation, and syngas composition.

REFERENCES

[1] International Energy Agency (IEA). Key world energy statistics. 2017.

[2] Republic of Turkey Ministry of Energy and Natural Resources 2018. http://www.enerji.gov.tr/en-US/Pages/Electricity (accessed September 10, 2018).

[3] International Energy Agency (IEA). Energy Policies of IEA Countries: Turkey, 2016 Review. Paris, France: 2016.

[4] Rokni E, Ren X, Panahi A, Levendis YA. Emissions of SO2, NOx, CO2, and HCl from Co-firing of coals with raw and torrefied biomass fuels. Fuel 2018;211:363–74. doi:10.1016/j.fuel.2017.09.049.

[5] Hein KR., Bemtgen J. EU clean coal technology—co-combustion of coal and biomass. Fuel Process Technol 1998;54:159–69. doi:10.1016/S0378-3820(97)00067-2.

[6] Spliethoff H, Hein KRG. Effect of co-combustion of biomass on emissions in pulverized fuel furnaces. Fuel Process Technol 1998;54:189–205. doi:10.1016/S0378-3820(97)00069-6.

[7] Rokni E, Panahi A, Ren X, Levendis YA. Curtailing the generation of sulfur dioxide and nitrogen oxide emissions by blending and oxy-combustion of coals. Fuel 2016;181:772–84. doi:10.1016/j.fuel.2016.05.023.

[8] Rokni E, Panahi A, Ren X, Levendis YA. Reduction of Sulfur Dioxide Emissions by Burning Coal Blends. J Energy Resour Technol 2016;138:1–8. doi:10.1115/1.4032239.

[9] Sami M, Annamalai K, Wooldridge M. Co-firing of coal and biomass fuel blends. Prog Energy Combust Sci 2001;27:171–214. doi:10.1016/S0360-1285(00)00020-4.

[10] Baxter L. Biomass-coal co-combustion: Opportunity for affordable renewable energy. Fuel 2005;84:1295–302. doi:10.1016/j.fuel.2004.09.023.

[11] Al-Mansour F, Zuwala J. An evaluation of biomass co-firing in Europe. Biomass and Bioenergy 2010;34:620–9. doi:10.1016/j.biombioe.2010.01.004.

[12] UNFCCC. Conference of the Parties (COP). Paris Climate Change Conference-November 2015, COP 21. Adopt Paris Agreement Propos by Pres 2015;21932:32. doi:FCCC/CP/2015/L.9/Rev.1.

[13] Amanatidis G. European policies on climate and energy towards 2020, 2030 and 2050 2019:12.

[14] Republic of Turkey Ministry of Energy and Natural Resources 2018. http://www.enerji.gov.tr/en-US/Pages/Bio-Fuels (accessed September 10, 2018).

[15] Ferreiro AI, Giudicianni P, Grottola CM, Rabaçal M, Costa M, Ragucci R. Unresolved issues on the kinetic modeling of pyrolysis of woody and non-woody biomass fuels. Energy & Fuels 2017;31:4035–44. doi:10.1021/acs.energyfuels.6b03445.

[16] Roni MS, Chowdhury S, Mamun S, Marufuzzaman M, Lein W, Johnson S. Biomass co-firing technology with policies, challenges, and opportunities: A global review. Renew Sustain Energy Rev 2017;78:1089–101. doi:10.1016/j.rser.2017.05.023.

[17] Loo S Van, Koppejan J. The Handbook of Biomass Combustion & Co-firing. vol. 53. London: 2008. doi:10.1017/CBO9781107415324.004.

[18] Yu J, Paterson N, Blamey J, Millan M. Cellulose, xylan and lignin interactions during pyrolysis of lignocellulosic biomass. Fuel 2017;191:140–9. doi:10.1016/j.fuel.2016.11.057.

[19] Vassilev S V., Baxter D, Andersen LK, Vassileva CG. An overview of the chemical composition of biomass. Fuel 2010;89:913–33. doi:10.1016/j.fuel.2009.10.022.

[20] Schobert. H. Chemistry of fossil fuels and biofuels. Cambridge University

Press; 2013.

[21] Tana. J. L and J. Best available techniques (BAT) in solid biomass fuel processing, handling, storage and production of pellets from biomass. 2012.

[22] Krevelen. DW. Coal – typology, physics, chemistry, constitution. Elsevier Science; 1993.

[23] Bridgeman TG, Jones JM, Shield I, Williams PT. Torrefaction of reed canary grass, wheat straw and willow to enhance solid fuel qualities and combustion properties. Fuel 2008;87:844–56. doi:10.1016/j.fuel.2007.05.041.

[24] van der Stelt MJC, Gerhauser H, Kiel JHA, Ptasinski KJ. Biomass upgrading by torrefaction for the production of biofuels: A review. Biomass and Bioenergy 2011. doi:10.1016/j.biombioe.2011.06.023.

[25] Colin B, Dirion JL, Arlabosse P, Salvador S. Quantification of the torrefaction effects on the grindability and the hygroscopicity of wood chips. Fuel 2017;197:232–9. doi:10.1016/j.fuel.2017.02.028.

[26] Varol M, Atimtay a. T, Bay B, Olgun H. Investigation of co-combustion characteristics of low quality lignite coals and biomass with thermogravimetric analysis. Thermochim Acta 2010;510:195–201. doi:10.1016/j.tca.2010.07.014.

[27] Lu JJ, Chen WH. Investigation on the ignition and burnout temperatures of bamboo and sugarcane bagasse by thermogravimetric analysis. Appl Energy 2015;160:49–57. doi:10.1016/j.apenergy.2015.09.026.

[28] QH Nie, SZ Sun, ZQ Li, XJ Zhang, SH Wu YQ. Thermogravimetric analysis on the combustion characteristics of brown coal blends. J Combust Sci Technol 2001:72–6.

[29] Chen Y, Chao J, Yang H, Lv J, Zhang H, Liu Q. The Investigation of the Coal Ignition Temperature in Oxygen-Enriched Atmosphere by TGA. Clean. Combust. Sustain. World, Springer-Verlag Berlin Heidelberg and Tsinghua

University Press; 2013, p. 579–82. doi:10.1007/978-3-642-30445-3.

[30] Vamvuka D, El Chatib N, Sfakiotakis S. Measurements of ignition point and combustion characteristics of biomass fuels and their blends with lignite. Proc. Eur. Combust. Meet., 2011.

[31] Yuzbasi NS, Selçuk N. Air and oxy-fuel combustion characteristics of biomass/lignite blends in TGA-FTIR. Fuel Process Technol 2011;92:1101–8. doi:10.1016/j.fuproc.2011.01.005.

[32] Vamvuka D, Sfakiotakis S. Combustion behaviour of biomass fuels and their blends with lignite. Thermochim Acta 2011;526:192–9. doi:10.1016/j.tca.2011.09.021.

[33] Moon C, Sung Y, Ahn S, Kim T, Choi G, Kim D. Thermochemical and combustion behaviors of coals of different ranks and their blends for pulverized-coal combustion. Appl Therm Eng 2013;54:111–9. doi:10.1016/j.applthermaleng.2013.01.009.

[34] Idris SS, Rahman NA, Ismail K. Combustion characteristics of Malaysian oil palm biomass, sub-bituminous coal and their respective blends via thermogravimetric analysis (TGA). Bioresour Technol 2012;123:581–91. doi:10.1016/j.biortech.2012.07.065.

[35] Atibeh EA, Yozgatligil A. Combustion Characteristics of Biomass Ash and Lignite Blend Under Oxy-Fuel Conditions. ASME 2013 Int. Mech. Eng. Congr. Expo., 2013, p. V06AT07A089-V06AT07A089.

[36] García Torrent J, Ramírez-Gómez Á, Fernandez-Anez N, Medic Pejic L, Tascón A. Influence of the composition of solid biomass in the flammability and susceptibility to spontaneous combustion. Fuel 2016;184:503–11. doi:10.1016/j.fuel.2016.07.045.

[37] Garcia Torrent J, Fernandez Anez N, Medic Pejic L, Montenegro Mateos L. Assessment of self-ignition risks of solid biofuels by thermal analysis. Fuel 2015;143:484–91. doi:10.1016/j.fuel.2014.11.074.

[38] Ramírez Á, García-Torrent J, Tascón A. Experimental determination of self-heating and self-ignition risks associated with the dusts of agricultural materials commonly stored in silos. J Hazard Mater 2010;175:920–7. doi:10.1016/j.jhazmat.2009.10.096.

[39] Jones JM, Saddawi A, Dooley B, Mitchell EJS, Werner J, Waldron DJ, et al. Low temperature ignition of biomass. Fuel Process Technol 2015;134:372–7. doi:10.1016/j.fuproc.2015.02.019.

[40] Toptas A, Yildirim Y, Duman G, Yanik J. Bioresource Technology Combustion behavior of different kinds of torrefied biomass and their blends with lignite. Bioresour Technol 2015;177:328–36. doi:10.1016/j.biortech.2014.11.072.

[41] Chen Y, Mori S, Pan WP. Studying the mechanisms of ignition of coal particles by tg-dta. Thermochim Acta 1996;275:149–58. doi:10.1016/0040-6031(95)02727-0.

[42] García Torrent, J. ; Medic Pejic, L. Querol Aragón E. A self-combustion characterisation index based in thermogravimetric and differential scanning calorimetry Description of the techniques, n.d., p. 1–10.

[43] Arag QGTCR. Spontaneous combustion testing n.d.:1–8.

[44] Levendis YA, Joshi K, Khatami R, Sarofim AF. Combustion behavior in air of single particles from three different coal ranks and from sugarcane bagasse. Combust Flame 2011;158:452–65. doi:10.1016/j.combustflame.2010.09.007.

[45] Khatami R, Stivers C, Levendis Y a. Ignition characteristics of single coal particles from three different ranks in O2/N2 and O2/CO2 atmospheres. Combust Flame 2012;159:3554–68. doi:10.1016/j.combustflame.2012.06.019.

[46] Simões G, Magalhães D, Rabaçal M, Costa M. Effect of gas temperature and oxygen concentration on single particle ignition behavior of biomass fuels.

Proc Combust Inst 2016;36:2235–42. doi:10.1016/j.proci.2016.06.102.

[47] Zou C, Cai L, Wu D, Liu Y, Liu S, Zheng C. Ignition behaviors of pulverized coal particles in O2/N2 and O2/H2O mixtures in a drop tube furnace using flame monitoring techniques. Proc Combust Inst 2015;35:3629–36. doi:10.1016/j.proci.2014.06.067.

[48] Riaza J, Khatami R, Levendis YA, Álvarez L, Gil M V., Pevida C, et al. Combustion of single biomass particles in air and in oxy-fuel conditions. Biomass and Bioenergy 2014;64:162–74. doi:10.1016/j.biombioe.2014.03.018.

[49] Shaddix CR, Molina A. Particle imaging of ignition and devolatilization of pulverized coal during oxy-fuel combustion. Proc Combust Inst 2009;32:2091–8. doi:10.1016/j.proci.2008.06.157.

[50] Yuan Y, Li S, Zhao F, Yao Q, Long MB. Characterization on hetero-homogeneous ignition of pulverized coal particle streams using CH∗ chemiluminescence and 3 color pyrometry. Fuel 2016;184:1000–6. doi:http://dx.doi.org/10.1016/j.fuel.2015.11.032.

[51] Yuan Y, Li S, Li G, Wu N, Yao Q. The transition of heterogeneous–homogeneous ignitions of dispersed coal particle streams. Combust Flame 2014;161:2458–68. doi:10.1016/j.combustflame.2014.03.008.

[52] Molina A, Shaddix CR. Ignition and devolatilization of pulverized bituminous coal particles during oxygen/carbon dioxide coal combustion. Proc Combust Inst 2007;31:1905–12. doi:10.1016/j.proci.2006.08.102.

[53] Liu Y, Geier M, Molina A, Shaddix CR. Pulverized coal stream ignition delay under conventional and oxy-fuel combustion conditions. Int J Greenh Gas Control 2011;5:S36–46. doi:10.1016/j.ijggc.2011.05.028.

[54] Howard JB, Essenhigh RH. Mechanism of solid-partical combustion with simultaneous gas-phase volatiles combustion. Proc Combust Inst 1967;11:399–408.

[55] Howard JB, Essenhigh RH. The mechanism of ignition of pulverized coal. Combust Flame 1965;9:337–9.

[56] Khatami R, Levendis YA. An overview of coal rank influence on ignition and combustion phenomena at the particle level. Combust Flame 2016;164:22–34. doi:http://dx.doi.org/10.1016/j.combustflame.2015.10.031.

[57] Riaza J, Khatami R, Levendis YA, Álvarez L, Gil M V., Pevida C, et al. Single particle ignition and combustion of anthracite, semi-anthracite and bituminous coals in air and simulated oxy-fuel conditions. Combust Flame 2014;161:1096–108. doi:10.1016/j.combustflame.2013.10.004.

[58] Khatami R, Stivers C, Joshi K, Levendis YA, Sarofim AF. Combustion behavior of single particles from three different coal ranks and from sugar cane bagasse in O 2/N 2 and O 2/CO 2 atmospheres. Combust Flame 2012;159:1253–71. doi:10.1016/j.combustflame.2011.09.009.

[59] Ozer B. A Study on Coal Combustion: Experiments and Modelling. Middle East Technical University, 2019. doi:10.1109/MTAS.2004.1371634.

[60] Rabaçal M. Large Eddy Simulation of Coal and Biomass Combustion in Large-Scale Laboratory Furnaces INSTITUTO SUPERIOR TÉCNICO Large Eddy Simulation of Coal and Biomass Combustion in Large-Scale Laboratory Furnaces. INSTITUTO SUPERIOR TÉCNICO, 2016.

[61] Atibeh EA, Yozgatligil A. IMECE2013-65182 COMBUSTION CHARACTERISTICS OF BIOMASS ASH AND LIGNITE BLEND 2015:1–10.

[62] Pintana P, Tippayawong N. Nonisothermal thermogravimetric analysis of Thai lignite with high CaO content. ScientificWorldJournal 2013;2013:216975. doi:10.1155/2013/216975.

[63] Gil M V., Casal D, Pevida C, Pis JJ, Rubiera F. Thermal behaviour and kinetics of coal/biomass blends during co-combustion. Bioresour Technol 2010;101:5601–8. doi:10.1016/j.biortech.2010.02.008.

[64] Yousefzad Farrokhi F, Kazanç F. Combustion Behavior and Kinetics of Turkish Lignite Blended with Biomass/Magnesite Dust. J Energy Eng 2018;144:1–13. doi:10.1061/(ASCE)EY.1943-7897.0000579.

[65] Kök M V. Temperature-controlled combustion and kinetics of different rank coal samples. J Therm Anal Calorim 2005;79:175–80. doi:10.1007/s10973-004-0581-6.

[66] Yuzbasi NS, Selçuk N. Air and oxy-fuel combustion behaviour of petcoke / lignite blends. Fuel 2012;92:137–44. doi:10.1016/j.fuel.2011.08.026.

[67] Vamvuka D, Tsamourgeli V, Galetakis M. Study on Catalytic Combustion of Biomass Mixtures with Poor Coals. Combust Sci Technol 2014;186:68–82. doi:10.1080/00102202.2013.846331.

[68] Wang G, Silva RB, Azevedo JLT, Martins-Dias S, Costa M. Evaluation of the combustion behaviour and ash characteristics of biomass waste derived fuels, pine and coal in a drop tube furnace. Fuel 2014;117:809–24. doi:10.1016/j.fuel.2013.09.080.

[69] Costa FF, Wang G, Costa M. Combustion kinetics and particle fragmentation of raw and torrified pine shells and olive stones in a drop tube furnace. Proc Combust Inst 2015;35:3591–9. doi:10.1016/j.proci.2014.06.024.

[70] Branco V, Costa M. Effect of particle size on the burnout and emissions of particulate matter from the combustion of pulverized agricultural residues in a drop tube furnace. Energy Convers Manag 2017;149:774–80. doi:10.1016/j.enconman.2017.03.012.

[71] Pereira S, Martins PCR, Costa M. Kinetics of Poplar Short Rotation Coppice Obtained from Thermogravimetric and Drop Tube Furnace Experiments. Energy and Fuels 2016;30:6525–36. doi:10.1021/acs.energyfuels.6b01313.

[72] Ndibe C, Grathwohl S, Paneru M, Maier J, Scheffknecht G. Emissions reduction and deposits characteristics during cofiring of high shares of

torrefied biomass in a 500 kW pulverized coal furnace. Fuel 2015;156:177–89. doi:10.1016/j.fuel.2015.04.017.

[73] Wang X, Hu Z, Deng S, Xiong Y, Tan H. Effect of biomass/coal co-firing and air staging on NOx emission and combustion efficiency in a drop tube furnace. Energy Procedia 2014;61:2331–4. doi:10.1016/j.egypro.2014.11.1196.

[74] Khatami R, Levendis YA. An overview of coal rank influence on ignition and combustion phenomena at the particle level. Combust Flame 2016;164:22–34. doi:10.1016/j.combustflame.2015.10.031.

[75] Vorobiev N, Becker A, Kruggel-Emden H, Panahi A, Levendis YA, Schiemann M. Particle shape and Stefan flow effects on the burning rate of torrefied biomass. Fuel 2017;210:107–20. doi:10.1016/j.fuel.2017.08.037.

[76] Panahi A, Levendis YA, Vorobiev N, Schiemann M. Direct observations on the combustion characteristics of Miscanthus and Beechwood biomass including fusion and spherodization. Fuel Process Technol 2017;166. doi:10.1016/j.fuproc.2017.05.029.

[77] Panahi A, Vorobiev N, Schiemann M, Tarakcioglu M, Delichatsios M, Levendis YA. Combustion details of raw and torrefied biomass fuel particles with individually-observed size, shape and mass. Combust Flame 2019;207:327–41. doi:10.1016/j.combustflame.2019.06.009.

[78] Zou C, Zhang L, Cao S, Zheng C. A study of combustion characteristics of pulverized coal in O2/H2O atmosphere. Fuel 2014;115:312–20. doi:10.1016/j.fuel.2013.07.025.

[79] Rabaçal M, Pereira S, Costa M. Review on Pulverized Combustion of Non-Woody Residues. Energy & Fuels 2018;32:4069–95. doi:10.1021/acs.energyfuels.7b03258.

[80] Panahi A, Levendis YA, Vorobiev N, Schiemann M. Direct observations on the combustion characteristics of Miscanthus and Beechwood biomass

including fusion and spherodization. Fuel Process Technol 2017;166:41–9. doi:10.1016/j.fuproc.2017.05.029.

[81] Khatami R, Stivers C, Levendis YA. Ignition characteristics of single coal particles from three different ranks in O2/N2 and O2/CO2 atmospheres. Combust Flame 2012;159:3554–68. doi:10.1016/j.combustflame.2012.06.019.

[82] Panahi A, Tarakcioglu MB, Schiemann M, Delichatsios M, Levendis YA. On the Particle Sizing of Torrefied Biomass for Co-firing with Pulverized Coal. Combust Flame 2018;194:72–84. doi:10.1016/j.combustflame.2018.04.014.

[83] Mock C, Lee H, Choi S, Manovic V. Combustion Behavior of Relatively Large Pulverized Biomass Particles at Rapid Heating Rates. Energy and Fuels 2016;30:10809–22. doi:10.1021/acs.energyfuels.6b01457.

[84] Mason PE, Darvell LI, Jones JM, Williams A. Observations on the release of gas-phase potassium during the combustion of single particles of biomass. Fuel 2016;182:110–7. doi:10.1016/j.fuel.2016.05.077.

[85] Mason PE, Darvell LI, Jones JM, Pourkashanian M, Williams a. Single particle flame-combustion studies on solid biomass fuels. Fuel 2014;151:21–30. doi:10.1016/j.fuel.2014.11.088.

[86] Shan L, Kong M, Bennet TD, Sarroza AC, Eastwick C, Sun D, et al. Studies on combustion behaviours of single biomass particles using a visualization method. Biomass and Bioenergy 2018;109:54–60. doi:10.1016/j.biombioe.2017.12.008.

[87] Weng W, Costa M, Aldén M, Li Z. Single particle ignition and combustion of pulverized pine wood, wheat straw, rice husk and grape pomace. Proc Combust Inst 2018;000:1–9. doi:10.1016/j.proci.2018.05.095.

[88] Kops RB, Pereira FM, Rabacal M, Costa M. Effect of steam on the single particle ignition of solid fuels in a drop tube furnace under air and simulated

oxy-fuel conditions. Proc Combust Inst 2018;000:1–9. doi:10.1016/j.proci.2018.05.091.

[89] Carvalho A, Rabaçal M, Costa M, Alzueta MU, Abián M. Effects of potassium and calcium on the early stages of combustion of single biomass particles. Fuel 2017;209:787–94. doi:10.1016/j.fuel.2017.08.045.

[90] Rabaçal M, Kops RB, Pereira FM, Costa M. Direct observations of single particle fragmentation in the early stages of combustion under dry and wet conventional and oxy-fuel conditions. Proc Combust Inst 2018;000:1–8. doi:10.1016/j.proci.2018.07.001.

[91] Magalhães D, Kazanç F, Ferreira A, Rabaçal M, Costa M. Ignition behavior of Turkish biomass and lignite fuels at low and high heating rates. Fuel 2017;207:154–64.

[92] Jones JM, Darvell LI, Bridgeman TG, Pourkashanian M, Williams A. An investigation of the thermal and catalytic behaviour of potassium in biomass combustion. Proc Combust Inst 2007;31 II:1955–63. doi:10.1016/j.proci.2006.07.093.

[93] Zhang Z, Zhu M, Zhang Y, Setyawan HY, Li J, Zhang D. Ignition and combustion characteristics of single particles of Zhundong lignite: Effect of water and acid washing. Proc Combust Inst 2017;36:2139–46. doi:10.1016/J.PROCI.2016.07.072.

[94] Panahi A, Levendis YA, Vorobiev N. Combustion behavior of herbaceous and woody biomass. 41st Int. Tech. Conf. Clean Coal Fuel Syst., 2016. doi:10.13140/RG.2.1.4414.4244.

[95] Thomas H. Fletcher, Kerstein AR, Pugmire RJ, Solum M, Grant DM. A Chemical Percolation Model for Devolatilization: Summary 2015;1:1–66. doi:10.1017/CBO9781107415324.004.

[96] Ranzi E, Cuoci A, Faravelli T, Frassoldati A, Migliavacca G, Pierucci S, et al. Chemical kinetics of biomass pyrolysis. Energy and Fuels 2008;22:4292–

300. doi:10.1021/ef800551t.

[97] Laurendeau NM. Heterogeneous kinetics of coal char gasification and combustion. Prog Energy Combust Sci 1978;4:221–70. doi:10.1016/0360-1285(78)90008-4.

[98] Hurt R, Sun JK, Lunden M. A kinetic model of carbon burnout in pulverized coal combustion. Combust Flame 1998;113:181–97. doi:10.1016/S0010-2180(97)00240-X.

[99] Coats AW RJ. Kinetic parameters from thermogravimetric data. J Polym Sci, Part B Polym Phys 1964;3:917–20.

[100] Freeman ES, Carroll B, 62 V, Free ES, And M. The Application of Thermoanalytical Techniques To the Kinetics O F the Decomposition of Calcium Oxalate Monohydrate 1967;62:394–7. doi:10.1021/j150562a003.

[101] Álvarez A, Pizarro C, García R, Bueno JL, Lavín AG. Determination of kinetic parameters for biomass combustion 2016;216:36–43. doi:10.1016/j.biortech.2016.05.039.

[102] Islam A, Auta M, Kabir G, Hameed BH. Bioresource Technology A thermogravimetric analysis of the combustion kinetics of karanja (Pongamia pinnata) fruit hulls char. Bioresour Technol 2016;200:335–41. doi:10.1016/j.biortech.2015.09.057.

[103] Gai C, Liu Z, Han G, Peng N, Fan A. Combustion behavior and kinetics of low-lipid microalgae via thermogravimetric analysis. Bioresour Technol 2015;181:148–54. doi:10.1016/j.biortech.2015.01.045.

[104] Das T, Baruah BP, Saikia BK. Thermal behaviour of low-rank Indian coal fines agglomerated with an organic binder. J Therm Anal Calorim 2016. doi:10.1007/s10973-016-5564-x.

[105] Jayaraman K, Gökalp I. Pyrolysis, combustion and gasification characteristics of miscanthus and sewage sludge. Energy Convers Manag 2015;89:83–91. doi:10.1016/j.enconman.2014.09.058.

[106] Duvvuri MS, Muhlenkamp SP, Iqbal KZ WJ. Pyrolysis of natural fuels. J Fire Flammabl 1975;6:468–77.

[107] Ebrahimi-Kahrizsangi R, Abbasi MH. Evaluation of reliability of Coats-Redfern method for kinetic analysis of non-isothermal TGA. Trans Oahmetf Nonferrous Met Soc China (English Ed 2008;18:217–21. doi:10.1016/S1003-6326(08)60039-4.

[108] IARC. IARC Scientific Publication No. 161: air pollution and cancer. n.d. http://www.iarc.fr/en/publications/books/sp161/index.php (accessed February 26, 2018).

[109] Xu M, Yu D, Yao H, Liu X, Qiao Y. Coal combustion-generated aerosols: Formation and properties. Proc Combust Inst 2011;33:1681–97. doi:10.1016/j.proci.2010.09.014.

[110] Linak WP, Miller CA, Seames WS, Wendt JOL, Ishinomori T, Endo Y, et al. On trimodal particle size distributions in fly ash from pulverized-coal combustion. Proc Combust Inst 2002;29:441–7. doi:10.1016/S1540-7489(02)80058-X.

[111] Wang W, Wen C, Li C, Wang M, Li X, Zhou Y, et al. Emission reduction of particulate matter from the combustion of biochar via thermal pre-treatment of torrefaction, slow pyrolysis or hydrothermal carbonisation and its co-combustion with pulverized coal. Fuel 2019;240:278–88. doi:10.1016/j.fuel.2018.11.117.

[112] Zhang L, Ninomiya Y. Emission of suspended PM10from laboratory-scale coal combustion and its correlation with coal mineral properties. Fuel 2006;85:194–203. doi:10.1016/j.fuel.2005.03.034.

[113] Wen C, Gao X, Yu Y, Wu J, Xu M, Wu H. Emission of inorganic PM10from included mineral matter during the combustion of pulverized coals of various ranks. Fuel 2015;140:526–30. doi:10.1016/j.fuel.2014.09.114.

[114] Kazanc F, Levendis YA, Maffei T. Chemical Composition of Submicrometer Particulate Matter (PM1) Emitted from Combustion of Coals of Various Ranks in O2/N2 and O2/ CO2 Environments. Energy & Fuels 2013;27:4984–98.

[115] Fix G, Seames W, Mann M, Benson S, Miller D. The effect of combustion temperature on coal ash fine-fragmentation mode formation mechanisms. Fuel 2013;113:140–7. doi:10.1016/j.fuel.2013.05.096.

[116] Zhang L, Ninomiya Y, Yamashita T. Formation of submicron particulate matter (PM1) during coal combustion and influence of reaction temperature. Fuel 2006;85:1446–57. doi:10.1016/j.fuel.2006.01.009.

[117] Zhuo JK, Li SQ, Yao Q, Song Q. The progressive formation of submicron particulate matter in a quasi one-dimensional pulverized coal combustor. Proc Combust Inst 2009;32 II:2059–66. doi:10.1016/j.proci.2008.06.108.

[118] Zhan Z, Fry A, Zhang Y, Wendt JOL. Ash aerosol formation from oxy-coal combustion and its relation to ash deposit chemistry. Proc Combust Inst 2015;35:2373–80. doi:10.1016/j.proci.2014.07.001.

[119] Li G, Li S, Dong M, Yao Q, Guo CY, Axelbaum RL. Comparison of particulate formation and ash deposition under oxy-fuel and conventional pulverized coal combustions. Fuel 2013;106:544–51. doi:10.1016/j.fuel.2012.10.035.

[120] Fryda L, Sobrino C, Glazer M, Bertrand C, Cieplik M. Study of ash deposition during coal combustion under oxyfuel conditions. Fuel 2012;92:308–17. doi:10.1016/j.fuel.2011.08.013.

[121] Han J, Yu D, Yu X, Liu F, Wu J, Zeng X, et al. Effect of the torrefaction on the emission of PM 10 from combustion of rice husk and its blends with a lignite. Proc Combust Inst 2019;37:2733–40. doi:10.1016/j.proci.2018.07.011.

[122] Chao CYH, Kwong PCW, Wang JH, Cheung CW, Kendall G. Co-firing coal

with rice husk and bamboo and the impact on particulate matters and associated polycyclic aromatic hydrocarbon emissions. Bioresour Technol 2008;99:83–93. doi:10.1016/j.biortech.2006.11.051.

[123] Li C, Wen C, Wang W, Wang W, Chen H, Yu D, et al. Reduction effect of co-firing of torrefied straw and bituminous coal on PM1emission under both air and oxyfuel atmosphere. Proc Combust Inst 2018;000:1–9. doi:10.1016/j.proci.2018.07.012.

[124] Gao X, Rahim MU, Chen X, Wu H. Inorganic PM10 emission from the combustion of individual mallee components and whole-tree biomass. Proc Combust Inst 2017;36:3313–9. doi:10.1016/J.PROCI.2016.08.072.

[125] Shao J, Cheng W, Zhu Y, Yang W, Fan J, Liu H, et al. Effects of Combined Torrefaction and Pelletization on Particulate Matter Emission From Biomass Pellet Combustion. Energy and Fuels 2019;33:8777–85. doi:10.1021/acs.energyfuels.9b01920.

[126] Yang W, Zhu Y, Cheng W, Sang H, Yang H, Chen H. Characteristics of Particulate Matter Emitted from Agricultural Biomass Combustion. Energy and Fuels 2017;31:7493–501. doi:10.1021/acs.energyfuels.7b00229.

[127] Yani S, Gao X, Wu H. Emission of inorganic PM10 from the combustion of torrefied biomass under pulverized-fuel conditions. Energy and Fuels 2015;29:800–7. doi:10.1021/ef5023237.

[128] Wang Q, Yao H, Yu D, Dai L, Xu M. Emission behavior of particulate matter during co-combustion of coal and biomass in a drop tube furnace. Energy and Fuels 2007;21:513–6. doi:10.1021/ef060410u.

[129] Wang X, Adeosun A, Hu Z, Xiao Z, Khatri D, Li T, et al. Effect of feedstock water leaching on ignition and PM1.0 emission during biomass combustion in a flat-flame burner reactor. Proc Combust Inst 2019;37:2705–13. doi:10.1016/j.proci.2018.05.096.

[130] Al-Naiema I, Estillore AD, Mudunkotuwa IA, Grassian VH, Stone EA.

Impacts of co-firing biomass on emissions of particulate matter to the atmosphere. Fuel 2015;162:111–20. doi:10.1016/J.FUEL.2015.08.054.

[131] Wang X, Hu Z, Wang G, Luo X, Ruan R, Jin Q, et al. Influence of coal co-firing on the particulate matter formation during pulverized biomass combustion. J Energy Inst 2019;92:450–8. doi:10.1016/j.joei.2018.05.003.

[132] Zhang L, Ninomiya Y, Wang Q, Yamashita T. Influence of woody biomass (cedar chip) addition on the emissions of PM10 from pulverised coal combustion. Fuel 2011;90:77–86. doi:10.1016/j.fuel.2010.08.017.

[133] Collard FX, Blin J. A review on pyrolysis of biomass constituents: Mechanisms and composition of the products obtained from the conversion of cellulose, hemicelluloses and lignin. Renew Sustain Energy Rev 2014;38:594–608. doi:10.1016/j.rser.2014.06.013.

[134] Seo DK, Park SS, Kim YT, Hwang J, Yu TU. Study of coal pyrolysis by thermo-gravimetric analysis (TGA) and concentration measurements of the evolved species. J Anal Appl Pyrolysis 2011;92:209–16. doi:10.1016/j.jaap.2011.05.012.

[135] Jayaraman K, Gokalp I, Bostyn S. High ash coal pyrolysis at different heating rates to analyze its char structure, kinetics and evolved species. J Anal Appl Pyrolysis 2015;113:426–33. doi:10.1016/j.jaap.2015.03.007.

[136] Trubetskaya A, Jensen PA, Jensen AD, Garcia Llamas AD, Umeki K, Glarborg P. Effect of fast pyrolysis conditions on biomass solid residues at high temperatures. Fuel Process Technol 2016;143:118–29. doi:10.1016/j.fuproc.2015.11.002.

[137] Trubetskaya A. Fast pyrolysis of biomass at high temperatures. Technical University of Denmark, 2016.

[138] Trubetskaya A, Jensen PA, Jensen AD, Steibel M, Spliethoff H, Glarborg P, et al. Comparison of high temperature chars of wheat straw and rice husk with respect to chemistry, morphology and reactivity. Biomass and

Bioenergy 2016;86:76–87. doi:10.1016/j.biombioe.2016.01.017.

[139] Trubetskaya A, Jensen PA, Jensen AD, Steibel M, Spliethoff H, Glarborg P. Influence of fast pyrolysis conditions on yield and structural transformation of biomass chars. Fuel Process Technol 2015;140:205–14. doi:10.1016/j.fuproc.2015.08.034.

[140] Le Manquais K, Snape CE, McRobbie I, Barker J. Evaluating the combustion reactivity of drop tube furnace and thermogravimetric analysis coal chars with a selection of metal additives. Energy and Fuels 2011;25:981–9. doi:10.1021/ef101577z.

[141] Farrow TS, Sun C, Snape CE. Impact of CO2 on biomass pyrolysis, nitrogen partitioning, and char combustion in a drop tube furnace. J Anal Appl Pyrolysis 2015;113:323–31. doi:10.1016/j.jaap.2015.02.013.

[142] Le Manquais K, Snape C, McRobbie I, Barker J, Pellegrin V. Comparison of the combustion reactivity of TGA and drop tube furnace chars from a bituminous coal. Energy Fuels 2009;23:4269–77. doi:10.1021/ef900205d.

[143] Kan T, Strezov V, Evans TJ. Lignocellulosic biomass pyrolysis: A review of product properties and effects of pyrolysis parameters. Renew Sustain Energy Rev 2016;57:126–1140. doi:10.1016/j.rser.2015.12.185.

[144] Trubetskaya A, Jensen PA, Jensen AD, Garcia Llamas AD, Umeki K, Glarborg P. Effect of fast pyrolysis conditions on biomass solid residues at high temperatures. Fuel Process Technol 2016;143:118–29. doi:10.1016/j.fuproc.2015.11.002.

[145] McNamee P, Darvell LI, Jones JM, Williams A. The combustion characteristics of high-heating-rate chars from untreated and torrefied biomass fuels. Biomass and Bioenergy 2015;82:63–72. doi:10.1016/j.biombioe.2015.05.016.

[146] Gil M V., Riaza J, Álvarez L, Pevida C, Pis JJ, Rubiera F. Oxy-fuel combustion kinetics and morphology of coal chars obtained in N2 and CO2

atmospheres in an entrained flow reactor. Appl Energy 2012;91:67–74. doi:10.1016/j.apenergy.2011.09.017.

[147] Gil M V., Riaza J, Álvarez L, Pevida C, Rubiera F. Biomass devolatilization at high temperature under N2 and CO2: Char morphology and reactivity. Energy 2015;91:655–62. doi:10.1016/j.energy.2015.08.074.

[148] Krerkkaiwan S, Fushimi C, Tsutsumi A, Kuchonthara P. Synergetic effect during co-pyrolysis/gasification of biomass and sub-bituminous coal. Fuel Process Technol 2013;115:11–8. doi:10.1016/j.fuproc.2013.03.044.

[149] Borrego AG, Garavaglia L, Kalkreuth WD. Characteristics of high heating rate biomass chars prepared under N2 and CO2 atmospheres. Int J Coal Geol 2009;77:409–15. doi:10.1016/j.coal.2008.06.004.

[150] Zhang Y, Zhai M, Wang X, Sun J, Dong P, Liu P, et al. Preparation and characteristics of biomass char. BioResources 2015;10:3017–26. doi:10.15376/biores.10.2.3017-3026.

[151] Zanzi R, Sjöström K, Björnbom E. Rapid pyrolysis of agricultural residues at high temperature. Biomass Bioenergy 2002;23:357–66. doi:10.1016/S0961-9534(02)00061-2.

[152] Farrow TS, Sun C, Snape CE. Impact of biomass char on coal char burn-out under air and oxy-fuel conditions. Fuel 2013;114:128–34. doi:10.1016/j.fuel.2012.07.073.

[153] Cetin E, Gupta R, Moghtaderi B. Effect of pyrolysis pressure and heating rate on radiata pine char structure and apparent gasification reactivity. Fuel 2005;84:1328–34. doi:10.1016/j.fuel.2004.07.016.

[154] Cetin E, Moghtaderi B, Gupta R, Wall TF. Influence of pyrolysis conditions on the structure and gasification reactivity of biomass chars. Fuel 2004;83:2139–50. doi:10.1016/j.fuel.2004.05.008.

[155] Zhai M, Xu Y, Guo L, Zhang Y, Dong P, Huang Y. Characteristics of pore structure of rice husk char during high-temperature steam gasification. Fuel

2016;185:622–9. doi:10.1016/j.fuel.2016.08.028.

[156] Çakal GO, Yücel H, Gürüz AG. Physical and chemical properties of selected Turkish lignites and their pyrolysis and gasification rates determined by thermogravimetric analysis. J Anal Appl Pyrolysis 2007;80:262–8. doi:10.1016/j.jaap.2007.03.005.

[157] Burhenne L, Damiani M, Aicher T. Effect of feedstock water content and pyrolysis temperature on the structure and reactivity of spruce wood char produced in fixed bed pyrolysis. Fuel 2013;107:836–47. doi:10.1016/j.fuel.2013.01.033.

[158] Tremel A, Spliethoff H. Gasification kinetics during entrained flow gasification - Part I; Devolatilisation and char deactivation. Fuel 2013;103:663–71. doi:10.1016/j.fuel.2012.09.014.

[159] Kastanaki E, Vamvuka D. A comparative reactivity and kinetic study on the combustion of coal-biomass char blends. Fuel 2006;85:1186–93. doi:10.1016/j.fuel.2005.11.004.

[160] Misra MK, Ragland KW, Baker AJ. Wood ash composition as a function of furnace temperature. Biomass and Bioenergy 1993;4:103–16. doi:10.1016/0961-9534(93)90032-Y.

[161] Jin-Mo H, Daugherty KE. Catalytic effect of alkali carbonates on the calcination of calcium carbonate. Thermochim Acta 1987;115:57–62. doi:10.1016/0040-6031(87)88351-X.

[162] Masnadi MS, Grace JR, Bi XT, Lim CJ, Ellis N. From fossil fuels towards renewables: Inhibitory and catalytic effects on carbon thermochemical conversion during co-gasification of biomass with fossil fuels. Appl Energy 2015;140:196–209. doi:10.1016/j.apenergy.2014.12.006.

[163] Ellis N, Masnadi MS, Roberts DG, Kochanek M a., Ilyushechkin AY. Mineral matter interactions during co-pyrolysis of coal and biomass and their impact on intrinsic char co-gasification reactivity. Chem Eng J

2015;279:402–8. doi:10.1016/j.cej.2015.05.057.

[164] Shen D, Xiao R, Gu S, Zhang H. The Overview of Thermal Decomposition of Cellulose in Lignocellulosic Biomass. Cellul - Biomass Convers 2013:193–226. doi:10.5772/51883.

[165] Couhert C, Commandre JM, Salvador S. Is it possible to predict gas yields of any biomass after rapid pyrolysis at high temperature from its composition in cellulose, hemicellulose and lignin? Fuel 2009;88:408–17. doi:10.1016/j.fuel.2008.09.019.

[166] Trubetskaya A, Timko MT, Umeki K. Prediction of fast pyrolysis products yields using lignocellulosic compounds and ash contents. Appl Energy 2020;257:113897. doi:10.1016/j.apenergy.2019.113897.

[167] Trubetskaya A, Brown A, Tompsett GA, Timko MT, Kling J, Broström M, et al. Characterization and reactivity of soot from fast pyrolysis of lignocellulosic compounds and monolignols. Appl Energy 2018;212:1489–500. doi:10.1016/j.apenergy.2017.12.068.

[168] Zhang J, Choi YS, Yoo CG, Kim TH, Brown RC, Shanks BH. Cellulose-hemicellulose and cellulose-lignin interactions during fast pyrolysis. ACS Sustain Chem Eng 2015;3:293–301.

[169] Hilbers TJ, Wang Z, Pecha B, Westerhof RJM, Kersten SRA, Pelaez-Samaniego MR, et al. Cellulose-Lignin interactions during slow and fast pyrolysis. J Anal Appl Pyrolysis 2015;114:197–207.

[170] Wang S, Guo X, Wang K, Luo Z. Influence of the interaction of components on the pyrolysis behavior of biomass. J Anal Appl Pyrolysis 2011;91:183–9.

[171] Raveendran K, Ganesh A, Khilar KC. Pyrolysis characteristics of biomass and biomass components. Fuel 1996;75:987–98. doi:10.1016/0016-2361(96)00030-0.

[172] Yang H, Yan R, Chen H, Zheng C, Lee DH, Uni V, et al. In-Depth Investigation of Biomass Pyrolysis Based on Three Major Components :

Hemicellulose , Cellulose and Lignin 2006:388–93. doi:10.1021/ie1025453.

[173] Pang CH, Gaddipatti S, Tucker G, Lester E, Wu T. Relationship between thermal behaviour of lignocellulosic components and properties of biomass. Bioresour Technol 2014;172:312–20.

[174] Fisher T, Hajaligol M, Waymack B, Kellogg D. Pyrolysis behavior and kinetics of biomass derived materials. J Anal Appl Pyrolysis 2002;62:331–49.

[175] Werner K, Pommer L, Broström M. Thermal decomposition of hemicelluloses. J Anal Appl Pyrolysis 2014;110:130–7. doi:10.1016/j.jaap.2014.08.013.

[176] Wu S, Shen D, Hu J, Zhang H, Xiao R. Cellulose-hemicellulose interactions during fast pyrolysis with different temperatures and mixing methods. Biomass and Bioenergy 2016;95:55–63.

[177] Dorez G, Ferry L, Sonnier R, Taguet A, Lopez-Cuesta JM. Effect of cellulose, hemicellulose and lignin contents on pyrolysis and combustion of natural fibers. J Anal Appl Pyrolysis 2014;107:323–31.

[178] Matsakas L, Nitsos C, Raghavendran V, Yakimenko O, Persson G, Olsson E, et al. A novel hybrid organosolv: Steam explosion method for the efficient fractionation and pretreatment of birch biomass. Biotechnol Biofuels 2018;11:1–14. doi:10.1186/s13068-018-1163-3.

[179] Matsakas L, Raghavendran V, Yakimenko O, Persson G, Olsson E, Rova U, et al. Lignin-first biomass fractionation using a hybrid organosolv – Steam explosion pretreatment technology improves the saccharification and fermentability of spruce biomass. Bioresour Technol 2019;273:521–8. doi:10.1016/j.biortech.2018.11.055.

[180] Kalogiannis KG, Matsakas L, Lappas AA, Rova U, Christakopoulos P. Aromatics from Beechwood Organosolv Lignin through Thermal and Catalytic Pyrolysis. Energies 2019;12:1606. doi:10.3390/en12091606.

[181] Wyman CE, Dale BE, Elander RT, Holtzapple M, Ladisch MR, Lee YY. Coordinated development of leading biomass pretreatment technologies. Bioresour Technol 2005;96:1959–66. doi:10.1016/j.biortech.2005.01.010.

[182] Constant S, Wienk HLJ, Frissen AE, Peinder P De, Boelens R, Van Es DS, et al. New insights into the structure and composition of technical lignins: A comparative characterisation study. Green Chem 2016;18:2651–65. doi:10.1039/c5gc03043a.

[183] Nitsos C, Rova U, Christakopoulos P. Organosolv Fractionation of Softwood Biomass for Biofuel and Biorefinery Applications. Energies 2017;11:50. doi:10.3390/en11010050.

[184] Huber GW, Iborra S, Corma A. Synthesis of transportation fuels from biomass: Chemistry, catalysts, and engineering. Chem Rev 2006;106:4044–98. doi:10.1021/cr068360d.

[185] Stefanidis SD, Kalogiannis KG, Iliopoulou EF, Michailof CM, Pilavachi PA, Lappas AA. A study of lignocellulosic biomass pyrolysis via the pyrolysis of cellulose, hemicellulose and lignin. J Anal Appl Pyrolysis 2014;105:143–50.

[186] Rinaldi R, Jastrzebski R, Clough MT, Ralph J, Kennema M, Bruijnincx PCA, et al. Paving the Way for Lignin Valorisation: Recent Advances in Bioengineering, Biorefining and Catalysis. Angew Chemie - Int Ed 2016;55:8164–215. doi:10.1002/anie.201510351.

[187] Trubetskaya A, Lange H, Wittgens B, Brunsvik A, Crestini C, Rova U, et al. Structural and Thermal Characterization of Novel Organosolv Lignins from Wood and Herbaceous Sources. Processes 2020;8:860. doi:10.3390/pr8070860.

[188] Amirabedin E, Pooyanfar M, Rahim MA, Topal H. Techno-environmental assessment of co-gasification of low-grade Turkish lignite with biomass in a trigeneration power plant. Environ Clim Technol 2014;13:5–11. doi:10.2478/rtuect-2014-0001.

[189] Kajitani S, Zhang Y, Umemoto S, Ashizawa M, Hara S. Co-gasification reactivity of coal and woody biomass in high-temperature gasification. Energy Fuels 2010;24:145–51. doi:10.1021/ef900526h.

[190] Qin K, Jensen PA, Lin W, Jensen AD. Biomass gasification behavior in an entrained flow reactor: Gas product distribution and soot formation. Energy Fuels 2012;26:5992–6002. doi:10.1021/ef300960x.

[191] Brar JS, Singh K, Wang J, Kumar S. Co-gasification of Coal and Biomass: A Review. Int J For Res 2012;2012. doi:10.1155/2012/363058.

[192] Collot AG. Matching gasification technologies to coal properties. Int J Coal Geol 2006;65:191–212. doi:10.1016/j.coal.2005.05.003.

[193] Kamble AD, Saxena VK, Chavan PD, Mendhe VA. Co-gasification of coal and biomass an emerging clean energy technology: Status and prospects of development in Indian context. Int J Min Sci Technol 2019;29:171–86. doi:10.1016/j.ijmst.2018.03.011.

[194] Ding L, Zhang Y, Wang Z, Huang J, Fang Y. Interaction and its induced inhibiting or synergistic effects during co-gasification of coal char and biomass char. Bioresour Technol 2014;173:11–20. doi:10.1016/j.biortech.2014.09.007.

[195] Howaniec N, Smoliński A. Steam co-gasification of coal and biomass - Synergy in reactivity of fuel blends chars. Int J Hydrogen Energy 2013;38:16152–60. doi:10.1016/j.ijhydene.2013.10.019.

[196] Wei J, Guo Q, Chen H, Chen X, Yu G. Study on reactivity characteristics and synergy behaviours of rice straw and bituminous coal co-gasification. Bioresour Technol 2016;220:509–15. doi:10.1016/j.biortech.2016.08.116.

[197] Zhang Y, Zheng Y, Yang M, Song Y. Effect of fuel origin on synergy during co-gasification of biomass and coal in CO2. Bioresour Technol 2016;200:789–94. doi:10.1016/j.biortech.2015.10.076.

[198] He Q, Guo Q, Ding L, Wei J, Yu G. CO2 gasification of char from raw and

torrefied biomass: Reactivity, kinetics and mechanism analysis. Bioresour Technol 2019;293. doi:10.1016/j.biortech.2019.122087.

[199] Zhu W, Song W, Lin W. Catalytic gasification of char from co-pyrolysis of coal and biomass. Fuel Process Technol 2008;89:890–6. doi:10.1016/j.fuproc.2008.03.001.

[200] Chen W-H, Chen C-J, Hung C-I, Shen C-H, Hsu H-W. A comparison of gasification phenomena among raw biomass, torrefied biomass and coal in an entrained-flow reactor. Appl Energy 2013;112:421–30. doi:10.1016/j.apenergy.2013.01.034.

[201] Jayaraman K, Gokalp I, Bonifaci E, Merlo N. Kinetics of steam and CO2gasification of high ash coal-char produced under various heating rates. Fuel 2015;154:370–9. doi:10.1016/j.fuel.2015.02.091.

[202] Zhang Y, Fan D, Zheng Y. Comparative study on combined co-pyrolysis/gasification of walnut shell and bituminous coal by conventional and congruent-mass thermogravimetric analysis (TGA) methods. Bioresour Technol 2016;199:382–5. doi:10.1016/j.biortech.2015.07.120.

[203] Mafu LD, Neomagus HWJP, Everson RC, Okolo GN, Strydom CA, Bunt JR. The carbon dioxide gasification characteristics of biomass char samples and their effect on coal gasification reactivity during co-gasification. Bioresour Technol 2018;258:70–8. doi:10.1016/j.biortech.2017.12.053.

[204] Dupont C, Jacob S, Marrakchy KO, Hognon C, Grateau M, Labalette F, et al. How inorganic elements of biomass influence char steam gasification kinetics. Energy 2016;109:430–5. doi:10.1016/j.energy.2016.04.094.

[205] Wang G, Zhang J, Shao J, Liu Z, Wang H, Li X, et al. Experimental and modeling studies on CO 2 gasification of biomass chars. Energy 2016;114:143–54. doi:10.1016/j.energy.2016.08.002.

[206] Jayaraman K, Gökalp I, Jeyakumar S. Estimation of synergetic effects of CO2 in high ash coal-char steam gasification. Appl Therm Eng

2017;110:991–8. doi:10.1016/j.applthermaleng.2016.09.011.

[207] Li R, Zhang J, Wang G, Ning X, Wang H, Wang P. Study on CO2 gasification reactivity of biomass char derived from high-temperature rapid pyrolysis. Appl Therm Eng 2017;121:1022–31. doi:10.1016/j.applthermaleng.2017.04.132.

[208] Xu C, Hu S, Xiang J, Zhang L, Sun L, Shuai C, et al. Interaction and kinetic analysis for coal and biomass co-gasification by TG-FTIR. Bioresour Technol 2014;154:313–21. doi:10.1016/j.biortech.2013.11.101.

[209] Mueller A, Haustein HD, Stoesser P, Kreitzberg T, Kneer R, Kolb T. Gasification Kinetics of Biomass- and Fossil-Based Fuels: Comparison Study Using Fluidized Bed and Thermogravimetric Analysis. Energy Fuels 2015;29:6717–23. doi:10.1021/acs.energyfuels.5b01123.

[210] Alvarez J, Lopez G, Amutio M, Bilbao J, Olazar M. Kinetic Study of Carbon Dioxide Gasification of Rice Husk Fast Pyrolysis Char. Energy Fuels 2015;29:3198–207. doi:10.1021/acs.energyfuels.5b00318.

[211] Wei J, Song X, Guo Q, Ding L, Yoshikawa K, Yu G. Reactivity, Synergy, and Kinetics Analysis of CO2 Co-pyrolysis/Co-gasification of Biomass after Hydrothermal Treatment and Coal Blends. Energy Fuels 2020;34:294–303. doi:10.1021/acs.energyfuels.9b03721.

[212] Di Blasi C. Combustion and gasification rates of lignocellulosic chars. Prog Energy Combust Sci 2009;35:121–40. doi:10.1016/j.pecs.2008.08.001.

[213] Lu L, Kong C, Sahajwalla V, Harris D. Char structural ordering during pyrolysis and combustion and its influence on char reactivity. Fuel 2002;81:1215–25. doi:10.1016/S0016-2361(02)00035-2.

[214] Tremel A, Haselsteiner T, Nakonz M, Spliethoff H. Coal and char properties in high temperature entrained flow gasification. Energy 2012;45:176–82. doi:10.1016/j.energy.2012.02.028.

[215] Chen D, Zhang Z, Li Z, Lv Z, Cai N. Optimizing in-situ char gasification

kinetics in reduction zone of pulverized coal air-staged combustion. Combust Flame 2018;194:52–71. doi:10.1016/j.combustflame.2018.04.015.

[216] Gonzalo-Tirado C, Jiménez S, Ballester J. Gasification of a pulverized sub-bituminous coal in CO2 at atmospheric pressure in an entrained flow reactor. Combust Flame 2012;159:385–95. doi:10.1016/j.combustflame.2011.07.001.

[217] Kajitani S, Hara S, Matsuda H. Gasification rate analysis of coal char with a pressurized drop tube furnace. Fuel 2002;81:539–46. doi:10.1016/S0016-2361(01)00149-1.

[218] Li R, Zhang J, Wang G, Ning X, Wang H, Wang P. Study on CO2 gasification reactivity of biomass char derived from high-temperature rapid pyrolysis. Appl Therm Eng 2017;121:1022–31. doi:10.1016/j.applthermaleng.2017.04.132.

[219] Wang L, Li T, Várhegyi G, Skreiberg Ø, Løvås T. CO2 Gasification of Chars Prepared by Fast and Slow Pyrolysis from Wood and Forest Residue: A Kinetic Study. Energy Fuels 2018;32:588–97. doi:10.1021/acs.energyfuels.7b03333.

[220] Jeong HJ, Park SS, Hwang J. Co-gasification of coal-biomass blended char with CO2 at temperatures of 900-1100 C. Fuel 2014;116:465–70. doi:10.1016/j.fuel.2013.08.015.

[221] Fermoso J, Corbet T, Ferrara F, Pettinau A, Maggio E, Sanna A. Synergistic effects during the co-pyrolysis and co-gasification of high volatile bituminous coal with microalgae. Energy Convers Manag 2018;164:399–409. doi:10.1016/j.enconman.2018.03.023.

[222] Wei J, Guo Q, Gong Y, Ding L, Yu G. Synergistic effect on co-gasification reactivity of biomass-petroleum coke blended char. Bioresour Technol 2017;234:33–9. doi:10.1016/j.biortech.2017.03.010.

[223] Zou X, Ding L, Gong X. Study on the Co-gasification Reactivity and

Interaction Mechanism of Coal with Different Components of Daily Food Waste. Energy Fuels 2020;34:1728–36. doi:10.1021/acs.energyfuels.9b01679.

[224] Wei J, Gong Y, Guo Q, Chen X, Ding L, Yu G. A mechanism investigation of synergy behaviour variations during blended char co-gasification of biomass and different rank coals. Renew Energy 2019;131:597–605. doi:10.1016/j.renene.2018.07.075.

[225] Satyam Naidu V, Aghalayam P, Jayanti S. Synergetic and inhibition effects in carbon dioxide gasification of blends of coals and biomass fuels of Indian origin. Bioresour Technol 2016;209:157–65. doi:10.1016/j.biortech.2016.02.137.

[226] Ma Z, Bai J, Li W, Bai Z, Kong L. Mineral transformation in char and its effect on coal char gasification reactivity at high temperatures, part 1: Mineral transformation in char. Energy and Fuels, vol. 27, American Chemical Society; 2013, p. 4545–54. doi:10.1021/ef4010626.

[227] Zhang H, Guo X, Zhu Z. Effect of temperature on gasification performance and sodium transformation of Zhundong coal. Fuel 2017;189:301–11. doi:10.1016/j.fuel.2016.10.097.

[228] Arnold RA, Hill JM. Catalysts for gasification: A review. Sustain Energy Fuels 2019;3:656–72. doi:10.1039/c8se00614h.

[229] Guo Q, Huang Y, Gong Y, Wei J, Yu G. A study on high-temperature co-gasification reactivity characteristics and kinetics analysis of Hami coal and its liquefaction residue. Asia-Pacific J Chem Eng 2020;15. doi:10.1002/apj.2376.

[230] Liang D, Xie Q, Zhou H, Yang M, Cao J, Zhang J. Catalytic effect of alkali and alkaline earth metals in different occurrence modes in Zhundong coals. Asia-Pacific J Chem Eng 2018;13:1–13. doi:10.1002/apj.2190.

[231] Mills S. Prospects for coal and clean coal technologies in Turkey. London,

UK: IEA Clean Coal Centre; 2014.

[232] Livingston W, Willeboer W, Tosney S, Sander Madrali BS, Hansen M. The status of large scale biomass firing The milling and combustion of biomass materials in large pulverised coal boilers. 2016.

[233] Friedl A, Padouvas E, Rotter H, Varmuza K. Prediction of heating values of biomass fuel from elemental composition. Anal Chim Acta 2005;544:191–8. doi:10.1016/j.aca.2005.01.041.

[234] Majumder AK, Jain R, Banerjee P, Barnwal JP. Development of a new proximate analysis based correlation to predict calorific value of coal. Fuel 2008;87:3077–81. doi:10.1016/j.fuel.2008.04.008.

[235] Mayoral MC, Izquierdo MT, Andrés JM, Rubio B. Different approaches to proximate analysis by thermogravimetry analysis. Thermochim Acta 2001;370:91–7. doi:10.1016/S0040-6031(00)00789-9.

[236] Li T, Geier M, Wang L, Ku X, Güell BM, Løvås T, et al. Effect of torrefaction on physical properties and conversion behavior of high heating rate char of forest residue. Energy and Fuels 2015;29:177–84. doi:10.1021/ef5016044.

[237] Gibbins JR, Kandiyoti R. The effect of variations in time-temperature history on product distribution from coal pyrolysis. Fuel 1989;68:895–903. doi:10.1016/0016-2361(89)90127-0.

[238] Mammadbaghir Baghirzade. INVESTIGATION OF TURKISH LIGNITES AND BIOMASS AT HIGH HEATING RATES BY USING WIRE MESH APPARATUS. Middle East Technical University, 2018.

[239] Magalhaes D, Riaza J, Kazanç F. A study on the reactivity of various chars from Turkish fuels obtained at high heating rates. Fuel Process Technol 2019;185:91–9. doi:10.1016/j.fuproc.2018.12.005.

[240] Magalhães D, Rabaçal M, Costa M. High Speed Imaging of Single Particle Ignition Behavior of Biomass Fuels 2015:1–5.

[241] Simões G. Single particle ignition of pulverized solid biomass fuels : experiments and modeling 2016:1–63.

[242] Levendis YA, Estrada KR, Hottel HC. Development of multicolor pyrometers to monitor the transient response of burning carbonaceous particles. Rev Sci Instrum 1992;63:3608–22. doi:10.1063/1.1143586.

[243] Chen Y, Mori S, Pan W. Studying the mechanisms of ignition of coal particles by TG-DTA 1996;275:149–58.

[244] Molina A, Shaddix CR. Ignition and devolatilization of pulverized bituminous coal particles during oxygen/carbon dioxide coal combustion. Proc Combust Inst 2007;31 II:1905–12. doi:10.1016/j.proci.2006.08.102.

[245] Shaddix CR. Correcting thermocouple measurements for radiation loss: a critical review. Proc 33rd Natl Heat Transf Conf 1999:HTD99-282. doi:10.1088/0957-0233/17/4/008.

[246] Parshetti GK, Quek A, Betha R, Balasubramanian R. TGA–FTIR investigation of co-combustion characteristics of blends of hydrothermally carbonized oil palm biomass (EFB) and coal. Fuel Process Technol 2014;118:228–34. doi:10.1016/j.fuproc.2013.09.010.

[247] Abbasi-Atibeh E, Yozgatligil A. A study on the effects of catalysts on pyrolysis and combustion characteristics of Turkish lignite in oxy-fuel conditions. Fuel 2014;115:841–9. doi:10.1016/j.fuel.2013.01.073.

[248] Pyle DL, Zaror CA. Heat transfer and kinetics in the low temperature pyrolysis of solids. Chem Eng Sci 1984;39:147–58. doi:10.1016/0009-2509(84)80140-2.

[249] Di Blasi C. Influences of physical properties on biomass devolatilization characteristics. Fuel 1997;76:957–64. doi:10.1016/S0016-2361(97)00096-3.

[250] Maloney DJ, Sampath R, Zondlo JW. Heat capacity and thermal conductivity considerations for coal particles during the early stages of rapid heating. Combust Flame 1999;116:94–104. doi:10.1016/S0010-

2180(98)00044-3.

[251] Haykiri-Acma H, Yaman S. Interaction between biomass and different rank coals during co-pyrolysis. Renew Energy 2010;35:288–92. doi:10.1016/j.renene.2009.08.001.

[252] Phadnis a. B, Deshpande VV. Determination of the kinetics and mechanism of a solid state reaction. A simple approach. Thermochim Acta 1983;62:361–7. doi:10.1016/0040-6031(83)85056-4.

[253] Yorulmaz SY, Atimtay A. Investigation of combustion kinetics of five waste wood samples with thermogravimetric analysis. Environ Earth Sci 2011;90:511–20. doi:10.1007/978-3-540-95991-5-46.

[254] Pottmaier D, Costa M, Farrow T, Oliveira AAM, Alarcon O, Snape C. Comparison of rice husk and wheat straw: From slow and fast pyrolysis to char combustion. Energy and Fuels 2013;27:7115–25. doi:10.1021/ef401748e.

[255] Morin M, Pécate S, Masi E, Hémati M. Kinetic study and modelling of char combustion in TGA in isothermal conditions. Fuel 2017;203:522–36. doi:10.1016/j.fuel.2017.04.134.

[256] Massman WJ. A review of the molecular diffusivities of H2O, CO2, CH4, CO, O3, SO2, NH3, N2O, NO, and NO2 in air, O2 and N2 near STP. Atmos Environ 1998;32:1111–27. doi:10.1016/S1352-2310(97)00391-9.

[257] P.L. Walker Jr, F. Rusinko LGA. Gas reactions of carbon. Adv Catal Relat Subj Acad Press London 1959;11.

[258] Bejarano PA, Levendis YA. Single-coal-particle combustion in O2/N2 and O2/CO2 environments. Combust Flame 2008;153:270–87. doi:10.1016/j.combustflame.2007.10.022.

[259] ASTM. Standard Test Method for Ash in the Analysis Sample of Coal and Coke from Coal D3174-12. ASTM Int 2011:1–6. doi:10.1520/D3174-12.2.

[260] ASTM. Standard test method for ash in biomass E1755 - 01. ASTM

2015;44:153–161. doi:10.1520/E1755-01R15.2.

[261] Scheffknecht G, Al-Makhadmeh L, Schnell U, Maier J. Oxy-fuel coal combustion-A review of the current state-of-the-art. Int J Greenh Gas Control 2011;5:16–35. doi:10.1016/j.ijggc.2011.05.020.

[262] Man CK, Gibbins JR, Witkamp JG, Zhang J. Coal characterisation for NOx prediction in air-staged combustion of pulverised coals. Fuel 2005;84:2190–5. doi:10.1016/j.fuel.2005.06.011.

[263] Russell N V., Gibbins JR, Man CK, Williamson J. Coal char thermal deactivation under pulverized fuel combustion conditions. Energy and Fuels 2000;14:883–8. doi:10.1021/ef990241w.

[264] Seo DK, Lee SK, Kang MW, Hwang J, Yu TU. Gasification reactivity of biomass chars with CO2. Biomass and Bioenergy 2010;34:1946–53. doi:10.1016/j.biombioe.2010.08.008.

[265] Liu L, Kong B, Jiao Q, Yang J, Liu Q, Liu X. Structure Characterization and CO2 Gasification Kinetics of Tri-High Coal-Chars Derived from Higherature Pyrolysis. ACS Omega 2019;4:19030–6. doi:10.1021/acsomega.9b02024.

[266] Szekely J, Evans JW. A structural model for gas-solid reactions with a moving boundary. Chem Eng Sci 1970;25:1091–107. doi:10.1016/0009-2509(70)85053-9.

[267] Fermoso J, Arias B, Pevida C, Plaza MG, Rubiera F, Pis JJ. Kinetic models comparison for steam gasification of different nature fuel chars. J Therm Anal Calorim 2008;91:779–86. doi:10.1007/s10973-007-8623-5.

[268] Uluca K. Infrared Measurement of Biomass Combustion in a Wire Mesh Reactor. Middle East Technical University, 2019.

[269] Werner K, Pommer L, Broström M. Thermal decomposition of hemicelluloses. J Anal Appl Pyrolysis 2014;110:130–7.

[270] Simões G, Magalhães D, Rabaçal M, Costa M. Effect of gas temperature and

oxygen concentration on single particle ignition behavior of biomass fuels. Proc Combust Inst 2016. doi:http://dx.doi.org/10.1016/j.proci.2016.06.102.

[271] Riaza J, Khatami R, Levendis Y a., Álvarez L, Gil M V., Pevida C, et al. Combustion of single biomass particles in air and in oxy-fuel conditions. Biomass and Bioenergy 2014;64:162–74. doi:10.1016/j.biombioe.2014.03.018.

[272] Wu H, Glarborg P, Frandsen FJ, Dam-johansen K. Solid fuel interactions in co-combustion – a literature survey 2011.

[273] Loo S Van, Koppejan J. The Handbook of Biomass Combustion and Co - firing. vol. 1. London: Earthscan; 2015. doi:10.1017/CBO9781107415324.004.

[274] López-González D, Avalos-Ramirez A, Giroir-Fendler A, Godbout S, Fernandez-Lopez M, Sanchez-Silva L, et al. Combustion kinetic study of woody and herbaceous crops by thermal analysis coupled to mass spectrometry. Energy 2015;90:1626–35. doi:10.1016/j.energy.2015.06.134.

[275] Ozbas KE, Hicyilmaz C, Kök MV, Bilgen S. Effect of cleaning process on combustion characteristics of lignite. Fuel Process Technol 2000;64:211–20. doi:10.1016/S0378-3820(00)00064-3.

[276] Pevida C, Gil M V, Riaza J, Pis JJ, Rubiera F. A study of oxy-coal combustion with steam addition and biomass blending by thermogravimetric analysis 2012:49–55. doi:10.1007/s10973-011-1342-y.

[277] Skodras G, Grammelis P, Basinas P, Kakaras E. Pyrolysis and Combustion Characteristics of Biomass and Waste-Derived Feedstock 2006:3791–9.

[278] Gil M V, Riaza J, Álvarez L, Pevida C, Pis JJ, Rubiera F. Kinetic models for the oxy-fuel combustion of coal and coal / biomass blend chars obtained in N 2 and CO 2 atmospheres. Energy 2012;48:510–8. doi:10.1016/j.energy.2012.10.033.

[279] Inmas S V., Kulah G, Selçuk N. Comparison Between Combustion Behavior

of Solid Fuels and Their Chars Under Oxy-Fuel Conditions. Combust Sci Technol 2014;186:398–408. doi:10.1080/00102202.2014.883199.

[280] Ferreiro AI, Rabaçal M, Costa M. A combined genetic algorithm and least squares fitting procedure for the estimation of the kinetic parameters of the pyrolysis of agricultural residues. Energy Convers Manag 2016. doi:10.1016/j.enconman.2016.04.104.

[281] Vamvuka D, Pasadakis N, Kastanaki E, Grammelis P, Kakaras E. Kinetic modeling of coal/agricultural by-product blends. Energy and Fuels 2003;17:549–58. doi:10.1021/ef020179u.

[282] Aboulkas A, El Harfi K, El Bouadili A. Non-isothermal kinetic studies on co-processing of olive residue and polypropylene. Energy Convers Manag 2008;49:3666–71. doi:10.1016/j.enconman.2008.06.029.

[283] Howard JB, Essenhigh RH. Mechanism of solid-partical combustion with simultaneous gas-phase volatiles combustion. Symp Combust 1967;11:399–408. doi:http://dx.doi.org/10.1016/S0082-0784(67)80164-4.

[284] Becker A, Scherer V. A comparison of the torrefaction behavior of wood, miscanthus and palm kernel shells: Measurements on single particles with geometries of technical relevance. Fuel 2018;224:507–20. doi:10.1016/j.fuel.2018.01.095.

[285] Levendis YA, Flagan RC, Nam SW, Lowenberg M, Gavalas GR. Catalysis of the Combustion of Synthetic Char Particles by Various Forms of Calcium Additives. Energy and Fuels 1989;3:28–37. doi:10.1021/ef00013a006.

[286] TÜRKİYE KÖMÜR İŞLETMELERİ KURUMU. KÖMÜR SEKTÖR RAPORU (LİNYİT). 2016.

[287] Repellin V, Govin A, Rolland M, Guyonnet R. Energy requirement for fine grinding of torrefied wood. Biomass and Bioenergy 2010;34:923–30. doi:10.1016/j.biombioe.2010.01.039.

[288] Svoboda K, Pohořelý M, Hartman M, Martinec J. Pretreatment and feeding

of biomass for pressurized entrained flow gasification. Fuel Process Technol 2009;90:629–35. doi:10.1016/j.fuproc.2008.12.005.

[289] Yang W, Zhu Y, Cheng W, Sang H, Yang H, Chen H. Characteristics of Particulate Matter Emitted from Agricultural Biomass Combustion. Energy and Fuels 2017;31:7493–501. doi:10.1021/acs.energyfuels.7b00229.

[290] Amanda Ruscio; Feyza Kazanc; and Yiannis A. Levendis. Characterization of Particulate Matter Emitted from Combustion of Various Biomasses in O2/N2 and O2/CO2 Environments. Energy & Fuels 2013;28:685–96. doi:dx.doi.org/10.1021/ef401796w.

[291] Kazanc F, Levendis YA. Physical Properties of Particulate Matter Emitted from Combustion of Coals of Various Ranks in O_2/N_2 and O_2/CO_2 Environments. Energy & Fuels 2012;26:7127–39. doi:10.1021/ef301087r.

[292] Gani A, Morishita K, Nishikawa K, Naruse I. Characteristics of co-combustion of low-rank coal with biomass. Energy and Fuels 2005;19:1652–9. doi:10.1021/ef049728h.

[293] Dong Z, Clark M, Gunderson T, Hecker WC, Fletcher TH. Swelling properties and intrinsic reactivities of coal chars produced at elevated pressures and high heating rates. Proc Combust Inst 2005;30 II:2213–21. doi:10.1016/j.proci.2004.07.038.

[294] Fermoso J, Gil M V., Borrego AG, Pevida C, Pis JJ, Rubiera F. Effect of the pressure and temperature of devolatilization on the morphology and steam gasification reactivity of coal chars. Energy and Fuels 2010;24:5586–95. doi:10.1021/ef100877t.

[295] Pugmire RJ, Solum MS, Grant DM, Critchfield S, Fletcher TH. Structural evolution of matched tar-char pairs in rapid pyrolysis experiments. Fuel 1991;70:414–23. doi:10.1016/0016-2361(91)90132-T.

[296] Solomon PR, Serio MA, Hamblen G. Network models decomposition of coal thermal. Fuel 1990;69:754–63. doi:10.1016/0016-2361(90)90042-O.

[297] Dall'Ora M, Jensen PA, Jensen AD. Suspension Combustion of Wood: Influence of Pyrolysis Conditions on Char Yield, Morphology, and Reactivity. Energy & Fuels 2008;22:2955–62. doi:10.1021/ef800136b.

[298] Wornat MJ, Hurt RH, Yang NYC, Headley TJ. Structural and compositional transformations of biomass chars during combustion. Combust Flame 1995;100:131–43. doi:10.1016/0010-2180(94)00055-W.

[299] Fei J, Zhang J, Wang F, Wang J. Synergistic effects on co-pyrolysis of lignite and high-sulfur swelling coal. J Anal Appl Pyrolysis 2012;95:61–7. doi:10.1016/j.jaap.2012.01.006.

[300] Chen J, Jiao F, Dong Z, Niyomura O, Namioka T, Yamada N, et al. Effect of kaolin on ash partitioning during combustion of a low-rank coal in O2/CO2atmosphere. Fuel 2018;222:538–43. doi:10.1016/j.fuel.2018.02.191.

[301] McClelland DJ, Motagamwala AH, Li Y, Rover MR, Wittrig AM, Wu C, et al. Functionality and molecular weight distribution of red oak lignin before and after pyrolysis and hydrogenation. Green Chem 2017;19:1378–89.

[302] Thring RW, Vanderlaan MN, Griffin SL. Fractionation of ALCELL® lignin by sequential solvent extraction. J Wood Chem Technol 1996;16:139–54.

[303] Cui C, Sun R, Argyropoulos DS. Fractional Precipitation of Softwood Kraft Lignin: Isolation of Narrow Fractions Common to a Variety of Lignins. ACS Sustain Chem Eng 2014;2:959–68.

[304] Brodin I, Sjöholm E, Gellerstedt G. The behavior of kraft lignin during thermal treatment. J Anal Appl Pyrolysis 2010;87:70–7.

[305] Nik-Azar M, Hajaligol MR, Sohrabi M, Dabir B. Effects of heating rate and particle size on the products yields from rapid pyrolysis of beech-wood. Fuel Sci Technol Int 1996;14:479–502.

[306] Trubetskaya A, Larsen FH, Shchukarev A, Ståhl K, Umeki K. Potassium and soot interaction in fast biomass pyrolysis at high temperatures. Fuel 2018;225:89–94. doi:10.1016/j.fuel.2018.03.140.

[307] Alén R, Kuoppala E, Oesch P. Formation of the main degradation compound groups from wood and its components during pyrolysis. J Anal Appl Pyrolysis 1996;36:137–48.

[308] Serio MA, Charpenay S, Bassilakis R, Solomon PR. Measurement and modeling of lignin pyrolysis. Biomass and Bioenergy 1994;7:107–24. doi:10.1016/0961-9534(94)00042-R.

[309] Zhou X, Li W, Mabon R, Broadbelt LJ. A critical review on hemicellulose pyrolysis. Energy Technol 2017;5:52–79.

[310] Wang Z, Mcdonald AG, Westerhof RJM, Kersten SRA, Cuba-torres CM, Ha S, et al. Effect of cellulose crystallinity on the formation of a liquid intermediate and on product distribution during pyrolysis. J Anal Appl Pyrolysis 2013;100:56–66.

[311] Smith MW, Pecha B, Helms G, Scudiero L, Garcia-perez M. Biomass and Bioenergy Chemical and morphological evaluation of chars produced from primary biomass constituents : Cellulose , xylan , and lignin. Biomass and Bioenergy 2017;104:17–35.

[312] Broido A, Forest PS, Station RE. Molecular Weight Decrease in the Early Pyrolysis of Crystalline and Amorphous Cellulose 1973;17:3627–35.

[313] Dussan K, Dooley S, Monaghan R. Integrating compositional features in model compounds for a kinetic mechanism of hemicellulose pyrolysis. Chem Eng J 2017;328:943–61. doi:10.1016/j.cej.2017.07.089.

[314] Basch A, Lewin M. Influence of Fine Structure on the Pyrolysis of Cellulose - 3. The Influence of Orientation. J Polym Sci Part A-1 Polym Chem 1974;12:2053–63.

[315] Dobele G, Rossinskaja G, Telysheva G, Meier D, Faix O. Cellulose dehydration and depolymerization reactions during pyrolysis in the presence of phosphoric acid. J Anal Appl Pyrolysis 1999;49:307–17.

[316] Franklin WE. Initial Pyrolysis Reactions in Unmodified and Flame-

Retardant Cotton. J Macromol Sci Part A - Chem 1983;19:619–41.

[317] W.E. Franklin. Kinetic and Thermogravimetric Analyses of Pyrolysis of COtton Finished with THPS-Urea-Phosphate Flame-Retardant. J Fire Retard Chem 1982;9.

[318] Kumar AK, Sharma S. Recent updates on different methods of pretreatment of lignocellulosic feedstocks: a review. Bioresour Bioprocess 2017;4:1–19.

[319] Delbecq F, Wang Y, Muralidhara A, El Ouardi KE, Marlair G, Len C. Hydrolysis of hemicellulose and derivatives-a review of recent advances in the production of furfural. Front Chem 2018;6:146.

[320] Tanjore D, Shi J WC. Chapter 4: Dilute acid and hydrothermal pretreatment of cellulosic biomass. In: Simmons B (ed) Chemical and biochemical catalysis for next generation biofuels. Royal Society of Chemistry, California, p. 64-88, Royal Society of Chemistry; 2011.

[321] Wyman C. Chapter 14 Physical and Chemical Features of Pretreated Biomass that Influence Macro-/Micro-accessibility and Biological Processing. Aqueous pretreatment of plant biomass for biological and chemical conversion to Fuels and Chemicals, Wiley; 2013.

[322] Yu J, Paterson N, Blamey J, Millan M. Cellulose, xylan and lignin interactions during pyrolysis of lignocellulosic biomass. Fuel 2017;191:140–9.

[323] Bradbury AGW, Sakai Y, Shafizadeh F. A kinetic model for pyrolysis of cellulose. J Appl Polym Sci 1979;23:3271–80.

[324] Farrow ST, Sun C, Liu H, Le Manquais K, Snape CE. Comparative study of the inherent combustion reactivity of sawdust chars produced by TGA and in the drop tube furnace. Fuel Process Technol 2020;201. doi:10.1016/j.fuproc.2020.106361.

[325] Clery DS, Mason PE, Rayner CM, Jones JM. The effects of an additive on the release of potassium in biomass combustion. Fuel 2018;214:647–55.

doi:10.1016/j.fuel.2017.11.040.

[326] Zhang Q, Li Q, Zhang L, Wang Z, Jing X, Yu Z, et al. Preliminary study on co-gasification behavior of deoiled asphalt with coal and biomass. Appl Energy 2014;132:426–34. doi:10.1016/j.apenergy.2014.07.014.

[327] Vassilev S V., Baxter D, Andersen LK, Vassileva CG. An overview of the composition and application of biomass ash. Part 1. Phase-mineral and chemical composition and classification. Fuel 2013;105:40–76. doi:10.1016/j.fuel.2012.09.041.

[328] Shen Q, Liaw SB, Costa M, Wu H. Rapid Pyrolysis of Pulverized Biomass at a High Temperature: The Effect of Particle Size on Char Yield, Retentions of Alkali and Alkaline Earth Metallic Species, and Char Particle Shape. Energy Fuels 2020. doi:10.1021/acs.energyfuels.0c00898.

[329] Yuan S, Dai ZH, Zhou ZJ, Chen XL, Yu GS, Wang FC. Rapid co-pyrolysis of rice straw and a bituminous coal in a high-frequency furnace and gasification of the residual char. Bioresour Technol 2012;109:188–97. doi:10.1016/j.biortech.2012.01.019.

[330] Liu L, Kong B, Jiao Q, Yang J, Liu Q, Liu X. Structure Characterization and CO_2 Gasification Kinetics of Tri-High Coal-Chars Derived from High-Temperature Pyrolysis. ACS Omega 2019;4:19030–6. doi:10.1021/acsomega.9b02024.

[331] Wei J, Gong Y, Ding L, Yu J, Yu G. Influence of Biomass Ash Additive on Reactivity Characteristics and Structure Evolution of Coal Char-CO2 Gasification. Energy Fuels 2018;32:10428–36. doi:10.1021/acs.energyfuels.8b02028.

[332] Nzihou A, Stanmore B, Sharrock P. A review of catalysts for the gasification of biomass char, with some reference to coal. Energy 2013;58:305–17. doi:10.1016/j.energy.2013.05.057.

[333] Vassilev S V., Baxter D, Vassileva CG. An overview of the behaviour of

biomass during combustion: Part II. Ash fusion and ash formation mechanisms of biomass types. Fuel 2014;117:152–83. doi:10.1016/j.fuel.2013.09.024.

[334] Masnadi MS, Grace JR, Bi XT, Lim CJ, Ellis N. From fossil fuels towards renewables: Inhibitory and catalytic effects on carbon thermochemical conversion during co-gasification of biomass with fossil fuels. Appl Energy 2015;140:196–209. doi:10.1016/j.apenergy.2014.12.006.

[335] Sluiter A, Hames B, Ruiz R, Scarlata C, Sluiter J, Templeton D, et al. Determination of Structural Carbohydrates and Lignin in Biomass. 2008.

[336] Hayes DJM. Development of near infrared spectroscopy models for the quantitative prediction of the lignocellulosic components of wet Miscanthus samples. Bioresour Technol 2012;119:393–405.

APPENDICES

A. DATA RELATIVE TO THE CO-PYROLYSIS OF BIOMASS WITH COAL

A.1 Polynomials fitted to the carbon burnout rate curves

Table A.1 Polynomial coefficients for the conversion curves of Figures 4.29 and 4.31.

	$p(x) = p_1x^6 + p_2x^5 + p_3x^4 + p_4x^3 + p_5x^2 + p_6x + p_7$						
	p_1	p_2	p_3	p_4	p_5	p_6	p_7
OR	0	0	-1.64e-06	0.000398	-0.033	0.909	0
AS	0	0	-6.65e-07	0.000222	-0.0244	0.895	0
SL	-4.99e-10	1.72e-07	-2.32e-05	0.00153	-0.0501	0.673	0
50OR-50SL	-2.44e-10	8.06e-08	-1.04e-05	0.000651	-0.0203	0.273	0
25OR-75SL	-6.43e-10	2.23e-07	-3.03e-05	0.00201	-0.0665	0.910	0
50AS-50SL	-2.43e-10	8.05e-08	-1.04e-05	0.000651	-0.0203	0.272	0
25AS-75SL	-5.31e-10	1.81e-07	-2.43e-05	0.00161	-0.0534	0.739	0

Table A.2 Fitting parameters for the polynomial functions represented in Figures 3.13, 4.29, and 4.31.

	Root-mean-square error (RMSE)			Coefficient of determination (r^2)		
	400 ºC	450 ºC	525 ºC	400 ºC	450 ºC	525 ºC
OR	1.02	2.17	4.99	0.776	0.916	0.752
AS	0.984	2.91	3.60	0.864	0.883	0.866
SL	-	0.347	-	-	0.712	-
50OR-50SL	-	0.197	-	-	0.706	-
25OR-75SL	-	0.367	-	-	0.805	-
50AS-50SL	-	0.222	-	-	0.810	-
25AS-75SL	-	0.368	-	-	0.749	-

B. DATA RELATIVE TO THE FAST PYROLYSIS OF LABORATORY-FRACTIONATED BIOMASS

B.1 Olive stones fractionation

Olive stones were fractionated to their main components: lignin, cellulose, and hemicellulose in an organosolv reactor at Luleå University of Technology following a laboratory procedure previously described [179]. More specifically, an air-heated multidigester apparatus was used, containing 2.5 L metallic cylinders. Olive stones were mixed with the solution of 60% v/v ethanol in water at a liquid to solid ratio of 10 (v/w) and placed in the cylinders. Treatment took place for 1 h at 170 ºC and 180 ºC in both the presence and absence of an acidic catalyst (1 % $w/w_{biomass}$ H_2SO_4), and at 190 ºC in the absence of acidic catalyst. At the end of the treatment time, the reactor was cooled to room temperature, and the pre-treated solids were removed from the slurry by vacuum filtration, washed with the 60 % v/v ethanol solution and air-dried at room temperature until further use. The flow through liquor was collected and the ethanol was removed in a rotary evaporator. Ethanol removal resulted in reducing the solubility of lignin in the liquor, which was recovered by centrifugation (14,000 rpm, 29,416× g, at 4 ºC for 15 min) and air-dried at room temperature. The remaining aqueous solution, containing the solubilised hemicellulose, was dried in an oven at 40-50 ºC to reduce the water content.

Various lignocellulosic biomass samples were examined in this study. Samples comprised olive stones, both in raw and torrefied forms, and a variety of commercially available hemicelluloses, crystalline cellulose, and lignin. Washed olive pits (*Olea europaea*) were sourced from Spain and are a by-product of the olive oil industry where they are separated, crushed to < 1 mm and air-dried. Olive stones were torrefied during 24 h at 280 ºC under nitrogen at the Arigna Fuels plant located in Leitrim, Ireland. A sample of the torrefied material was collected at the end of the experiment and held at ambient temperature in a desiccator. The commercial hemicelluloses were wheat arabinoxylan, tamarind seed xyloglucan, larch arabinogalactan, and guar galactomannan (Megazyme International, US). In

addition, crystalline cellulose and beechwood xylan (both from Sigma-Aldrich, US), and beechwood lignin (BOC Sciences, US) were used. The samples were used in different size cuts, and these were chosen to prevent loss of sample through the gaps in the wire mesh which were 40 µm, and to have uniform temperature throughout the particle. The particle size of the samples can be found in Table B.1.

B.2 Characterisation of components from fractionated olive stones

The hydrolysis of the samples was performed according to the National Renewable Energy Laboratory (NREL) standard operating procedure for the determination of structural carbohydrates and lignin in biomass [335]. The process included two main steps: a) two-stage acid hydrolysis of the samples and b) the gravimetric filtration of the hydrolysate in order to separate it from the Acid-Insoluble Residue (AIR). Klason Lignin (KL) was calculated by determining the weight difference between the AIR and its ash content, while Acid Soluble Lignin (ASL) was measured by determining the absorbance of an aliquot of the hydrolysate at 205 nm using an Agilent 8453 UV-Visible spectrophotometer and the results then converted to ASL based on Beer's law [335]. The concentrations of lignocellulosic sugars after hydrolysis were determined using ion chromatography (Dionex Corp., Sunnydale, CA) [336]. The process consisted of diluting the hydrolysate samples 20x with a deionised water solution containing known amounts of melibiose the internal standard. The diluted hydrolysates were filtered using 0.2 µm Teflon syringe filters and transferred into 1.5 mL vials. 10 µl of the diluted sample was injected to achieve sugar separation into arabinose, rhamnose, galactose, glucose, xylose, and mannose. Deionised water was used as the eluent; the flow rate applied was 1.5 mL/min, and the column/detector temperature was 21 ºC. Furthermore, NaOH (300 mM) was added to the post-column eluent stream due to the requirement of the photo-diode array detector to be in an alkaline environment in order to detect the presence of carbohydrates. NaOH was added using a Dionex GP40 pump, at a flow rate of 0.3 mL/min.

B.3 Composition of original samples

The particle size cuts (when available) are presented in Table B.1. Both ultimate and proximate analysis of raw and torrefied olive stones and all commercial samples are shown in Table B.2, along with the lower heating values (LHV) and higher heating values (HHV). The carbon content increased, and the hydrogen content decreased following torrefaction of olive stones since decrease in moisture content and sugars, mostly related to the degradation of thermally unstable monomers such as xylan and glucomannan that start to decompose at 200-300 ºC. Arabinoxylan, arabinogalactan and xyloglucan presented similar C and H contents (~40 and ~6 wt.%, respectively), whereas glucomannan showed higher C (53 wt.%) and lower H (5 wt.%).

Table B.1 Particle size cuts of the studied samples

Sample	Size cut (μm)
Olive stones	180-450
Torrefied olive stones	180-450
Crystalline cellulose (Sigma-Aldrich)	50-80
Beechwood xylan	50-125
Beechwood lignin	50-100
Wheat arabinoxylan	-
Tamarin seed xyloglucan	-
Larch arabinogalactan	-
Guar galactomannan	-

The chemical composition of original olive stones and sample torrefied at 280 ºC at Arigna Fuels is shown in Table B.3. Table B.3 shows the gradual change in the chemical composition of olive stones occurred during torrefaction with the reduction in hemicellulose and cellulose content from 25.6 to 19.9 % and from 25.4 to 19.9 %, whereas lignin content decreased only slightly from 30.5 to 28.1 %, respectively.

Table B.2 Proximate and ultimate analyses, and lower and higher heating values of the original samples.

Sample	Ultimate analysis	Moisture	Ash	HHV	LHV

	(wt. % dry basis)				(wt. %)	(wt. %)	(MJ/kg, ar)	
	C	H	N	O[a]				
Raw olive stones	44.8	5.8	0.2	48.4	15.5	0.8	20.3	18.8
Torrefied olive stones	54.9	5	1	37	0.6	2.1	22.7	21.7
Crystalline cellulose	42.5	6.2	0.03	50.9	4.3	0.3	18.0	16.1
Beechwood xylan	39.6	6	0.2	50.5	6	3.7	14.0	12.2
Beechwood lignin	31.4	4.3	0.5	63.2	2.2	0.6	26.1	24.3
Wheat arabinoxylan	36.7	5.7	0.08	56.8	14	0.7	-	-
Tamarind seed xyloglucan	41.9	6.1	0.35	50.5	8.3	1.2	-	-
Larch arabinogalactan	38.7	6	0.02	54.9	7.4	0.4	-	-
Guar galactomannan	53.2	5.1	0.08	41.5	14	0.1	-	-

[a]obtained by difference

Table B.3 Calculated content (in g) of cellulose, hemicellulose, lignin acid-soluble, lignin acid-insoluble and extractives for 100 g of original olive stones and sample torrefied at Arigna Fuels. HPLC and wet chemical analysis according to NREL technical reports.

	Yield	Cellulose	Hemicellulose	Lignin acid-soluble	Lignin acid-insoluble	Extractives
Raw olive stones	100	25.4	25.6	28.9	1.6	3
Torrefied olive stones, 280°C	82.3	19.9	19.9	26.7	1.4	4.2

B.4 Elemental composition of fractionated samples

The ultimate and proximate analyses of fractionated lignocellulosic compounds from olive stones are shown in Table B.4.

Table B.4 Proximate and ultimate analyses of the lignocellulosic compounds fractionated from raw olive stones.

Fractionation	Feedstock	Ultimate analysis (wt. % dry basis)				Moisture (wt. %)	Ash (wt. %)
		C	H	N	O[a]		
170°C, no acid	Cellulose	51.1	6	0.25	41.7	1.8	1.0
	Hemicellulose	41.5	6.6	0.23	51.1	10	0.6
	Lignin	44.4	5.8	0.21	47.5	5.6	2.1
170°C, acid	Cellulose	49.4	6.1	0.2	43.4	2.1	0.9
	Hemicellulose	47.2	6.2	0.32	45.1	9.4	1.2
	Lignin	62.9	6.1	0.3	30.2	2.1	0.5
180°C, no acid	Cellulose	36.3	5.9	1.3	55.2	4.7	1.3
	Hemicellulose	43.7	7.1	0.1	46.1	10.6	3
	Lignin	64.2	5.6	1	27.6	3.7	1.6
180°C, acid	Cellulose	39.7	6.2	1.8	51.1	4.7	1.2
	Hemicellulose	38.2	7.1	1.9	50.6	6.8	2.2
	Lignin	61.4	5.7	2.7	29	4.1	1.2
190°C, no acid	Cellulose	45.8	5.5	0	47.2	4.3	1.5
	Hemicellulose	44.2	6.6	0	46.8	7.2	2.4
	Lignin	63.6	5.8	0	26.3	2.3	4.3

[a]obtained by difference

B.5 Elemental composition of the chars

The ultimate and proximate analyses of the chars from commercial compounds and fractionated compounds are shown in Tables B.5 and B.6, respectively.

Table B.5 Proximate and ultimate analyses of the chars.

Sample	Condition #	Ultimate analysis (wt. % dry basis)				Moisture (wt. %)	Ash (wt. %)
		C	H	N	O[a]		
Olive stones	1	78.6	2.65	0.00	15.4	2.4	3.4
	2	84.2	0.76	0.00	9.14	4.5	5.9
	3	82.0	0.48	0.73	13.1	2.9	3.7
Olive stones (torrefied)	1	78.2	2.96	0.00	12.2	3.0	6.6
	2	85.4	0.73	0.00	9.87	4.1	4
	3	73.1	0.79	0.63	20.8	2.7	4.7
Beechwood xylan	2	70.6	1.50	0.00	11.3	4.7	16.8
Beechwood lignin	2	27.9	2.41	0.47	23.1	1.4	46.1
Wheat arabinoxylan	2	74.1	1.63	2.23	11.5	4.9	10.5
Tamarin xyloglucan	2	80.2	2.45	0.33	10.7	2.8	6.3
Larch arabinogalactan	2	77.2	1.99	0.00	7.81	3.6	13
Guar galactomannan	2	78.9	1.65	0.47	19.0	5.5	0

[a]obtained by difference

Table B.6 Proximate and ultimate analyses of the chars from fractionated olive stones.

Fractionation	Feedstock	Ultimate analysis (wt. % dry basis)				Moisture (wt. %)	Ash (wt. %)
		C	H	N	O[a]		
180°C, no acid (O1)	Cellulose	75.5	1.06	0.40	13.2	4.9	9.8
	Hemicellulose	75.9	0.43	0.23	15.8	6.5	7.6
	Lignin	86.7	1.29	0.15	11.8	3.7	0.04
180°C, acid (O2)	Cellulose	75.3	0.66	0.28	3.36	3.1	20.4
	Hemicellulose	69.2	0.36	0.00	21.4	10.1	9
	Lignin	87.5	1.68	0.24	9.88	1.8	0.7
170°C, no acid (O5)	Cellulose	63.8	2.29	0.50	25.2	3.8	8.2
	Hemicellulose	82.1	1.17	0.55	7.18	10	9
	Lignin	67.6	2.07	0.39	25.6	2.1	4.3
170°C, acid (O6)	Cellulose	66.9	1.86	0.42	10.2	2.7	20.6
	Hemicellulose	76.6	1.51	0.41	5.88	7.1	15.6
	Lignin	89.3	2.66	0.38	6.36	2.1	1.3

[a]obtained by difference

C. DATA RELATIVE TO THE CO-GASIFICATION OF BIOMASS WITH COAL

Table C.1. Rate constant values for the kinetic fitting of the volumetric model (VM), grain model (GM), and random pore model (RPM) of all chars.

rate constant (s^{-1}) x 10^2						
	VM		GM		RPM	
	OR	SL	OR	SL	OR	SL
800	0.626	0.0663	0.466	0.0502	0.359	0.0423
900	1.627	0.0980	1.191	0.0620	0.467	0.060
950	1.445	0.2042	1.945	0.2843	0.657	0.171
1000	2.747	0.468	2.297	0.339	0.923	0.289

Table C.2. R^2 values for the kinetic fitting of the volumetric model (VM), grain model (GM), and random pore model (RPM) of all chars.

R^2						
	VM		GM		RPM	
	OR	SL	OR	SL	OR	SL
800	0.9641	0.9752	0.9913	0.9963	0.9953	0.996
900	0.9411	0.9492	0.9757	0.9944	0.9964	0.9612
950	0.9466	0.9921	0.8967	0.9991	0.9802	0.9907
1000	0.9757	0.9942	0.9902	0.9995	0.9974	0.999

Table C.3. Activation energy and pre-exponential factor values for the kinetic fitting of the volumetric model (VM), grain model (GM), and random pore model (RPM) of all chars.

	VM		GM		RPM	
	OR	SL	OR	SL	OR	SL
Activation energy (kJ mol^{-1})	83.7	105.4	96.2	116.7	51.9	109.8
Pre-exponential factor (s^{-1})	7.49E+03	7.24E+03	2.29E+04	1.92E+04	1.11E+02	7.59E+03

Table C.4. R^2 values values for the Arrhenius fitting of the volumetric model (VM), grain model (GM), and random pore model (RPM) of all chars.

VM		GM		RPM	
OR	SL	OR	SL	OR	SL
0.8896	0.8573	0.9921	0.7845	0.9159	0.8613

Table C.5. Experimental rate constant values for the kinetic fitting of the volumetric model (VM), grain model (GM), and random pore model (RPM) for all experimental blends during gasification at 900 ºC.

rate constant (s^{-1}) x 10^2								
VM			GM			RPM		
50OR - 50SL	25OR - 75SL	10OR - 90SL	50OR - 50SL	25OR - 75SL	10OR - 90SL	50OR - 50SL	25OR - 75SL	10OR - 90SL
0.600	0.214	0.101	0.447	0.156	0.073	0.359	0.125	0.061

Table C.6. R^2 values for the kinetic fitting of the volumetric model (VM), grain model (GM), and random pore model (RPM) for all blends (experimental) during gasification at 900 ºC.

R^2								
VM			GM			RPM		
50OR - 50SL	25OR - 75SL	10OR - 90SL	50OR - 50SL	25OR - 75SL	10OR - 90SL	50OR - 50SL	25OR - 75SL	10OR - 90SL
0.9742	0.9944	0.9986	0.9964	0.9993	0.9955	0.9977	0.998	0.9945

CURRICULUM VITAE

PERSONAL INFORMATION

Surname, Name: Magalhaes, Duarte
Nationality: Portuguese
Date and Place of Birth: 26 March 1990, Lisbon, Portugal
Phone: +90 312 210 7233
email: duarte.magalhaes@metu.edu.tr

EDUCATION

Degree	Institution	Year of Graduation
MSc (Mechanical Engineering)	IST, University of Lisbon	2015
BSc (Mechanical Engineering)	IST, University of Lisbon	2012

WORK EXPERIENCE

Year	Place	Enrollment
2016-Present	METU	Research Assistant

LANGUAGES

Portuguese (native); English (C2); Spanish (B2); Turkish (A2)

PUBLICATIONS

1. Magalhaes D, Kazanç F, Influence of biomass thermal pre-treatment on the particulate matter formation during pulverized co-combustion with lignite coal, under preparation for submission to ***Fuel Processing Technology.***

2. Magalhaes D, Akgul A, Kazanç F, Costa M. Interactions during CO_2 co-gasification of biomass and coal chars obtained from fast pyrolysis in a drop tube furnace. ***Energy & Fuels*** 2021.

3. Magalhaes D, Gürel K, Matsakas L, Christakopoulos P, Pisano I, Leahy J.J., Kazanç F, Trubetskaya A. Prediction of yields and composition of char from fast pyrolysis of commercial lignocellulosic materials, organosolv fractionated and torrefied olive

stones. ***Fuel*** 2021; 119862

4. Trubetskaya A, Budarin V, Arshadi M, Magalhaes D, Kazanç F, Hunt A, Supercritical extraction of biomass as an effective pretreatment step for the char yield control in pyrolysis. ***Renewable Energy*** 2021; 170:107-117.

5. Uluca K, Sivasligil M, Magalhaes D, Kazanç F, Single particle combustion characterization of Turkish olive residue with infrared spectroscopy, under review in ***Combustion and Flame***.

6. Akin, S.Ş., Magalhaes, D., Kazanç, F., 2020. A study on the effects of various combustion parameters on the mineral composition of Tunçbilek fly ash. ***Fuel*** 2020; 275:117881

7. Magalhaes D, Panahi A, Kazanç F, Levendis YA. Comparison of single particle combustion behaviours of raw and torrefied biomass with Turkish lignites. ***Fuel*** 2019; 241:1085–94

8. Magalhaes D, Riaza J, Kazanç F. A study on the reactivity of various chars from Turkish fuels obtained at high heating rates. ***Fuel Processing Technology*** 2019; 185:91–9

9. Magalhaes D, Kazanç F, Ferreira A, Rabaçal M, Costa M. Ignition behavior of Turkish biomass and lignite fuels at low and high heating rates. ***Fuel*** 2017; 207:154–64

10. Magalhaes D, Kazanç F, Riaza J, Erensoy S, Kabaklı Ö, Chalmers H. Combustion of Turkish lignites and olive residue: Experiments and kinetic modelling. ***Fuel*** 2017; 203:868-876

11. Simões G, Magalhaes D, Rabaçal M, Costa M. Effect of gas temperature and oxygen concentration on single particle ignition behavior of biomass fuels. ***Proceedings of the Combustion Institute*** 2016; 36:2235–42